

MICROCOPY RESOLUTION TEST CHART
NATIONAL BUREAU OF STANDARDS-1963-A

**US Army Corps
of Engineers**Construction Engineering
Research Laboratory

USA-CERL TECHNICAL MANUSCRIPT M-87/15

September 1987

New Technology for EMP/EMI Shielded Structures

②

AD-A187 535

A Dynamic Analysis of the Parallel-Plate EMP Simulator Using a Wire Mesh Approximation and the Numerical Electromagnetics Code

by
Stephen Douglas Gedney

The Electromagnetic Pulse (EMP) produced by a high-altitude nuclear blast presents a severe threat to electronic systems due to its extreme characteristics. To test the vulnerability of large systems, such as airplanes, missiles, or satellites, they must be subjected to a simulated EMP environment.

One type of simulator that has been used to approximate the EMP environment is the Large Parallel-Plate Bounded-Wave Simulator. It is a guided wave simulator which has the properties of a transmission line and supports a single TEM mode at sufficiently low frequencies. This type of simulator consists of finite-width parallel-plate waveguides, which are excited by a wave launcher and terminated by a wave receptor.

This study addresses the field distribution within a finite-width parallel-plate waveguide that is matched to a conical tapered waveguide at either end. Characteristics of a parallel-plate bounded-wave EMP simulator were developed using scattering theory, thin-wire mesh approximation of the conducting surfaces, and the Numerical Electronics Code (NEC). Background is provided for readers to use the NEC as a tool in solving thin-wire scattering problems.

**DTIC
ELECTE
NOV 20 1987
S D**

The contents of this report are not to be used for advertising, publication, or promotional purposes. Citation of trade names does not constitute an official indorsement or approval of the use of such commercial products. The findings of this report are not to be construed as an official Department of the Army position, unless so designated by other authorized documents.

*DESTROY THIS REPORT WHEN IT IS NO LONGER NEEDED
DO NOT RETURN IT TO THE ORIGINATOR*

UNCLASSIFIED

SECURITY CLASSIFICATION OF THIS PAGE

AD-A187535

REPORT DOCUMENTATION PAGE				Form Approved OMB No 0704 0188 Exp Date Jun 30 1986	
1a REPORT SECURITY CLASSIFICATION UNCLASSIFIED		1b RESTRICTIVE MARKINGS			
2a SECURITY CLASSIFICATION AUTHORITY		3 DISTRIBUTION/AVAILABILITY OF REPORT Approved for public release; distribution is unlimited.			
2b DECLASSIFICATION/DOWNGRADING SCHEDULE		5 MONITORING ORGANIZATION REPORT NUMBER(S)			
4 PERFORMING ORGANIZATION REPORT NUMBER(S) USA-CERL TM M-87/15		7a NAME OF MONITORING ORGANIZATION			
6a NAME OF PERFORMING ORGANIZATION U.S. Army Construction Engr Research Lab		6b OFFICE SYMBOL (If applicable)		7b ADDRESS (City, State, and ZIP Code)	
6c ADDRESS (City, State, and ZIP Code) P.O. Box 4005 Champaign, IL 61820-1305		9 PROCUREMENT INSTRUMENT IDENTIFICATION NUMBER			
3a NAME OF FUNDING SPONSORING ORGANIZATION Office of the Chief of Engr		3b OFFICE SYMBOL (If applicable)		10 SOURCE OF FUNDING NUMBERS	
9c ADDRESS (City, State, and ZIP Code)		PROGRAM ELEMENT NO 4A162731	PROJECT NO AT41	TASK NO B	WORK UNIT ACCESSION NO 036
11 TITLE (Include Security Classification) A Dynamic Analysis of the Parallel-Plate EMP Simulator Using a Wire Mesh Approximation and the Numerical Electromagnetics Code (Unclassified)					
12 PERSONAL AUTHOR(S) Gedney, Stephen Douglas					
13a TYPE OF REPORT Final		13b TIME COVERED FROM _____ TO _____		14 DATE OF REPORT (Year, Month, Day) September 1987	
15 PAGE COUNT 160					
16 SUPPLEMENTARY NOTES Copies are available from the National Technical Information Service Springfield, VA 22161					
17 COSAT CODES		18 SUBJECT TERMS (Continue on reverse if necessary and identify by block number)			
FIELD	GROUP	SUB-GROUP		electromagnetic pulse simulators Parallel-Plate EMP Simulator wire mesh approximation (Cont'd)	
20	15				
19 ABSTRACT (Continue on reverse if necessary and identify by block number) The Electromagnetic Pulse (EMP) produced by a high-altitude nuclear blast presents a severe threat to electronic systems due to its extreme characteristics. To test the vulnerability of large systems, such as airplanes, missiles, or satellites, they must be subjected to a simulated EMP environment, which is characterized by a high peaked transient pulse with a planar wavefront that will uniformly illuminate a test object. One type of simulator that has been used to approximate the EMP environment is the Large Parallel-Plate Bounded-Wave Simulator. It is a guided wave simulator which has the properties of a transmission line and supports a single Transverse Electromagnetic Mode (TEM) at sufficiently low frequencies. This type of simulator consists of finite-width parallel-plate waveguides, which are excited by a wave launcher and terminated by a wave receptor. (Cont'd)					
20 DISTRIBUTION STATEMENT OF THIS ABSTRACT <input type="checkbox"/> UNCLASSIFIED <input checked="" type="checkbox"/> CONFIDENTIAL <input type="checkbox"/> RESTRICTED		21 ABSTRACT SECURITY CLASSIFICATION UNCLASSIFIED			
22 AUTHOR (Last Name, First Name) Gloria Wienke		23 TELEPHONE (Include Area Code) (217) 352-6511 (x353)		24 OFFICE SYMBOL CECER-IMI	

DD FORM 1473, 4-78

This form and its instructions may be used without restriction, provided the original source is properly acknowledged.

FORM PREPARED BY THE ARMY RESEARCH OFFICE-DURHAM

UNCLASSIFIED

UNCLASSIFIED

BLOCK 18 (Cont'd)

Numerical Electronics Code

BLOCK 19 (Cont'd)

This study addresses the field distribution within a finite-width parallel-plate waveguide that is matched to a conical tapered waveguide at either end. Characteristics of a parallel-plate bounded-wave EMP simulator were developed using scattering theory, thin-wire mesh approximation of the conducting surfaces, and the Numerical Electronics Code (NEC). Background is provided for readers to use the NEC as a tool in solving thin-wire scattering problems.

An alternate approach is to treat the simulator as a large conducting body and use scattering theory to solve the finite length simulator problem.

UNCLASSIFIED

TABLE OF CONTENTS

CHAPTER	PAGE
1 INTRODUCTION TO PARALLEL-PLATE EMP SIMULATORS	1
2 SOLUTION OF THE THIN-WIRE SCATTERING PROBLEMS USING THE NUMERICAL ELECTROMAGNETICS CODE	9
2.1 Theoretical Background of NEC	9
2.2 Solution of the Scattered Fields of Thin-Wire Structures	14
2.2.1 Thin-wire monopole	14
2.2.1.1 The Problem of over-sampling	17
2.2.1.2 The source model	19
2.2.2 Rhombic EMP simulator	20
2.2.2.1 Numerical solution using NEC	21
2.2.2.2 Characteristics of the rhombic EMP simulator	24
2.2.3 Scattering of a PEC plate	28
2.2.3.1 Numerical results	28
3 NUMERICAL ANALYSIS OF THE PARALLEL-PLATE BOUNDED-WAVE EMP SIMULATOR	91
3.1 Development of the Scattering Problem	91
3.2 Numerical Results	94
3.2.1 Computational considerations	98
3.3 Interpolation of the Wire Mesh Currents	99
3.3.1 One-dimensional smoothing of the wire currents	100
3.4 Simulator-Obstacle Interaction	105
4 CONCLUDING REMARKS	153
REFERENCES	157

CHAPTER I

INTRODUCTION TO PARALLEL-PLATE EMP SIMULATORS

The Electromagnetic Pulse (EMP) produced by a high-altitude nuclear burst presents a severe threat to electronic systems due to its extreme characteristics. In order to test the vulnerability of large systems, such as airplanes, missiles, or satellites, they must be subjected to a simulated EMP environment, which is characterized by a high peaked transient pulse with a planar wavefront that will uniformly illuminate a test object. One type of simulator that has been used to approximate the EMP environment is the Large Parallel-Plate Bounded-Wave Simulator. The parallel-plate bounded-wave simulator is a guided wave simulator which has the properties of a transmission line and supports a single TEM mode at sufficiently low frequencies. Ideally, it has a uniform characteristic impedance that is independent of frequency along the direction of propagation, and can be terminated by a matched impedance providing a pure traveling wave.

Parallel-plate bounded-wave EMP simulators consist of finite-width parallel-plate waveguides, which are excited by a wave launcher and terminated by a wave receptor. Typically, conical tapered waveguides are matched to the parallel-plate region in order to excite and terminate a plane wave in the parallel-plate region. This geometry is illustrated in Figure 1.1 (all tables and figures are located at the end of each chapter). The apex of the wave launcher is excited by a transient source which has a very fast rise time that is significantly smaller than the transit time of the waveguide, on the order of 1-5 nanoseconds, and a fall time on the order of 1 microsecond. In theoretical computations, the pulse is usually represented as a double exponential waveform and has broadband characteristics.

The problem being considered in this thesis is the solution of the field distribution within a finite-width parallel-plate waveguide that is matched to a conical tapered

waveguide at either end. The complete field representation is a superposition of discrete and continuous modes. At very low frequencies, where the plate separation is much less than one-half of a wavelength, only the TEM modes of the discrete spectrum will propagate along the waveguide. By assuming a finite-width parallel-plate waveguide of infinite length, the TEM field distribution can be obtained by means of a quasi-static approximation [1,2,3]. This analogy is useful in establishing the characteristic impedance and the field distribution of the line for low frequencies. Furthermore, quasi-static analysis on the conical tapered waveguide has been performed [4,5] by use of stereographic-projection and conformal-mapping techniques.

Under a transient pulse excitation of the parallel-plate simulator, there will be significant energy distributed throughout a very broad band, extending into the high frequency region. Unfortunately, for all practical purposes, the plate separation is quite large and the bandwidth of single-mode operation is much smaller than that of interest under pulse excitation. As a result, higher-order TE and TM modes will propagate along the waveguide. Furthermore, in the high-frequency region, the open simulator will act as a radiator and will no longer support purely guided modes.

In order to develop an accurate approximation of the field distribution within the simulator, non-TEM modes must be studied. Initially, assume the parallel-plate section to be infinitely wide and long. In this case, the modes can be thought of as those existing in a rectangular waveguide whose width goes to infinity [6]. For lower frequencies, it has been shown that a detailed field mapping, carried out at a single CW frequency, can be well approximated with the superposition of propagating modes when using the rectangular waveguide approximation. However, if further accuracy is desired, a more complete analysis can be derived by computing the discrete modes of a very long, finite-width parallel-plate waveguide. This problem was first approached by assuming either narrow plates [7] or wide plates [8,9,10]. In [7], Marin found that

for narrow plates (width \ll separation), the TE modes suffer greater attenuation as they propagate than the TM modes. Furthermore, it was found that for wide plates (width \gg separation), the TM modes have a greater attenuation than the TE modes [8,9,10]. Therefore, for the case of an arbitrary width, one should expect the existence of both propagating TE and TM modes inside the parallel-plate region.

A more complete analysis was performed at the University of Illinois [11,12,13] on the study of the source excitation of the finite-width parallel-plate waveguide. This analysis involved the computation of the total E field, as a superposition of the discrete and continuous spectrum. The results of [11,12] are valid for waveguides whose cross sections are large compared to a wavelength, whereas the results of [13] are valid for a small-to-moderate cross section.

It is important to understand that these techniques approximate the fields for an infinitely long parallel-plate waveguide. However, the parallel-plate region of the simulator is finite in length and is excited and terminated by conical transmission lines. Unfortunately, the previous quasi-static analyses do not account for the generation of spurious modes due to the mismatch at the interface of the two waveguides. A paper written by John Lam [14] develops an analytic expression for the TEM modes of a semi-infinite, finite-width, parallel-plate waveguide, excited by a conical transmission line. Although the formulation does not include the effects of any reflected fields, it does yield insight into the excitation process of the parallel-plate section. It should be realized that interfacing the two waveguides requires the matching of a spherical wavefront, which has E_θ and H_ϕ components, into a planar wavefront supported by the parallel-plate region. Along the vertical plane $y = a$ constant, the fields are matched across the transition as $E_z = -E_\theta \sin \theta$, $E_y = E_\theta \cos \theta$, $H_x = -H_\phi \cos \phi$ and $H_y = -H_\phi \sin \phi$; ϕ represents the angle between the center axis and the observation point, θ its elevation, and the origin is at the apex of the conical

waveguide. As a result, there will exist both transverse and longitudinal electric and magnetic fields at the interface, contributing to a superposition of TEM, TE, and TM modes. However, for gradual tapered end sections the mismatch is relatively small and the higher-order modes are quite small for low frequencies.

Furthermore, at the transition, there exists a certain time dispersion in matching the spherical wave into a plane wave [15] since the cross section is not a plane of constant phase. Referring to Figure 1.2, a dispersion distance is defined and is related to the time dispersion as

$$\Delta = \Delta\rho + \Delta y . \quad (1.1)$$

When the wavelength is less than or equal to four times the dispersion distance, the higher-order modes produced become significant in amplitude leading to a large distortion of the waveform. Therefore, the dispersion distance determines the so-called "band width" of the simulator.

The analyses that have been reviewed thus far in this chapter all offer excellent physical and theoretical interpretations of the parallel-plate bounded-wave EMP simulator by considering ideal situations. Through such modal analyses, the explanation of notches in the magnetic field has been determined [16], optimum loads designed, and other standards in design have been developed [17]. Furthermore, accurate field mappings have been generated, although they require the use of experimental data for their generation. This is quite efficient for simulators that have been constructed and for frequencies well within the simulator band-width. When designing a parallel-plate EMP simulator, the engineer has much more to consider than the transmission line properties of the simulator itself. It is very important to understand that once a test object is placed within the parallel-plate region the relative amplitudes of the modes may differ greatly from those calculated in an empty

working volume. Therefore, one cannot treat the calculated fields of the empty working volume as the incident field that establishes the charge and current on the test object. This so-called "simulator-obstacle interaction" can be analysed only for certain geometries [18,19,20,21], such as an infinite cylinder in a parallel-plate waveguide. Furthermore, the design engineer should be interested in the fields that will be radiated into the external environment over the entire frequency spectrum. There will be a number of resonant frequencies that exist due to various mismatches in geometries and loads, as well as to resonances of the parallel-plate region.

For the design of an alternate geometry or configuration, an in-depth analysis may be necessary and would prove to be quite time-consuming and difficult. However, to develop further theoretical insight into the problem, the ability to easily perform an accurate analysis using a dynamic field solution could be quite useful. The purpose of this thesis is to evaluate the well-known Numerical Electromagnetics Code (NEC), developed by Lawrence Livermore Laboratory [22], as a potential tool in generating a readily available analysis of the parallel-plate bounded-wave simulator in the frequency domain. The NEC code is a user-oriented code that is widely distributed, and if the problem is interpreted correctly, it can be a very useful tool for many electromagnetic scattering and antenna problems.

In Chapter 2, NEC is examined and the validity of solving scattering problems using the thin-wire approximation is developed. More specifically, the two-wire rhombic EMP simulator, as well as a two-dimensional plate scattering problem, are analyzed. The emphasis of the analogies is placed on interpreting the results and applying them to the development of a wire mesh model of the bounded-wave parallel-plate EMP simulator.

In Chapter 3, the wire mesh approximation of the surface of the conducting plates of the parallel-plate simulator is devised. The field distribution within the parallel-

plate region due to a continuous-wave excitation across the source gap is then computed using NEC. These results are interpreted and the limitations of the wire mesh approximation are investigated. Finally, various mechanisms contributing to phenomena such as the simulator band width and simulator-obstacle interaction are investigated.

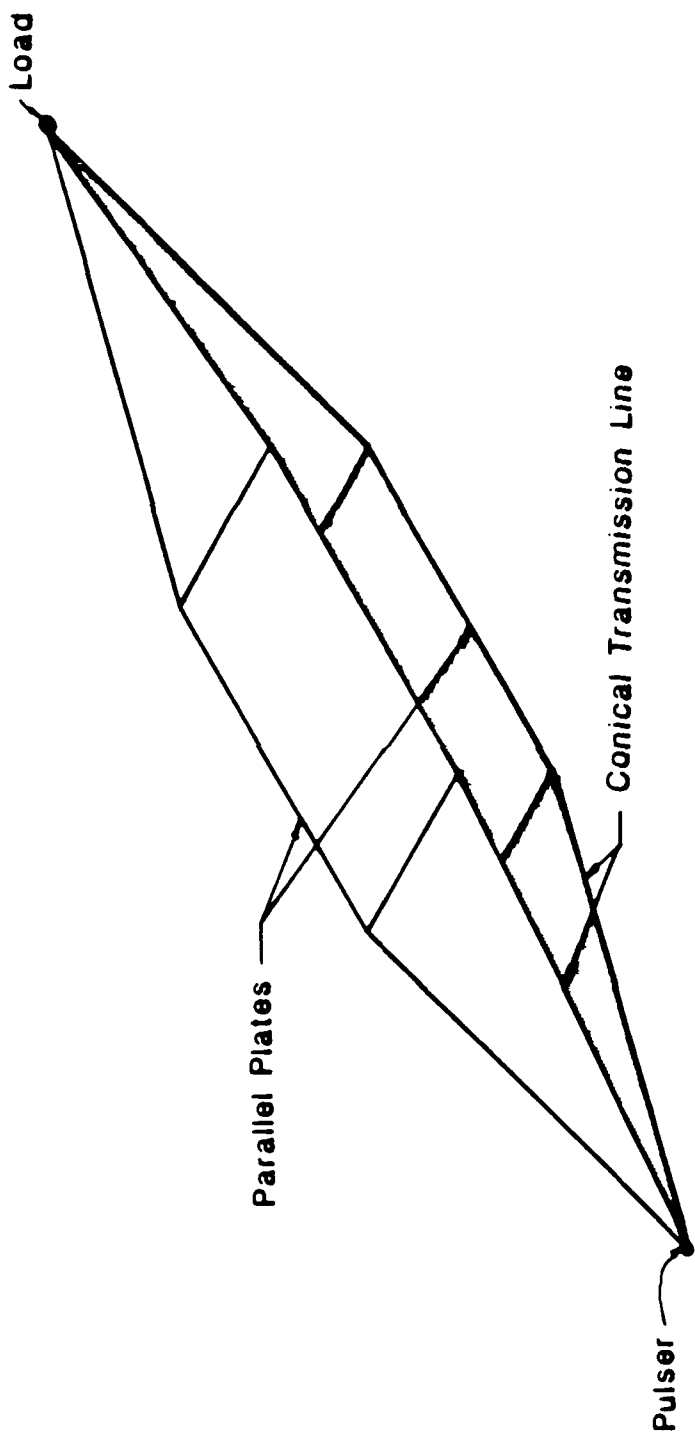


Figure 1.1. Symmetric parallel-plate bounded waveguide simulator.

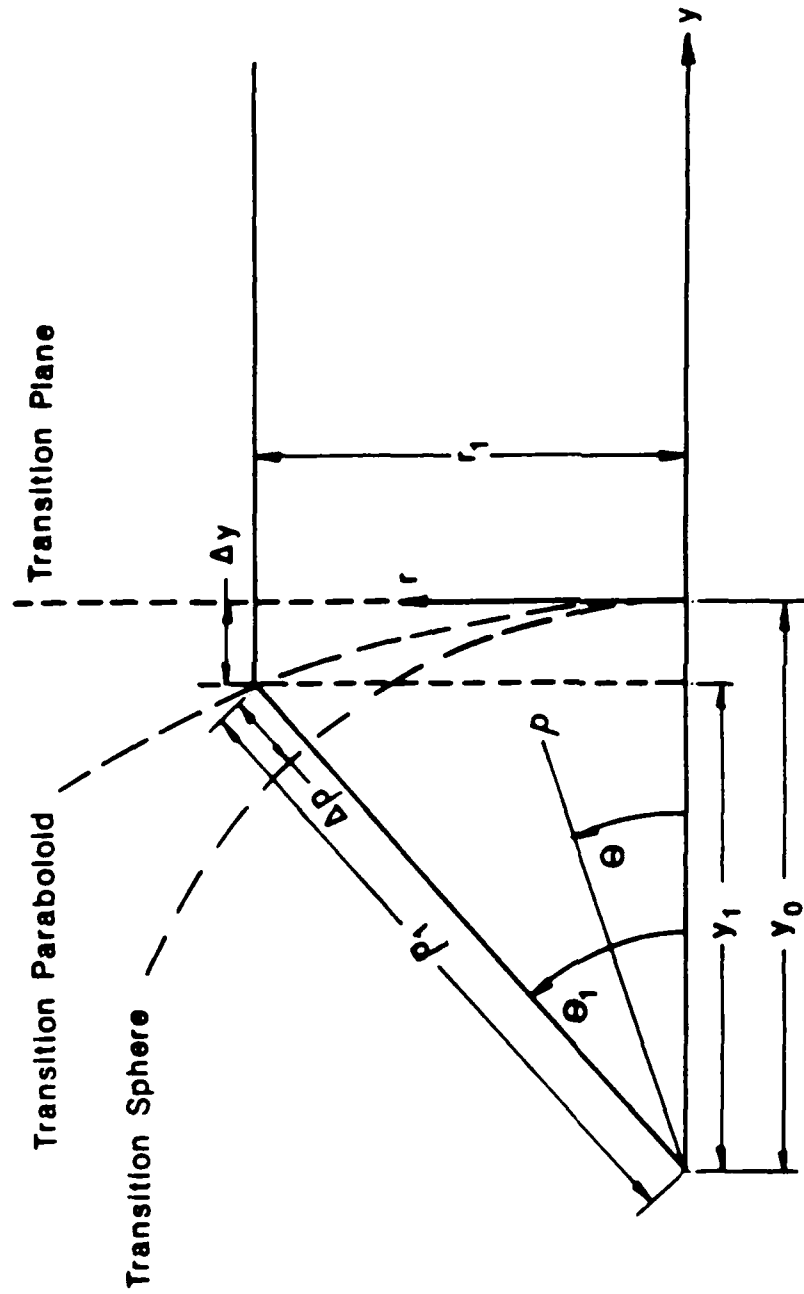


Figure 1.2. Matching of the conical tapered end section and the associated dispersion distance of the spherical wavefront.

CHAPTER 2

SOLUTION OF THIN-WIRE SCATTERING PROBLEMS USING THE NUMERICAL ELECTROMAGNETICS CODE

This chapter is intended to give the reader a useful background to employ the Numerical Electromagnetics Code (NEC) as a tool in solving thin-wire scattering problems. Initially, a brief theoretical background of NEC will be presented. Then, the validity of its solutions will be analyzed for the following problems: Thin monopole over a PEC ground plane, the rhombic EMP simulator, and the scattering of a thin square PEC plate. The goal of this analysis is to determine how to best model a conducting surface using a thin-wire approximation, as well as how to best model source excitations. With the understanding of how to interpret the results of the thin-wire approximation, this analysis will provide useful insight into the dynamic solution of the parallel-plate bounded-wave EMP simulator using NEC, which is presented in Chapter 3.

2.1 Theoretical Background of NEC

In this section, NEC will be used to solve thin-wire scattering problems, which involves solving for the induced currents on the wire's surface due to some incident field. However, the method of solution used by NEC must be understood before the thin-wire scattering problem can properly be developed. The complete analysis of NEC is provided in [22]. The following presents an overview of the theory used and provides the basis for our analysis.

The Numerical Electromagnetics Code is based on a moment method solution of the Electric Field Integral Equation (EFIE) for thin-wire scatterers and the Magnetic Field Integral Equation (MFIE) for closed volumes. In this analysis, only the solution

of the EFIE will be considered. The EFIE used by NEC is based on the thin-wire approximation in which the surface current can be assumed to be translationally invariant and a function of the direction of its wire axis only. This is valid if the radius of the wire scatterer is much smaller than a wavelength. Then the surface current can be approximated by a single filament on the wire axis, and the boundary conditions can be applied on the wire surface. This is better known as the Extended Boundary Condition [23]. Assuming a PEC surface, the applied boundary condition on the tangential field is limited to the axially directed field and is expressed as

$$E_z^i + E_z^s = 0 \quad (2.1.1)$$

where E_z^i is the axially directed incident field and E_z^s is the axially directed scattered field on the conducting surface which is produced by the current filament on the wire axis. With the use of the Extended Boundary Condition, the EFIE can then be reduced to a line integral, integrating over the wire axis, and can be expressed as

$$E_z^i = \frac{-1}{j\omega\epsilon_0} \int_L I(z') \left[\frac{d^2}{dz'^2} + k^2 \right] G(z, z') dz' + I(z) Z(z) \quad (2.1.2)$$

where

$I(z)$ = the unknown axial current

$G(z, z') = \frac{e^{-jk\sqrt{a^2 + (z-z')^2}}}{4\pi\sqrt{a^2 + (z-z')^2}}$ is the thin-wire approximation of the free-

space Green's function along the wire axis

$Z(z)$ = the distributed impedance loading along the wire surface

a = the wire radius and

$k = \frac{2\pi}{\lambda}$ = the free-space wave number.

The left-hand side of Equation (2.1.2) is the axially directed incident field on the wire surface and is assumed to be known while the axial current is the unknown.

However, this cannot be solved analytically, in general, and must be solved numerically. The numerical solution of the EFIE is then obtained with the use of the moment method solution [24].

The unknown axial current is expanded into a truncated series of basis functions weighted by unknown constant coefficients. The basis function was chosen to be a weighted three-term basis function, with the n^{th} basis function represented as

$$I_n(z) = A_n + B_n \sin(kz) + C_n \cos(kz). \quad (2.1.3)$$

Therefore, three unknowns have been introduced and three conditions are needed to solve for the constant weighting coefficients.

Initially, the wire geometry is broken up into a set of N individual wire segments, each of length Δ_n . Each basis function has a finite support lying on an interval that is centered on a wire segment, and extends to the center of adjacent segments at either end of the specified wire segment. The inner product of both sides of the EFIE is taken with a set of N testing functions. The testing functions are chosen to be mathematical point functions, where the n^{th} point function is located at the center of the n^{th} wire segment. The integral over the point function can be evaluated analytically, and the current basis functions can be rewritten as

$$I_n(z) = A_n + B_n \sin k(z - z_n) + C_n \cos k(z - z_n) \quad (2.1.4)$$

where $|z - z_n| < \frac{\Delta_n}{2}$ and z_n is the center of the n^{th} segment. Now, two of the three unknowns can be satisfied by enforcing charge and current continuities at the endpoints of the wire segments ($z = \pm \frac{\Delta_n}{2}$), where the line charge density is related to the current by the continuity equation

$$\frac{dI(z)}{dz} = -i\omega q. \quad (2.1.5)$$

Therefore, with the use of the three-term basis function, problems such as open-ended and/or tapered-wire structures, as well as multiple wire junctions, can be handled, within limitations of the approximations.

At the junction of two or more wire segments, current continuity is enforced by Kirchoff's law, which states that the sum of all the currents entering a common node must be zero. Furthermore, the total charge is assumed to be distributed over each individual wire corresponding to its wire radius.

For the case of an open-ended wire, one cannot expect the current to go to zero at the wire end if the wire has a finite radius. For a wire of radius a , the current at the wire end can be represented as a function of its derivative as [22]

$$I(z)|_{z \text{ at end}} = \frac{-(\hat{z} \cdot \hat{n}_c)}{k} \frac{J_1(ka)}{J_0(ka)} \frac{dI(z)}{dz} |_{z \text{ at end}} \quad (2.1.6)$$

where \hat{n}_c = the unit normal vector of the end cap and $\hat{z} = \pm 1$ indicates the direction of the normal. By applying the current and charge conditions at both ends of each wire segment, two of the three coefficients can be solved for. This leaves one coefficient to be solved for by the matrix inversion.

The incident E-field, E^i , on the left-hand side of Equation (2.1.2), is to be dictated by the physical problem. In this application, it is desirable to excite a thin-wire structure with a vertically directed E-field distributed over the surface of a small region. For the EMP simulator problem, this would denote the source gap region. The NEC offers two voltage source models. The first is the Current Slope Discontinuity (CSD) model, which consists of a highly localized voltage source across the biconical junction of two wires. The second type of source is an Applied Electric Field (AEF) source model. This model is a voltage source, of constant magnitude,

applied over a designated region of the wire structure. The resultant electric field can be represented as a pulse function, whose magnitude can be expressed as

$$E_j^i = \frac{V_j}{\Delta_j} e^{i\omega t} \quad (2.1.7)$$

where V_j is the complex amplitude of the applied voltage on the j^{th} segment and Δ_j is the length of the j^{th} segment.

The AEF is a desirable source model for defining a distributed field over the source gap region of the EMP simulator problem, and will be used for this application. However, one must realize its limitations before using it for any application. The AEF is constant over the entire wire segment it is applied and is assumed to be zero everywhere else. Therefore, on the left-hand side of the matrix formulation of Equation (2.1.2), the E-field is assumed to be a pulse function. However, the step discontinuity of the field is nonphysical and the actual incident field must be calculated from the computed currents. In this study, it is found that under certain conditions the field can vary a significant amount from its assumed value. Understanding this is quite important for two reasons. The first is the desire to accurately model the incident E-field source for a reliable approximation of the problem being solved. Second, the input impedance of the source is calculated by NEC assuming a constant current and E-field over the entire source region. However, in certain applications, this may not be a good approximation, and the result could be misleading. The reader is referred to the paper presented by Halpern and Mittra [25] for a complete analysis on the validity of the AEF and CVD voltage source models for the case of a thin-wire antenna. It was found that for source regions much smaller than the length of the antenna, and for the radius of the wire sufficiently small (\ll length of the source), the calculated AEF is much like the desired pulse. This is true since the thin-wire approximation being used, and the smaller the wire radius, the

better the approximation.

2.2 Solution of the Scattered Fields of Thin-Wire Structures

Before attempting the EMP simulator problem, a much simpler example will be analyzed first. It will then be possible to characterize the simulator problem by realizing certain limitations encountered when using NEC. Therefore, this section will emphasize: (1) The accuracy of the solution due to the number of unknowns, or wire segments, (2) The validity of the source model due to the characteristics of the antenna model, (3) The determination of conditions necessary to render the solution invalid. Three examples are analyzed for this purpose: (1) Thin-wire monopole over a PEC ground plane, (2) Two-wire rhombic antenna, (3) Plane-wave scattering of a thin PEC plate. These three examples are presented since they directly relate to the accuracy of various aspects of the parallel-plate EMP simulator model. The thin-wire *monopole helps to characterize the source model and the accuracy of the solution due to the number of basis functions chosen.* The rhombic antenna problem is treated as a transmission-line type of EMP simulator and enables one to evaluate the construction of the source and load regions as well as aid in the interpretation of results of the parallel-plate EMP simulator. Finally, the scattering of the PEC plate enables the characterization of the validity of the solution for the thin-wire mesh approximation of a surface when subject to an incident field.

2.2.1 Thin-wire monopole

Figure 2.1 illustrates the thin-wire monopole considered in this section. The NEC is used to solve for the axial current produced by a source excitation. The axial current is represented by the three-term basis functions. Recall that the testing functions used to generate the impedance matrix of the moment method solution were

chosen to be mathematical point functions. However, when using point matching one has to try to avoid sampling error, which leads to an incorrect approximation of the current. Therefore, it is important to perform a boundary condition check on the axially directed surface E-field to guarantee that

$$E_z^s = -E_z^i \quad (2.2.1)$$

is satisfied. It is recommended that at least 10 samples be taken per wavelength in order to minimize sampling error.

First, consider the case of a monopole that has a height $H=0.47 \lambda$ and radius a , where $H/a = 1000$. Figure 2.2 illustrates the resultant scattered axial E-field computed along the antenna surface in the axial direction. Note that there is boundary condition error at the trailing edge of the source region, and at the free wire end of the monopole. The singularity due to the free wire end is nonphysical, and is a result of the thin-wire approximation.

In the study of most antenna problems, it is desirable to compute the input impedance in order to best design a matching network for the antenna excitation. From the reciprocity theorem, it is easy to develop the relationship between the terminal voltage and the source field as [26]

$$V_{in} I_{in} = \int E^s(z) I(z) dz \quad (2.2.2)$$

where

$z = \text{the axial direction}$

$E^s = \text{MF source}$

$I(z) = \text{the axial current}$

and the integration is performed over the source region. Furthermore, by realizing that $E^s = -E^i$

$$Z_{in} = \frac{V_{in}}{I_{in}} = -\frac{1}{I_{in}^2} \int E^s(z) I(z) dz \quad (2.2.3)$$

which represents the antenna input impedance in terms of the computed scattered

field.

It can be shown that the above expression is stationary and is very insensitive to small errors in the computed current [25]. As the limit of the wire segment size becomes very small, the current becomes nearly constant on the wire. Therefore, assuming $I(z) = \text{a constant} = I_{in}$, the above integral equation reduces to

$$Z_{in} = -\frac{1}{I_{in}} \int E^s(z) dz \quad (2.2.4)$$

where the integral is over the source region. Now, if there is little boundary condition error on the wire surface, then it can be assumed that

$$V_s = -V_{in} = \int E^s(z) dz \quad (2.2.5)$$

Therefore, using the expression given in (2.1.6), the input impedance of the antenna can be approximated as

$$Z_{in} = \frac{V_{in}}{I_{in}} \quad (2.2.6)$$

where

$$V_{in} = \text{input source voltage}$$

and

$$I_{in} = \text{the current at the center of the wire segment.}$$

This is the particular approximation used by NEC. In this formulation the scattered field, which is computed from the axial wire current, is assumed to be a pulse function, such that the field is constant over the input wire segment, and zero everywhere else. Figure 2.3 illustrates the actual scattered field and the axial current computed over the source region for the example considered earlier (Figure 2.2) and provides a comparison with the AEF. The scattered field deviates somewhat from the expected pulse function, which leads to a small error in the input impedance. However, for antennas with much larger radii, the scattered field deviates greatly from the pulse function, and the approximate expression for the input impedance is no

longer valid. In this case, the stationary form of Equation (2.2.3) must be relied upon. A thorough analysis of this problem is provided in [25]. In that analysis it was found that if the radius of the wire was on the order of one-thousandth of the length of the monopole antenna, the boundary condition error became very small, and the approximate form of the input impedance was accurate to within a small percentage. However, for thicker antennas, where the radius is on the order of one-hundredth of the length of the antenna, the approximate form is not as accurate, and the stationary form of the input impedance should be used. Furthermore, for the thin-wire approximation to be valid, one should not use wire segments that have radii larger than one-eighth of the segment length; otherwise, the approximation breaks down.

There is one important limitation encountered when using NEC that is not considered by [25], and that is the problem of over sampling. In other words, what happens if the segment size becomes too small? The following is an analysis of this problem.

2.2.1.1. The problem of over-sampling. Over-sampling can occur if too many wire segments are chosen to represent the geometry such that the segment size becomes too small. This leads to unreliable results for the axial current, and, hence, the scattered fields. The reason for this error is purely numerical. As discussed earlier, the current is expanded into a series of three-term current basis functions. The current expression is given by Equation (2.1.4). Initially, A_i is chosen to be equal to -1 to reduce the number of computations. Then, after satisfying Kirchoff's law and charge continuity, the complete basis function is defined by

$$A_i = -1$$

$$B_i = (a_i^- Q_i^- + a_i^+ Q_i^+) \frac{\sin k \Delta_i / 2}{\sin k \Delta_i}$$

$$C_i = (a_i^- Q_i^- - a_i^+ Q_i^+) \frac{\cos k \Delta_i / 2}{\sin k \Delta_i} \quad (2.2.7)$$

where

$$Q_i^- = \frac{a_i^+ (1 - \cos k \Delta_i) - P_i^+ \sin k \Delta_i}{(P_i^- P_i^+ + a_i^- a_i^+) \sin k \Delta_i + (P_i^- a_i^+ - P_i^+ a_i^-) \cos k \Delta_i}$$

$$Q_i^+ = \frac{a_i^- (\cos k \Delta_i - 1) - P_i^- \sin k \Delta_i}{(P_i^- P_i^+ + a_i^- a_i^+) \sin k \Delta_i + (P_i^- a_i^+ - P_i^+ a_i^-) \cos k \Delta_i}$$

and

$$P_i^- = \sum_{j=1}^{N^-} \left(\frac{1 - \cos k \Delta_j}{\sin k \Delta_j} \right) a_j^+$$

is the summation of the N^- segments connected to end 1 of the i^{th} segment.

Furthermore,

$$P_i^+ = \sum_{j=1}^{N^+} \left(\frac{\cos k \Delta_j - 1}{\sin k \Delta_j} \right) a_j^+$$

is the summation of the N^+ segments connected to end 2 of the i^{th} wire segment.

Finally, a_i contains the unknown coefficients, and is a function of the segment wire radius. However, it is important to understand what happens to the Q_i^\pm as Δ_i

becomes much smaller than λ , or as $\frac{2\pi\Delta_i}{\lambda}$ becomes very small. Analysing the

expressions for P_i^+ and P_i^- shows that they are a function of

$$\pm \frac{1 - \cos k \Delta_j}{\sin k \Delta_j}.$$

Therefore, as $\Delta_j \rightarrow 0$, both $1 - \cos k \Delta_j \rightarrow 0$ and $\sin k \Delta_j \rightarrow 0$. Similarly, in Q_i^\pm , both the numerator and denominator tend to zero as the segment length becomes increasingly smaller. Numerically, a computer cannot handle this and the program will suffer from underflow during the matrix fill. Subsequently, serious errors will result in the computed current. It should be noted that the exact place that underflow will occur depends on the precision of the computer used. The following results were obtained for NEC written in double-precision Micro-Soft Fortran, which has 32 bytes

of precision, and running on an AT&T PC6300 desktop computer.

In Volume II, Section 2 of [22], it is recommended that the segment length should not be smaller than $10^{-3}\lambda$ due to this underflow error. However, the program itself does not flag the user if underflow does occur, and an erroneous solution does result. Therefore, the user must be very careful in interpreting his/her results. The following is a good example of this over-sampling problem.

Consider a short monopole over a PEC ground plane, where $H/\lambda = 0.1$, and $H/a = 1000$. Table 2.1 illustrates the self-term of the matrix, computed over the source segment, as well as the current and surface E-field, as a function of the number of wire segments. Note that the AEF is applied over the first segment only in each case, and all segments are of equal lengths. For this example, it was found that if the segment length becomes $< 0.005\lambda$, the solution becomes quite unreliable. Therefore, when the segment length is on the order of $10^{-3}\lambda$, it is very important to check the accuracy of the solution with at least a boundary condition check of the axial surface E-field, or by monitoring the self-terms of the short wire segments.

2.2.1.2. The source model. This thesis is concerned with the time domain pulse excitation of an antenna. Therefore, when solving for the currents and scattered fields in the frequency domain, it is necessary to solve the problem over a broad frequency range. However, for each frequency it is desirable to minimize the number of unknowns to reduce the computation time, but still obtain an accurate solution. In order to model the antenna in a consistent manner, the source region must be the same for all frequencies. Therefore, the segments denoting the source region must be small enough such that the wire segments do not exceed 0.1λ in length. This can easily be avoided by cascading voltage sources in series if necessary. However, one must also be careful to ensure that the source does not become too small; otherwise, the result will suffer from over-sampling error. This could be a severe limitation when considering

problems where the wavelength is much longer than the source region. For much larger problems, such as the parallel-plate bounded-wave simulator, this obviously is much more of a concern since the source region is much smaller than the size of the structure. Finally, one must be careful that the wire radius does not exceed one-eighth of the wire length; otherwise, the thin-wire approximation will break down.

With the use of the monopole antenna problem some intuitive insight to the interpretation of the results of the larger EMP simulator problem can be gained. The cases of the antenna being 2λ and 1λ in length are considered. In the example, the source region will be composed of 2 wire segments, where the AEF is distributed only on the first segment, and is of height HS . The effects on the segment current as the source region becomes very small is illustrated in Table 2.2. As was found previously, error in the self-term arises when the length of the segment is on the order 10^{-3} . Figure 2.4 illustrates the axially directed E-field on the wire surface over the source region as HS reduces in size. A significant boundary condition error is noted in Figure 2.4(c), when $HS/\lambda = \text{self-term}$.

2.2.2 Rhombic EMP simulator

The parallel-plate bounded-wave EMP simulator is usually referred to as a transmission line type of simulator since it supports guided waves, and is typically terminated by a matching impedance. Therefore, the fields can be expressed as a superposition of discrete and continuous modes. Various modal solutions for the finite width plate geometry are discussed in Chapter 1. However, these analogies do not treat the problem as a finite length transmission line, but as an infinite, or semi-infinite problem. In order to develop a better understanding of the parallel-plate bounded-wave EMP simulator as a transmission line type of simulator, it will be instructive to analyze an elementary configuration first. In order to do this the

physical attributes of the simulator geometry is utilized.

As a result of the finite width of the conducting plates of the parallel-plate simulator, most of the current will be distributed at the edges of the plate. Therefore, a first-order approximation would be to limit the current to a line current located at the outer edges of the plates. Furthermore, if the line currents follow the edges of the conical end sections and meet in the center above the parallel-plate region, the geometry resembles that of the well-known rhombic antenna. The far-field characteristics of the two-wire conductor rhombic antenna are well known [27]; however, it is the near-field characteristics, computed between the conducting wires, that are of interest for the EMP simulator application. More recently, Shen and King have identified the usefulness of the rhombic antenna as a transmission-line type of EMP simulator [28-32]. Not only did they show the fields to be quite uniform between the conducting wires, and predominately TEM, but they also identified its usefulness as an analogous problem to the parallel-plate type of simulator. In their works, an extensive experimental and theoretical analysis of the problem is provided, and the reader is encouraged to review them.

2.2.2.1. Numerical solution using NEC. In this section, the solution of the field distribution within the bounded region of the conducting wires, when the rhombic EMP simulator is excited by a continuous-wave excitation across the source-gap region and terminated by a purely resistive load impedance, is derived numerically using NEC. The results are then compared to the theoretical and experimental results published by Shen and King [28-32].

The rhombic antenna is modeled as a thin-wire structure, and the currents on the wires are assumed by the three-term basis function described earlier in this chapter. However, complications arise while trying to establish a proper source and load model for the transmission-line type of simulator. Therefore, an analysis of this problem

will be extremely useful in establishing a model of the source and load regions that successfully approximates previous theoretical and experimental results. These results will be used in the analysis of the parallel-plate simulator problem. The following is the development of the source and load models using a thin-wire approximation.

Source Model.

The source model is extremely important in establishing the proper excitation of the transmission-line type of EMP simulator. The fields produced in the region between the conducting wires, usually referred to as the working volume, are expected to be TEM for lower frequencies as the structure is essentially a simple transmission line. The source must be oriented such that the TEM mode, which contains a vertical E-field component, is excited. Therefore, the desired source is a time harmonic potential of constant amplitude established by a vertical E-field distributed across the 2-dimensional source gap. However, using a thin-wire antenna, modeled by NEC, one is limited to a finite length line source. The Applied E-Field (AEF) source discussed in Section 2.1, which is a constant E-field distributed over a wire segment, best approximates the desired excitation. Figure 2.5(a) illustrates the thin-wire model of the source region. The applied voltage is expressed as

$$V = \int \vec{E}^t \cdot d\vec{l}.$$

It must be realized that there is a definite tradeoff to this configuration due to the introduction of a sharp bend in the thin-wire geometry. In Section 2.1 it was discussed that charge and current continuities are established at the junction of two or more wires. However, even though the continuity of total current is maintained, the individual basis vectors of the current are discontinuous. This discontinuity in the current leads to a nonphysical singular behavior in the E-field, resulting in a

boundary-condition error of the tangential E-field on the wire surface. Therefore, one must be careful that this singularity does not significantly affect computed current distribution on the conducting wires throughout the structure or the characteristics of the simulator.

Figure 2.6 illustrates the computed scattered E-field along the axial direction on the surface of the source-gap wire segment due to a constant incident E-field distributed over the length of the wire. The boundary condition error is apparent at the bend; however, it was found that this configuration yielded the best results in comparison to Shen and King's data.

Terminating Load Impedance.

In order to avoid standing waves on the transmission line, the rhombic simulator must be terminated in its characteristic impedance. For low frequencies, where the center height is much smaller than a wavelength, the characteristic impedance is nearly constant and the simulator is best matched by a purely resistive load. The dominant mode is TEM to y, and the E-field is in the vertical direction, z. Therefore, the load should be oriented in the same direction as the vertical E-field such that the energy is dissipated by the load. Since \vec{E} is related to the electric vector potential as

$$\vec{E} = -j\omega\mu\vec{A} + \nabla\nabla\cdot\vec{A}$$

the current induced on the wire will be in the direction of the incident E-field. Therefore, the wire load should be oriented in the z-direction. The geometrical configuration of the wire-load is similar to that of the source, where the loading resistance is distributed uniformly over the wire. It was found that the transmission line was best matched by placing the load in parallel across the load gap. This is illustrated in Figure 2.5(b) (page 45). Again, one must be aware of the existence of boundary-condition error due to the abrupt bend in the wire.

Characteristic Impedance.

It is expected that if the transmission-line-type simulator is indeed terminated in its characteristic impedance, then the current along the wires will be purely traveling wave. However, because of the existence of higher-order modes, there will be some reflection from the load. Furthermore, the characteristic impedance of the line will change with frequency, and in order to determine its value, the analogy used by Shen and King [28] will be followed. The Standing Wave Ratio (SWR) of the current is found as a function of the load impedance. When the SWR is minimized, the line can be assumed to be matched. At lower frequencies, the simulator fields are bounded and most of the energy is dissipated by the load. However, small deviations in load impedance will lead to large changes in the SWR of the line. At higher frequencies, the structure will radiate a significant amount of energy. Therefore, there is less energy to be dissipated by the load, and the resultant reflected waves will be smaller. This is illustrated by Figure 2.7. At lower frequencies, more energy is distributed in the vertical E-field, which is predominately TEM, and is dissipated by the load. However, at higher frequencies, higher-order modes exist, and a larger percentage of the energy is distributed in the transverse and longitudinal components of the field, which are not dissipated by the load. Therefore, the load is often sloped or distributed such that these higher-order modes can be dissipated, and not reflected back into the center parallel-plate region.

2.2.2.2. Characteristics of the rhombic EMP simulator. The purpose of this analysis is to investigate the computed characteristics of the transmission-line-type rhombic EMP simulator using the Numerical Electromagnetics Code. Initially, the characteristic impedance is determined by finding the terminating load impedance that minimizes the standing-wave ratio of the conducting wire currents. The currents and the input impedances are analyzed as a function of the load as well as a function of

frequency. Finally, the electric field distribution within the area between the conducting wires is examined, and its uniformity as a function of frequency is determined. The results are compared to both the experimental and theoretical results published by Shen and King. Therefore, the same simulator geometry studied by Shen and King [28] is used here. This is illustrated in Figure 2.8.

The broad-band characteristics of the simulator can be defined by three regions of interest. In the low-frequency region, where the wavelength is much larger than the maximum height of the simulator, the field has predominately TEM characteristics and is quite uniform. In the middle-frequency region, the height of the simulator is on the order of a wavelength and higher-order modes become more significant. Finally, in the high-frequency region, the structure acts as a radiator, and very little energy is actually dissipated by the terminating load impedance. For simplicity, each of the three regions is defined by a single frequency. The regions are defined by: 1) $\lambda = 4 m$, 2) $\lambda = 1 m$, 3) $\lambda = 0.5 m$.

Initially, the characteristic impedance of the rhombic simulator in each of the three frequency regions is determined. Table 2.3 illustrates the Standing Wave Ratio (SWR) of the current as a function of load impedance, computed from the NEC model. Furthermore, it also lists the efficiency of the simulator, which is a measure of the percentage of power radiated to the total input power available. When the line is properly matched, the efficiency is near minimum since a maximum amount of power is being dissipated by the load. Therefore, the efficiency can also be used as a means to determine the characteristic impedance. Table 2.4 provides a comparison of the results obtained from the NEC approximation with those obtained by Shen and King. In the middle- and low-frequency regions, the results compare fairly well. The deviation is mainly due to the source and load model deficiencies. However, in the high-frequency region the results deviate by a significant amount. This is due to limitations associated

with the source and load models. As the wavelength becomes comparable with the dimension of the source and load gaps, the approximation seems to break down. Although it is interesting that even though the matching impedance is much lower in the high-frequency region, the near fields and the conducting wire currents still compare quite well with those obtained by Shen and King.

It should be noted that even though the characteristic impedance changes with frequency, the SWR of the mismatch throughout the band of interest can be less than 1.25 when matched to the low frequency characteristic impedance. Furthermore, it should be realized that under pulse excitation, most of the energy typically lies in the low- to mid-frequency region. This is encouraging since it means that a load impedance can be developed that will efficiently terminate the simulator.

Figure 2.9 provides a comparison of the wire currents of the open-circuited simulator computed by NEC, with those published by Shen and King, when $\lambda = 4 \text{ m}$. Figure 2.10 compares the computed wire currents for the short circuit case, when $\lambda = 1 \text{ m}$. In each case, the NEC solution compares quite well with Shen and King's results. However, a slight shift in the peaks of currents provided by the NEC model should be noted. The amount of shift is equal to the height of the source and load regions. Therefore, in the high-frequency region, when the gap height becomes more significant in terms of a wavelength, large errors can occur in the computed matched terminating impedance.

Figures 2.11 - 2.13 illustrate the currents along the conducting wire axis as computed by NEC. These results can be compared to Shen and King's work, illustrated in Figure 2.14, and are found to compare quite well in all frequency regions.

Figures 2.15 - 2.23 illustrate the E-fields in the center region of the simulator computed for matched terminations by both the NEC model, and by Shen and King. It

should be noted that in the experimental results presented from Shen and King's work [29], when the geometry is scaled down by 3/4, the operating wavelengths are scaled down as well. Again the results are in good agreement.

At low frequencies, the magnitude of the vertical E-field is quite uniform within the center region, and has an SWR very close to one. Furthermore, E_z is a progressive wave with a linear phase shift. In the middle- and high-frequency regions, the vertical fields are again quite uniform and continue to maintain a nearly linear phase shift over distance. However, due to the existence of higher-order modes, the SWR of the field is much larger, and is approximately 1.25 for the middle-frequency region, and 1.75 for the high-frequency region. It should also be noted that the longitudinal component of the E-field, E_y , is of significant amplitude, although it is still less than the vertical component.

In conclusion, good agreement was found between the Numerical Electromagnetics Code's model of the rhombic EMP simulator and the theoretical and experimental results published by Shen and King. The source and load models were developed using a thin-wire model and a distributed E-field source and resistive-load, respectively. The computed characteristic impedance of the simulator in the low- and middle-frequency regions compared quite well with experimental data. However, due to the wire model of the source and load gap, the matching load impedance suffered significant error in the high-frequency region. Finally, in all frequency regions the computed currents and E-fields compared extremely well with those of Shen and King under matched conditions, regardless of the error in the value of the characteristic impedances.

2.2.3 Scattering of a PEC plate

The conducting surface of the parallel-plate simulator is to be approximated by a thin-wire mesh. Initially, it will be instructive to develop a similar problem such that the accuracy of the wire mesh approximation and the limitations associated with it can easily be studied. However, in order to do this effectively, the physical attributes of the currents induced on the conducting plates of the simulator must be understood. The geometry of the simulator is an open, finite-width transmission line. Due to the finite width, there will be a singularity in the current at the plate edge. Furthermore, the current will be highly oriented in the longitudinal direction, and very little current will actually flow in the transverse direction. In this section, the currents induced on a PEC plate scatterer, when illuminated by an incident plane wave, are studied. A comparison will be made between the solutions derived by NEC, using a wire mesh approximation, and that derived by a more accurate technique that solves for the two-dimensional surface current distribution. The PEC plate scatterer has a finite width and the dimension will be chosen to be on the order of one wavelength in order to reduce the number of unknowns. Furthermore, in order to reproduce some of the limitations associated with the parallel-plate simulator's wire mesh approximation, the induced currents are predominately oriented in one direction. Therefore, the case of a normally incident TE plane wave excitation is considered.

2.2.3.1 Numerical Results. Figure 2.21 illustrates the geometry of the PEC plate. The plane wave incident is TE to y , with the E-field directed along the z -direction. The magnitude of the tangential H-field, H_x , is chosen to be unity. Therefore, from a geometrical optics point of view, the induced electric currents are expected to be on the order of one for a normally incident excitation. The plate is chosen to be square, with

a width of 1.1 wavelengths.

Initially, solution of the thin PEC plate problem is obtained using a spectral Galerkin procedure combined with the method of Conjugate Gradients. The procedure was developed by Ray and Mittra at the University of Illinois, and is described in detail in [32]. The two-dimensional current is expanded in terms of a general set of basis functions, referred to as triangular patch basis functions. These basis functions were first considered by Glisson in [33]. The basis functions are identically spaced such that the FFT operator can be used to compute the discretized integral operator. They also guarantee that the current normal to an interior edge of the patch is continuous, and does not generate any nonphysical line charges. Furthermore, only parallel components of the current will be nonzero on the edge of the plate. The 1.1 wavelength plate was discretized into an array of 16 by 16 patches, each containing three basis functions, leading to 768 unknowns. Convergence to less than 0.1% error required only 68 iterations. However, since the source is highly oriented in the z -direction, the current in the x -direction still had considerable error. Figures 2.22 and 2.23 illustrate the surface current densities in the z - and x -directions, respectively, after 300 iterations. As expected, the parallel current along the edges of the patch is singular. Furthermore, J_x , which is the current perpendicular to the polarization of the incident E-field, is approximately three orders of magnitude less than J_z .

With the use of NEC, the patch surface is approximated by a wire mesh. As was discussed in Section 2.1, at least 10 basis functions per wavelength must be used in order to ensure the proper convergence of the solution. However, it should first be realized that there are limitations associated with the wire grid representation. Initially, the currents are limited to a one-dimensional flow along individual wires, and are coupled to transverse wires at multiple wire junctions. In Section 2.1, it was

discussed that at each wire junction, Kirchoff's current law and charge continuity are being applied as boundary conditions. However, this results in a step discontinuity in the current at each junction. Since J_z is the dominant current, its discontinuity is relatively small. However, J_x is much smaller in magnitude. As a result, the discontinuity in the current is quite large.

The 1.1 wavelength patch surface was approximated by a 12 by 12 square grid, leading to a total of 288 unknowns. Figures 2.24 and 2.25 illustrate the surface current densities in the z- and x-directions, respectively. We find that J_z compares extremely well in magnitude with the PEC plate problem. The singularity in the current along the plate edge is apparent; however it is not nearly as significant as that computed by the iterative procedure. Furthermore, there is significant error in the x component of the current and this result is unreliable, although it cannot be thrown away since it does contribute to J_z at the wire junctions. Figure 2.26 illustrates the comparison of the NEC and iterative solutions of J_z along the z-direction. Near the plate edge, the normal current should vanish. As discussed earlier, this is ensured by the choice of basis functions in the iterative procedure; however, in the NEC solution the wire segment terminates into a multiple wire junction, and is nonzero because it must satisfy Kirchoff's law at this point.

Figure 2.26 illustrates the current distribution of the NEC solution located at the center of each wire segment. However, Figure 2.27 illustrates the current computed along the length of each segment. This clearly shows the discontinuity that exists in the current, which is a result of the multiple wire junctions. Recall that the current in the x direction is on the order of a magnitude smaller than the z-directed current; however, as a result of Kirchoff's law, the discontinuity in J_z at the wire junction is equal, but opposite, to the discontinuity in J_x . Therefore, the error due to the discontinuity in J_x is quite significant. This is illustrated in Figures 2.28 and 2.29.

Furthermore, the discontinuities in the currents lead to nonphysical singularities in the E-field near the wire mesh surface.

The analysis of the parallel-plate EMP simulator will require the computation of the near-field distribution in the volume directly underneath the top conducting plate. Therefore, when the conducting surface is approximated by a wire mesh, the amount of distortion of the E-field, due to these singularities, must be determined. Therefore, in Chapter 3, an analysis of smoothing of the current along both directions will be performed, and the effect on the near fields will be presented.

TABLE 2.1 OVER SAMPLING

N	Δ_t/λ	self term	$E_z(0) \times \Delta_t$ (volts)	$I(\Delta_t, z)$ (amps ($\times 10^{-9}$))
10	0.01	-0.0312 + j 817.5	1.02 + j 0.0	1.72 + j 194.0
20	0.005	-0.0389 + j 688.5	1.03 + j 0.0	1.76 + j 201.0
21	0.00476	0.0287 + j 3294.	-0.020 + j 0.0	-0.49 - j 36.5
30	0.00333	0.0098 + j 3342.	-0.018 + j 0.0	-0.39 - j 33.2

TABLE 2.2 ANTENNA CHARACTERISTICS DUE TO AEF SOURCE HEIGHT

$$\frac{H}{d} = 1000.$$

$\frac{HS}{\lambda}$	$\frac{HS}{HL}$	self term	I_{in} (amps (10^{-3}))	Z_{in} (Ω)
0.1	1.000	-36.2 + j499.	1.54 - j 3.67	614.2 + j 146.1
0.05	0.500	-4.03 + j523.	1.63 + j 4.73	566.5 - j 164.4
0.025	0.250	-0.49 + j422.	1.68 + j 4.73	433.7 - j 264.7
0.01	0.100	-0.32 + j262.	1.80 + j 1.56	317.9 - j 274.7
0.005	0.050	-0.04 + j150.	1.93 + j 1.91	261.4 - j 259.7
0.005	0.100	-0.04 + j262.	1.20 + j 1.20	415.3 - j 416.0
0.0025	0.050	+0.04 - j1909.	0.0015 - j 0.046	729.0 + j 21577.

TABLE 2.3(a)
 NEC MODEL OF THE RHOMBIC EMP SIMULATOR: $\lambda = 4 m$

Z_L (Ω)	$\text{Re}(Z_{in})$ (Ω)	$\text{Im}(Z_{in})$ (Ω)	η_{ef} (%)	SWR
0.0	38.80	-20.28	100.0	11.90
50.0	73.22	-22.54	40.28	4.20
100.0	104.80	-29.50	22.73	2.56
150.0	132.40	-34.26	15.84	1.88
200.0	155.70	-43.02	13.11	1.51
250.0	182.80	-52.59	12.34	1.30
300.0	203.80	-62.86	12.63	1.20
315.0	209.70	-66.03	12.84	1.19
375.0	231.30	-78.98	14.08	1.25
500.0	268.20	-106.20	17.64	1.51
1000.0	347.20	-198.50	32.64	2.46
10000.0	406.20	-435.40	85.12	6.54

TABLE 2.3(b)
 NEC MODEL OF THE RHOMBIC EMP SIMULATOR: $\lambda = 1 m$

Z_L (Ω)	$\text{Re}(Z_{in})$ (Ω)	$\text{Im}(Z_{in})$ (Ω)	η_{ef} (%)	SWR
0.0	157.0	42.20	100.00	2.55
50.0	169.2	24.19	86.72	1.78
100.0	179.0	9.82	81.43	1.43
150.0	183.5	-8.17	79.40	1.23
200.0	186.2	-10.43	78.84	1.13
240.0	187.5	-16.34	78.92	1.11
250.0	187.8	-17.66	78.99	1.12
300.0	188.8	-23.56	79.47	1.18
500.0	185.9	-38.99	82.25	1.40
1000.0	185.2	-55.07	87.50	1.72
10000.0	187.2	-75.90	97.96	2.30

TABLE 2.3(c)
 NEC MODEL OF THE RHOMBIC EMP SIMULATOR: $\lambda = 0.5 m$

Z_L (Ω)	$\text{Re}(Z_{in})$ (Ω)	$\text{Im}(Z_{in})$ (Ω)	η_{eff} (%)	SWR
0.0	186.2	31.82	100.00	1.66
50.0	185.5	18.88	93.72	1.28
100.0	184.9	11.70	91.87	1.12
150.0	181.6	7.18	91.46	1.10
180.0	180.0	5.21	91.49	1.14
200.0	179.0	4.10	91.57	1.17
240.0	177.5	2.27	91.81	1.22
500.0	172.1	-3.77	93.61	1.44
1000.0	168.7	-7.60	95.59	1.66
10000.0	164.5	-12.78	99.34	1.88

TABLE 2.4 CHARACTERISTIC IMPEDANCE OF THE RHOMBIC EMP SIMULATOR

λ (m)	NEC (Ω)	Theory [29] (Ω)	Experiment [29] (Ω)
4.0	315	400	360
1.0	240	300	290
0.5	150	370	330

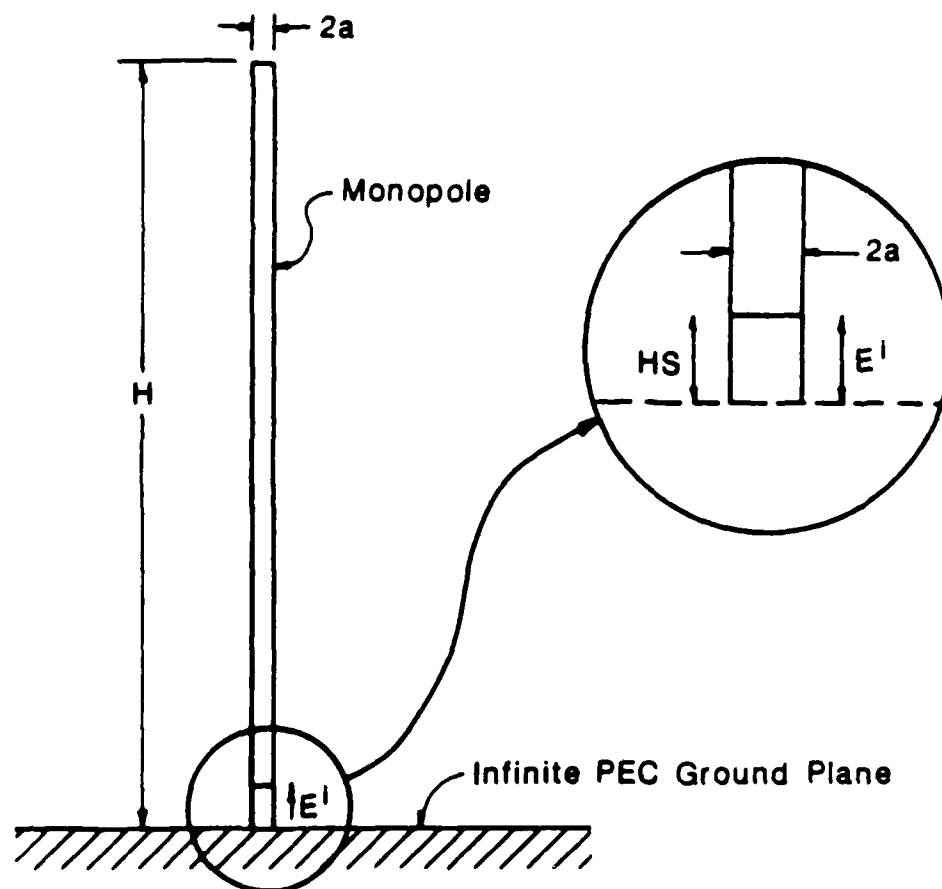


Figure 2.1. Thin-wire monopole antenna excited by the applied E-field source.

Scattered E-Field along Wire Surface

(Monopole Antenna, $H = .47$ wavelength)

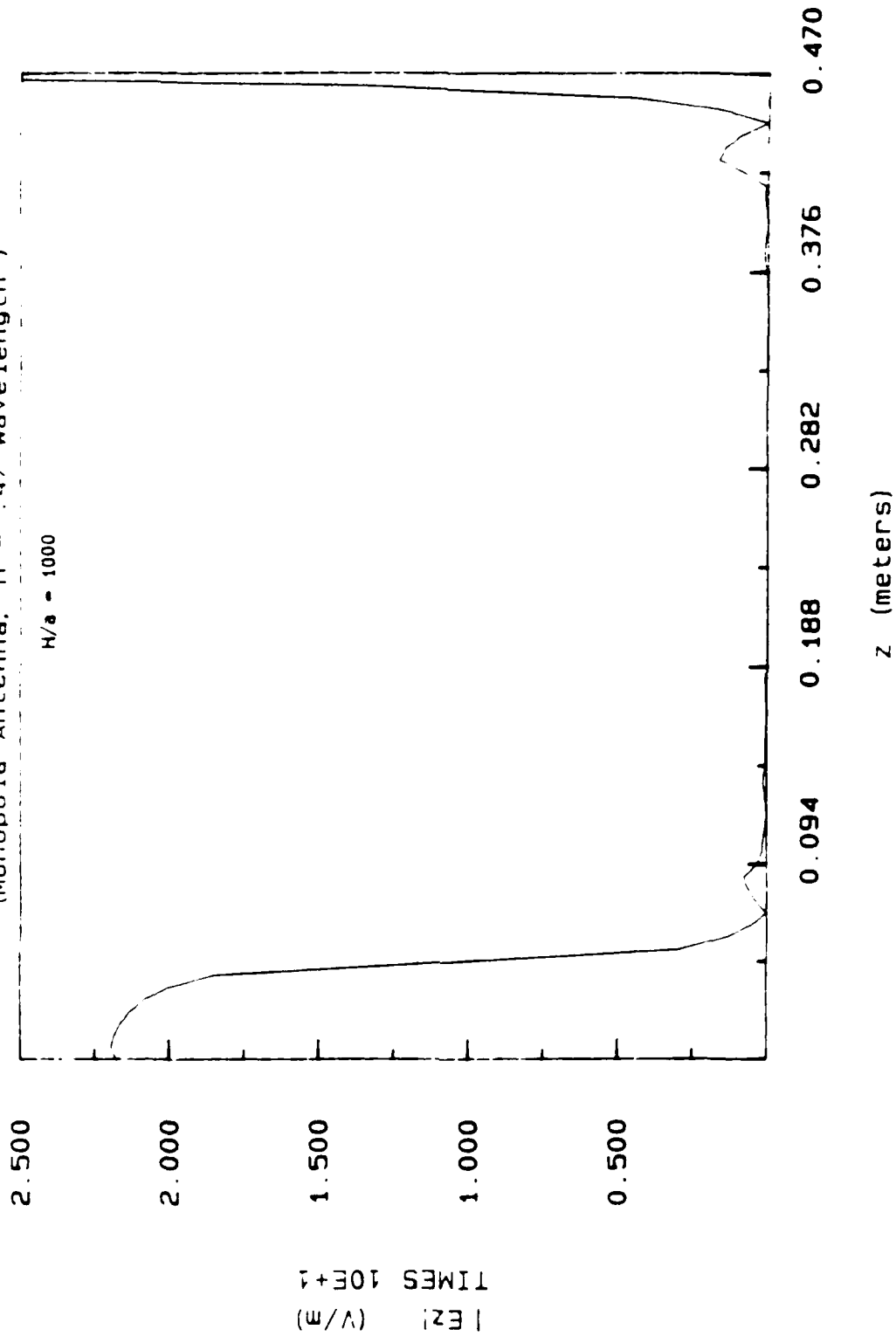
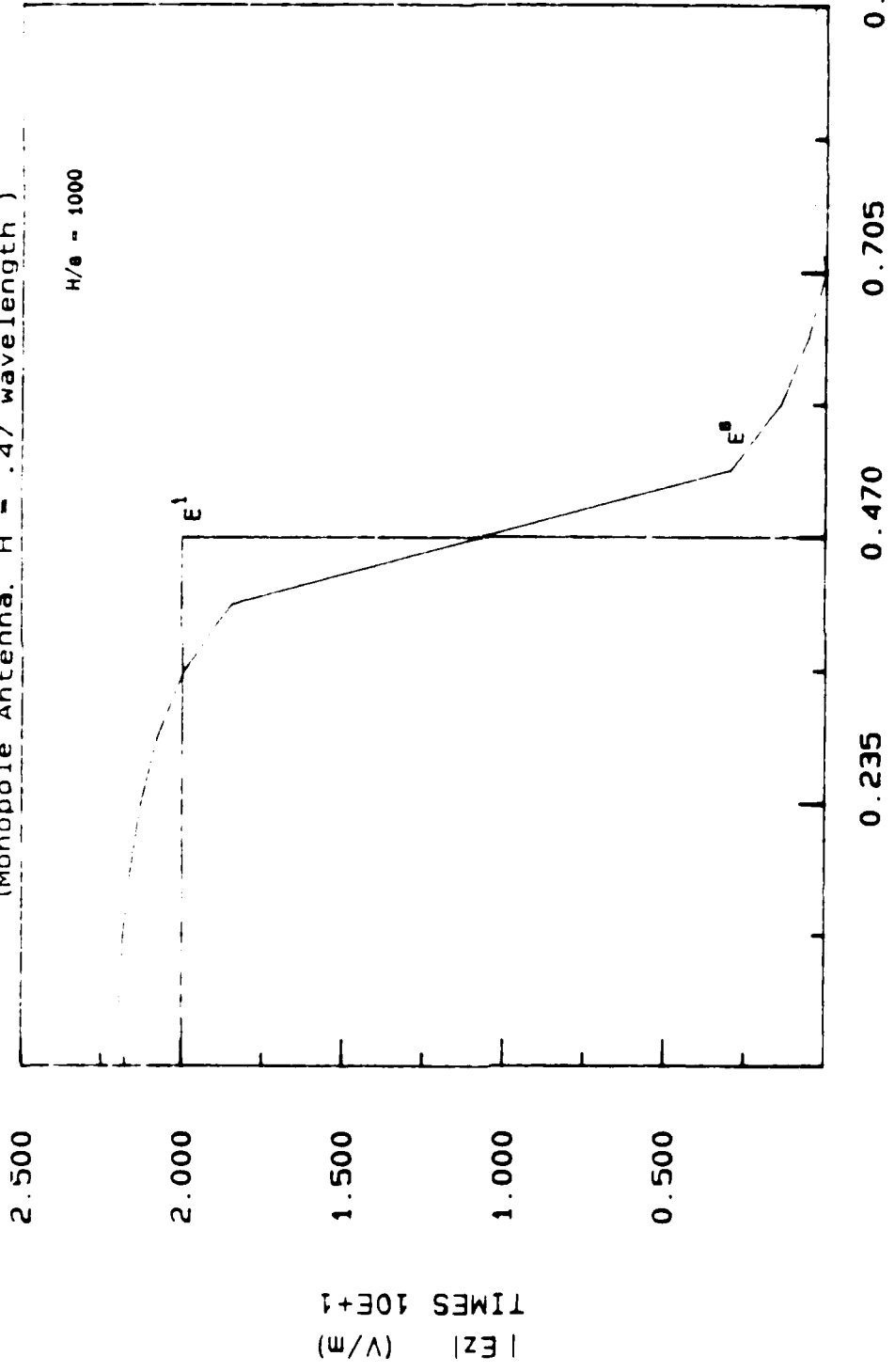


Figure 2.2. Axially directed E-field over the surface of a vertical monopole antenna excited by a unit A.P. source (H is the antenna height, a is the radius).

Axial E-Field over Source Region

(Monopole Antenna, $H = .47$ wavelength)

$H/\lambda = 1000$



z (meters) TIMES 10E-1

Figure 2.3. (a) Boundary condition error of the surface tangential E-field magnitude in the source region. E^1 is the AIEF source; E^0 is the computed scattered field.

Current Distribution over Source Segment
(Monopole Antenna, $H = .4/\text{wavelength}$)

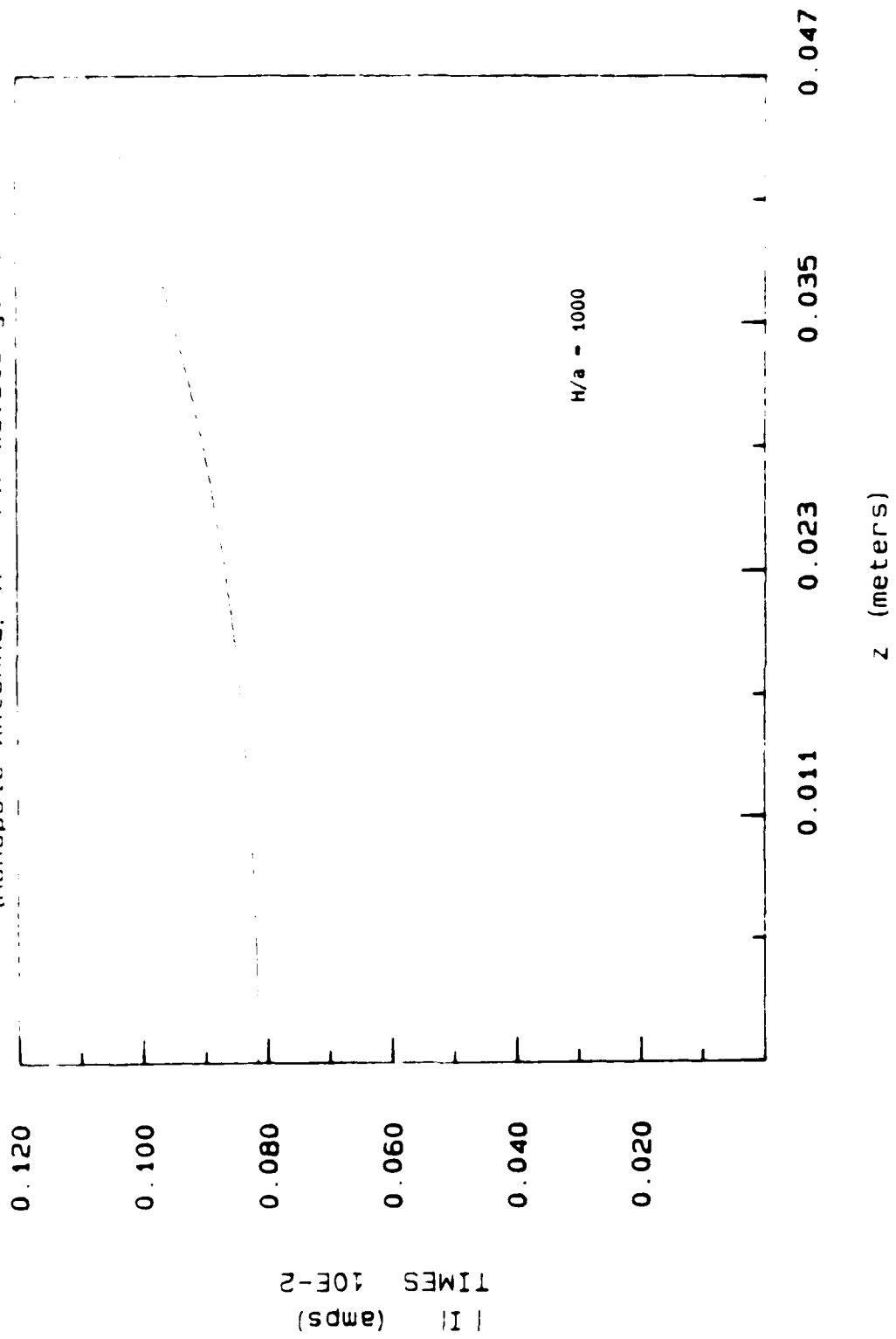


Figure 2.3. (b) Axial current magnitude computed over the source segment.

Phase of Current over Source Segment
(Monopole Antenna, $H = .47$ wavelength)

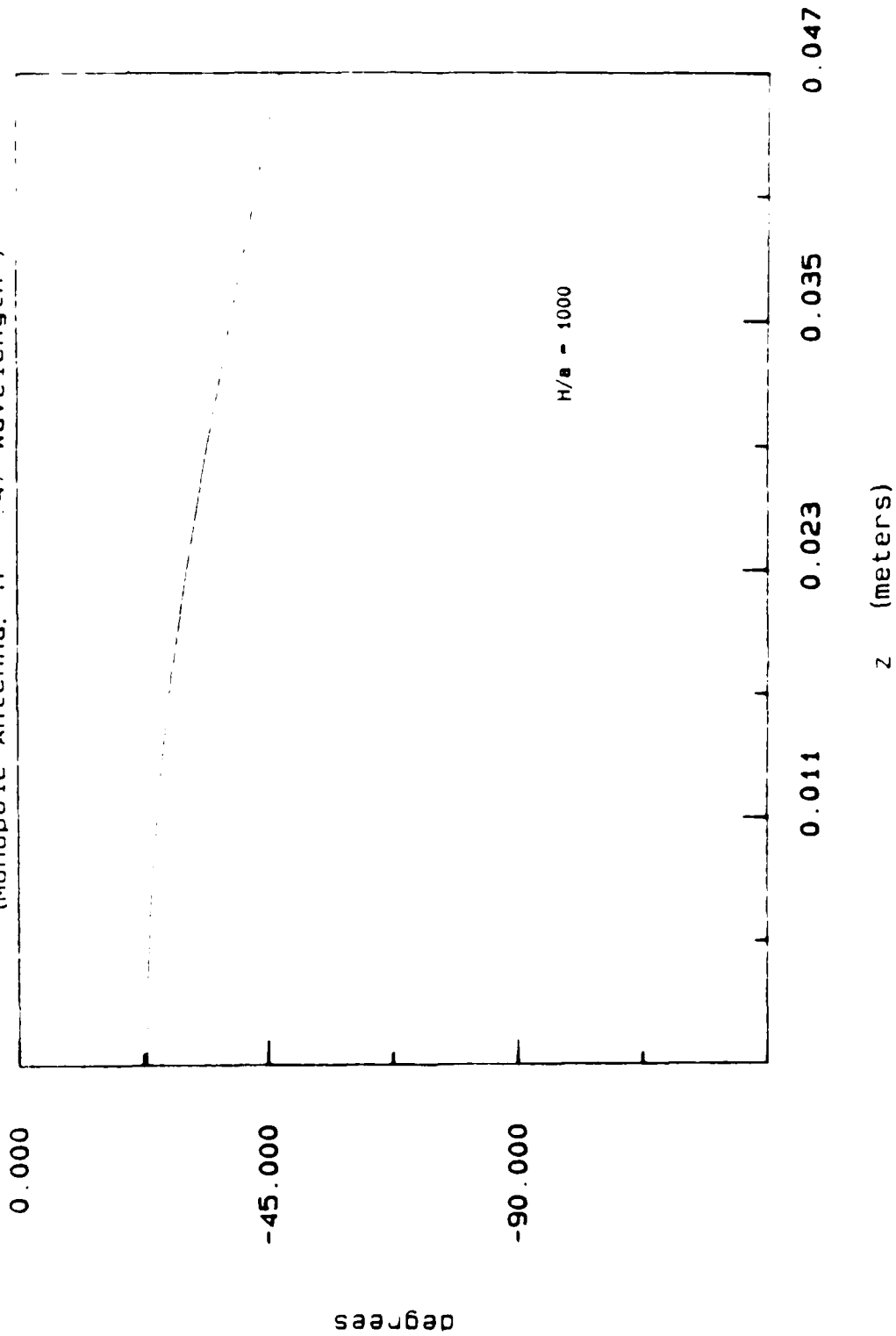


Figure 2.3. (c) Axial current phase computed over the source segment.

Axial E-Field over Source Region

(Monopole Antenna, $H = 1$ wavelength)

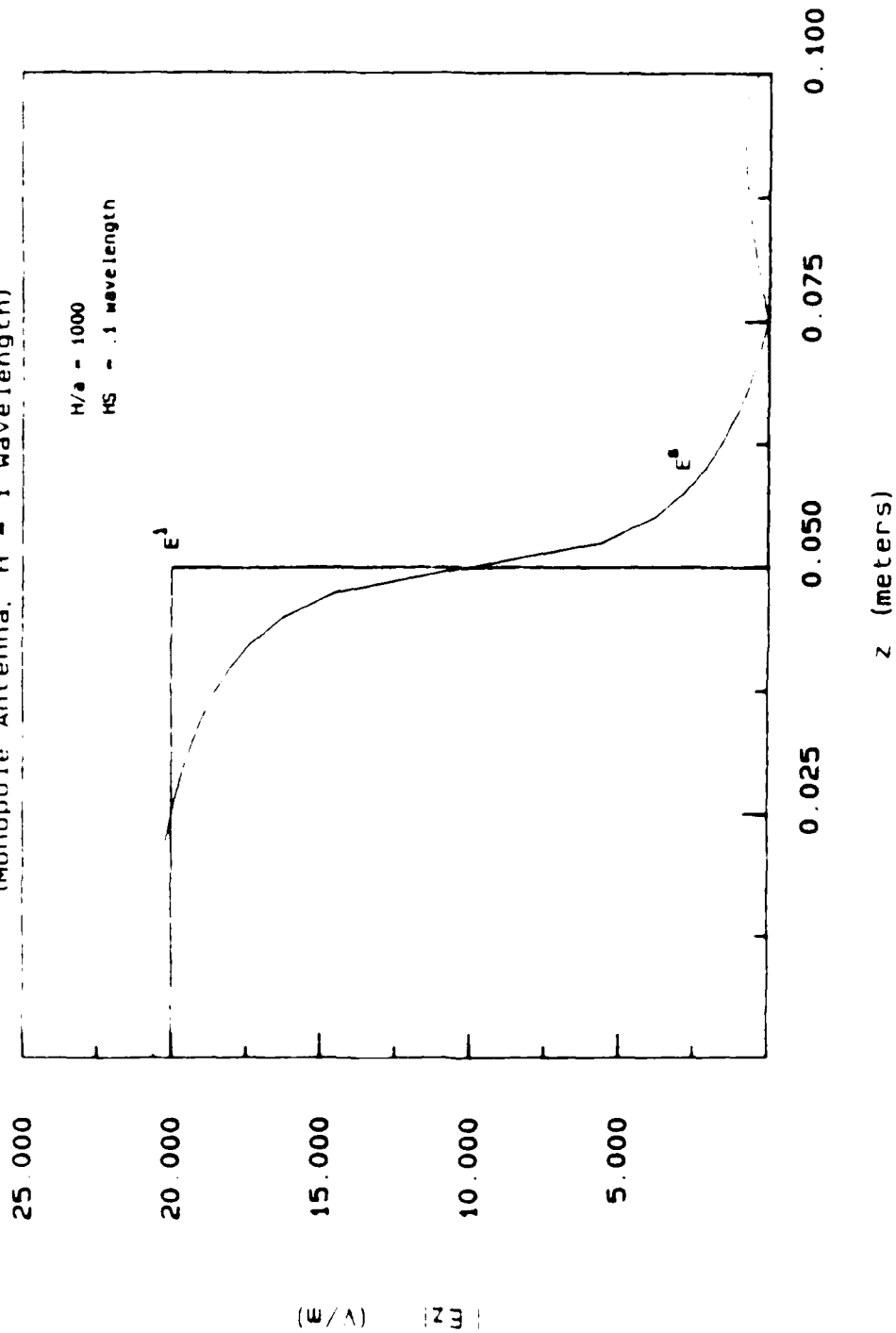


Figure 2.4. (a) Boundary condition check of the surface E-Field in the axial direction computed over the monopole antenna base ($HS = \text{A/E}$ source height).

Axial E-Field over Source Region

(Monopole Antenna, $H = 1$ wavelength)

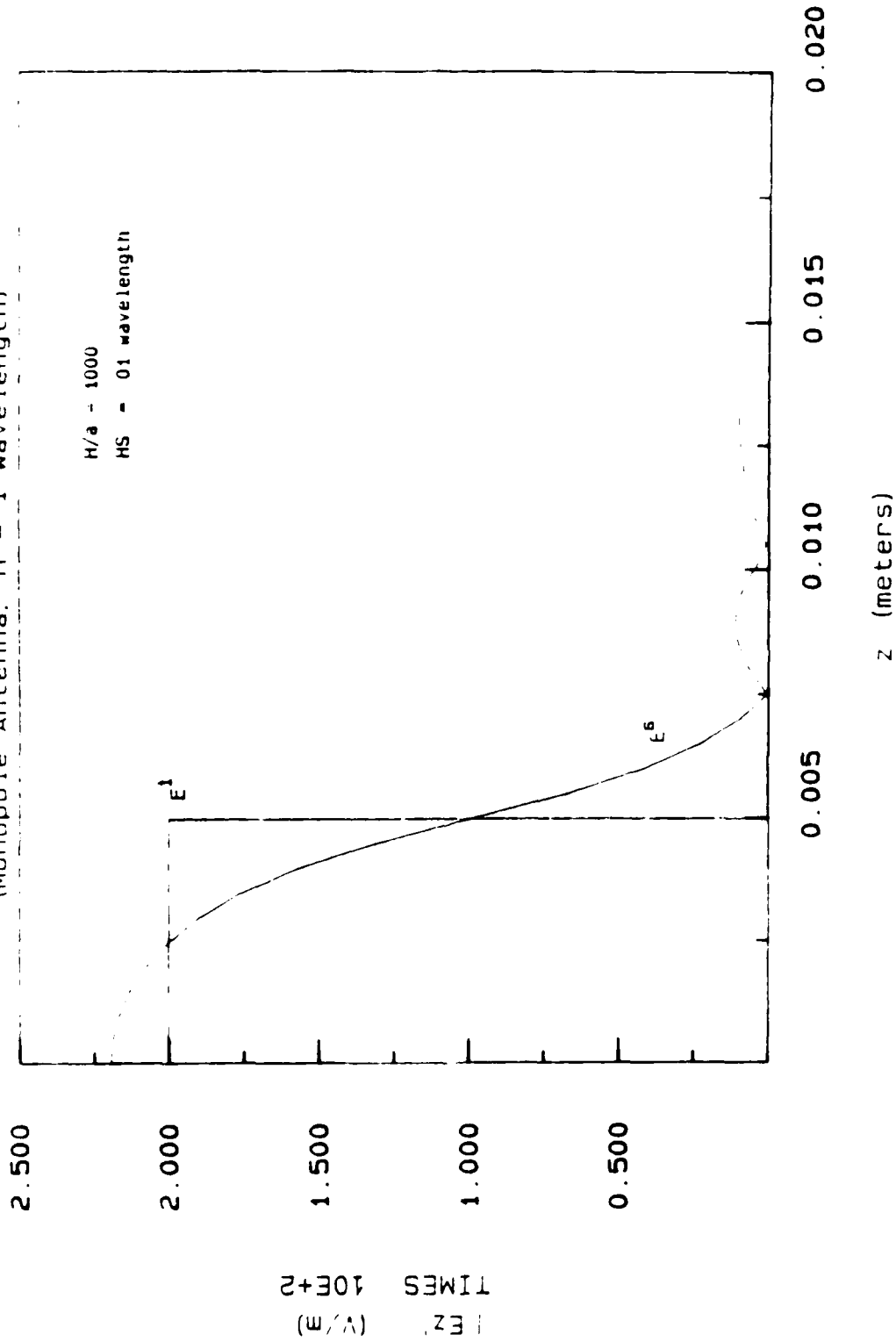


Figure 2.4. (b) Boundary condition check of the surface E-field in the axial direction computed over the monopole antenna base.

Axial E-Field over Source Region (Monopole Antenna, $h = 1$ wavelength)

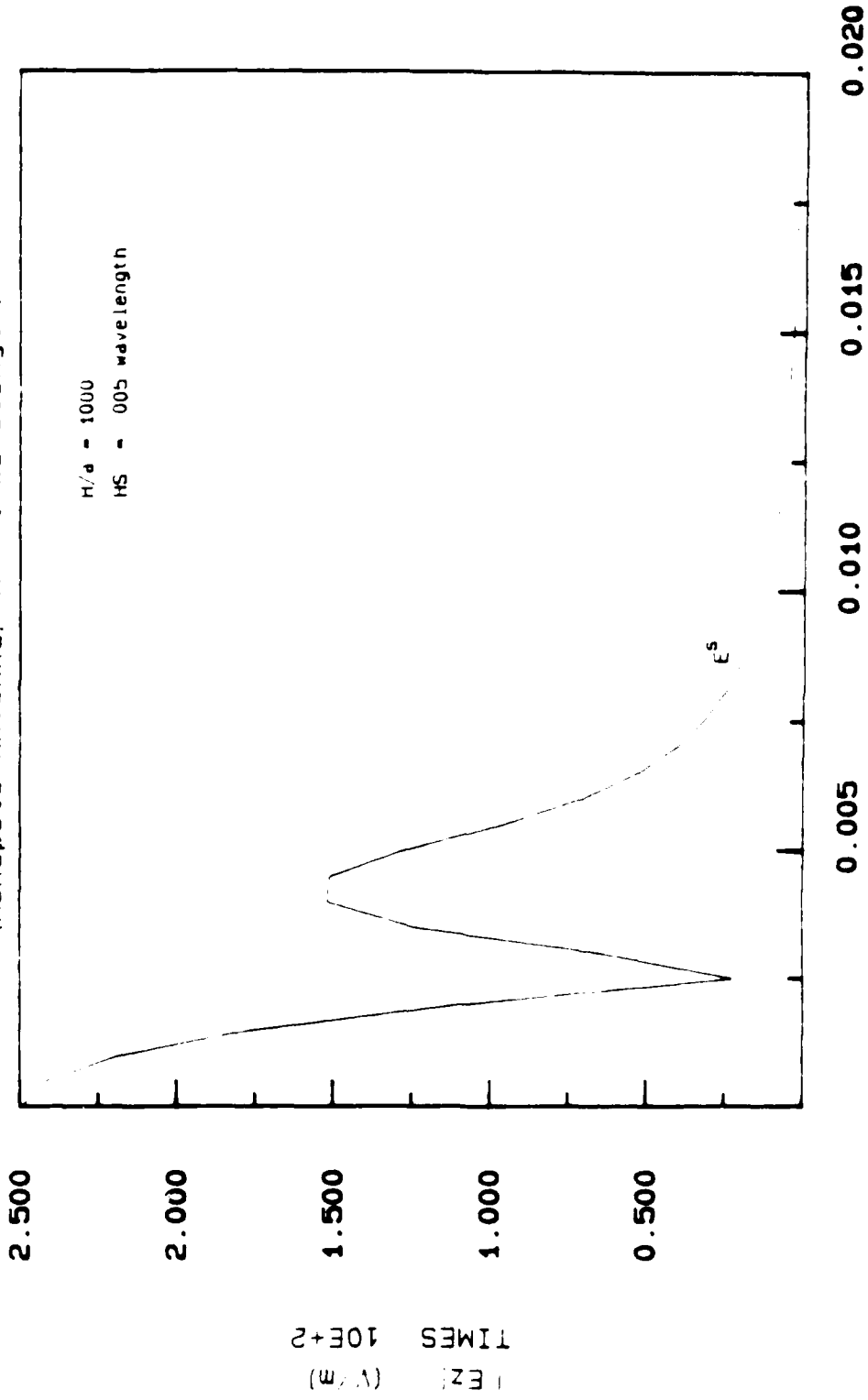


Figure 2.4. (c) Scattered E field magnitude computed over antenna base when affected by over sampling.

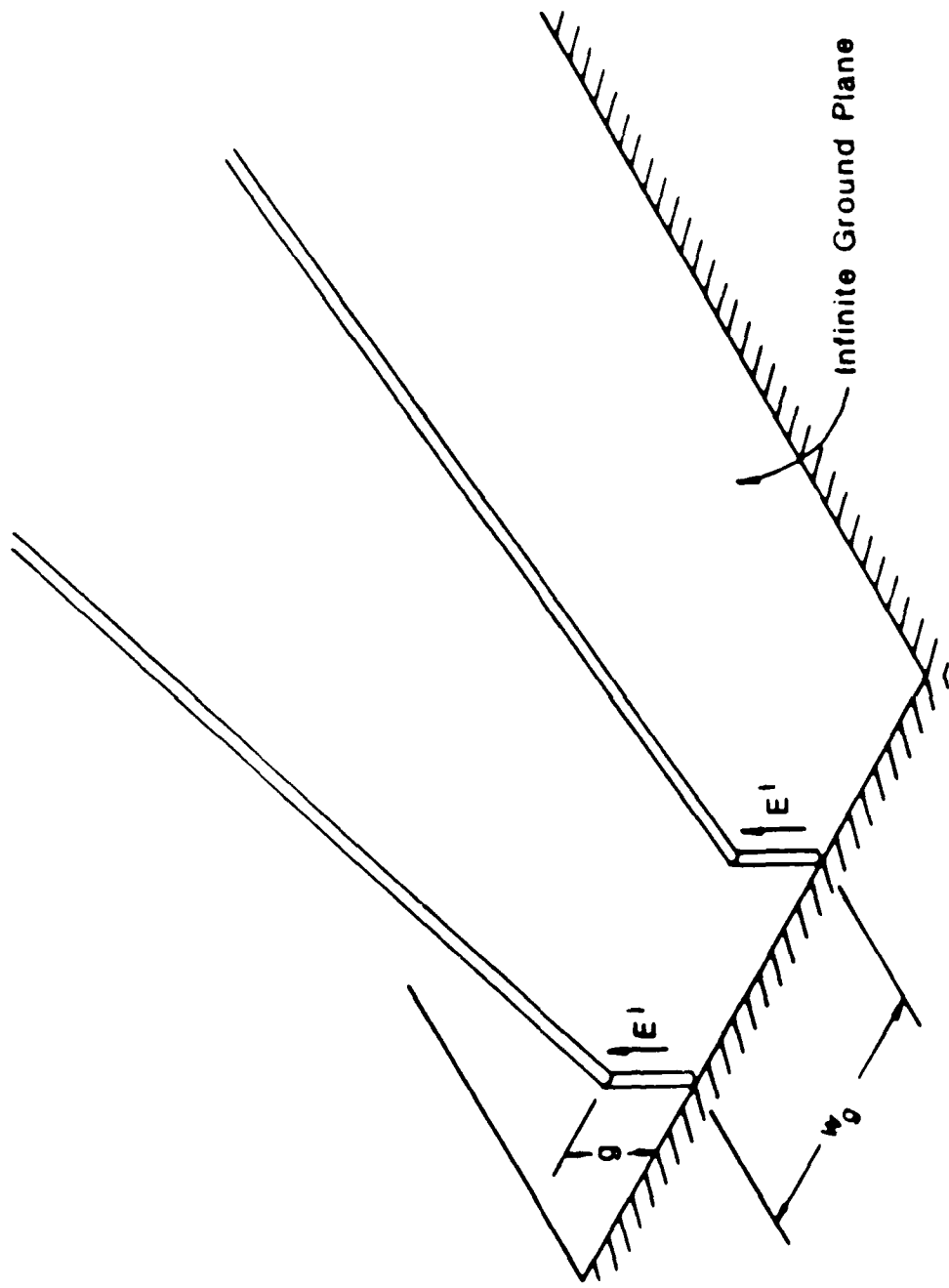


Figure 2.5. (a) Thin wire model of the source gap region of the rhombic EMP simulator.

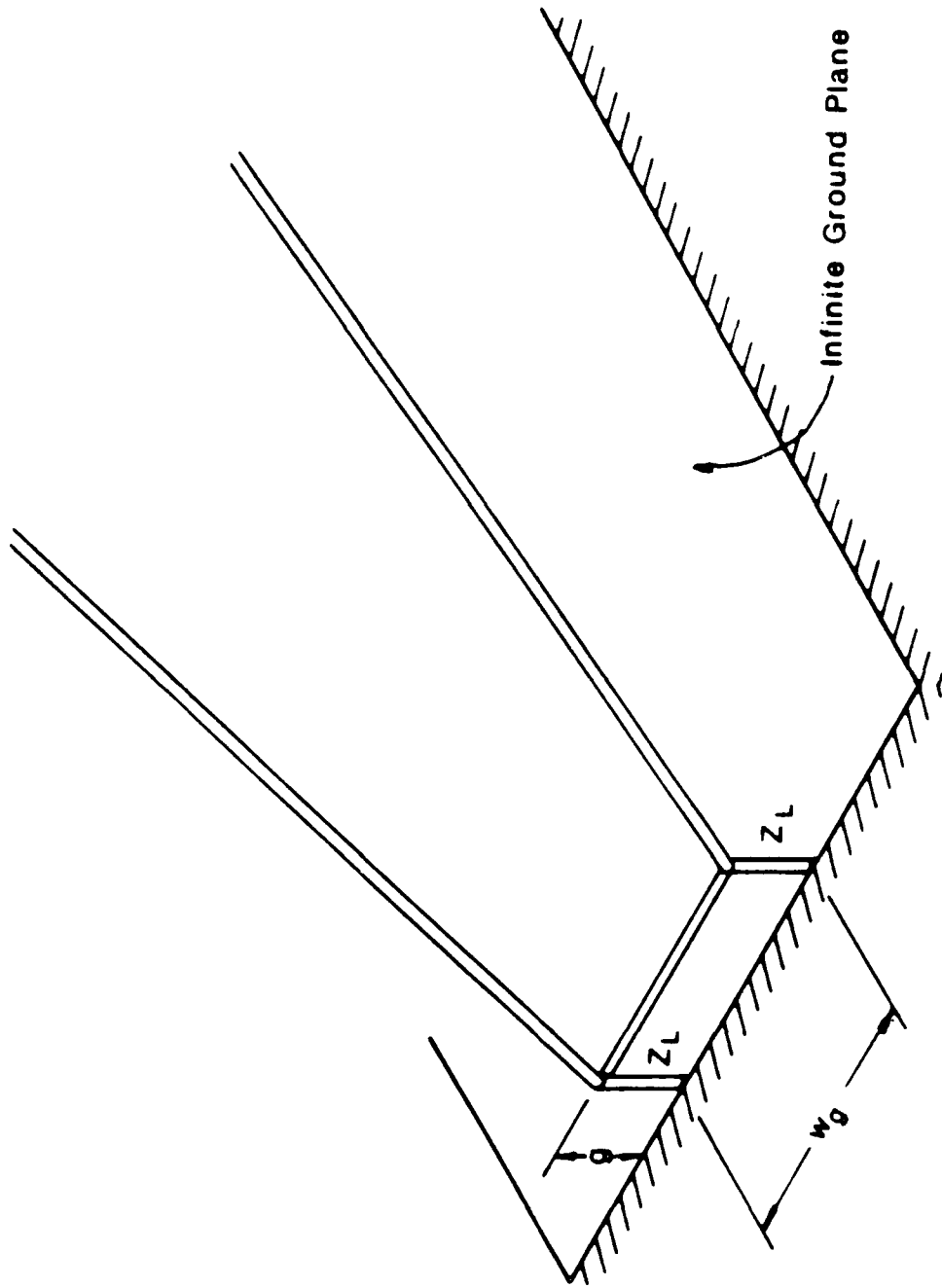
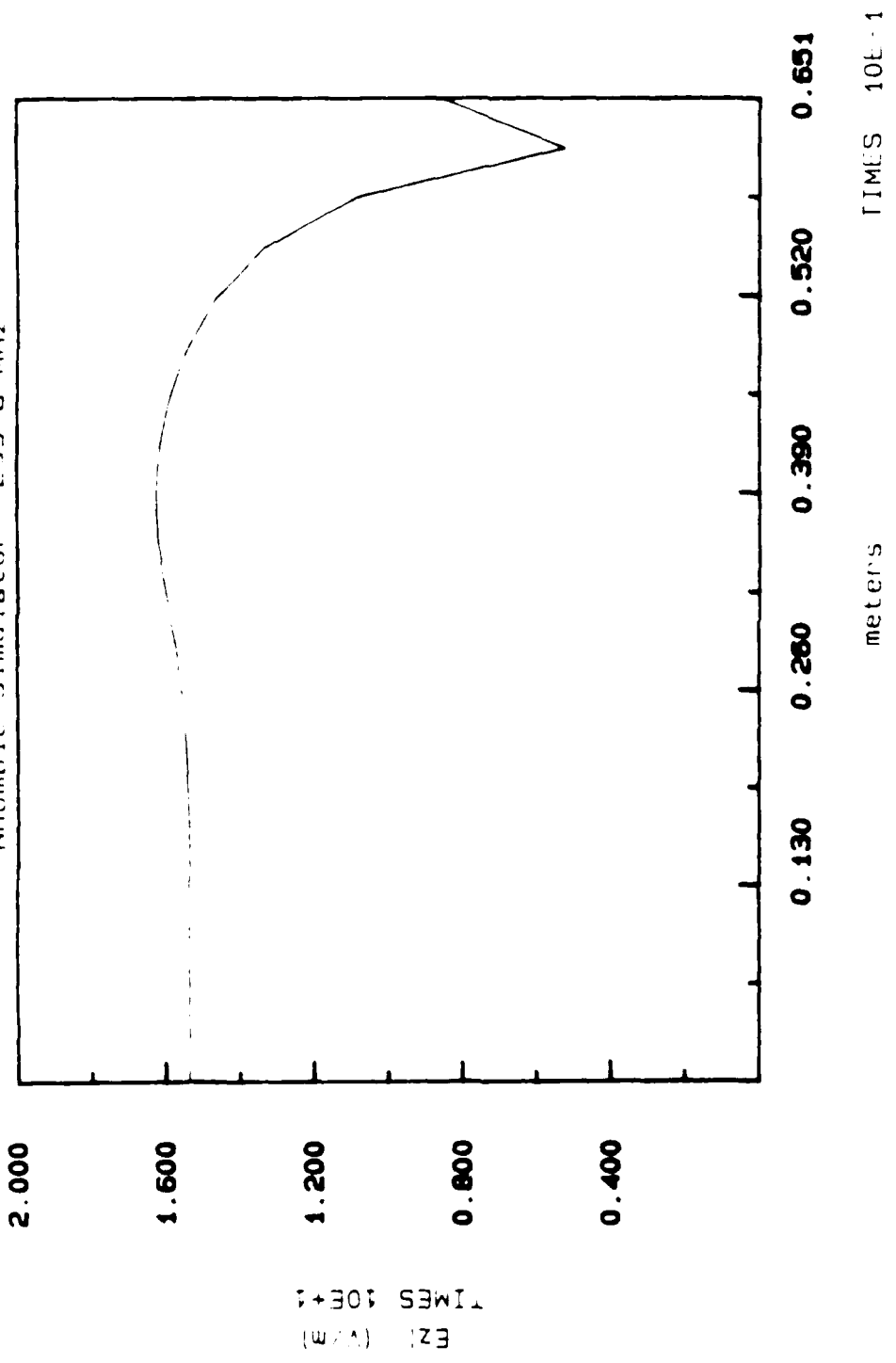


Figure 2.5. (b) Thin-wire model of the terminating load gap region of the rhombic EMP simulator.

Scattered E field Over Source Segment
 Rhombic Simulator 299.8 MHz



(a) Magnitude of axial E field.

Figure 2.6. Scattered axial E field due to an APF on the surface of the source segment.

Scattered E-field Phase Over Source Segment
Rhombic Simulator, 299.8 MHz

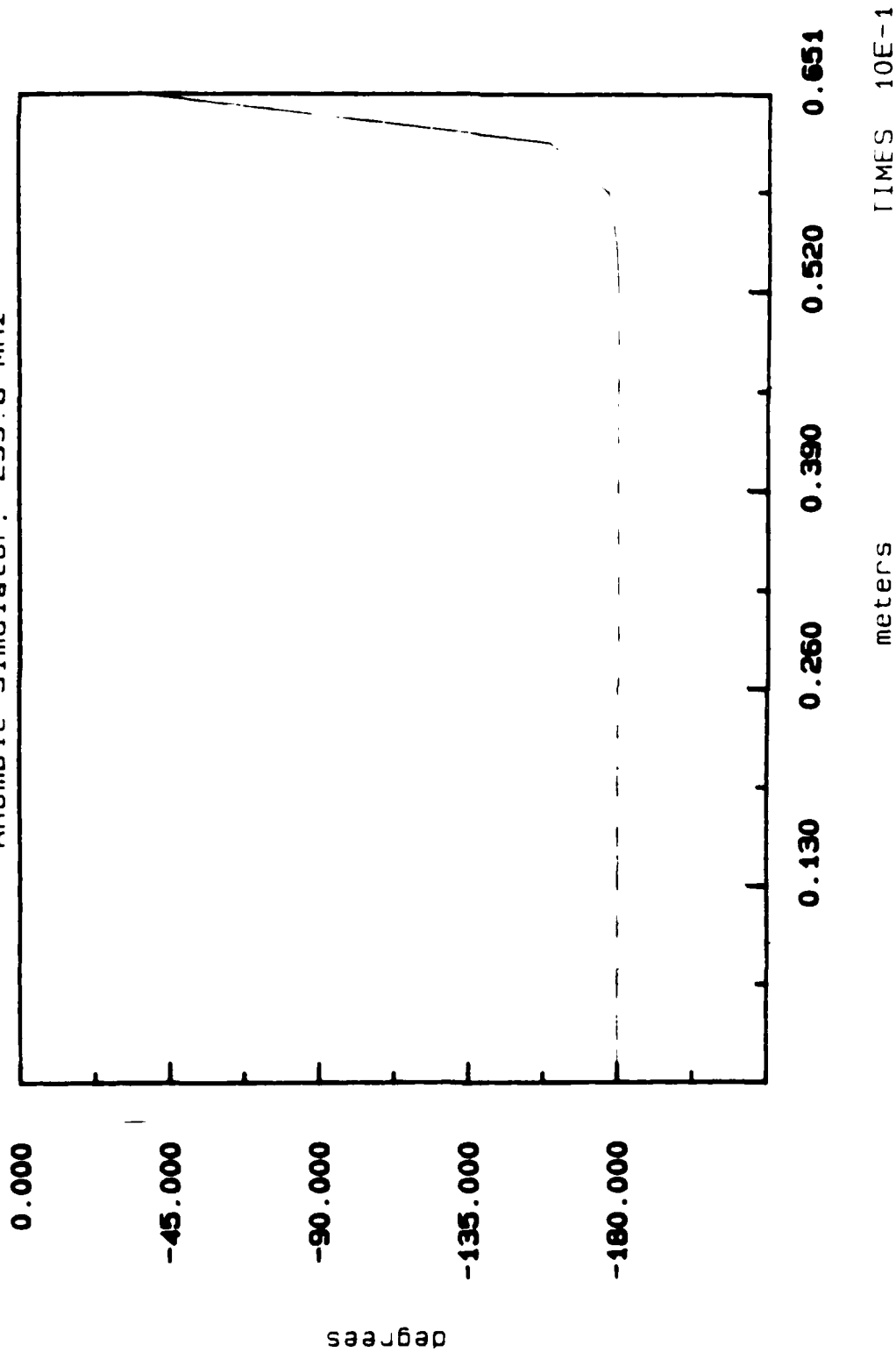


Figure 2.6. (b) Phase of axial E field.

E Field Distributed Over Load Gap Region

(matched termination, 74.95 MHz)

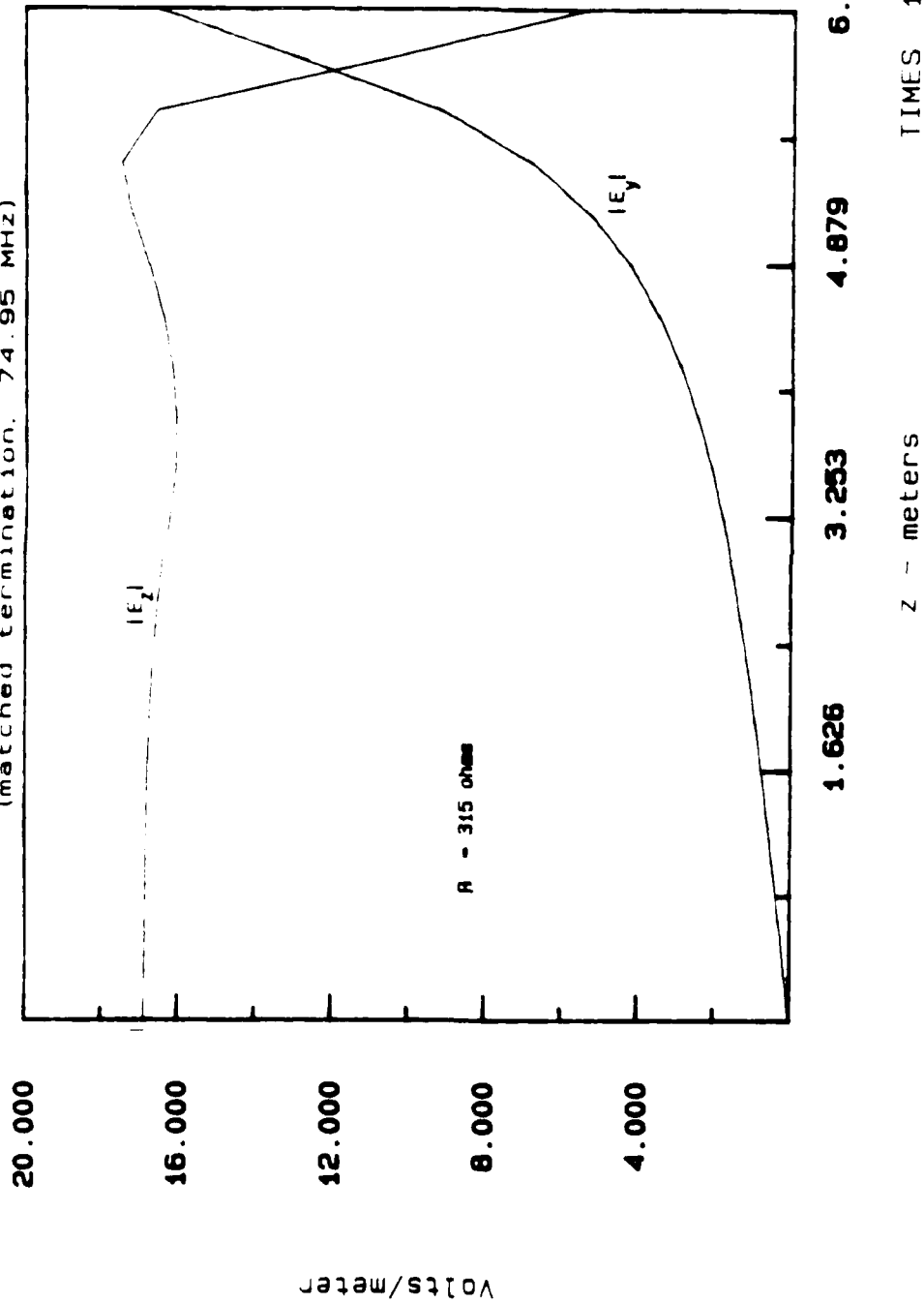


Figure 2.7. E field magnitude computed on the wire surface of the load segment along the axial direction. E_z is the vertical E field; E_y is the longitudinal E field.

Field Distributed Over Load Gap Region
 (matched termination, 599.6 MHz)

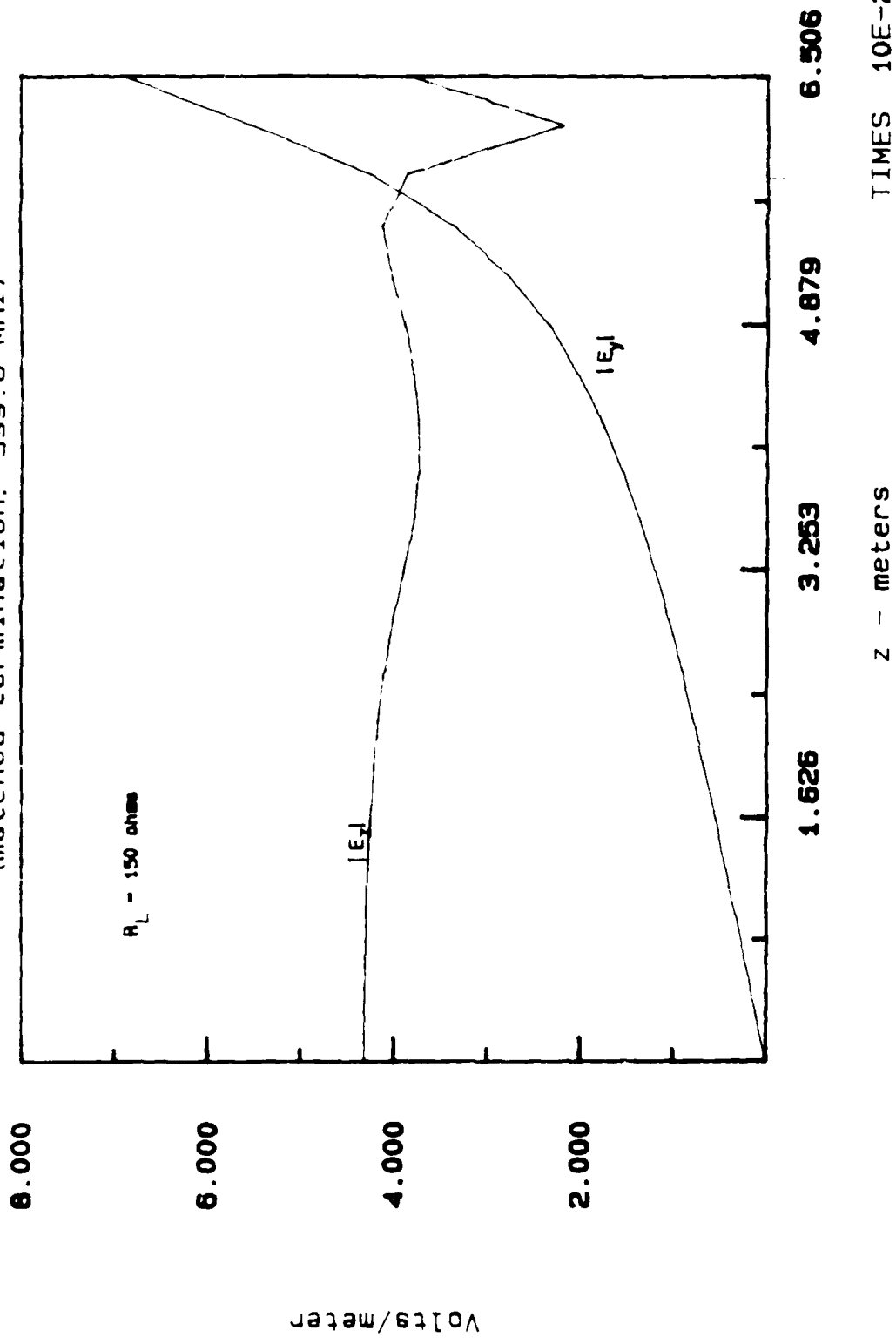


Figure 2.7. (b) High-frequency excitation.

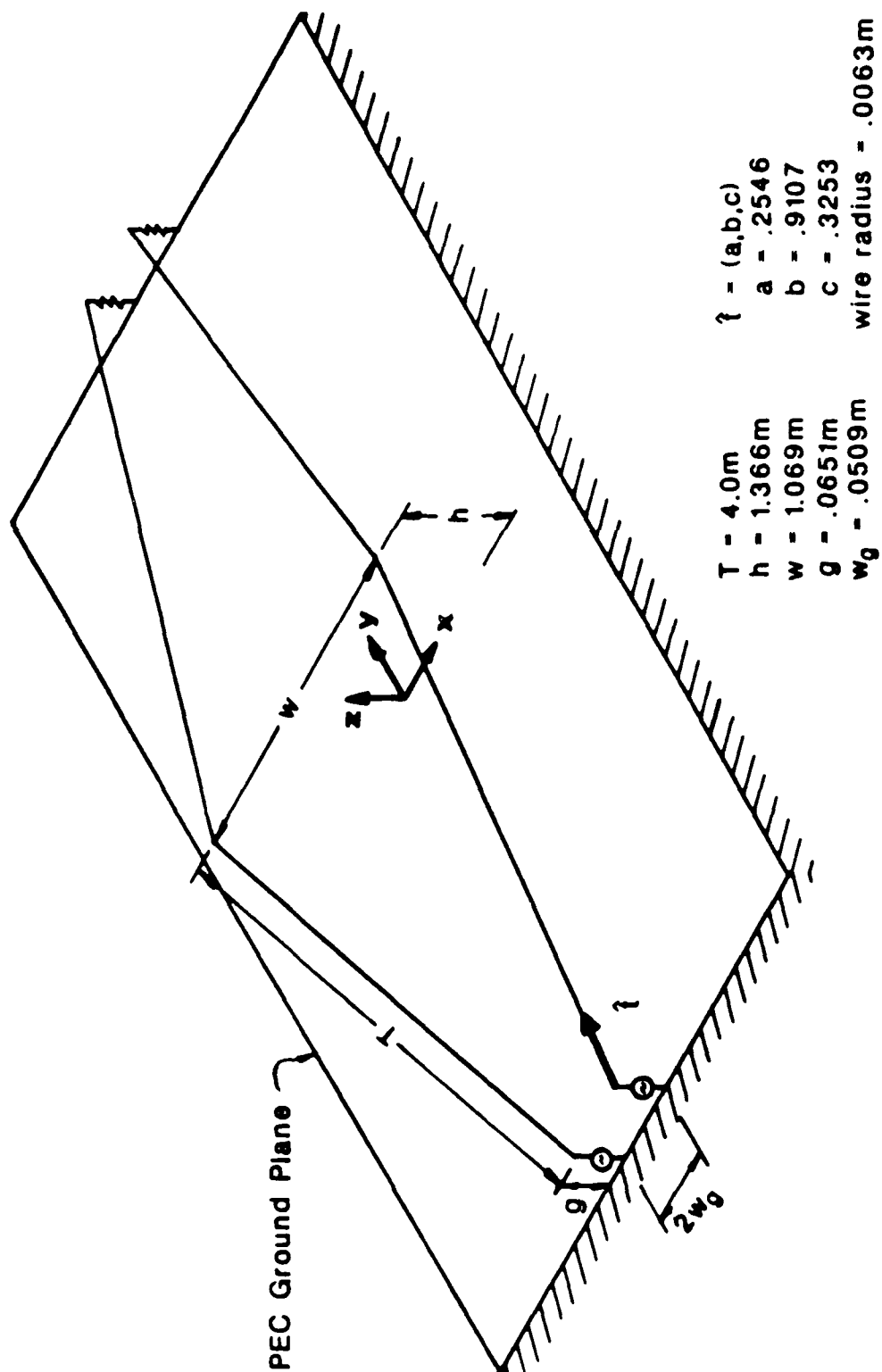
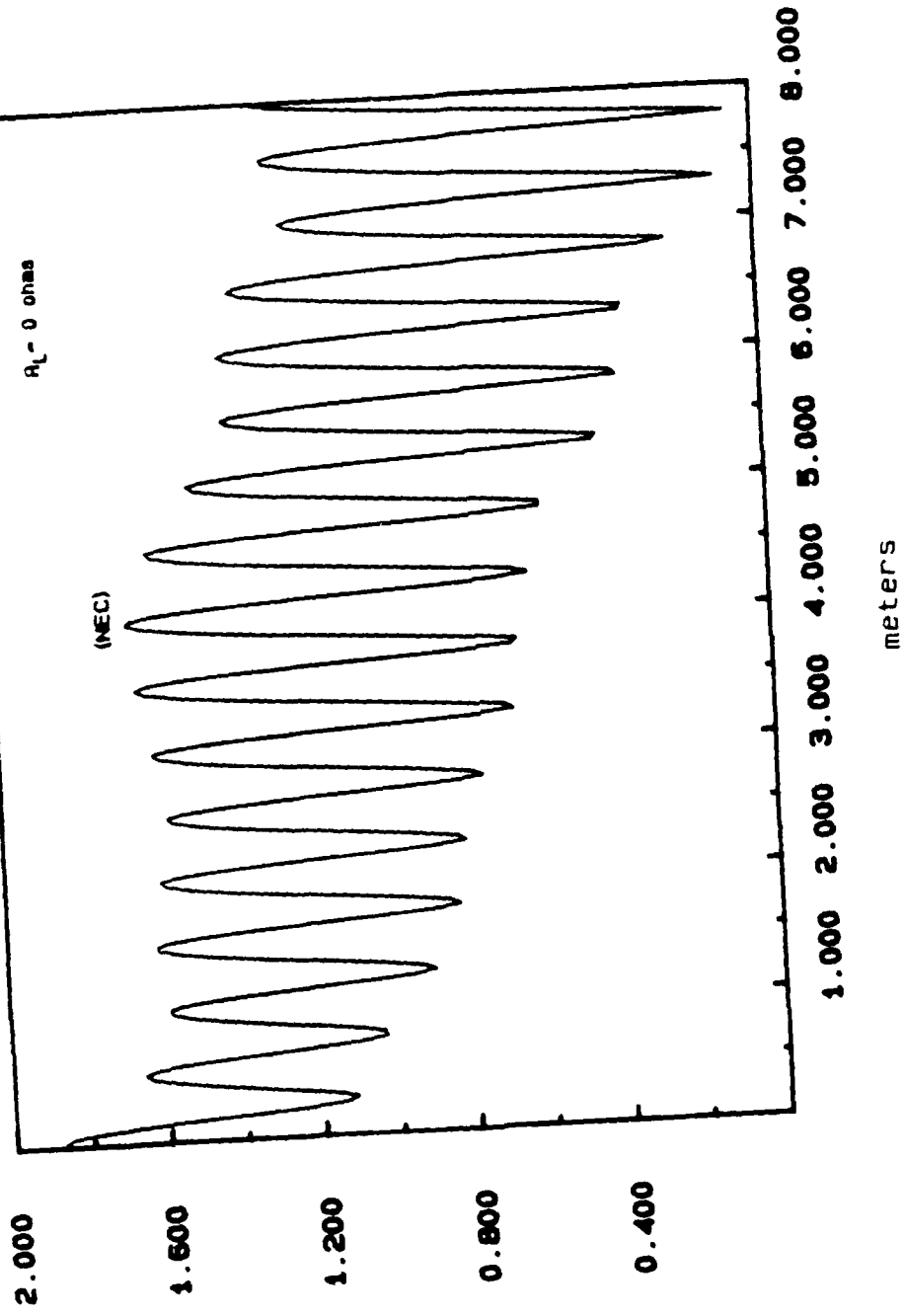


Figure 2.8. Thin-wire model of the two-wire rhombic EMP simulator.

Current Along Wire Axis (299.8 MHz)
short circuit termination



(a) Computed using NEC.
Figure 2.9. Axial current magnitude along the conducting wires of the rhombic EMP simulator with a short circuit termination.

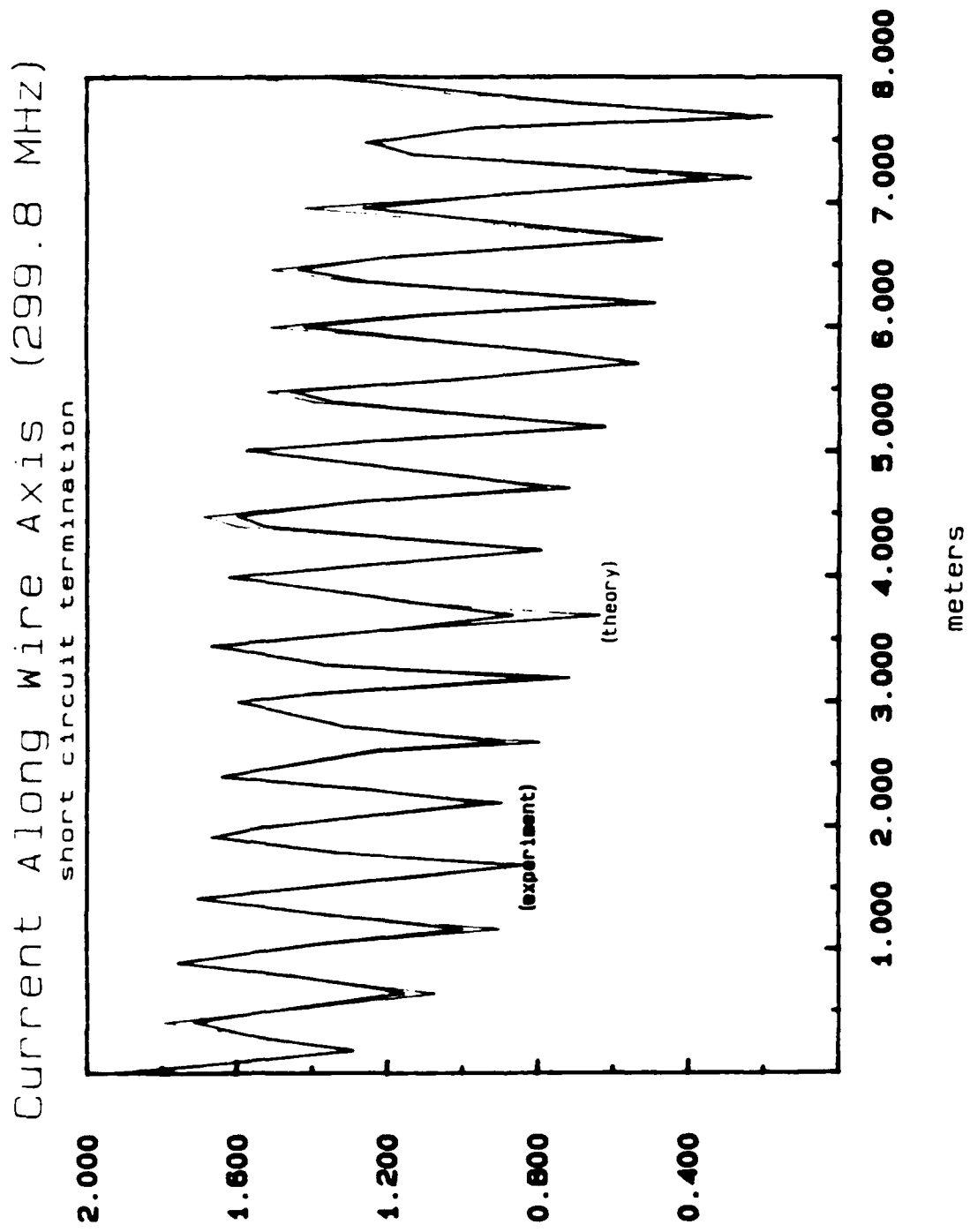
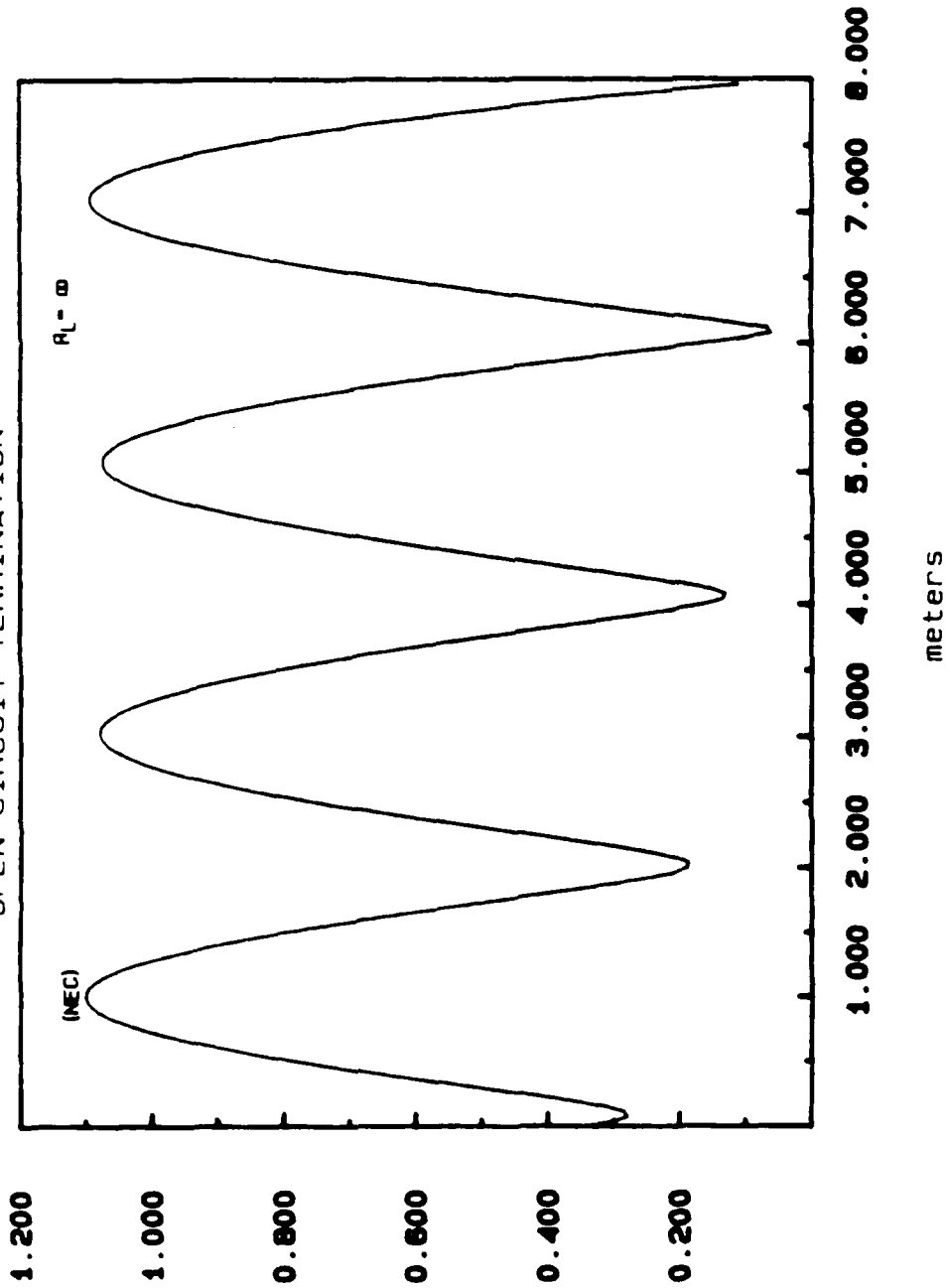


Figure 2.9. (b) Computed by Shen and King [29].

Current Along Wire Axis (74.95 MHz)
OPEN CIRCUIT TERMINATION



(a) Computed using NEC.

Figure 2.10. Axial current magnitude along the conducting wires of the rhombic EMP simulator with an open circuit termination.

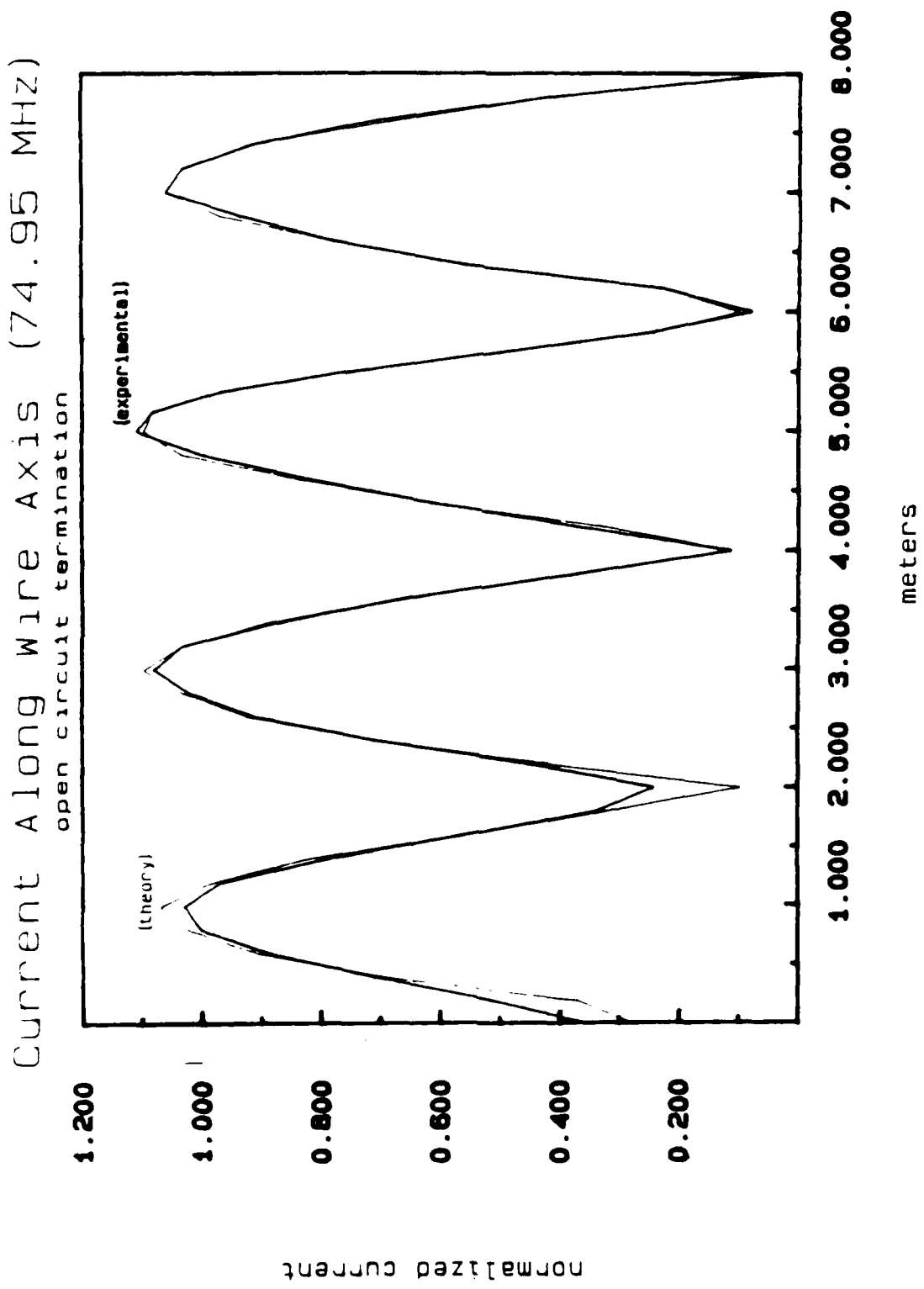
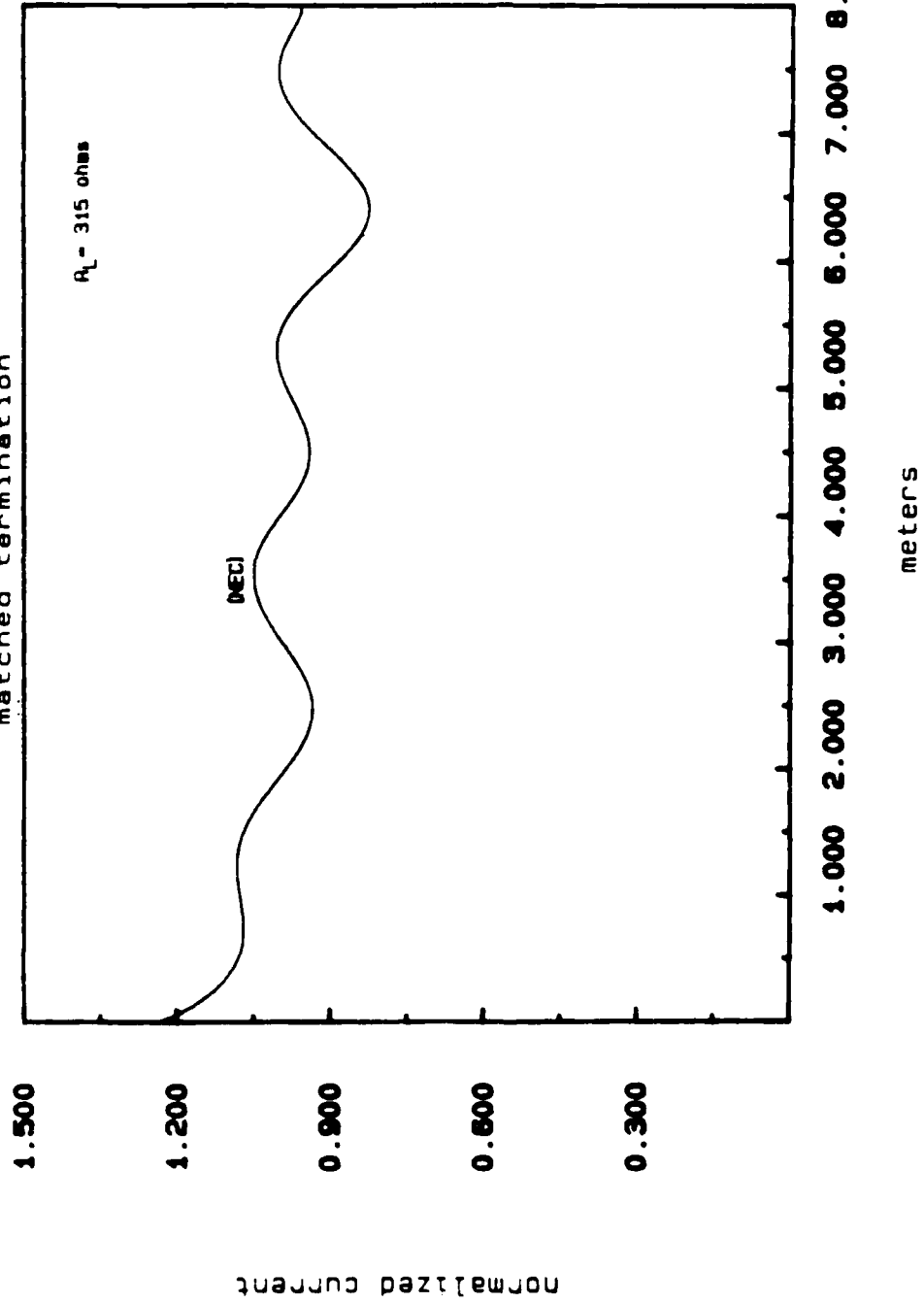


Figure 2.10. (b) Computed by Shen and King [29].

Current Mag. Along Wire Axis (74.95MHz)
 matched termination



(a) Magnitude of axial current.
 Figure 2.11. Normalized current computed along the conducting wires of the rhombic EMP simulator by NEC under matched conditions when $\lambda = 4 \text{ m}$.

Current Phase Along Wire Axis (74.95 MHz)
matched termination

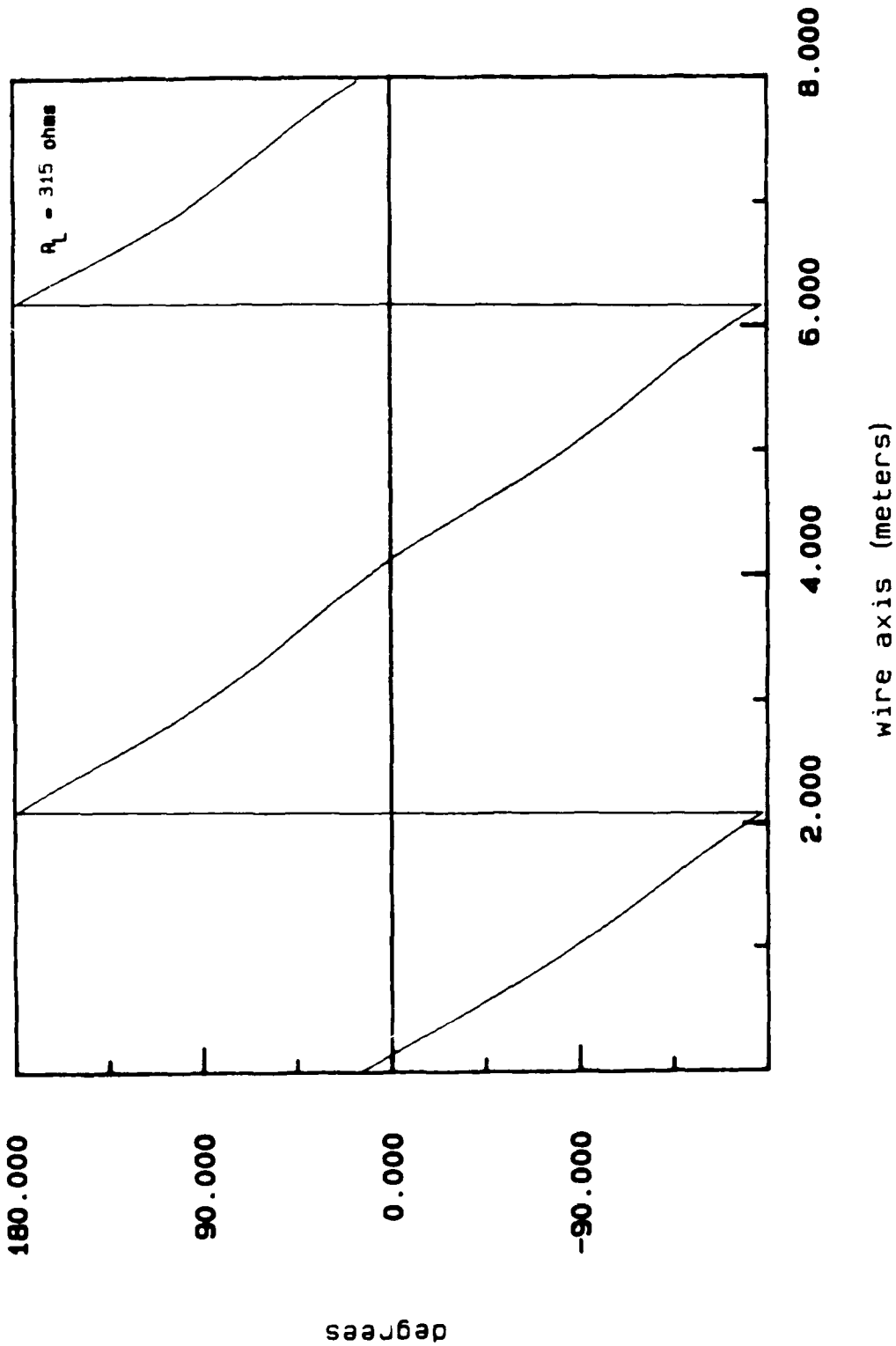
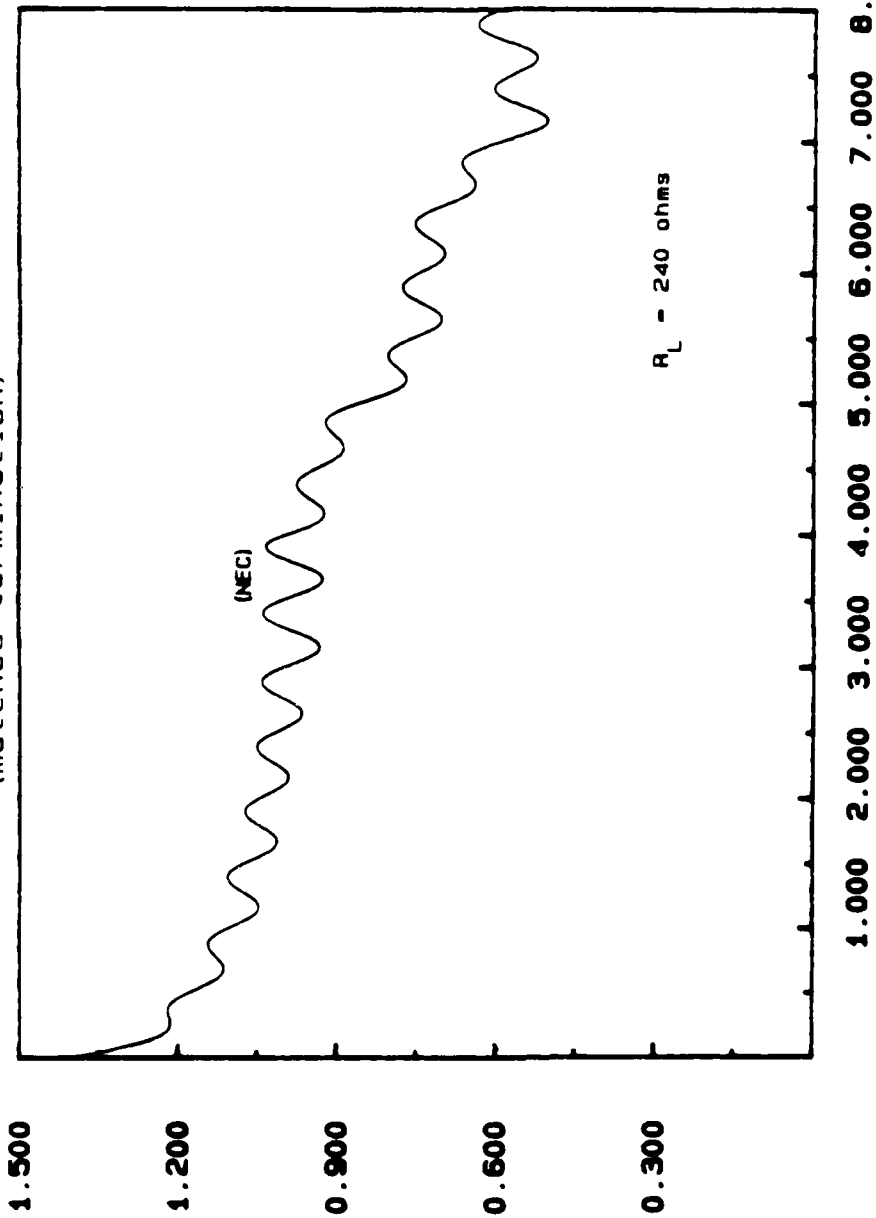


Figure 2.11. (b) Phase of axial current.

Current Along Wire Axis (299.8 MHz)
(matched termination)



(a) Magnitude of axial current.

Figure 2.12. Normalized current computed along the conducting wires of the rhombic EMP simulator by NEC under matched conditions when $\lambda = 1 \text{ m}$.

Current Phase Along Wire Axis (299.8 MHz)

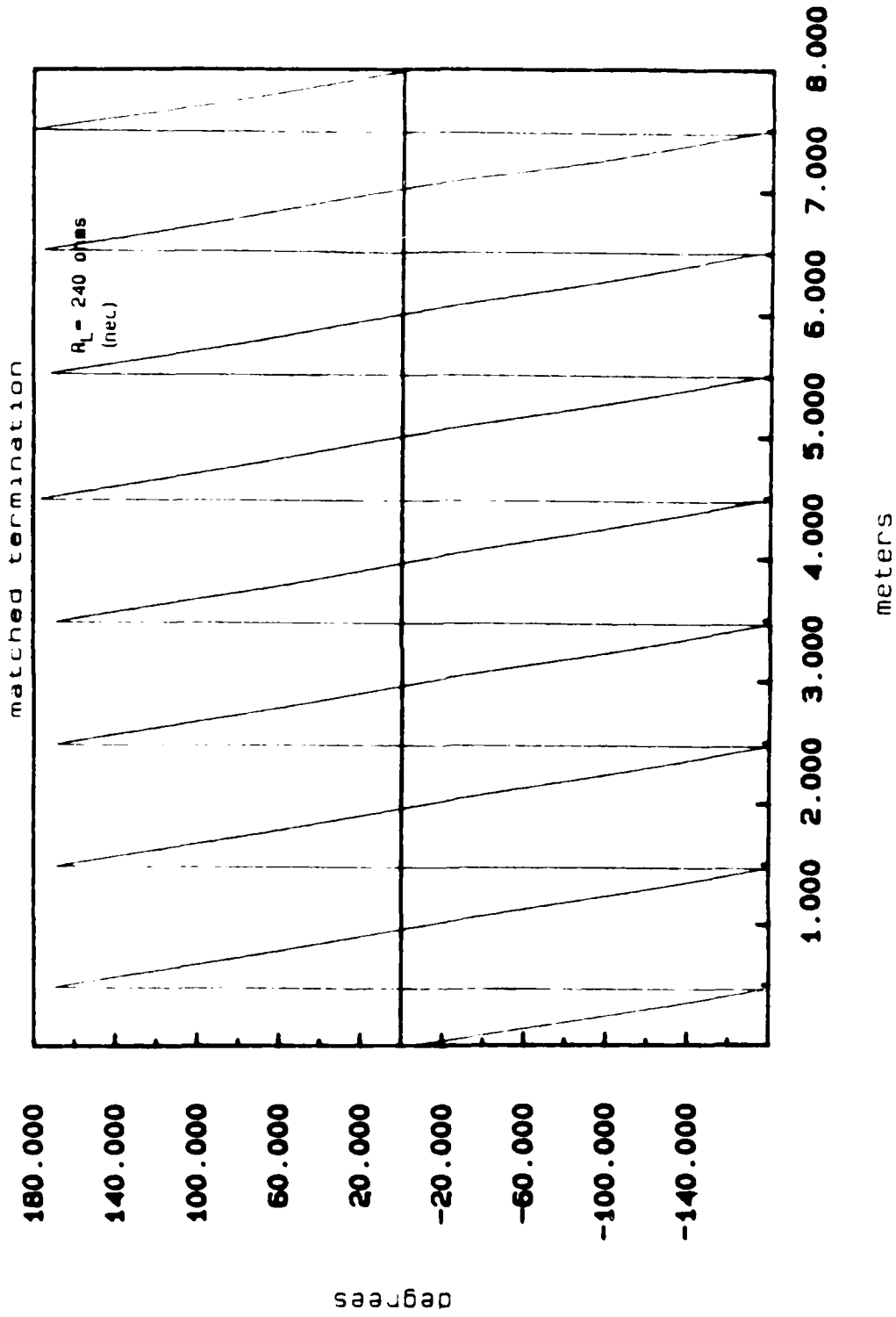


Figure 2.12. (b) Phase of axial current.

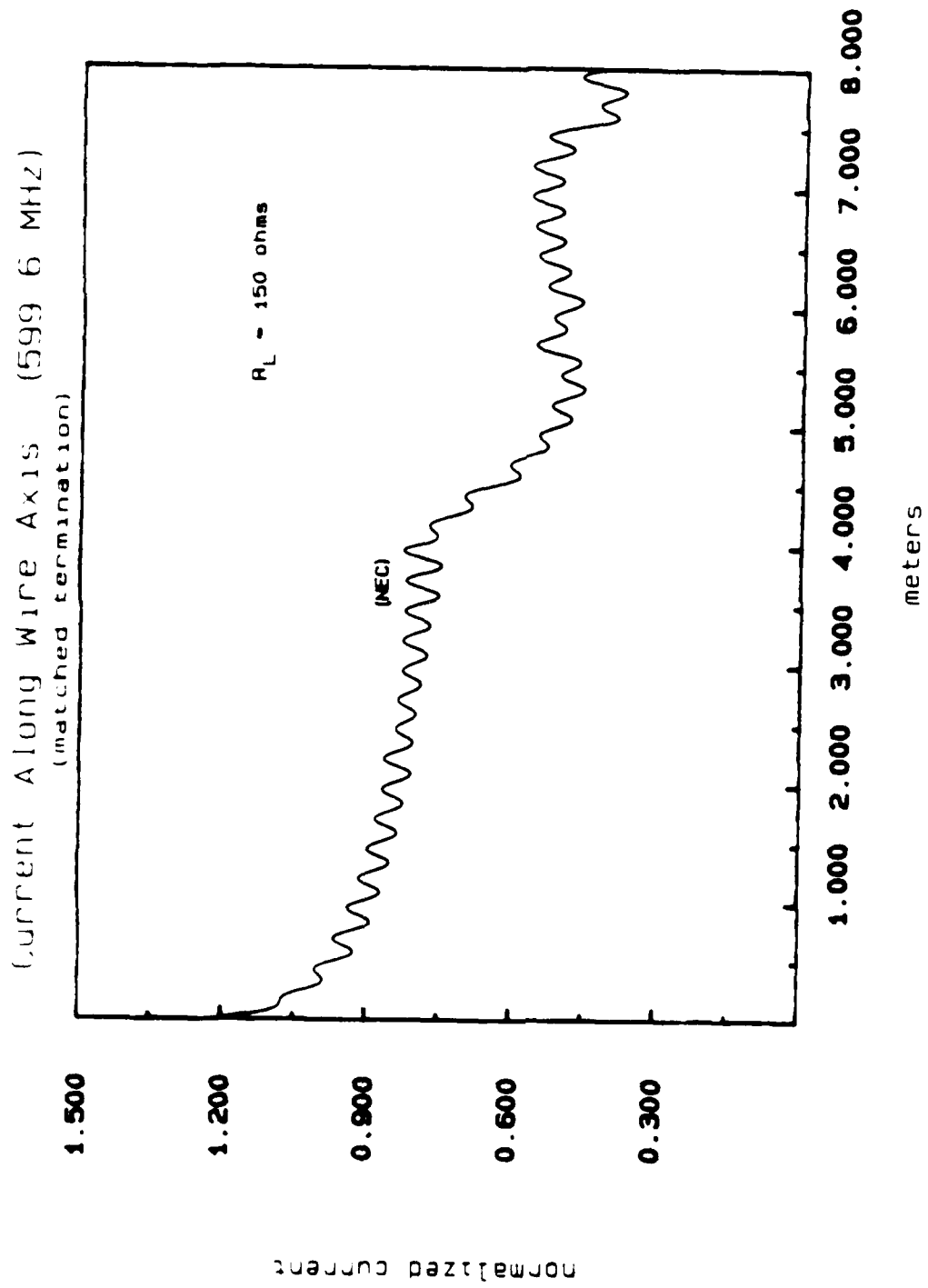


Figure 2.13. Normalized current computed along the conducting wires of the rhombic EMP simulator by NEC under matched conditions when $\lambda = 0.5 \text{ m}$.

Current Phase Along Wire Axis (599.6 MHz)
(matched termination, $R_L = 150 \text{ ohms}$)

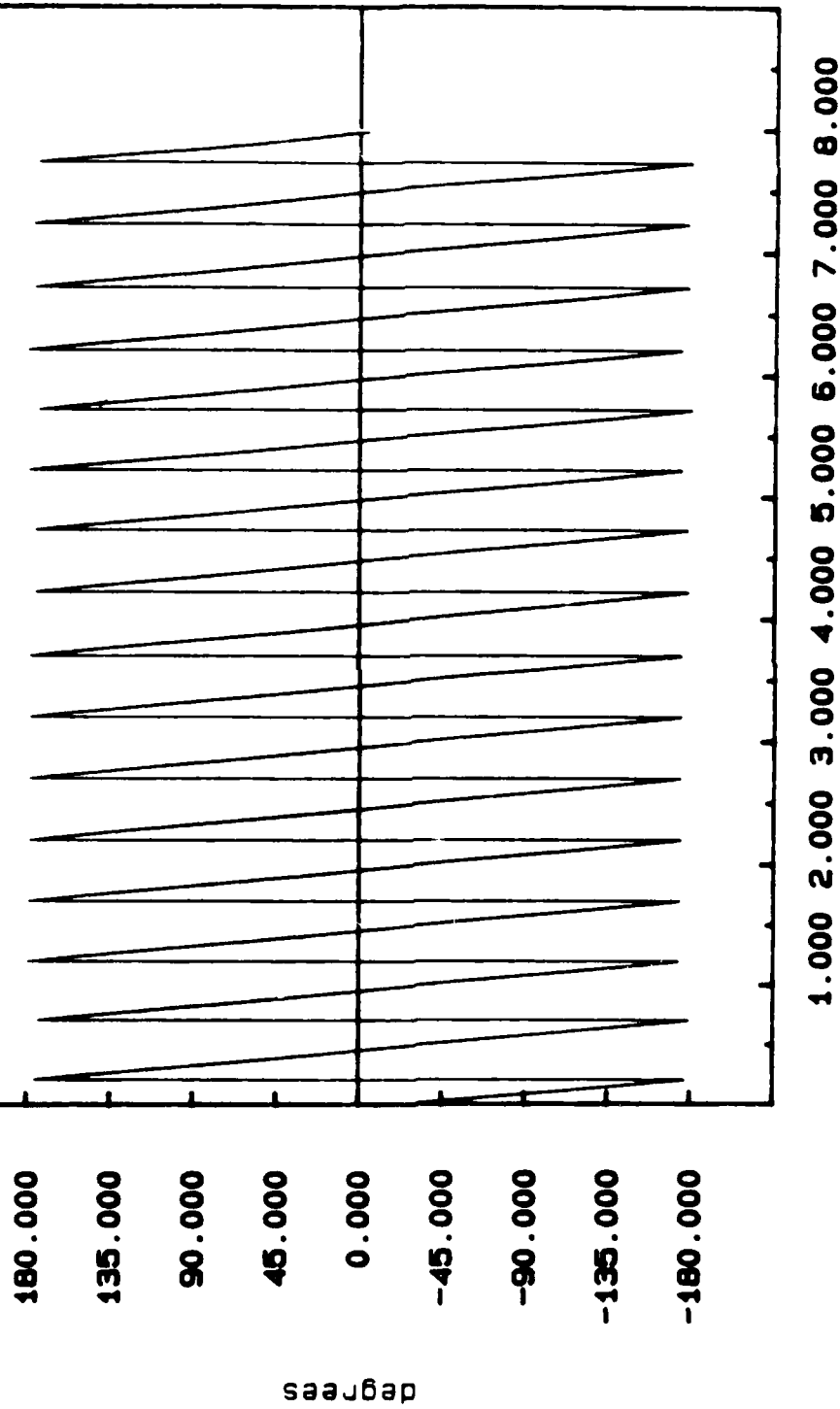


Figure 2.13. (b) Phase of axial current.

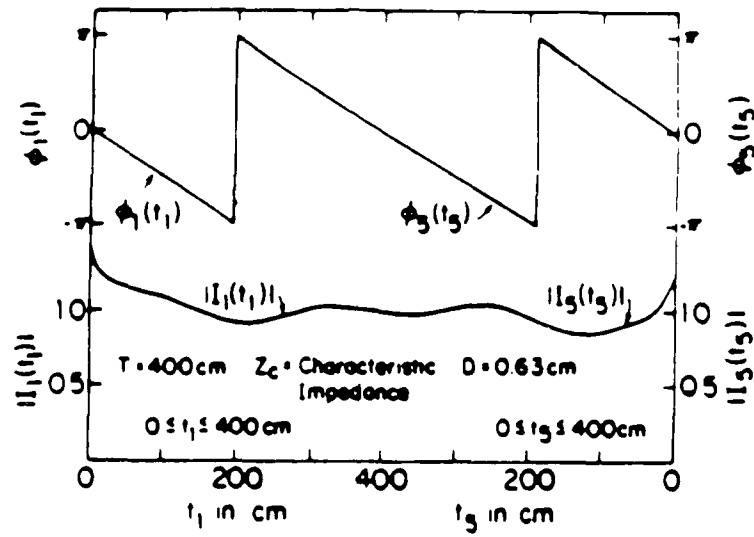
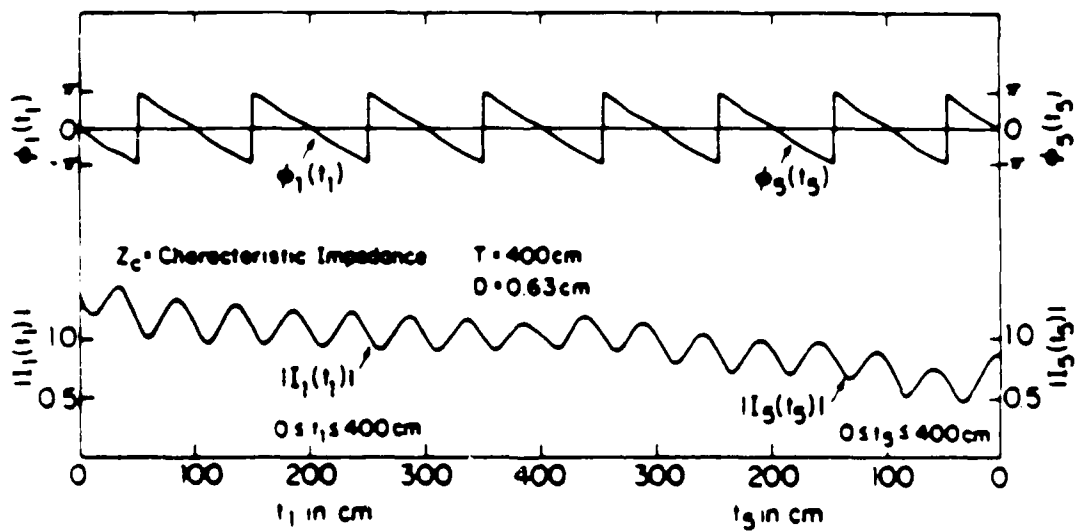
(a) $\lambda = 4$ m(b) $\lambda = 1$ m.

Figure 2.14. Normalized current computed along the conducting wires of the rhombic EMP simulator by Shen and King [28].

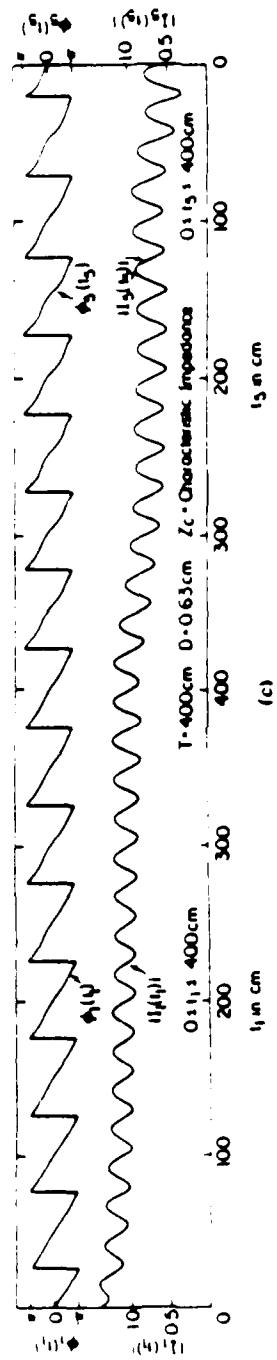


Figure 2.14. (c) $\lambda = 0.5$ m.

$|E_z|$ in Center Region (74.95 MHz)
 matched termination

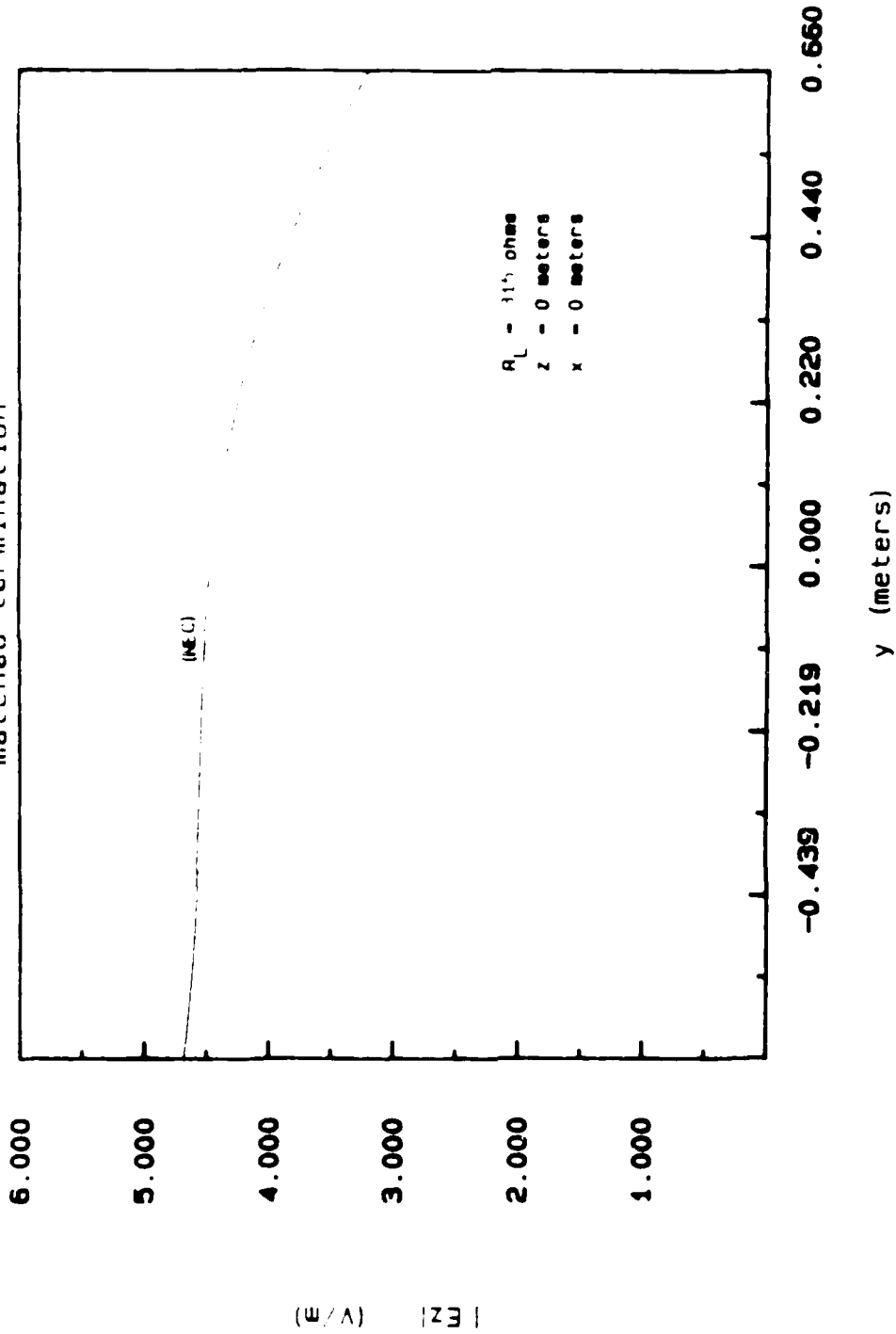


Figure 2.15. (a) Vertical E-field magnitude produced by a unit AEF excitation. Computed along the ground plane in the longitudinal direction, y , under matched load conditions for $\lambda = 4 \text{ m}$.

Ez Phase in Center Region (74.95 MHz)

matched termination

$R_L = 315 \text{ ohms}$
 $z = 0 \text{ meters}$
 $x = 0 \text{ meters}$

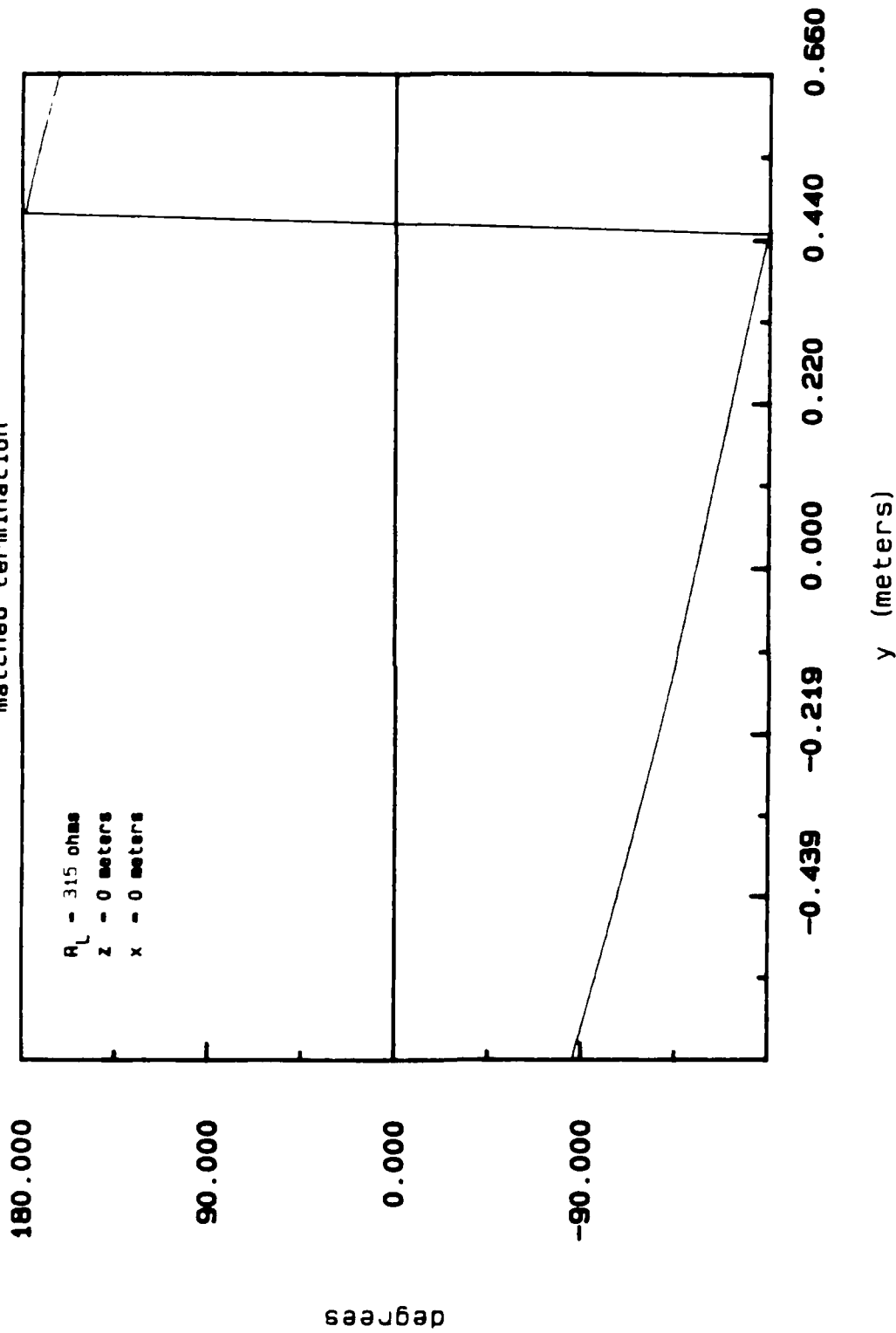


Figure 2.15. (b) Vertical E-field phase computed along the ground plane in the longitudinal direction for $\lambda = 4 \text{ m}$.

E-field in Center Region (74.95 MHz)
(matched termination)

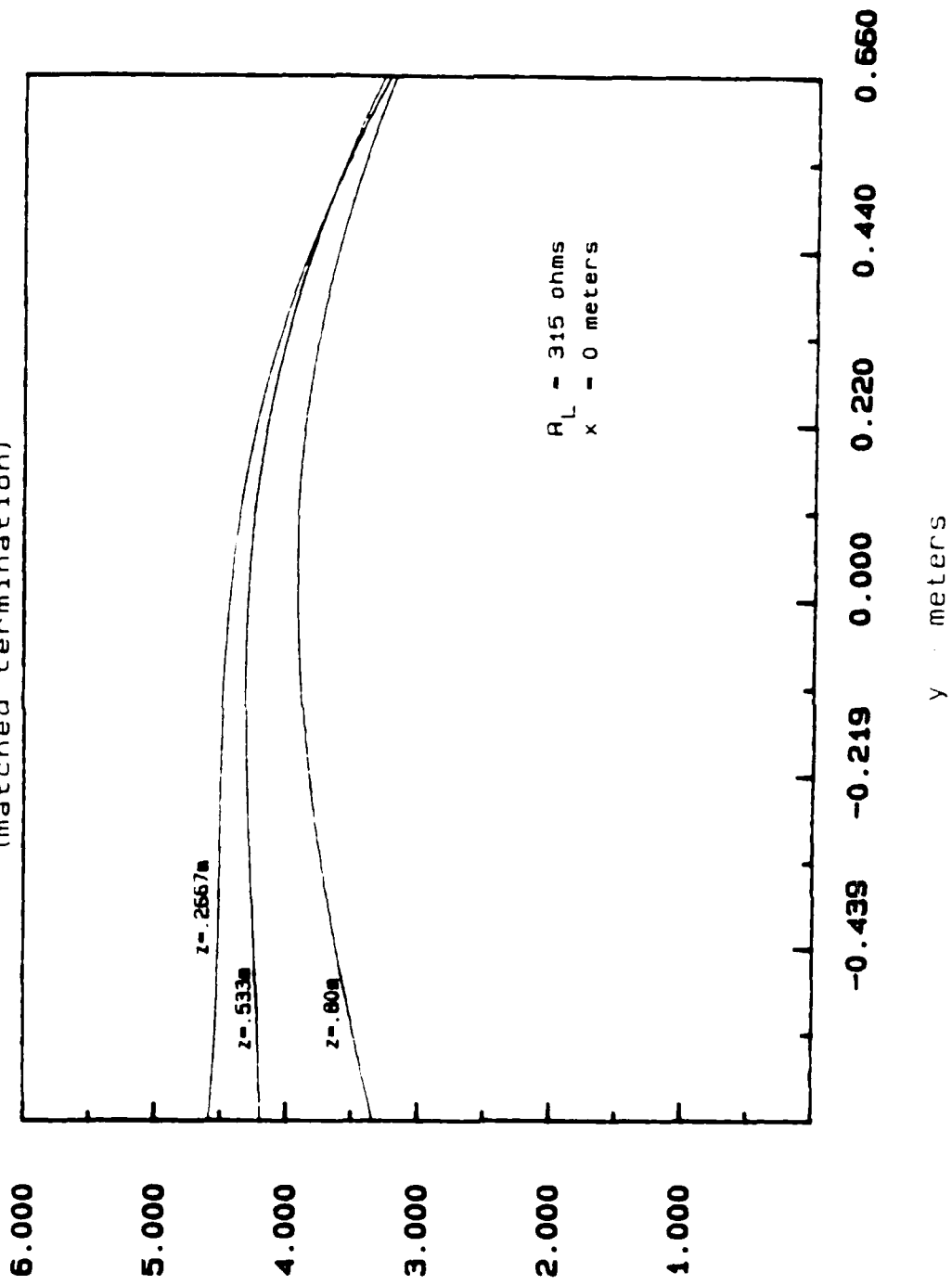


Figure 2.15. (c) Vertical E-field magnitude computed at various heights in the working volume in the $x=0$ plane for $\lambda = 4 \text{ m}$.

$|E_y|$ in Center Region (74.95MHz)
(matched termination)

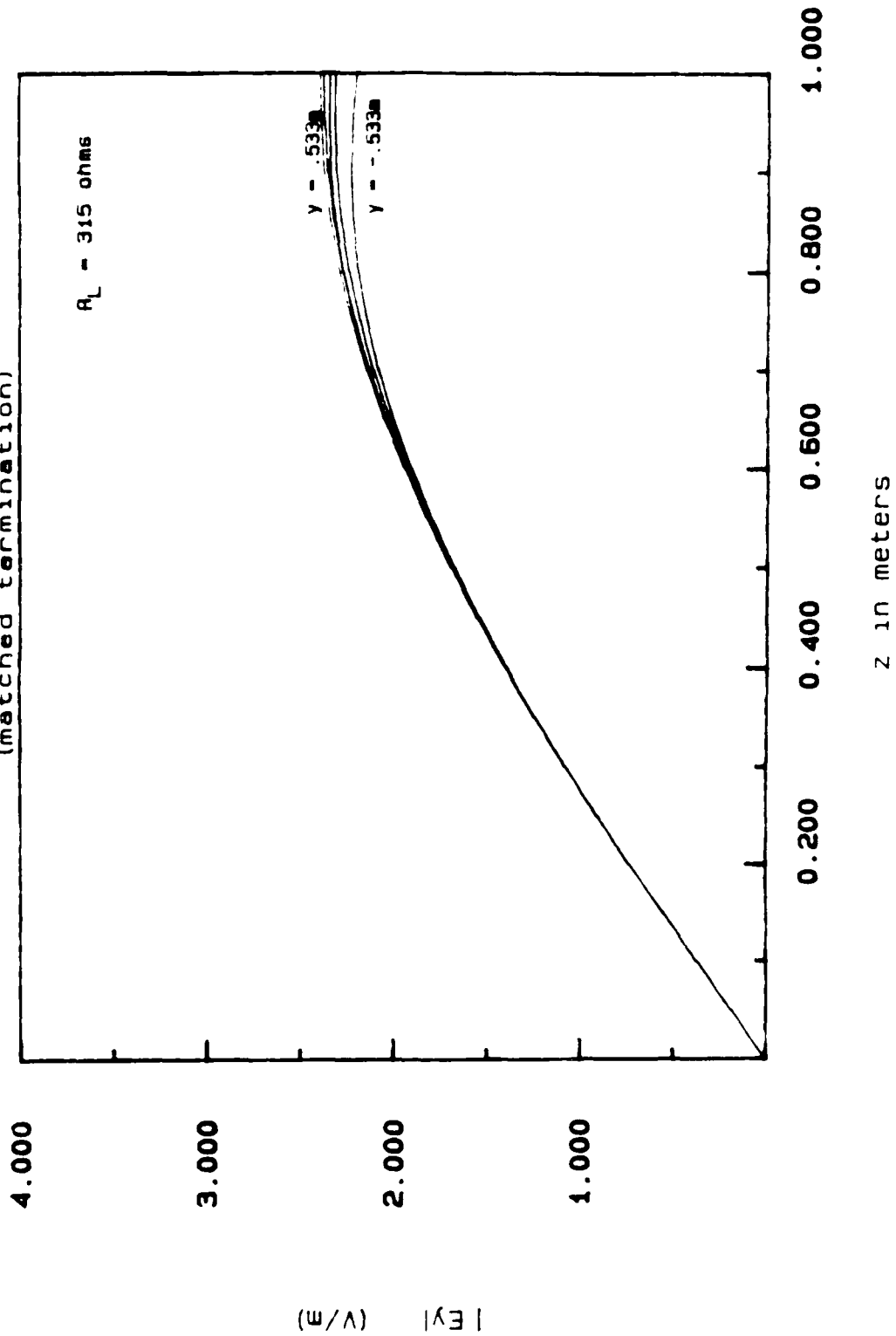
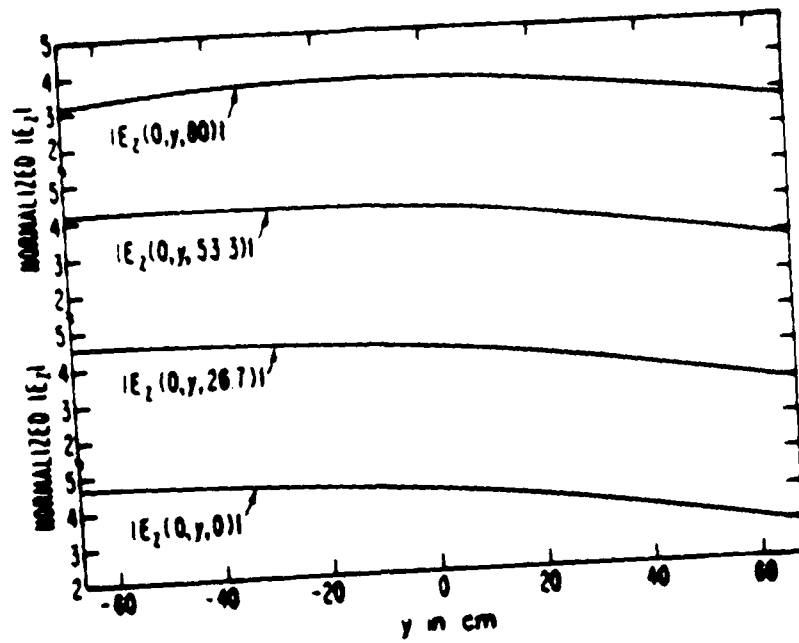
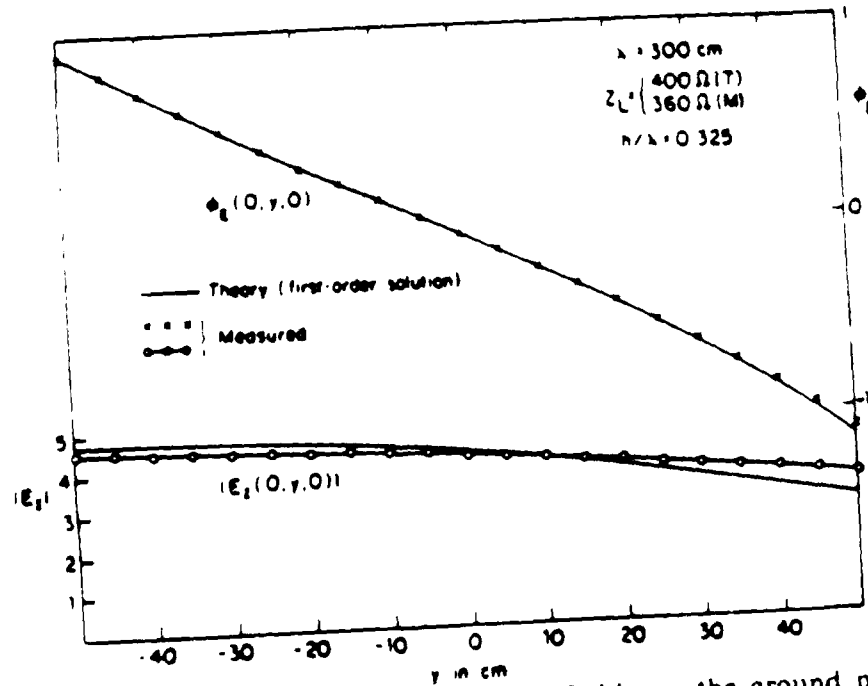


Figure 2.15. (d) Longitudinal E-field magnitude computed along the vertical direction in the x=0 plane at various longitudinal positions in the working volume for $\lambda = 4 \text{ m}$.



(a) Theoretical vertical E-field computed along the longitudinal direction [28].



(b) Theoretical and experimental vertical E-fields on the ground plane computed along the longitudinal direction [29]. Dimensions are scaled down by $3/4$.

Figure 2.16. Theoretical and experimental results of the distributed E-field in the $x=0$ plane, presented by Shen and King for $\lambda = 4$ m.

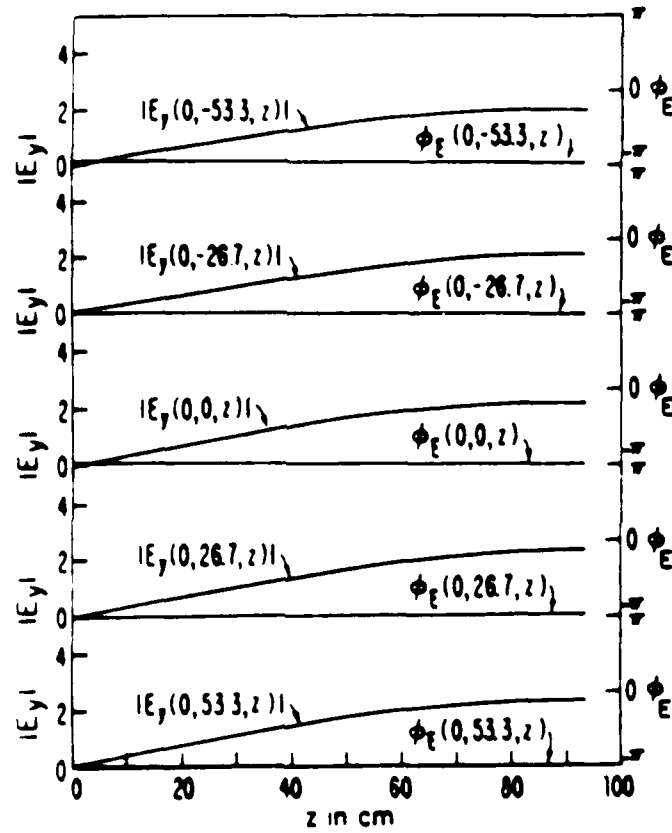


Figure 2.16. (c) Theoretical longitudinal E-field computed along the vertical direction at various longitudinal positions [28].

$|E_z|$ in Center Region (299.8 MHz)
matched termination

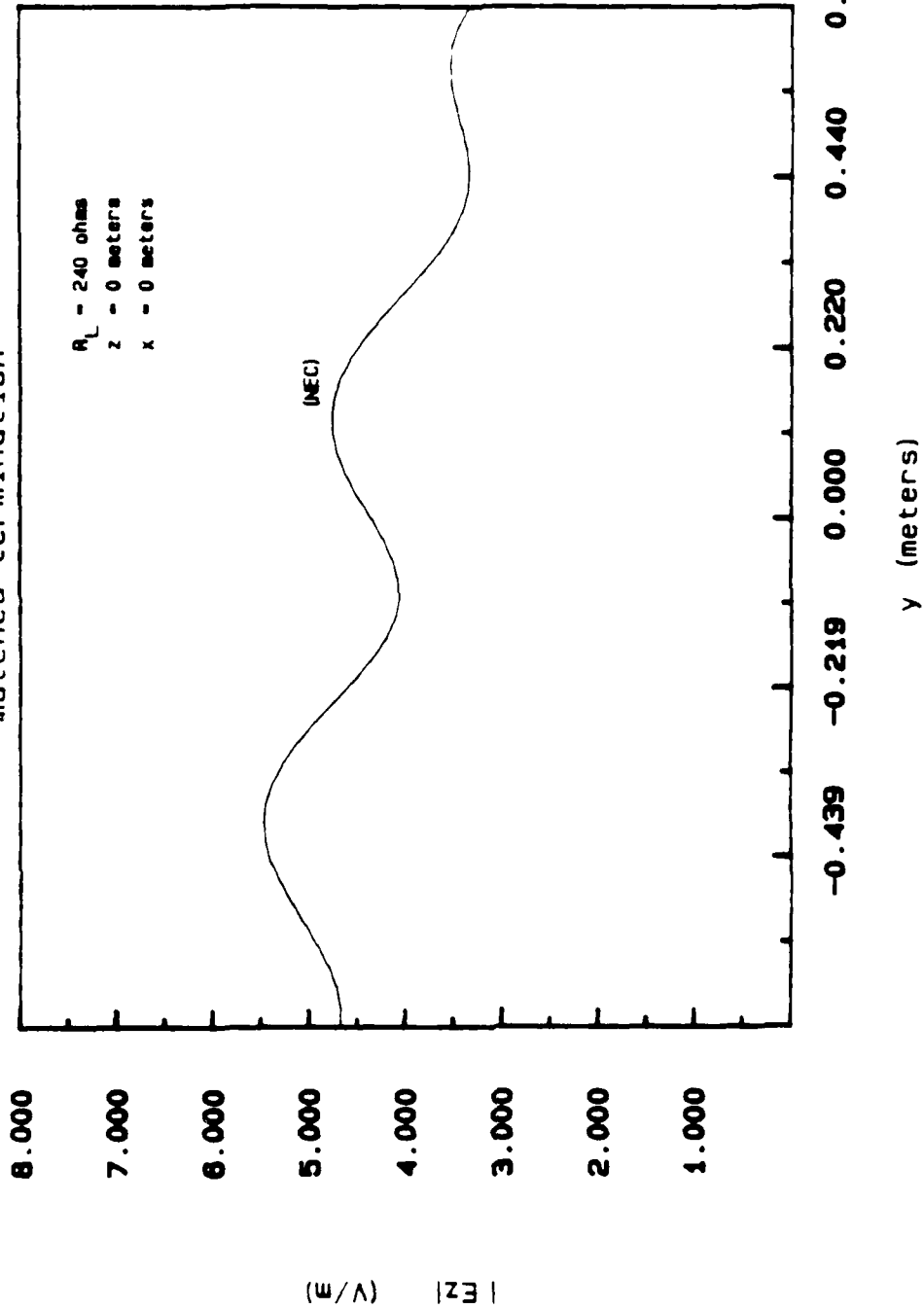


Figure 2.17. (a) Vertical E-field magnitude produced by a unit AEF excitation. (Computed along the ground plane in the longitudinal direction, y , under matched load conditions for $\lambda = 1 \text{ m}$.)

Ez Phase in Center Region (299.8 MHz)
 matched termination

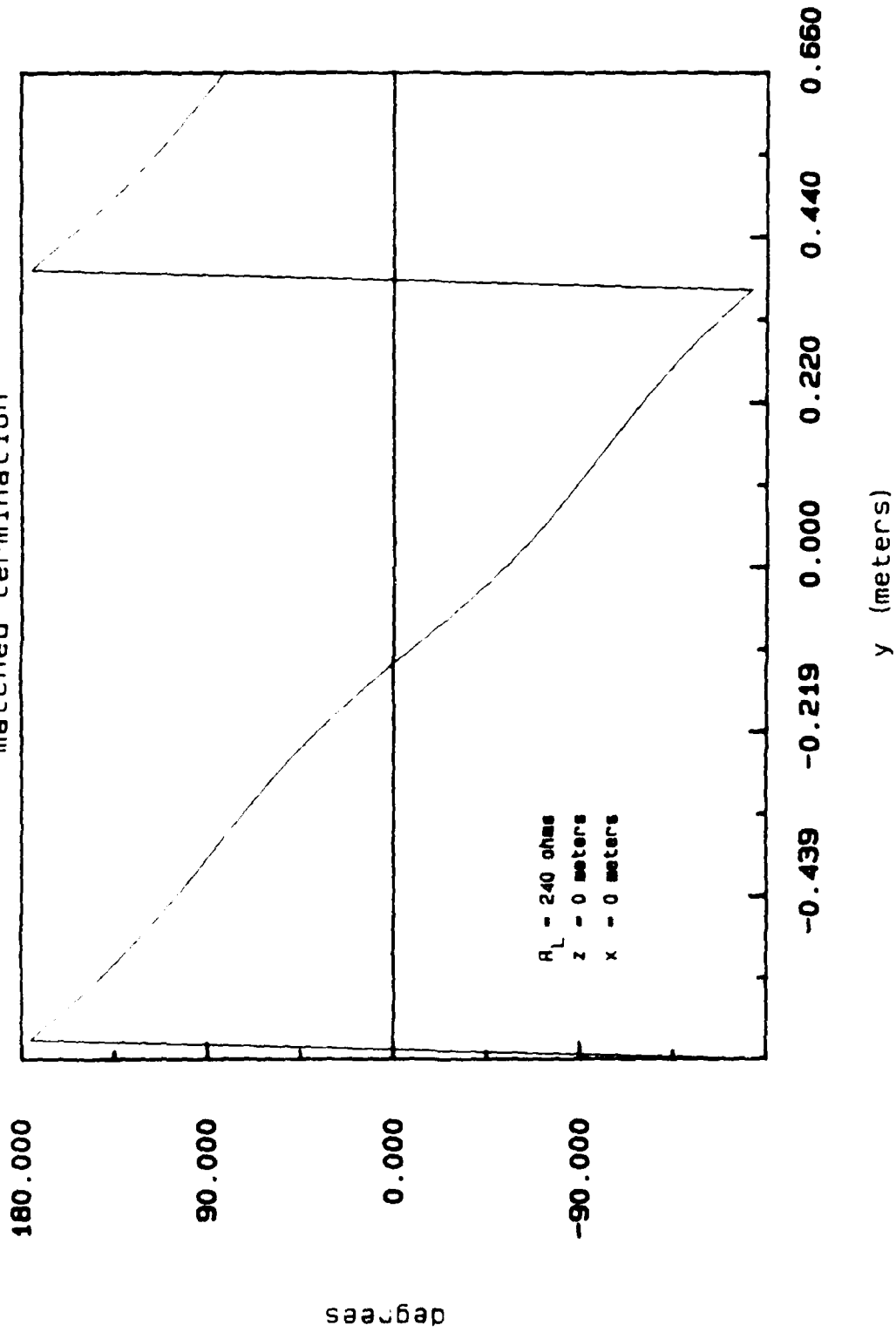


Figure 2.17. (b) Vertical E: field phase computed along the ground plane in the longitudinal direction for $\lambda \approx 1 \text{ m}$.

$|E_z|$ in Center Region (299.8 MHz)
 (matched termination)

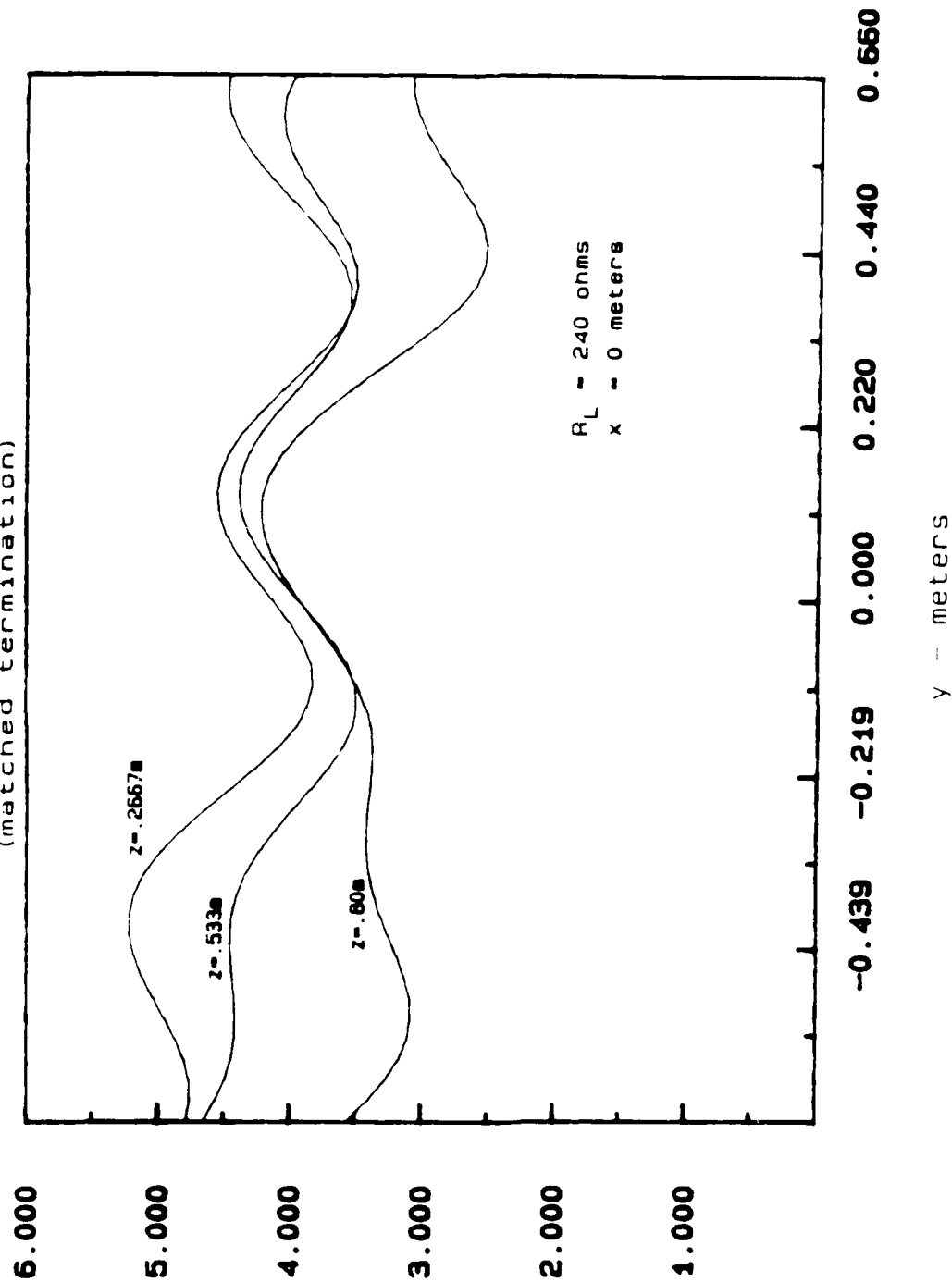


Figure 2.17. (c) Vertical E-field magnitude computed at various heights in the working volume in the $x=0$ plane for $\lambda = 1 \text{ m}$.

|E_y| in Center Region (299.8MHz)

(matched termination)

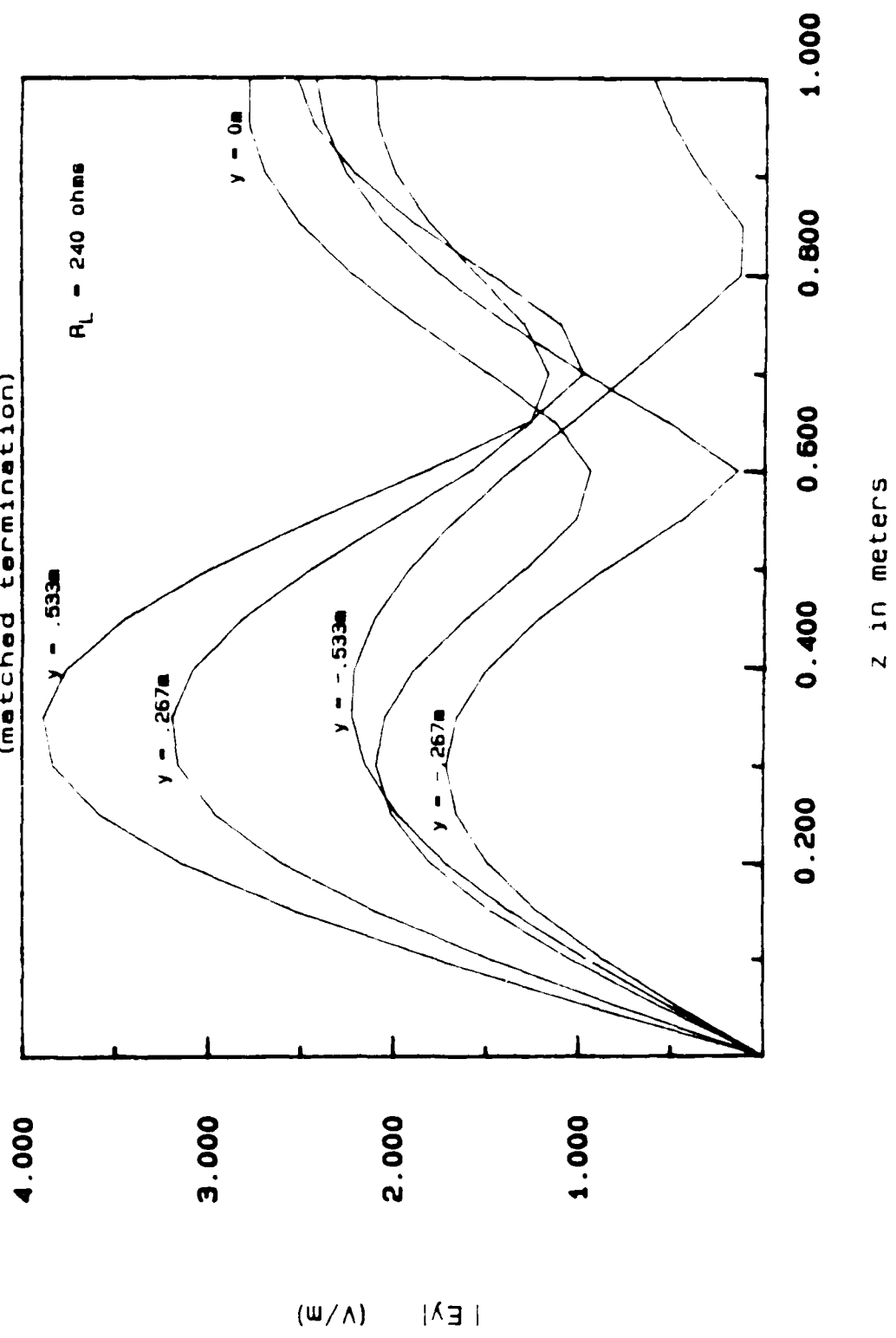
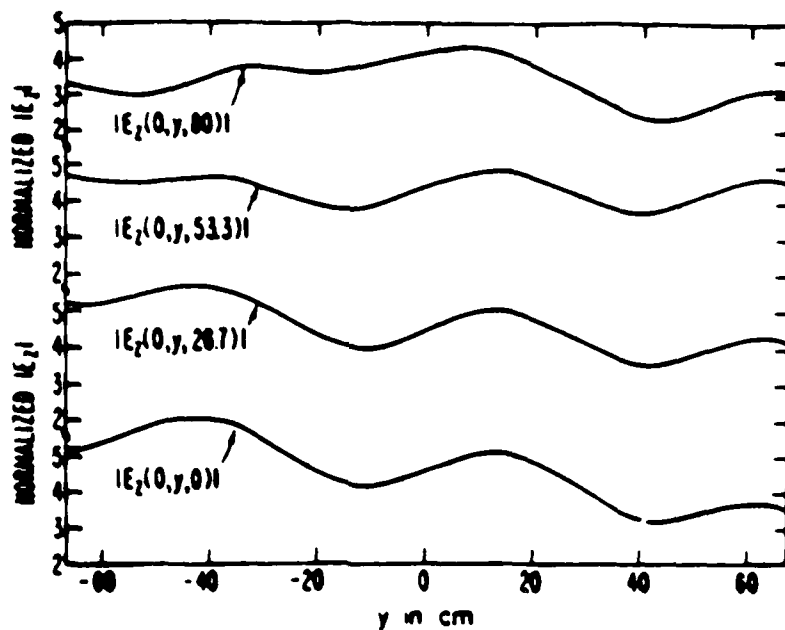
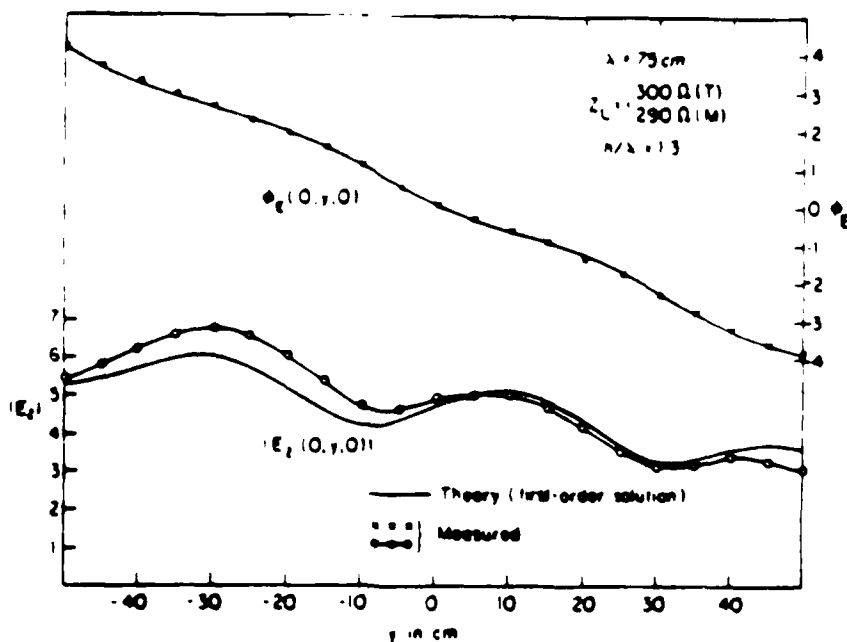


Figure 2.17. (d) Longitudinal E field magnitude computed along the vertical direction in the $x=0$ plane at various longitudinal positions in the working volume for $\lambda = 1 \text{ m}$.



(a) Theoretical vertical E-field computed along the longitudinal direction [28].



(b) Theoretical and experimental vertical E-fields on the ground plane computed along the longitudinal direction [29]. Dimensions are scaled down by $3/4$.

Figure 2.18. Theoretical and experimental results of the distributed E-field in the $x=0$ plane, presented by Shen and King for $\lambda = 1 \text{ m}$.

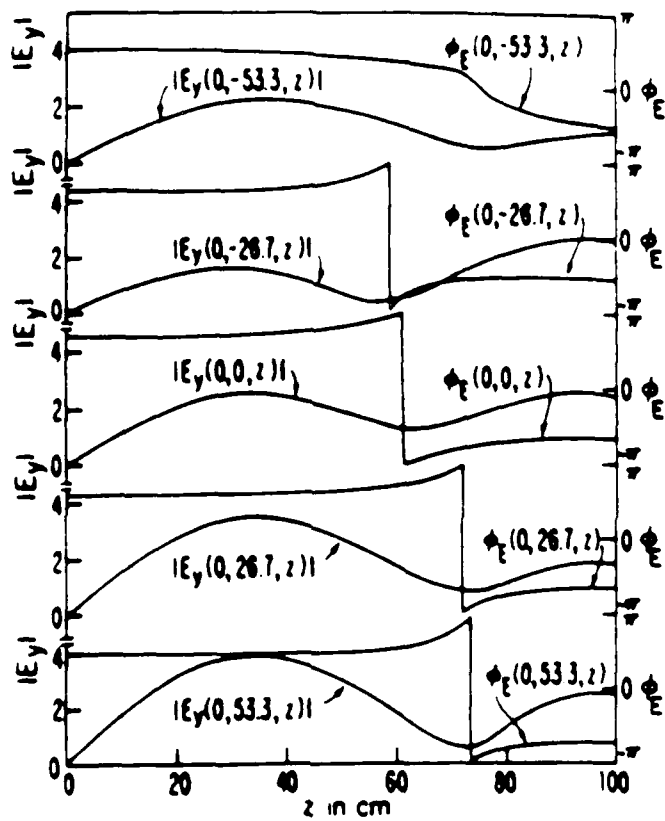


Figure 2.18. (c) Theoretical longitudinal E-field computed along the vertical direction at various longitudinal positions [28].

$|E_z|$ in Center Region (599.6 MHz)
(matched termination)

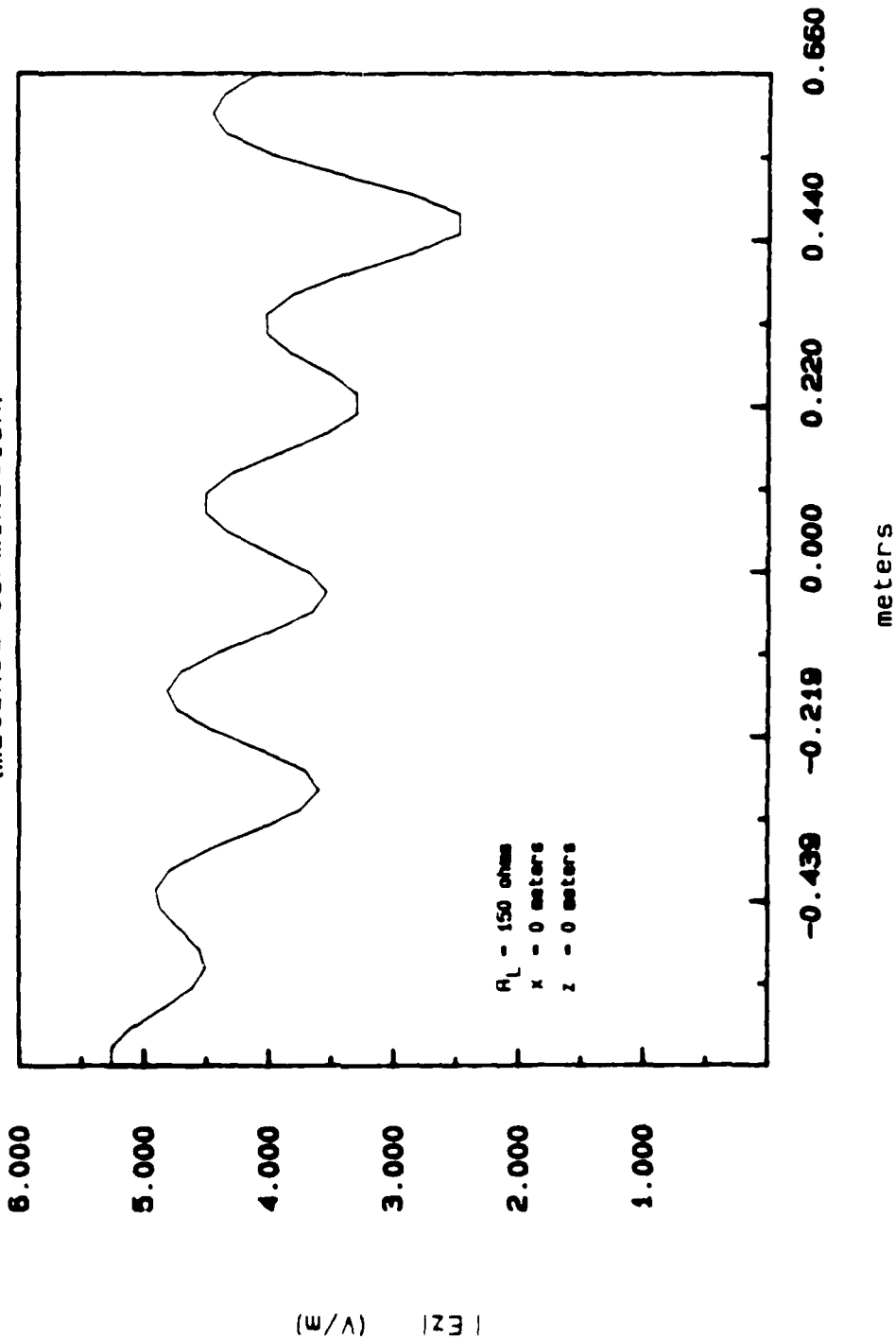


Figure 2.19. (a) Vertical E-field magnitude produced by a unit AEF excitation. Computed along the ground plane in the longitudinal direction, y , under matched load conditions. $\lambda = 0.5 \text{ m}$.

$|E_z|$ in Center Region (599.6 MHz)
(matched termination)

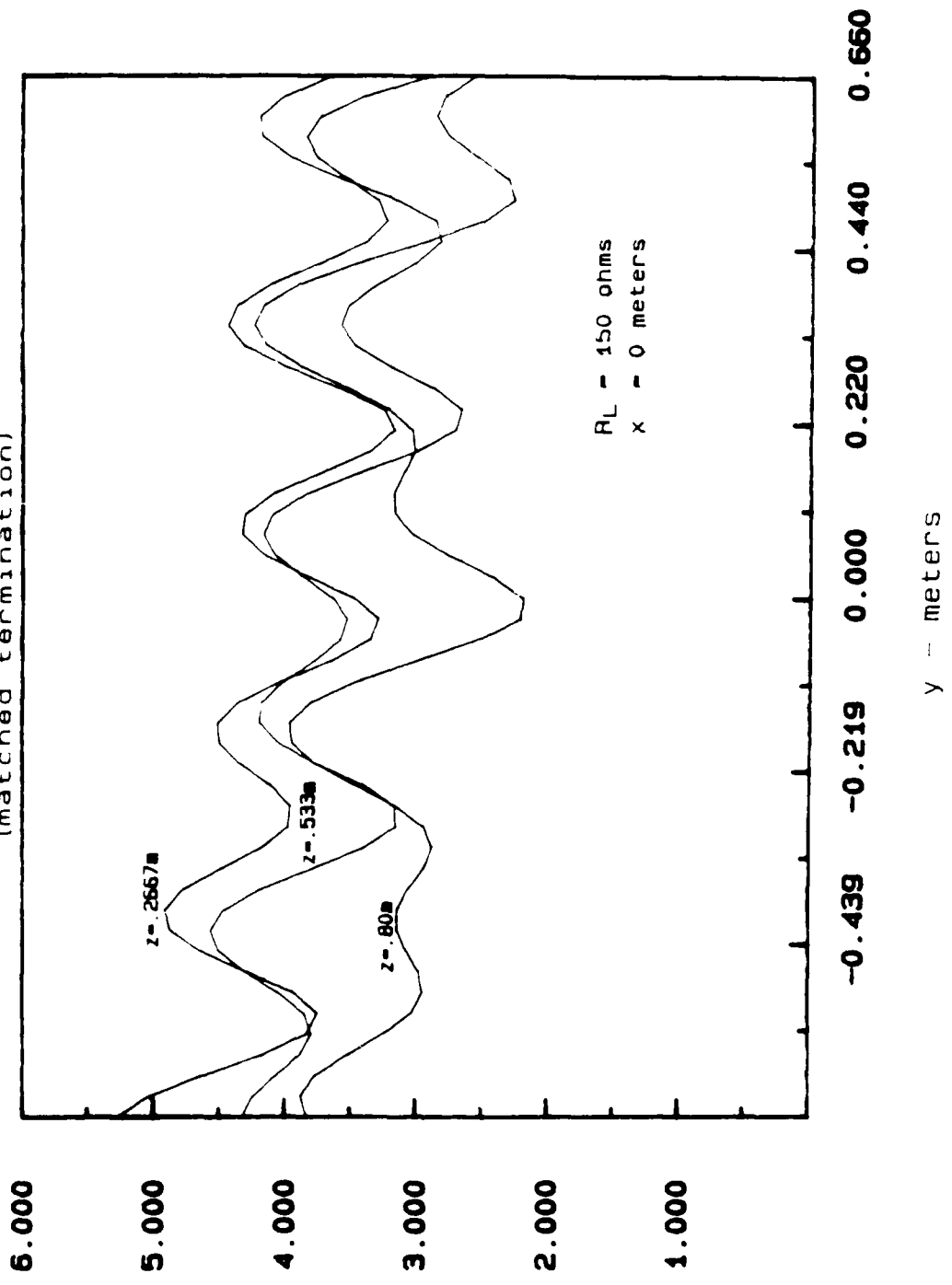


Figure 2.19. (b) Vertical E field magnitude computed at various heights in the working volume in the $x=0$ plane for $\lambda = 0.5 m$.

$|E_y|$ in Center Region (599.6 MHz)
(matched termination)

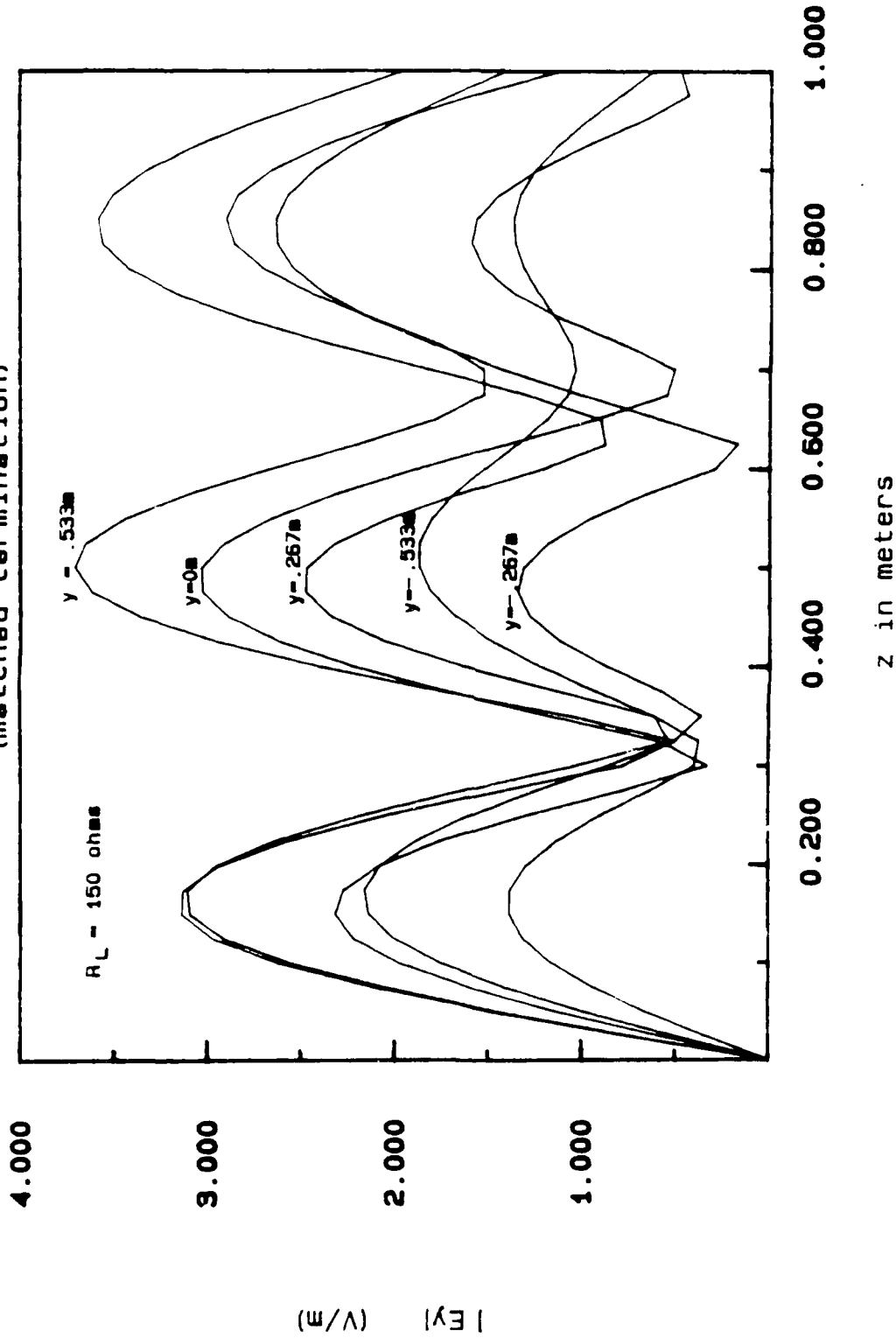
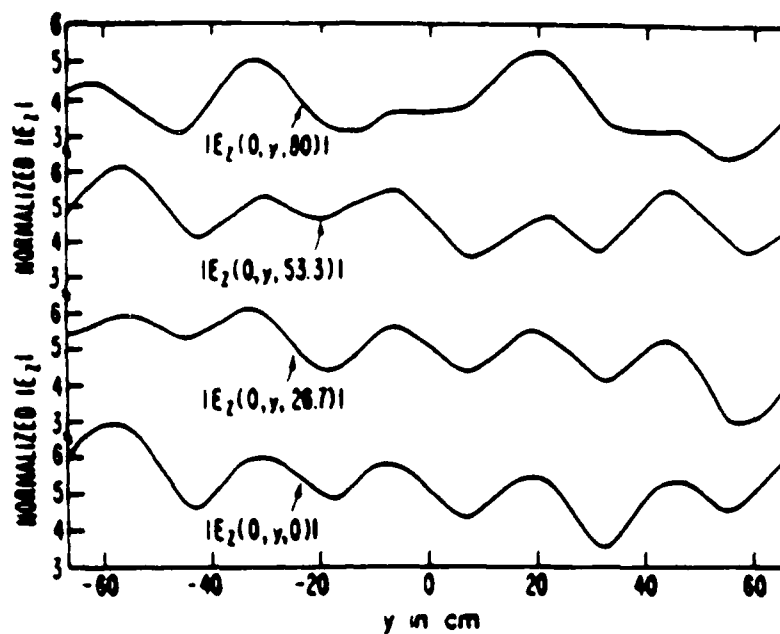
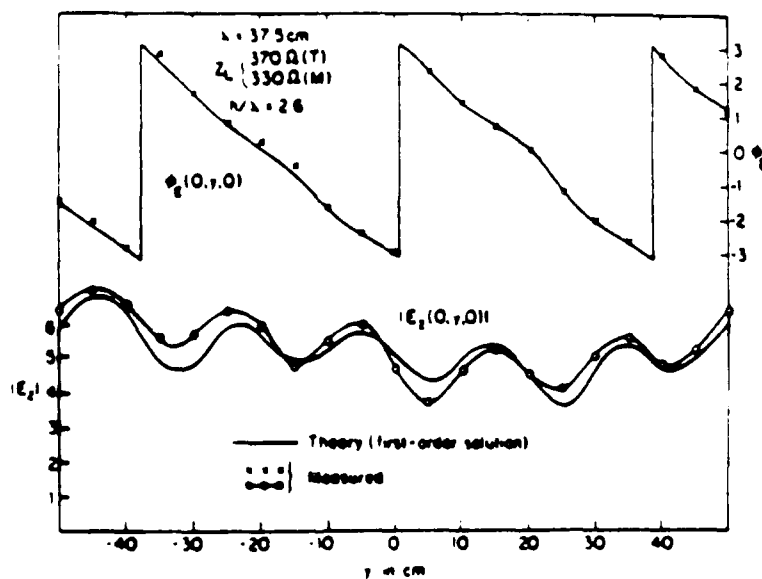


Figure 2.19. (c) Longitudinal E-field magnitude computed along the vertical direction in the $x=0$ plane at various longitudinal positions in the working volume for $\lambda = 0.5 \text{ m}$.



(a) Theoretical vertical E-field computed along the longitudinal direction [28].



(b) Theoretical and experimental vertical E-fields on the ground plane computed along the longitudinal direction [29]. Dimensions are scaled down by $3/4$.

Figure 2.20. Theoretical and experimental results of the distributed E-field in the $x=0$ plane, presented by Shen and King for $\lambda = 0.5 \text{ m}$.

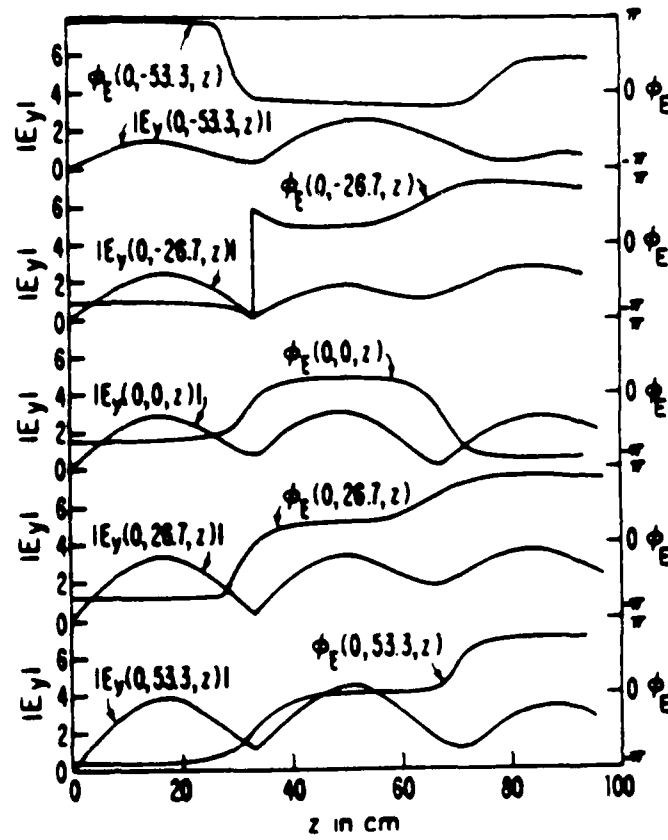


Figure 2.20. (c) Theoretical longitudinal E-field computed along the vertical direction at various longitudinal positions [28].

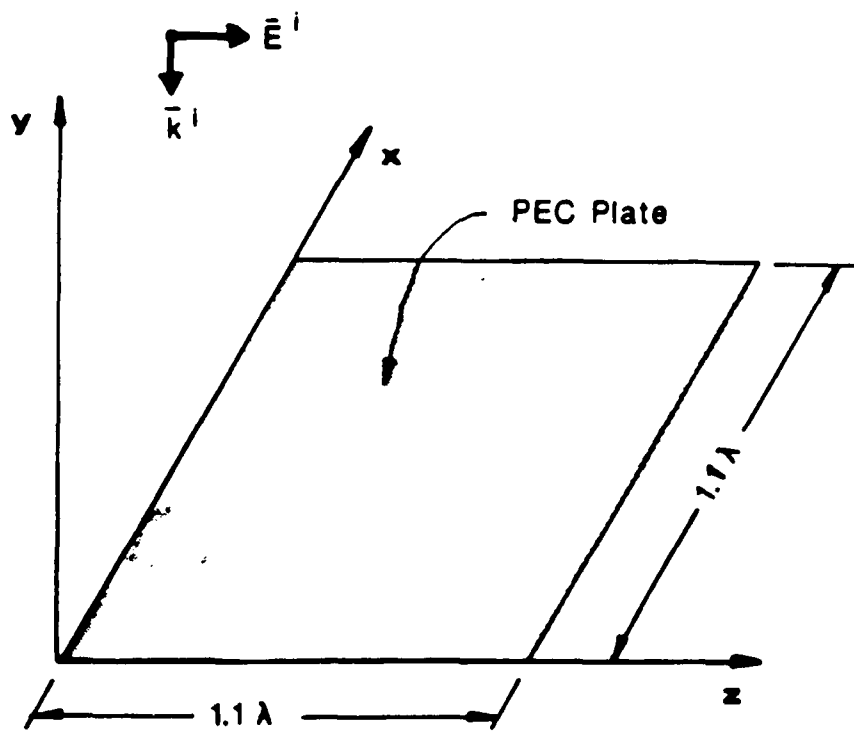
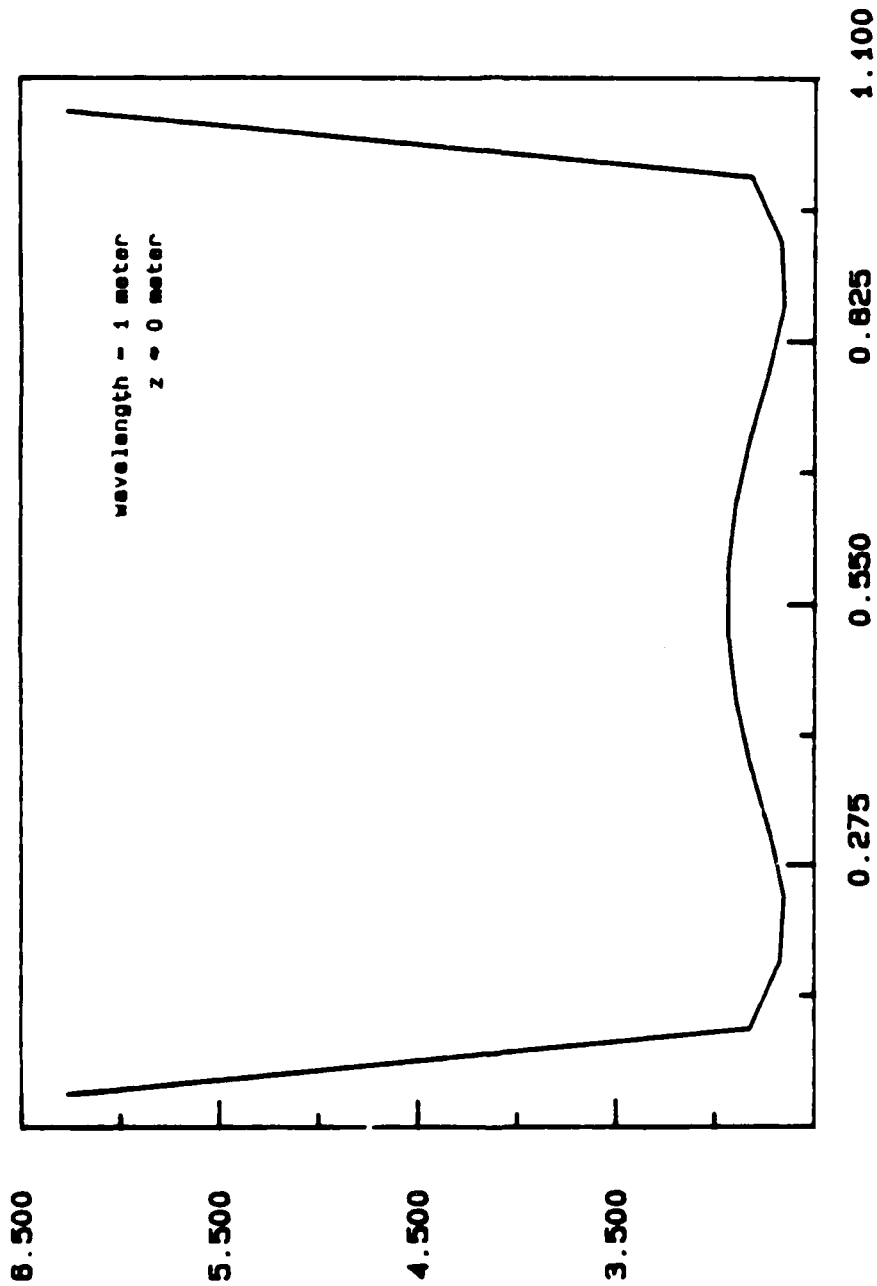


Figure 2.21. Geometry of the PEC plate illuminated by a normally incident TE plane wave ($E^i = \hat{z}E_z$).

TE Excitation of a Square Patch (1.1m)

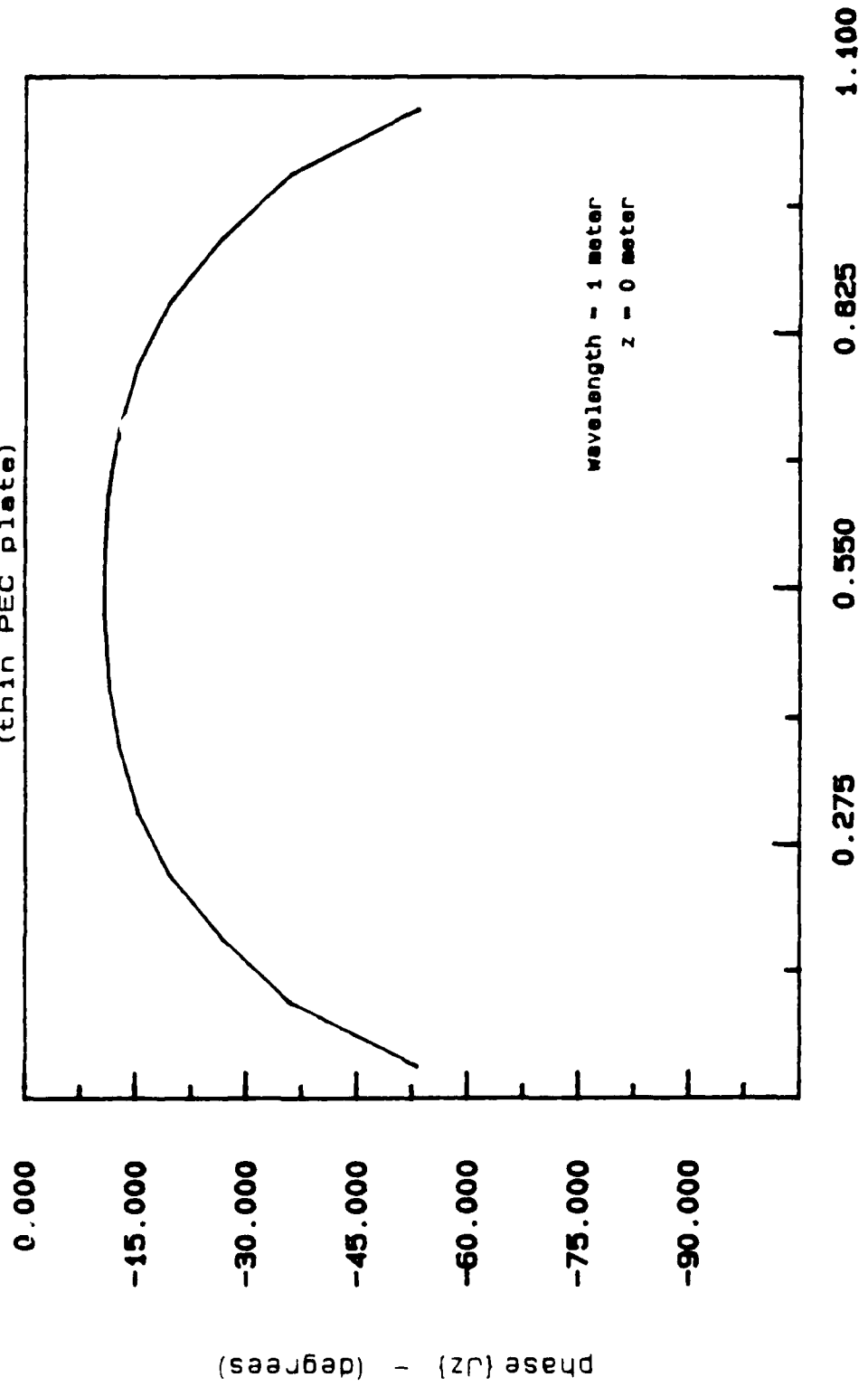


x - meters

(a) Magnitude of J_z .

Figure 2.22. J_z along the x-direction at $z=0$ m produced by a normally incident TE plane wave ($H/H_0 = 1$). Solution obtained by method of conjugate gradients and the spectral Galerkin technique.

TE Excitation of a Square Patch (1.1m)
(thin PEC plate)



x - meters

Figure 2.22. (b) Phase of J_z .

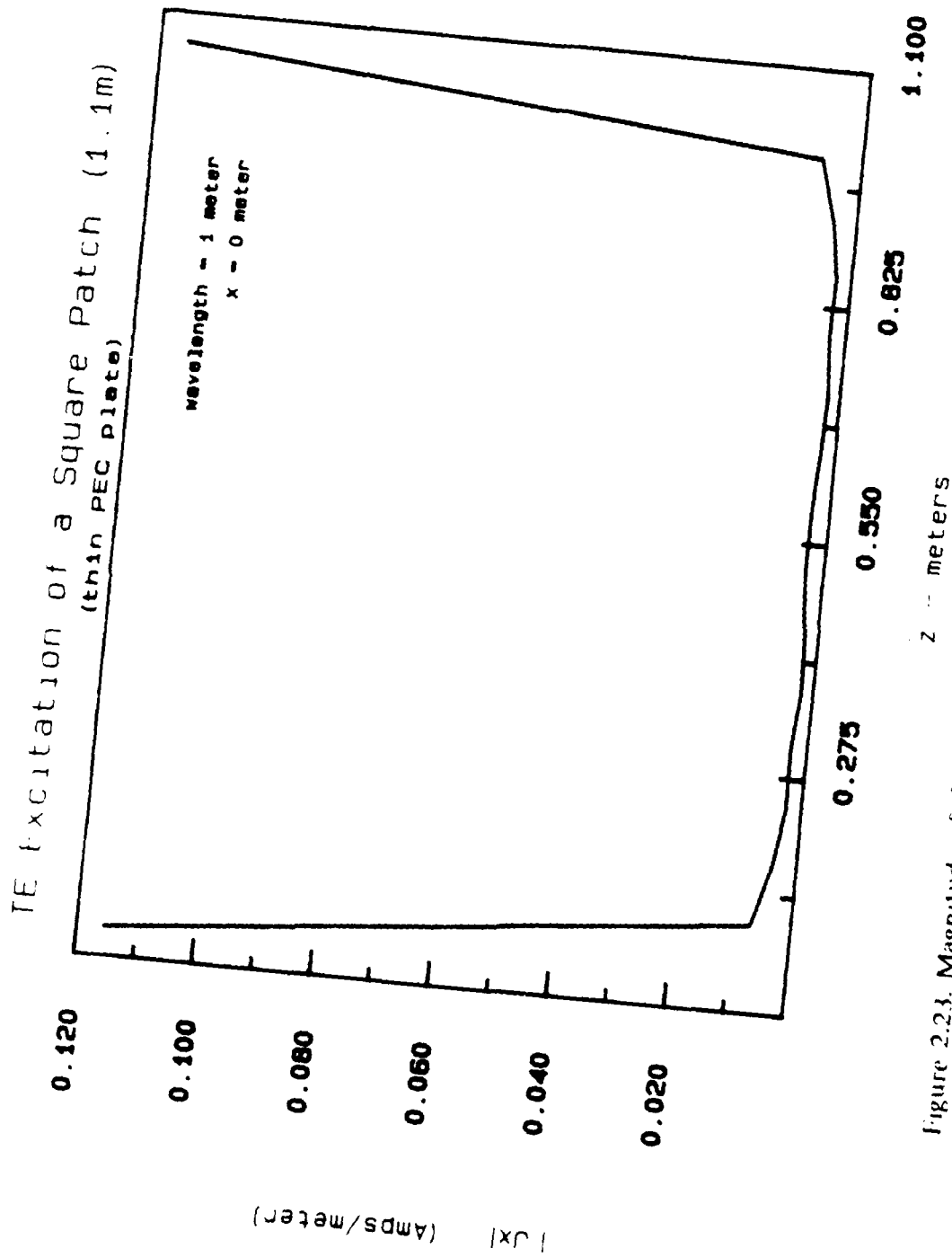
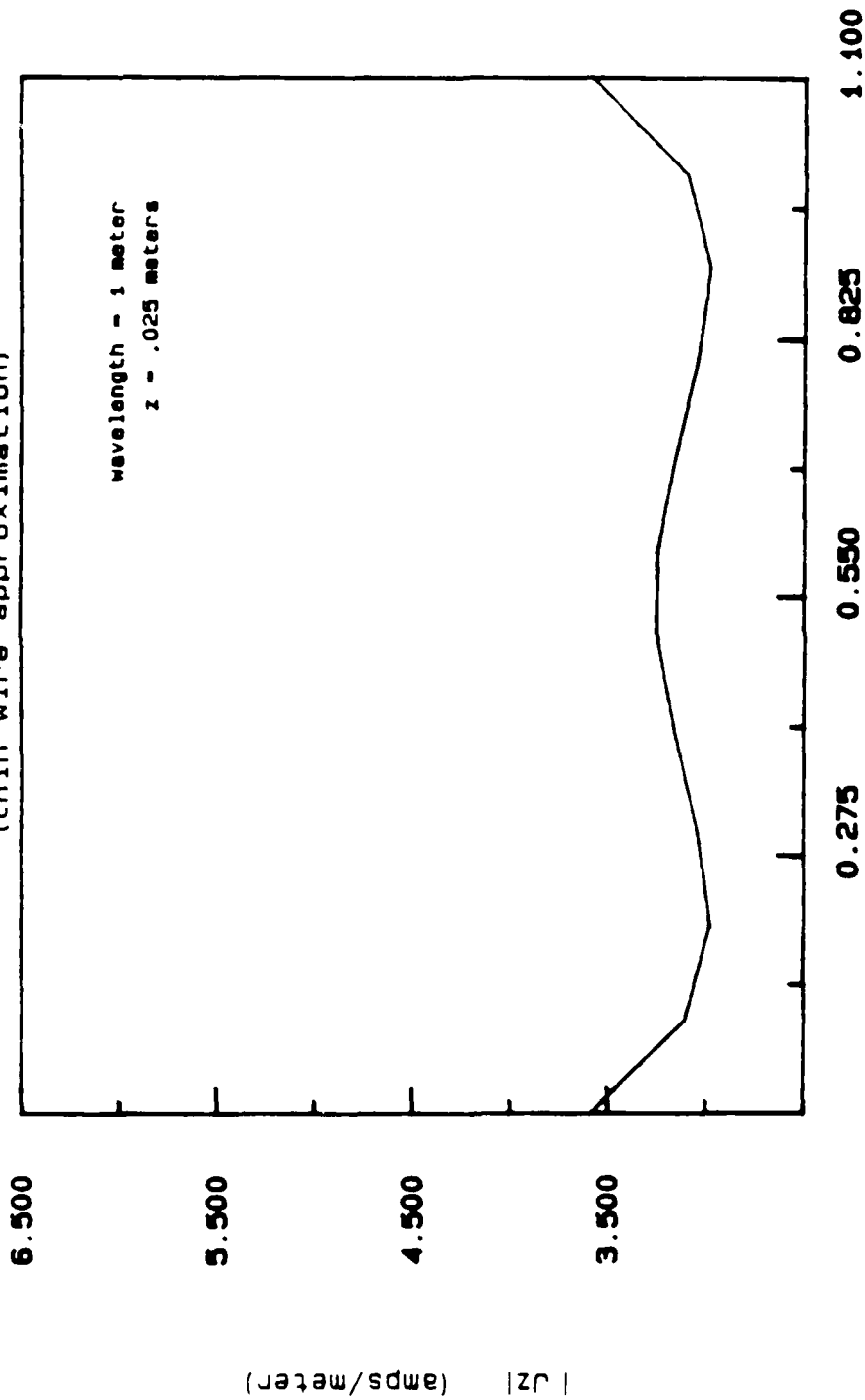


Figure 2.2.3. Magnitude of J_x along the z -direction at $x=0$ m produced by a normally incident TE plane wave ($H_x = 1$). Solution obtained by method of Conjugate Gradients (CG) and the spectral Galerkin technique (300 iterations).

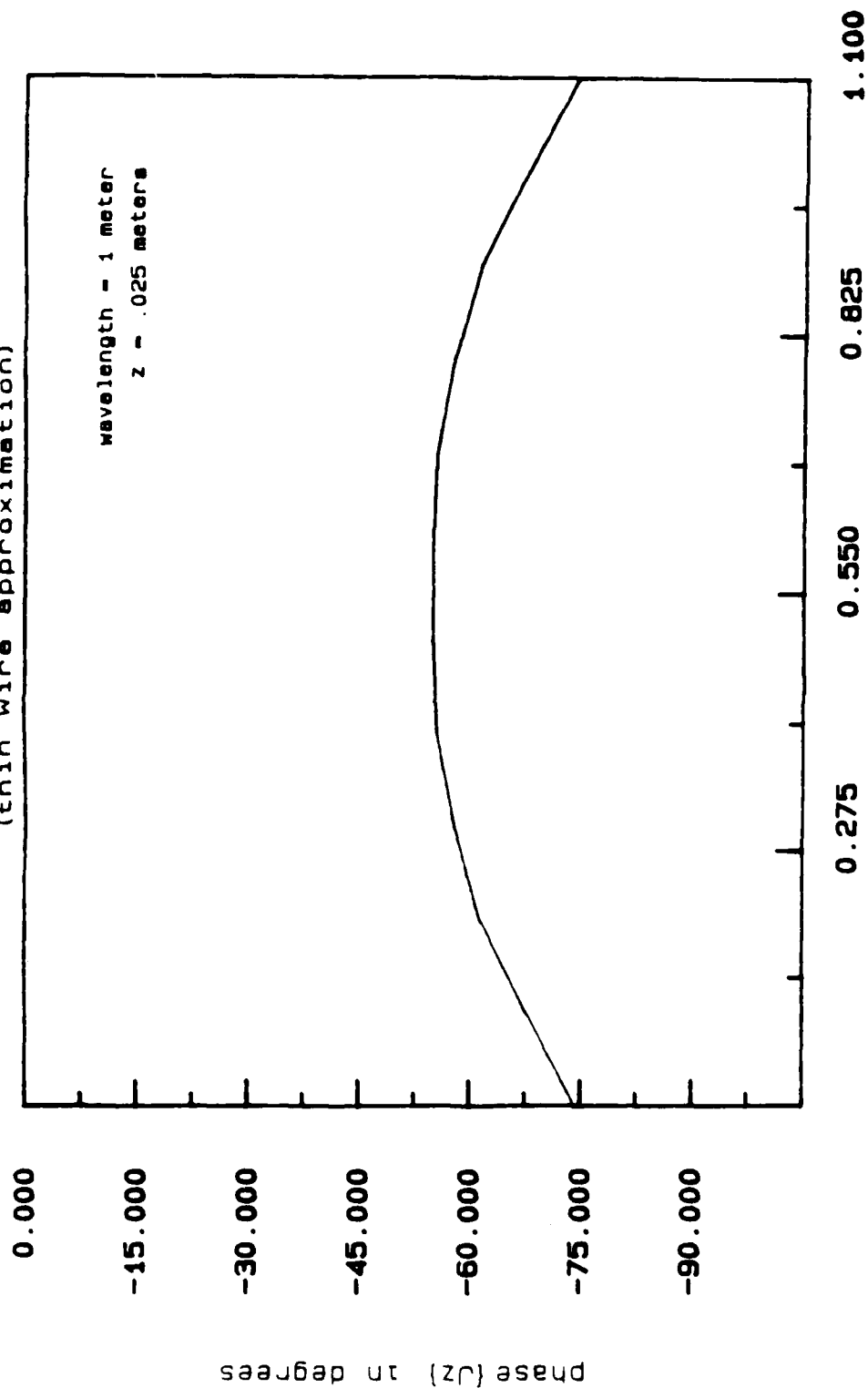
HF Excitation of a Square Grid (1.1m)
 (thin wire approximation)



(a) Magnitude of J_z .

Figure 2.24. J_z along the x-direction and at $z=0.05$ m, produced by a normally incident TE plane wave ($H/H_0 = 1$). Solution obtained with the use of NRC (288 unknowns). Current evaluated at segment center.

TE Excitation of a Square Grid (1.1m)
(thin wire approximation)



x - meters
Figure 2.24. (b) Phase of J_z .

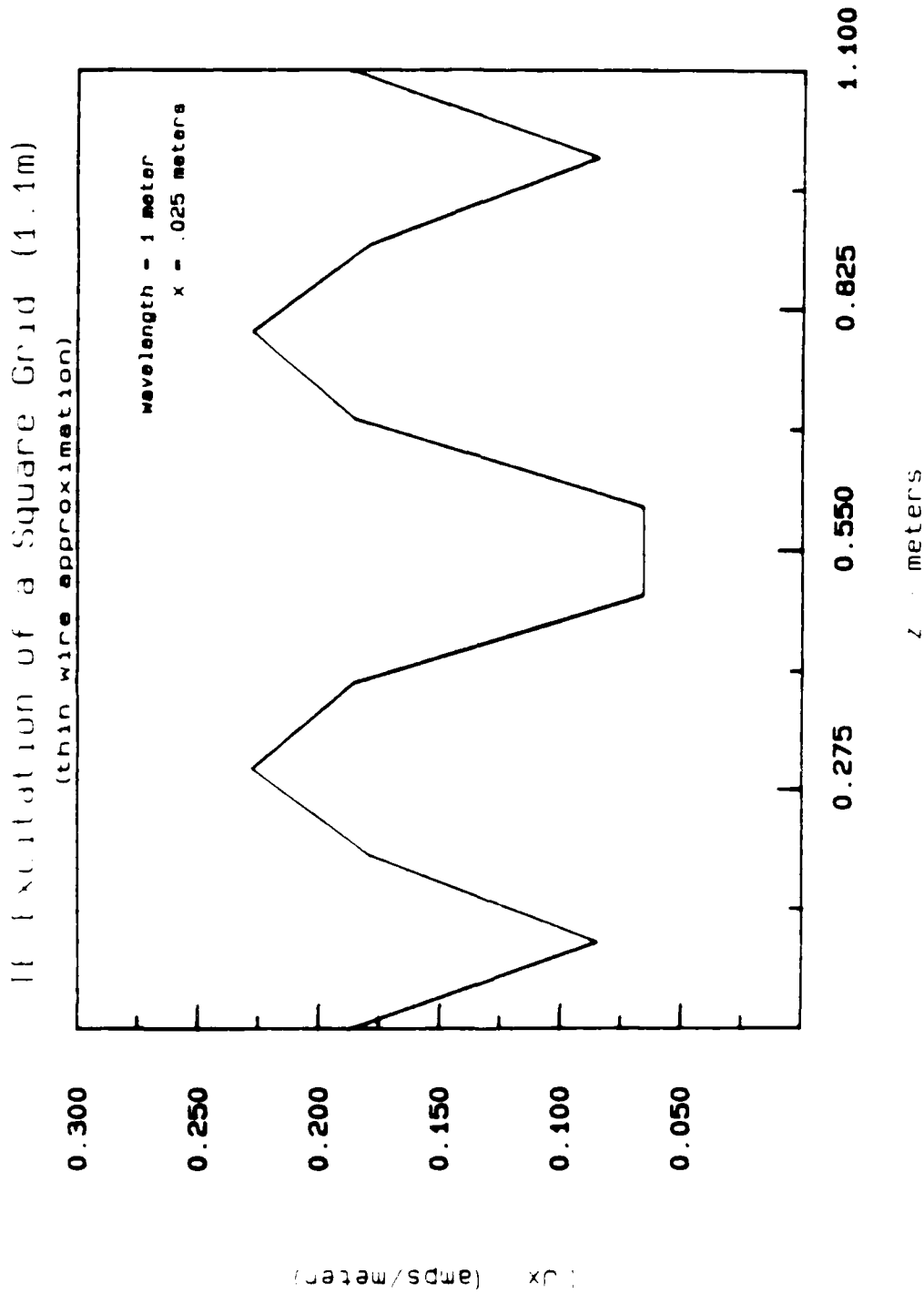


Figure 2.25. Magnitude of J_z along the z direction and at $x=0.05$ m, produced by a normally incident TE plane wave ($H/H_0 = 1$). Solution obtained with the use of NEC (288 unknowns).

Comparison of NEC and Iterative Solution

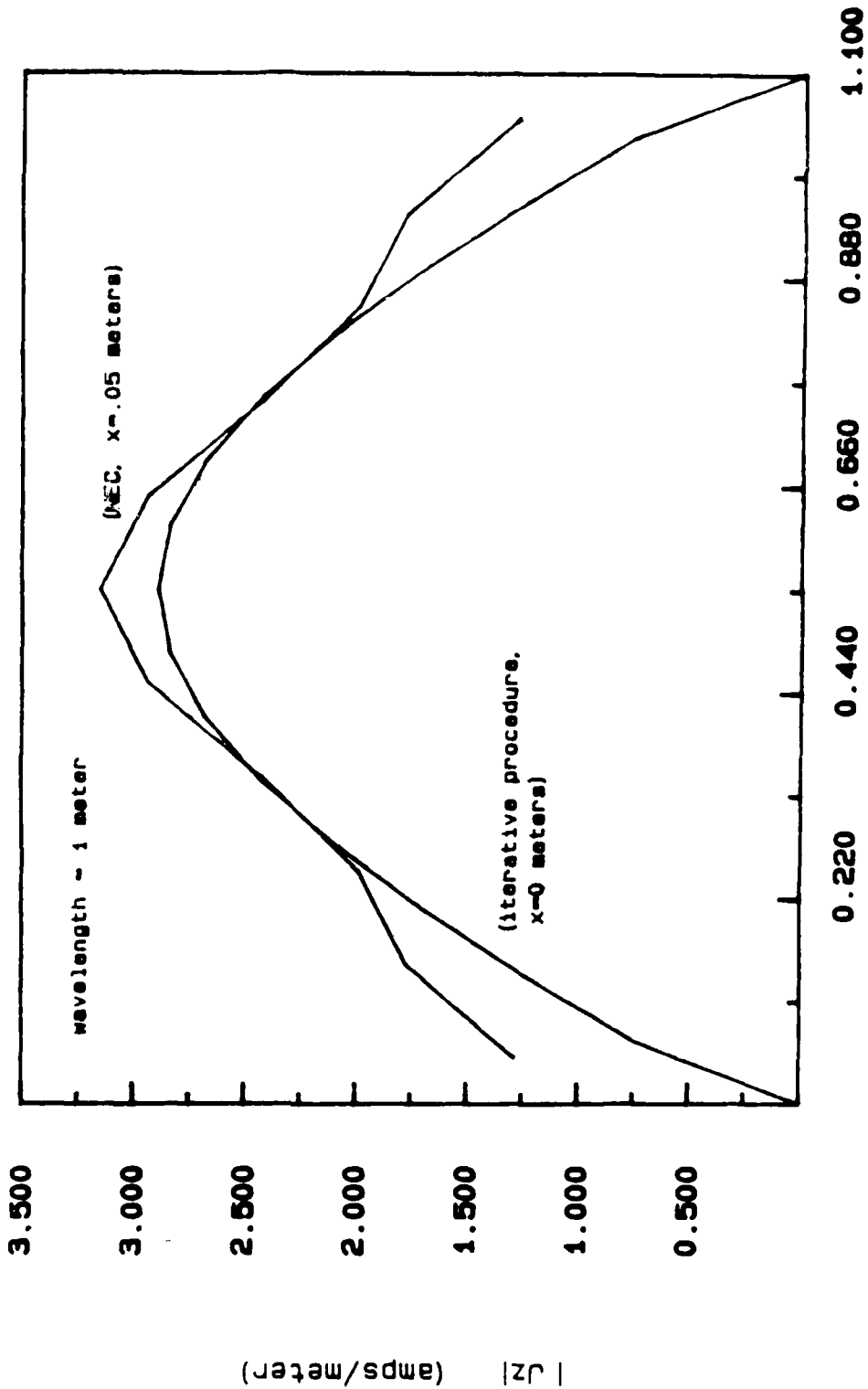


Figure 2.2b. Comparison of the magnitude of J_z in the z -direction when computed by a wire mesh approximation (NEC) and by the spectral Galerkin technique (iterative solution by CG). NEC current computed at the segment center.

Comparison of NEC and Iterative Solution

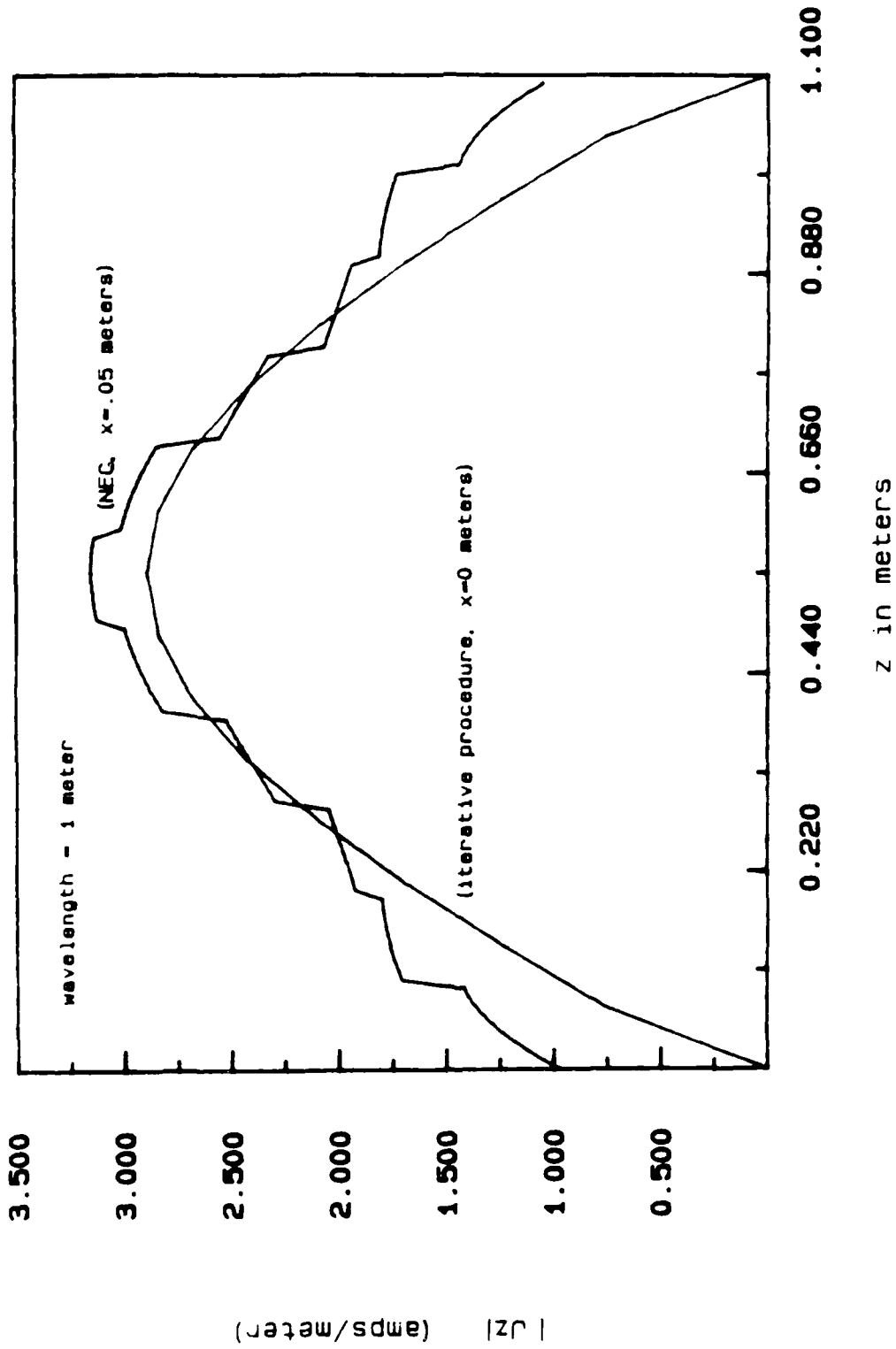


Figure 2.27. Comparison of the magnitude of J_z in the z -direction when computed by a wire mesh approximation (NEC) and by the spectral Galerkin technique (iterative solution by CG). NEC current computed along segment length.

TE Excitation of a Square Grid (1.1m)

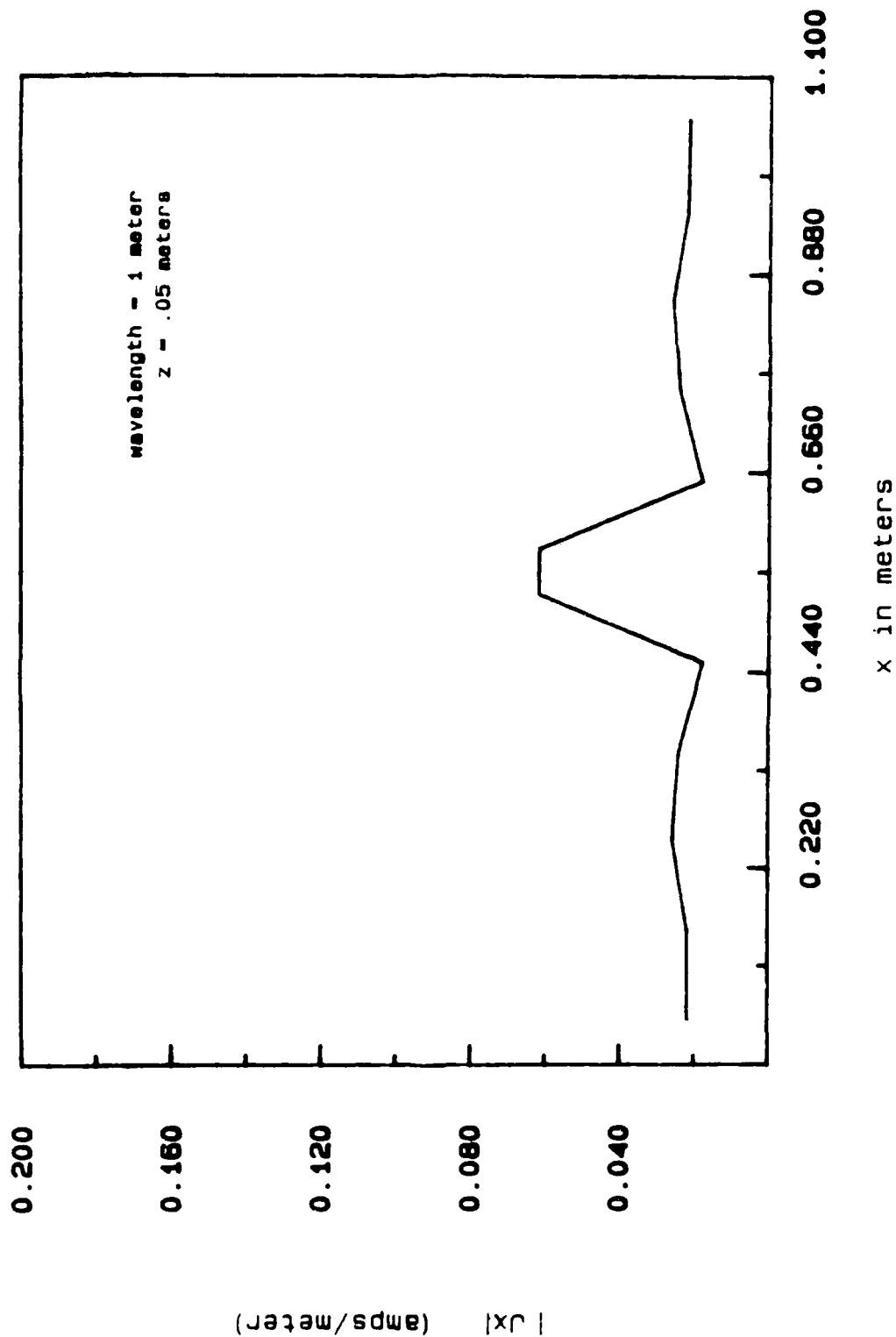


Figure 2.28. Magnitude of J_x computed along the x-direction at $z=0.05$ m. Obtained from a wire mesh approximation and NkC. Currents computed at segment center.

TE Excitation of a Square Grid (1.1m)

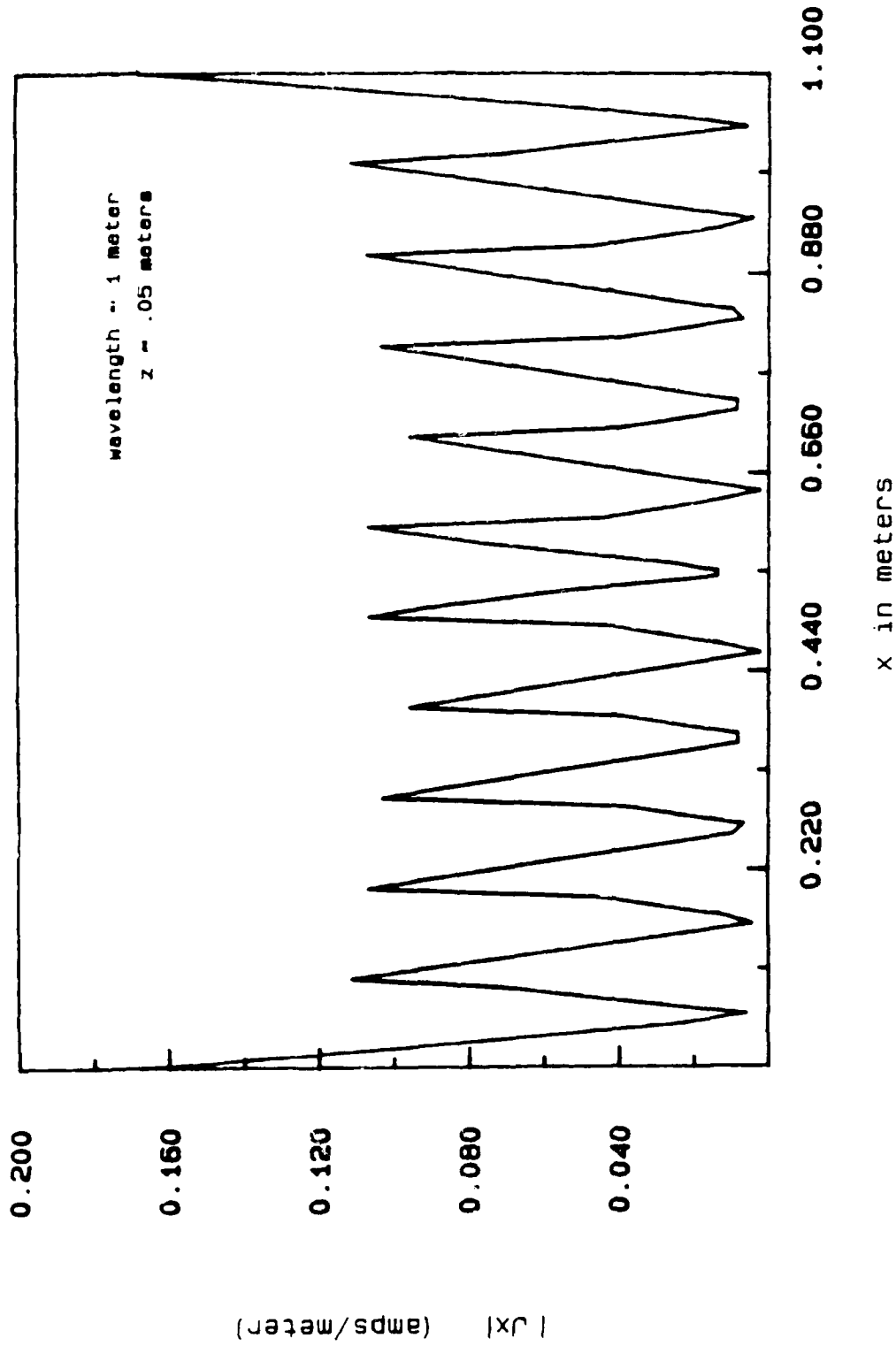


Figure 2.29. Magnitude of J_x computed along the x-direction at $z=0.05$ m. Obtained from a wire mesh approximation and NEC. Currents computed along segment length.

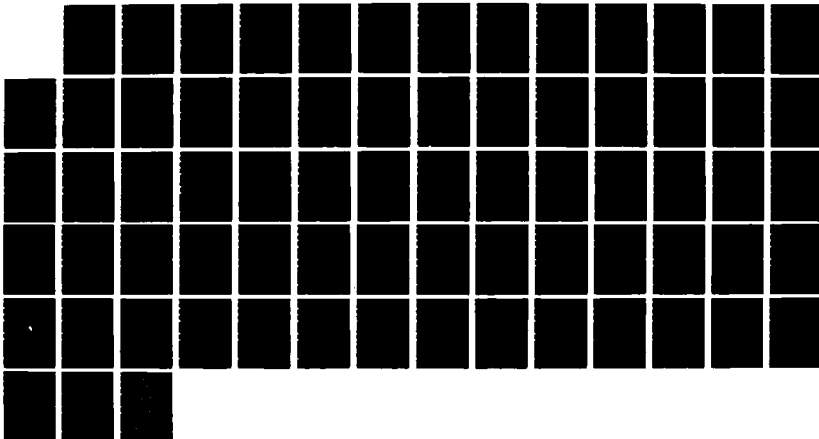
AD-A187 535

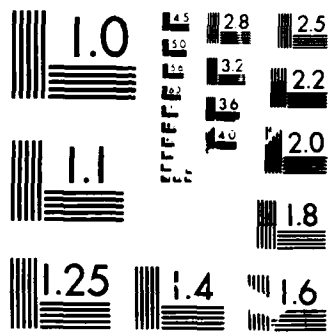
A DYNAMIC ANALYSIS OF THE PARALLEL-PLATE EMP
(ELECTROMAGNETIC PULSE)SSINU (U) CONSTRUCTION
ENGINEERING RESEARCH LAB (ARMY) CHAMPAIGN IL
S D GEDNEY SEP 87 CERL-TECHNICAL-MS-M-87/15 F/G 20/15

2/2

UNCLASSIFIED

ML





MICROCOPY RESOLUTION TEST CHART
NATIONAL BUREAU OF STANDARDS-1963-A

CHAPTER 3

NUMERICAL ANALYSIS OF THE PARALLEL-PLATE BOUNDED-WAVE EMP SIMULATOR

In Chapter 1, a number of analogies for approximating the field distributions within the parallel-plate region of the parallel-plate bounded wave EMP simulator were presented. These approximations are all limited to the case of a parallel-plate transmission line that is either semi-infinite or infinite in length. Furthermore, the approximations are typically only valid for low frequencies, and for the strict parallel-plate geometry. However, in practice, the simulator consists of a finite length parallel-plate transmission line and is generally excited and terminated by tapered end sections. In this chapter, an alternate solution is considered. The simulator is treated as a large conducting body and the finite length simulator problem is solved with the use of scattering theory. This approach will not only be applied to the typical parallel-plate simulator configuration, but will also be applied to the analysis of the simulator-obstacle interaction.

3.1 Development of the Scattering Problem

The scattered field is the field produced by the induced currents and charge distributed on some body when illuminated by an incident field. For the finite length simulator problem, the incident field is taken to be the E-field distributed over the source gap. The scattered field is then found by satisfying the boundary conditions of the E-field on the conducting surface of the simulator, and over the distributed terminating impedance, and subsequently solving the EFIE.

As was discussed in Chapter 2, the EFIE cannot be solved analytically in general, and a numerical solution for the current on the conducting surface must be developed. To solve the integral equation, one must discretize the two-dimensional surface current into a truncated series of known basis functions, and subsequently solve for

the unknown coefficients by moment methods or an iterative procedure. Although computer memory and speed are becoming more accommodating for larger problems, the amount of programming required to derive a solution is inexpedient. Furthermore, the size of the simulator is generally much larger than the wavelength of interest, and the number of unknowns required to converge would be too large to justify this approach.

In Chapter 2, three problems leading to the development of a thin-wire approximation of the conducting surface of the parallel-plate simulator were illustrated. From these examples, it is seen that NEC can be a very useful tool for analyzing the parallel-plate EMP simulator. Not only can it provide a good approximation of the problem, but it provides an easy alternative to analyzing the problem.

The conducting surface of the parallel-plate simulator is two dimensional and can easily be approximated by a rectangular wire mesh. This configuration ensures both longitudinal and transverse current flows along the conducting surface. The size of the mesh is very important to ensure the convergence of the solution and should be made much smaller than a wavelength in order to better approximate the surface currents. However, if it is too small, it will increase the number of unknowns and the problem becomes too large. In Chapter 2, it was observed that at least 10 basis functions per wavelength were required in order to properly converge to a solution. Therefore, the dimensions of the mesh opening will be chosen to be at most $.1 \lambda$ by $.1 \lambda$.

The simulator is an open waveguide structure, and consists of flat conducting plates that are finite in width. As observed in the PEC plate problem, a large amount of current will be distributed near the edge of the plate. Therefore, in our configuration, it is extremely important to include an edge wire to approximate this

singular current. It should also be recognized that there are currents on both sides of the conducting surface in the physical problem. However, with the use of a thin-wire mesh approximation the induced current lies on the axis of each wire segment. Furthermore, the current on each segment is limited to one dimension. This problem also consists of a symmetrical structure about the center longitudinal axis. By imposing symmetry on the problem, the computation time of the matrix inversion can be reduced by a factor of $N^2/4$. However, in doing so, an odd mode solution is enforced in the transverse direction, and E_x is zero in the $x=0$ plane.

The source and load configurations will be the same as those developed for the rhombic EMP simulator in Chapter 2. The source consists of a constant E-field distributed over wire vertical wire segments placed symmetrically about the y-axis. It must be realized that the desired source of the parallel-plate simulator is an E-field distributed evenly over the entire source gap region.

When the simulator is terminated by its characteristic impedance, a large amount of the energy available is dissipated by the load and very little reflection is encountered. Since the load is to be matched to the dominant TEM mode, which contains only a vertical E-field component, the loading wire segments have been placed vertically across the load gap region in a similar configuration used to terminate the rhombic EMP simulator. Although at higher frequencies, where TE and TM modes will propagate, the line is no longer matched, and less energy will be dissipated by the load. As a result, more energy has the potential of being reflected back into the simulator. A common technique used to minimize reflections is to use a sloped distributed load. In doing so, not only the vertical E-field is matched, but the longitudinal fields of the TM modes will be matched as well. Furthermore, the load is generally slightly inductive to account for the change in characteristic impedance at higher frequencies. Another advantage of sloping the load is that the required current

in the termination will reach its late time value much faster during pulse excitation. This can be explained in a simplified manner by the fact that the currents entering the load from the conducting plates will reach a position on the terminating load much faster after the arrival of the incident wave. In doing so, the load becomes better matched in its quasi-static characteristic impedance. Furthermore, since the incident wave arrives at different times along the surface of the load, the reflections encountered are dispersed in time, and the incident wave is reflected back at an oblique angle, and not directly back into the simulator. For a detailed study of sloped terminations of parallel-plate simulators, the reader is referred to [35], [36], and [37]. Our analysis with NEC will not be able to consider a sloped termination due to the limitations of the load gap model.

3.2 Numerical Results

The first case to be analyzed is that of an asymmetrical parallel-plate simulator, with conical tapered end sections. The dimensions will be modeled after the ACHATES simulator, which was designed by the Air Force Weapons Laboratory [34]. The ACHATES simulator is chosen for its unique characteristics, which will subsequently enable the results to be interpreted easily.

The ACHATES simulator has a height to width ratio of

$$\frac{h}{a} = 1.2335. \quad (3.1)$$

This aspect ratio is chosen such that the simulator has a quasi-static characteristic impedance of 100Ω . Furthermore, it can be shown that one-volt of input voltage across the source gap of ACHATES will produce a field of one-volt per meter at the center of the ground plane (at $x=0$). In Chapter 1 the bandwidth of a parallel-plate simulator, which is determined by the dispersion distance associated with the spherical wavefront that is launched into the parallel-plate region from the conical tapered end

section, was discussed. It was found that the more gradual the taper, the higher the bandwidth of the simulator. The design of ACHATES initially considered is one that has very long tapered end sections, resulting in a bandwidth of 450 MHz. The dimensions of the simulator are illustrated in Figure 3.1, and the wire mesh approximation generated for NEC is illustrated in Figure 3.2.

Three different operating frequencies are chosen for this example: 1) 75 MHz, 2) 100 MHz, and 3) 125 MHz excitations. For each case the characteristic impedance of the simulator is computed by determining the load resistance that minimizes the current standing wave ratio and also minimizes the radiation efficiency. Then the distribution of E-fields in the center parallel-plate region, which is often referred to as the "working volume," is analyzed.

Table 3.1 illustrates the characteristics of the simulator for various terminating loads. The computed characteristic impedance is 120Ω for a 75 MHz excitation, 120Ω for a 100 MHz excitation, and 95Ω for a 125 MHz excitation. In comparison to the rhombic EMP simulator, the characteristic impedance seems to be much more stable over a broad frequency range. Furthermore, if the simulator is matched into a 100Ω load, at most, an SWR of 1.3 in the current will be experienced over the frequency range considered.

The E-field distribution in the working volume due to a one-volt continuous wave excitation across the source gap is illustrated in Figures 3.3 through 3.11. The vertical E-field, E_z , along the y-direction, is illustrated in Figures 3.3 to 3.5 for the three cases considered. The fields are quite uniform and have a linear progressive phase shift throughout the working volume. It should also be noted that the phase has little change along the vertical direction since the propagating waves have planar equiphase fronts. Recall that the design of ACHATES is such that one-volt of input voltage produced one-volt per meter at the ground plane (at $x=0$), in the quasi-static

case. This is true for all three cases. The deviation is due to the existence of non-TEM modes, which become more significant as the frequency is increased.

Figures 3.6 to 3.8 illustrate the vertical E-field as a function of the vertical direction. The fields are quite uniform throughout the height of the simulator. However, it is apparent that there is error in the computed field close to the thin-wire mesh. Figures 3.9 to 3.11 illustrate the longitudinal component, E_y , in the $x=0$ plane and is representative of the propagating TM field. The longitudinal field is on the order of a magnitude smaller than the vertical E-field. However, it becomes more significant in the higher-frequency regions. This can be explained as follows. A "quasi-spherical" wavefront propagates from the wave launching conical tapered end section into the parallel-plate region. Along the ground plane, the incident E-field is vertical and there is no longitudinal component. Moving above the ground plane, in the $x=0$ plane, the field consists of both TM and TEM modes. Then, getting closer to the top plate, the TM component becomes more significant since E_y is larger, due to the characteristics of the incident wavefront. Therefore, at higher frequencies the trailing edge of the spherical wavefront will become comparable to a wavelength and significant TM modes are generated. This happens at the upper-frequency cutoff of the simulator, which is 450 MHz for this example. Furthermore, it is noted that E_y tends to be a minimum at $y=0$ and increases again as y progresses due to the mismatch with the terminating conical end section.

In order to develop a better understanding for the mechanism contributing to the large aberration in the planar wavefront of the parallel-plate region, the field distribution within the simulator is analyzed near its cutoff. By shortening the conical tapered end sections from 4.5 m to 1.95 m, the bandwidth of the simulator is reduced from 450 MHz to 200 MHz [34]. In doing so, the simulator has a computed characteristic impedance of 110Ω for a 100 MHz excitation and a corresponding

current SWR of 1.125. Furthermore, at 175 MHz, which is very near cutoff, the simulator is matched when loaded by 95 Ω , and has a corresponding current SWR of 1.08. It should also be noted that the radiation efficiency for the 175 MHz case is 80.19%. Therefore, very little energy is being dissipated by the load resistance, and most of the energy is either being reflected or radiated. Figures 3.12 to 3.17 illustrate the E-field distribution in the working volume due to a one-volt excitation across the source gap.

The vertical E-field as a function of y is illustrated in Figures 3.12 and 3.13. At 100 MHz, the field is uniform and has a linear progressive phase shift. However, close to the simulator cutoff frequency, there is a large contribution from higher-order TM and continuous modes. The vertical field deviates significantly from its uniformity and, in fact, has a $1/R$ contribution, where R is the distance from the source. Furthermore, the phase shift is no longer linear. It should be noted, although it is not illustrated, that off of the $x=0$ plane, there is a large contribution to the field from higher-order TE modes as well. The distribution of the vertical E-field in the vertical direction is illustrated in Figures 3.14 and 3.15. At 100 MHz, the field is relatively uniform, and the phase is approximately constant over the height of the parallel plate. However, at 175 MHz, the field is no longer uniform. Furthermore, the phase indicates that the modes contributing to the spherical wavefront are propagating with little attenuation into the working volume. At y equals -0.25 m, there is a 45 degree phase lag from z equals 0 to z equals 0.94 m. Doing a rough computation, the maximum deviation of the spherical wavefront at the planar interface is $2.165 - 1.95$, or 0.215 m (where 2.165 is the length the wavefront has to travel along the top plate of the conical taper). At 175 MHz, this corresponds to a $\frac{2\pi}{\lambda} \times .215$ phase shift of 45.15 degrees. The wavefront becomes planar as the wave propagates with y , although it loses a considerable amount of energy.

Figures 3.16 and 3.17 illustrate the longitudinal E-field along the vertical direction. Initially comparing Figure 3.16 to Figure 3.10, the longitudinal component of the E-field is much larger towards the waveguide interface at $y = -.50$ m. However, at 175 MHz, there is a significant increase in the amplitude of E_y throughout the parallel-plate region. An interesting observation in Figure 3.17 is that the location of the peak amplitude of E_y along the vertical occurs at shorter heights as the wavefront travels from one end of the parallel-plate region to the other. This can be explained from ray optics. The incident field is a diverging wavefront, bounded by the conical tapered end section. Near the ground plane, the waves propagate directly into the parallel-plate region. However, for larger angles of incidence, the waves are reflected by the surface of the top parallel plate. The maximum angle is determined by the angle of the tapered end section. Once reflected, this ray determines the reflected shadow boundary, which is propagating in the negative z direction as it progresses in y . Therefore, due to the constructive interference of the longitudinal component of the E-field, the peak field progressively occurs at shorter distances above ground.

3.2.1 Computational considerations

All computations were done on an AT&T PC6300 desktop microcomputer or a compatible DOS machine. The NEC code was rewritten and compiled in double precision MicroSoft Fortran. The program itself requires 450 kbytes of RAM to load, and approximately 8 Mbytes free on a hard disk for out of core solutions of matrices with 600×600 elements. Table 3.2 lists the computation times required to fill and factor the moment matrix for the ACHATES simulator with a 450 MHz bandwidth. The computation times were recorded from runs on the AT&T and are listed in Table 3.2. It should be noted that the above computations include one plane of symmetry about the x -axis, which reduces the computation time by about $\frac{N^2}{4}$. As the

frequency becomes larger, the number of unknowns becomes significantly larger, and the problem becomes extremely time-consuming to solve. Furthermore, note that it will require 3.5 Mbytes to store a matrix of 466 by 466 in double precision. In the high-frequency region, such that the wavelength is shorter than the parallel-plate height, the problem becomes too big to be practically handled by NEC. For instance, if we increase the frequency to 150 MHz, this will require 656 unknowns, nearly 7 Mbytes to store, approximately 22,982 seconds to fill, and approximately 33,640 seconds to factor.

3.3 Interpolation of the Wire Mesh Currents

While studying the PEC plate problem in Chapter 2, it was found that discontinuities appear in the wire segment currents at multiwire junctions. This is a result of enforcing Kirchoff's Law as a condition in solving for the unknown weighting coefficients. However, a discontinuity in the current will lead to nonphysical singular behavior in the near fields, which will be referred to as "singular distortion." Due to the wire mesh approximation of the conducting surface of the EMP simulator, there are discontinuities in the wire current as well. Figure 3.18 illustrates the real and imaginary components of the current along the center wire of the simulator. Each step discontinuity is located at a multiple wire junction in the wire mesh. Figure 3.19 illustrates the resultant scattered E-field computed in the tangential direction on the center wire surface along the conical wave launching end section. Note that the singularity in the E-field is the largest at the source gap. This is due to boundary condition error suffered by the source, as well as the oblique angle the source segment makes with the conical tapered end section. It is obvious that these singularities are nonphysical; however, they are a trade-off that one must take when using NEC to solve wire mesh scattering problems. In Section 3.2, it was obvious that the results were plagued by error as the position of the near-field computation moved

closer to the conducting surface. These singularities can be removed by smoothing the current. Therefore, once the currents are smoothed, it can be determined how close to the wire mesh the field can be computed before suffering significant error from the field singularities.

3.3.1 One-dimensional smoothing of the wire currents

Consider a one-dimensional current described by some function $f(x)$ whose support lies on the interval $(0,L)$. The function $f(x)$ can be expanded into a Fourier sine series as

$$f(x) = \sum_{k=1}^{\infty} b_k \sin \frac{k \pi x}{L}. \quad (3.3.1)$$

However, the expansion of $f(x)$ will have a very poor convergence since the boundary conditions at $x=0$ or $x=L$ will not be fulfilled unless $f(x)$ vanishes smoothly at the endpoints. Next, a function $g(x)$ is introduced such that

$$g(0) = 0 \quad (3.3.2)$$

$$g(L) = 0$$

and

$$g(-x) = -g(x).$$

Therefore, $g(x)$ is chosen to be

$$g(x) = f(x) - (a + bx) \quad (3.3.3)$$

where

$$a = f(0)$$

$$b = \frac{f(L) - f(0)}{L}.$$

As a result, a function that has no discontinuities, and is periodic with a period of $2L$, is obtained. A discontinuity does appear in the second derivative at the end points; however, any singularities in the first two derivatives have been eliminated. $g(x)$ can then be expressed by a Fourier sine series expansion with excellent convergence for a

well-behaved $f(x)$. Subsequently, $f(x)$ can be obtained from $g(x)$ as

$$f(x) = g(x) + a + bx. \quad (3.3.4)$$

The next step is to discretize $f(x)$ at equidistant points, with a separation h . Therefore, choosing N discrete points on the interval $(0,L)$ leads to

$$y_k = f(kh) \quad (k=0,1,\dots,N) \quad (3.3.5)$$

and

$$y_k' = g(kh) \quad (k=0,1,\dots,N). \quad (3.3.6)$$

The Fourier series is expressed as

$$y_k' = \sum_{\alpha=1}^{\infty} b_{\alpha} \sin \left[\frac{\alpha \pi k h}{L} \right]. \quad (3.3.7)$$

The constant coefficients, b_{α} , are solved by taking the inner product of Equation (3.3.7) with $\sin \frac{m \pi k h}{L}$. However, since $g(kh)$ has a discrete finite support on the interval $k \in [0,N]$, and the constant coefficients can be derived by the finite summation

$$b_m = \frac{2}{N} \sum_{k=1}^{N-1} y_k' \sin \left[\frac{km \pi}{N} \right]. \quad (3.3.8)$$

However, the spacing, h , of the discrete points and the number of coefficients needed for proper convergence must be established. The Fourier series expansion is a superposition of Fourier harmonics. There exists a cutoff frequency, ν_0 , where the function $g(x)$ has no more existing harmonics [38]. Therefore, in the absence of noise, the Fourier coefficients, b_1, b_2, \dots, b_N , will become increasingly smaller above some value ξ . However, in the presence of noise, the higher-order coefficients are no longer negligible. If the noise were random, the frequency spectrum would be a constant over all frequencies. Therefore, the higher-order coefficients are relatively constant in magnitude and have a random phase which introduces undesirable harmonic distortion in the interpolated function. Therefore, the series has to be truncated at some finite value of $k = \xi$. This number is best determined by analyzing the data and subjectively

choosing the cutoff frequency, ν_0 , which is expressed as [38]

$$\frac{m \pi}{L} x = 2\pi \nu_0 x \quad (3.3.9)$$

$$\frac{m}{N} = 2\nu_0 h$$

$$L = Nh .$$

The real and imaginary currents to be interpolated are periodic in nature, and the noise is introduced by the discontinuities at each multiple wire junction. Since the function is relatively well behaved, the coefficients diminish rather quickly. However, due to the noise, the harmonic distortion introduces a ringing. By experimenting, it was found that the cutoff frequency is best chosen to be

$$\nu_0 = \frac{6}{\lambda} . \quad (3.3.10)$$

This leads to $\xi = 12$ coefficients per wavelength.

Figure 3.20 illustrates the interpolated current, in the longitudinal direction, for the case of a 100 MHz excitation of the 450 MHz bandwidth ACHATES simulator. The real and imaginary currents are interpolated separately in order to preserve the phase. It is easily seen that smoothing by Fourier sine-series interpolation provides excellent results for this case.

The transverse currents, which are on an order of magnitude smaller than the longitudinal currents, are subject to a large amount of relative error. This was observed in the PEC patch problem discussed in Chapter 2. Since Kirchoff's law is being satisfied at the wire junction, small discontinuities in the longitudinal current lead to relatively large discontinuities in the transverse current. There are also a few other limitations that are encountered due to the wire mesh approximation. The first is that the edge wire is not solely in the y-direction along the tapered end sections, and it has a vector component in the transverse direction. However, the vector contribution of current is not accounted for at junctions with the transverse wires.

Furthermore, the current does not vanish in the $x=0$ plane, due to the discontinuity of the junction of the transverse wires with the center longitudinal wire. When interpolating the transverse current these factors will have to be taken into account.

Recall that the impedance matrix of the moment method solution was generated by point matching. Therefore, the boundary condition on the tangential E-field is being satisfied at the center of each wire segment. Furthermore, the large discontinuity being suffered at either endpoint is due to the perpendicular longitudinal currents. As a result, only the segment center currents are interpolated while enforcing the end-point boundary conditions and imposing odd-symmetry across the $x=0$ plane. Finally, the real and imaginary currents are interpolated separately by a Fourier sine-series expansion as was previously described. Figures 3.21 and 3.22 illustrate the interpolated transverse current magnitude.

Once the currents are interpolated, the near E-field can be easily computed with the use of the integral differential equation derived from Maxwell's equations. However, since the currents are one-dimensional, the current and the Green's function are parameterized, leaving only one variable of integration. The resultant equation is given as

$$E(\mathbf{r}) = -\frac{j\omega\mu}{4\pi k^2} \int_0^T (\nabla \nabla \cdot \hat{\mathbf{r}} + k^2) I(t') G(\mathbf{r}, \mathbf{r}') dt' \quad (3.3.11)$$

where

$$G(\mathbf{r}, \mathbf{r}') = \frac{e^{-jkR}}{R}$$

$$R = ((x-x')^2 + (y-y')^2 + (z-z')^2)^{1/2}$$

$$x' = x_{0t} + at$$

$$y' = y_{0t} + bt$$

$$z' = z_{0t} + ct$$

(x_{0t}, y_{0t}, z_{0t}) is the position of the wire starting point in cartesian coordinates, and

$$\hat{i} = a\hat{x} + b\hat{y} + c\hat{z}$$

is in the direction of the wire axis, and $a, b,$ and c are its directional cosines. The integral with respect to ϕ was performed analytically, since the integrand has no ϕ dependence: hence, the integration reduced to a single integral. After performing the differentiation, the integral can be simplified as

$$E(\mathbf{r}) = -\frac{j\omega\mu}{4\pi k^2} \int_0^r \left| k^2 - \frac{jk}{R} - \frac{1}{R^2} \right| \hat{i} \frac{e^{-jkR}}{R} \\ + (\mathbf{p}-\mathbf{p}') \hat{i} \cdot (\mathbf{p}-\mathbf{p}') \left| \frac{3jk}{R^3} + \frac{3}{R^4} - \frac{k^2}{R^2} \right| \frac{e^{-jkR}}{R} dt \quad (3.3.12)$$

where

$$\mathbf{p}-\mathbf{p}' = \hat{x}(x-x') + \hat{y}(y-y') + \hat{z}(z-z')$$

Figure 3.22 illustrates an example of the E-field computed from the interpolated currents. Initially, comparing Figure 3.22 to Figure 3.4, it is found that singular distortion in the vertical E-field is negligible at heights up to $\frac{h}{2}$, where h is the height of the parallel-plate above the ground plane. At a height of $\frac{3h}{4}$, it appears that the singular distortion in Figure 3.4 is still tolerable. Furthermore, it is interesting to note that there is very little distortion of the phase due to the presence of the discontinuities of the current.

It must be realized that interpolating the currents and enforcing the edge conditions do not improve the boundary condition error. In fact, it only eliminates the singularities in the near electric field. However, this analysis does give insight into how much the singularities contribute to the fields when computed directly by NEC. Therefore, combining these results with those in Section 3.2, it is found that a useful and valid approximation of the field distribution in the working volume has been provided by NEC. However, singular distortion occurs when the fields are computed

near the wire mesh. In the previous example, singular distortion has a significant contribution when the fields are computed within $\frac{\lambda}{12}$ of the top plate (where the height of the simulator is approximately $\frac{\lambda}{3}$ at 100 MHz). Therefore, when applying a thin-wire mesh approximation to a surface scattering problem, one should be aware of the singular distortion before interpreting the results.

3.4 Simulator-Obstacle Interaction

The purpose of the EMP simulator is to reproduce the electromagnetic environment of the EMP radiated by a high altitude nuclear burst and to subject various test objects to this environment. Thus far, the characteristics of the parallel-plate bounded wave EMP simulator have been discussed. The fields within the working volume of the simulator approximate those of the free-space EMP environment. However, once a test object is placed within the working volume of the simulator the characteristics of the simulator may change. From a quasi-static analysis it can be shown that the object capacitively couples to the upper conducting plate and the ground plane. Since the object is of finite length, it acts as a perturbation of the transmission line. Dynamically, the obstacle is a scatterer, and the fields are a superposition of incident fields and scattered fields, although multiple scattering occurs between the simulator and the obstacle. In both analyses it is this interaction between the obstacle and the simulator that causes a distortion of the simulator characteristics. It is the purpose of this section to investigate the changes in the characteristics of the EMP simulator when placing a large object in the working volume.

The obstacle, or test object, is a cube with a side length of $h/2$ (where h is the height of the parallel plate above ground). The cube will be placed symmetrically in the parallel-plate region between the top plate and ground, and in the x -direction.

Furthermore, the front face of the cube will be placed in the transition plane of the conical tapered end section and the parallel-plate region. This is illustrated in Figure 3.23. As an example, the 450 MHz bandwidth ACHATES EMP simulator, excited by a 100 MHz unit amplitude excitation is used.

For small simulator-obstacle interaction, negligible changes in the characteristics of the simulator are expected, such as the characteristic impedance, input impedance, or the radiation efficiency. However, in the presence of the object, a perturbation of the near fields is still expected in the working volume since the fields are a superposition of the incident field and the scattered fields. Referring to Table 3.1, the matched load condition for a 100 MHz excitation of the 450 MHz bandwidth simulator with an empty working volume is $R_L = 120 \Omega$. Furthermore, the simulator has an input impedance of $97.04 + j14.68 \Omega$ and a radiation efficiency of 20.77 %. Once the cube is placed in the working volume, as in Figure 3.23, the input impedance reduces to $76.64 + j17.03 \Omega$. By lowering the impedance, the available input power is increased; however, it is interesting that the radiation efficiency reduces to 19.14 %. This indicates that a larger amount of power is being dissipated by the load impedance. Figure 3.24 illustrates the longitudinal currents on the top plate of the simulator for the case of an empty working volume, and when the obstacle is in the working volume. Comparing Figure 3.24(a) with Figure 3.24(b) it is observed that a slight change in the longitudinal current is encountered with the presence of the object. This slight change in currents introduces a small change in the field distribution characteristics of the simulator, which can essentially be referred to as the incident field. Therefore, the field within the simulator is a superposition of this incident field and the scattered field produced by the currents induced on the test object. Figures 3.25 to 3.27 illustrate the comparison of the field distributions for the cases of an empty working volume, or free-space environment, and in the presence of an obstacle, or a perturbed field environment.

Following the above analysis, there is additional work that could be done to help characterize simulator-obstacle interaction. In particular, studying the changes in the simulator characteristics over a broad frequency range is necessary to interpret the broad band excitation of the test object. Furthermore, computation of the fields due to the perturbed simulator currents and in the absence of the obstacle currents could provide some useful results in determining the perturbation of the incident field in the presence of the obstacle. Finally, an analysis of the plane-wave scattering of the obstacle, in the absence of the top conducting plate, could provide useful results as well.

TABLE 3.1(a)
 NEC MODEL OF THE ACHATES EMP SIMULATOR; 75 MHz

Z_L (Ω)	$\text{Re}(Z_{in})$ (Ω)	$\text{Im}(Z_{in})$ (Ω)	η_{eff} (%)	SWR
0.0	33.07	100.50	100.0	15.920
50.0	83.25	60.03	18.34	2.350
75.0	93.09	38.09	12.17	1.685
95.0	96.42	22.69	10.09	1.384
100.0	96.82	19.19	9.80	1.326
110.0	97.20	12.60	9.41	1.225
120.0	97.15	6.54	9.23	1.141
150.0	95.32	-8.74	9.54	1.248
200.0	89.76	-26.75	11.53	1.331
500.0	63.27	-62.78	28.55	2.602
1000.0	48.11	-73.36	47.85	3.805
10000.0	31.96	-82.45	90.74	6.757

TABLE 3.1(b)
 NEC MODEL OF THE ACHATES EMP SIMULATOR; 100 MHz

Z_L (Ω)	$\text{Re}(Z_{in})$ (Ω)	$\text{Im}(Z_{in})$ (Ω)	η_{eff} (%)	SWR
0.0	20.49	16.82	100.00	8.830
50.0	56.23	15.90	28.51	1.980
75.0	71.89	15.45	22.88	1.475
90.0	80.67	15.19	21.49	1.292
100.0	86.31	15.02	20.99	1.196
110.0	91.76	14.85	20.78	1.137
120.0	97.04	14.68	20.77	1.129
150.0	112.00	14.20	21.54	1.218
200.0	134.10	13.44	24.20	1.502
300.0	170.20	12.12	42.41	2.710
1000.0	288.20	8.18	60.18	3.250
10000.0	408.60	22.87	93.56	5.200

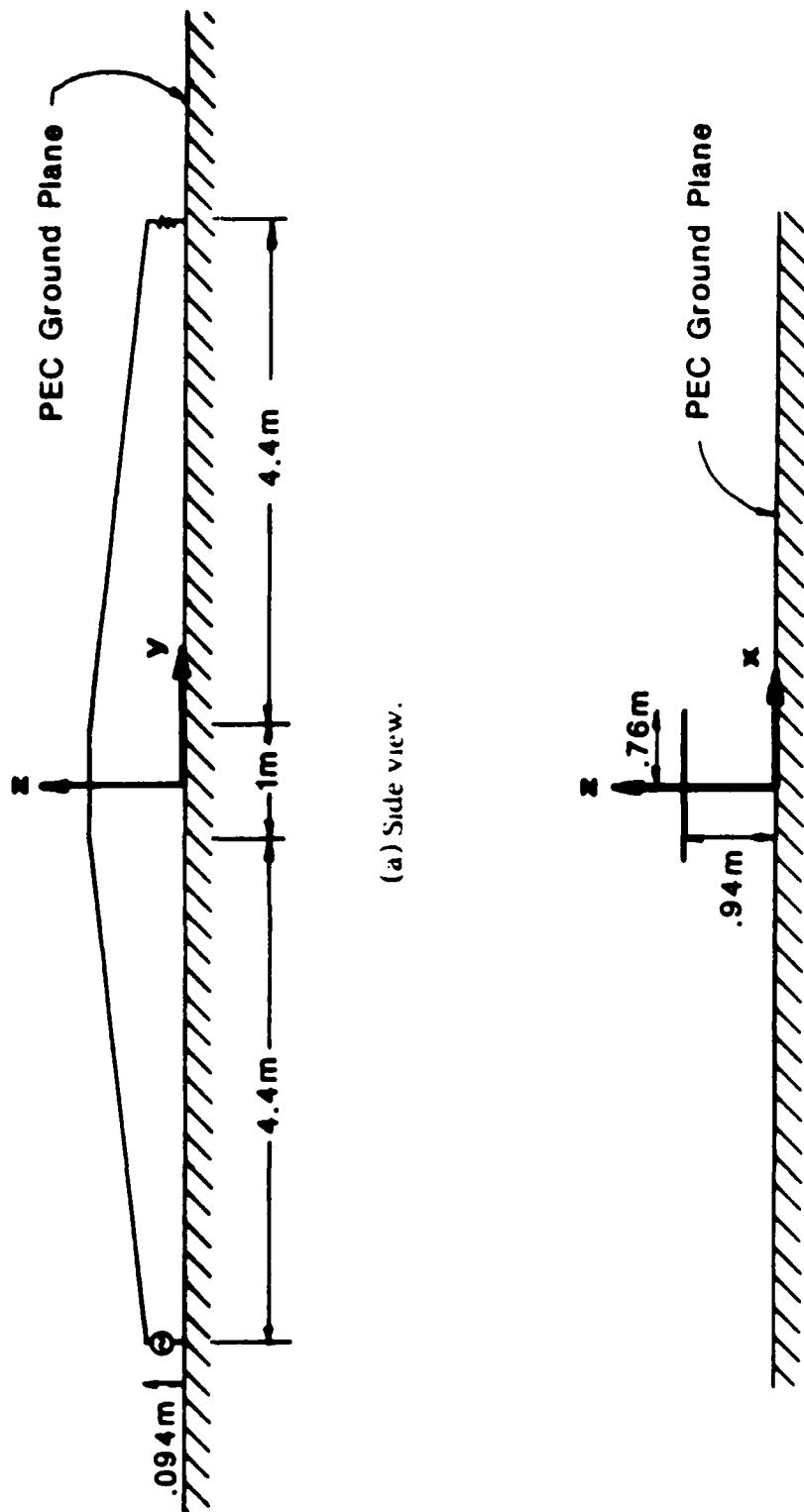
TABLE 3.1(c)
NEC MODEL OF THE ACHATES EMP SIMULATOR: 125 MHz

Z_L (Ω)	$\text{Re}(Z_{in})$ (Ω)	$\text{Im}(Z_{in})$ (Ω)	η_{ef} (%)	SWR
0.0	63.61	-99.67	100.00	6.143
50.0	90.78	-23.66	39.00	1.480
75.0	88.57	-4.20	33.39	1.164
95.0	85.35	6.80	32.56	1.126
100.0	84.49	9.07	32.55	1.139
110.0	82.76	13.18	32.63	1.163
120.0	81.04	16.76	33.01	1.373
150.0	76.24	25.12	34.58	1.474
200.0	69.65	34.03	38.13	1.837
500.0	51.73	50.27	56.81	3.504
1000.0	43.67	55.02	71.86	5.115
5000.0	35.84	57.66	92.16	8.380

TABLE 3.2 COMPUTATIONAL CHARACTERISTICS OF NEC

(run on an AT&T PC6300 microcomputer)

<i>Frequency</i> (MHz)	<i>No. of Segments</i>	<i>Matrix Fill</i> (sec)	<i>Factorization</i> (sec)
75	220	2.595.	1.003.
100	320	5.485.	3.095.
125	466	11.597.	12.059.



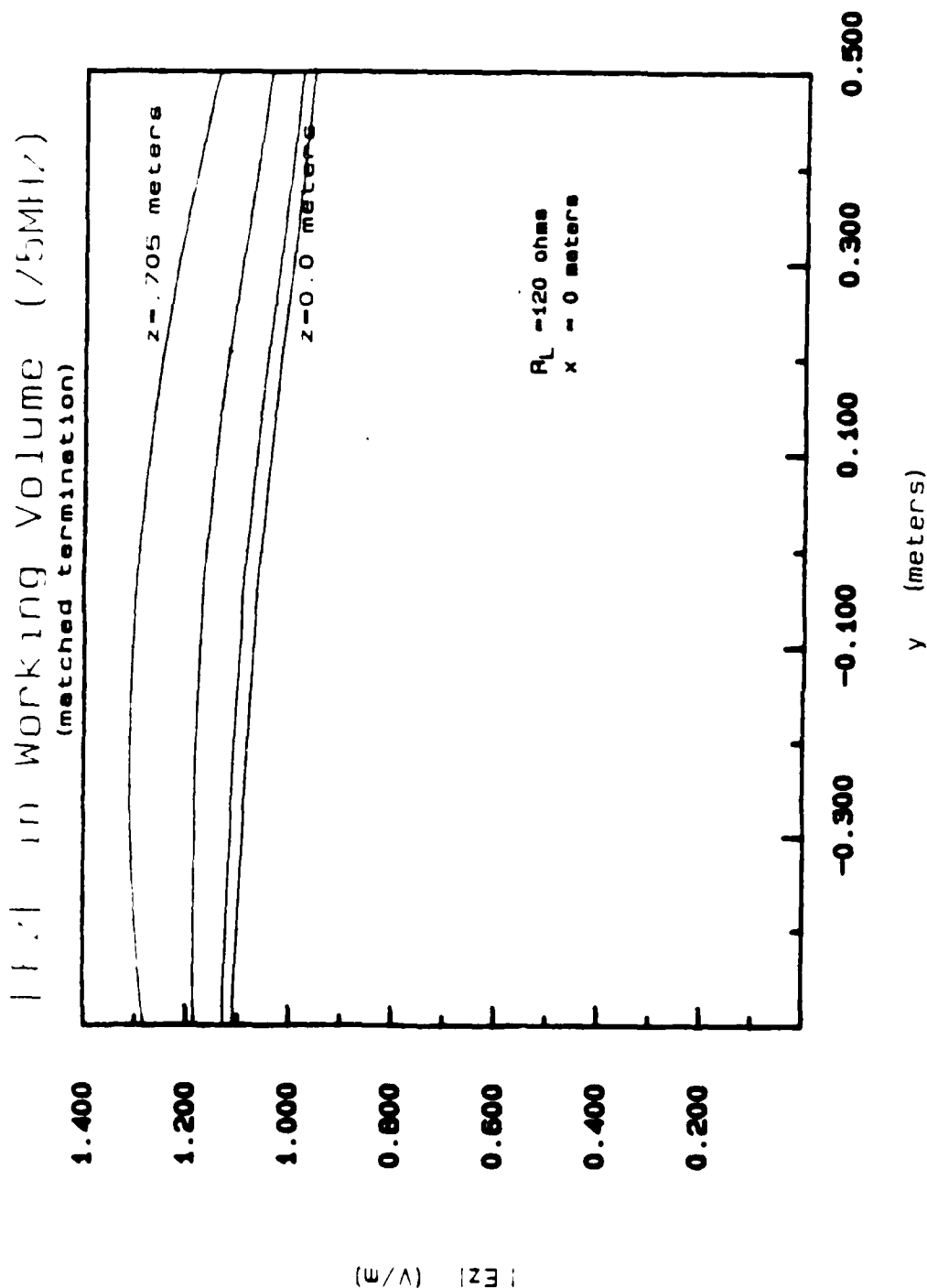
(a) Side view.

(b) Cross section; inside of parallel-plate region.

Figure 3.1. Dimensions of the ACHAFES asymmetric parallel plate bounded wave EMP simulator with a 450 MHz bandwidth.



Figure 3.2. Wire mesh approximation of the conducting surface of the asymmetric parallel-plate EMP simulator.



(a) Magnitude of E_z .

Figure 3.3. Vertical E-field computed along the longitudinal direction in the parallel plate region of the 450 MHz bandwidth ACHIEFS EMP simulator due to a unit amplitude, 75 MHz excitation.

Phase of E_z in Working Volume (75MHz)
 (matched termination)

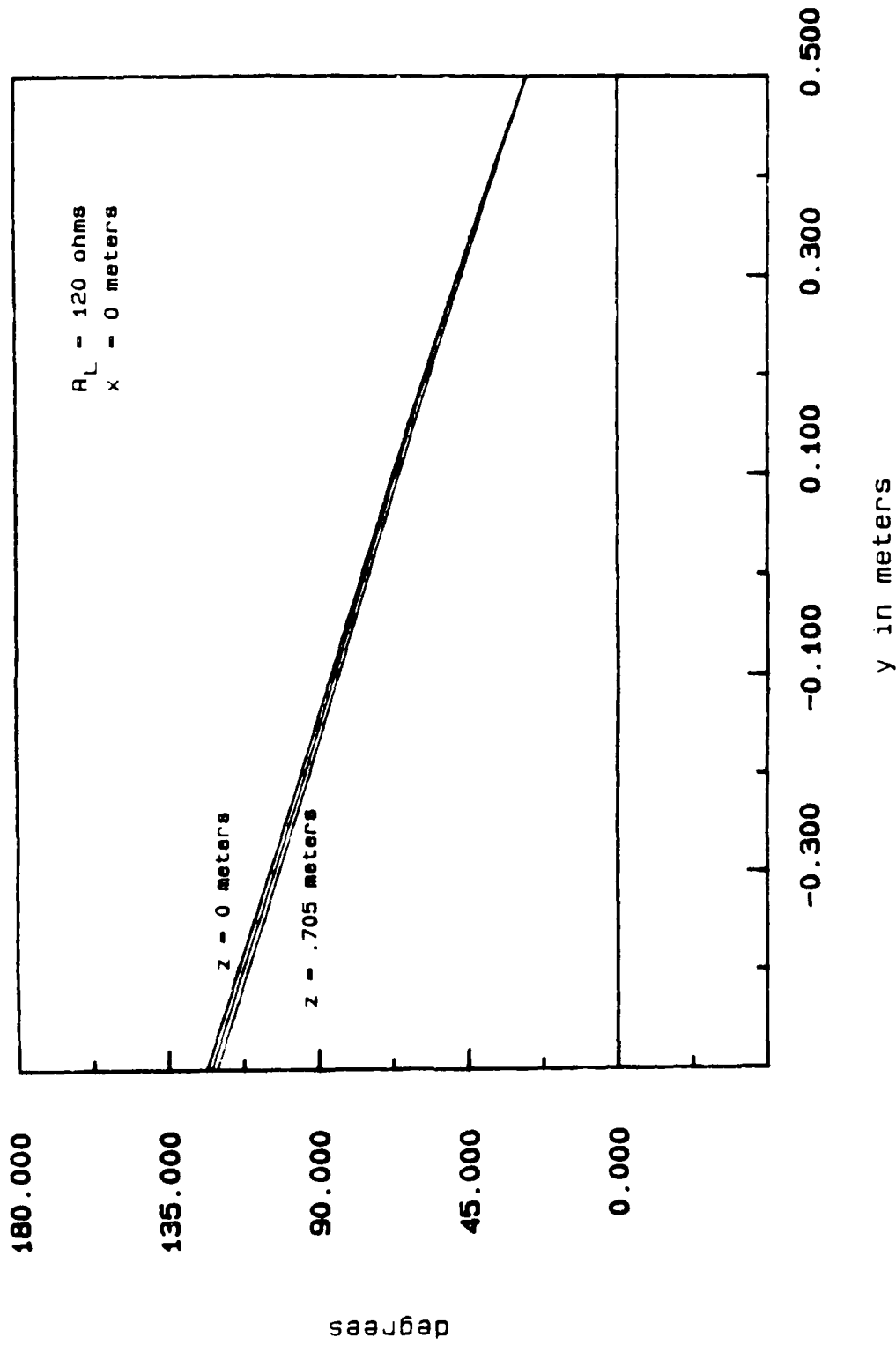
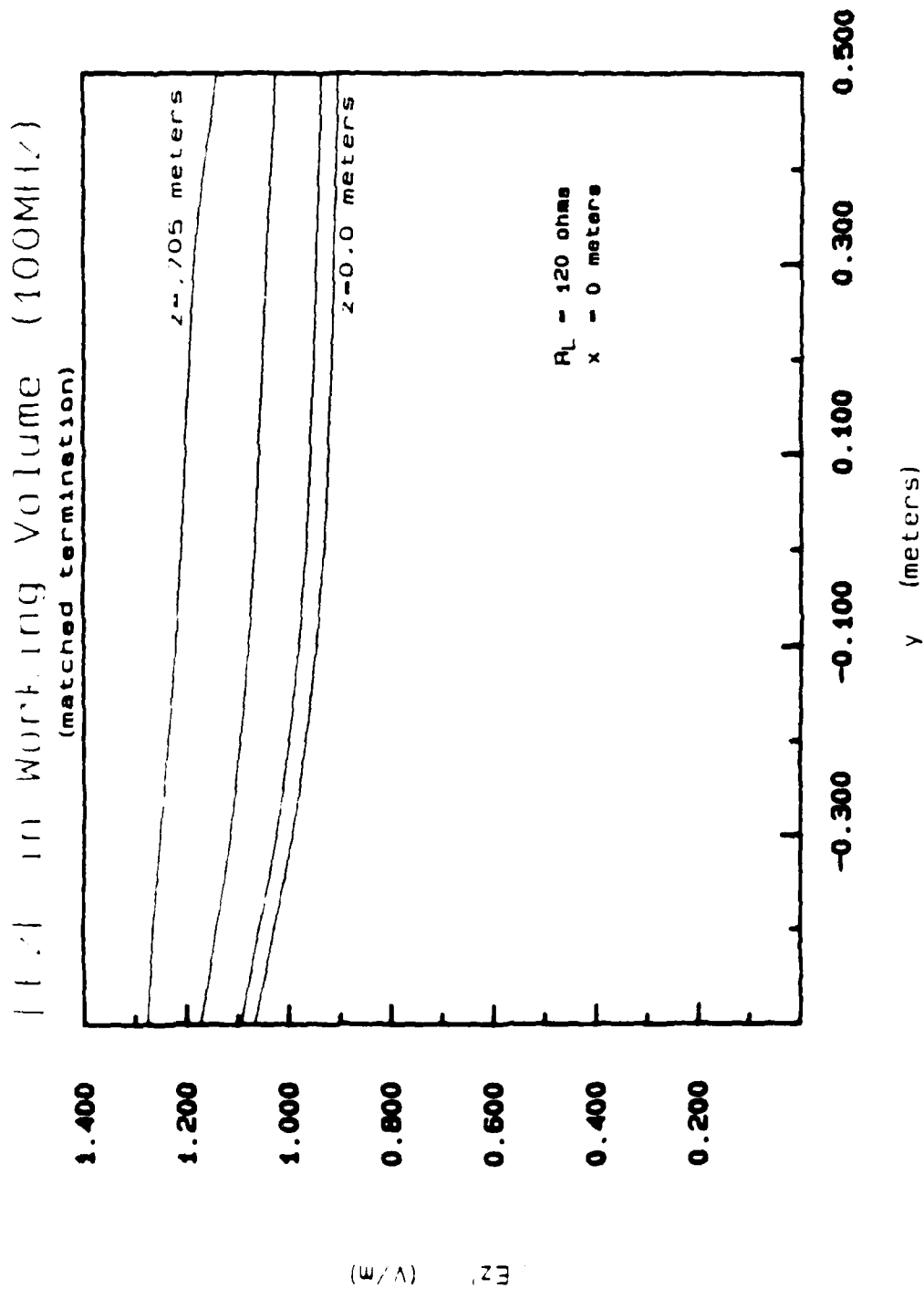


Figure 3.3. (b) Phase of E_z .



(a) Magnitude of E_z .

Figure 3.4. Vertical E-field computed along the longitudinal direction in the parallel-plate region of the 450 MHz bandwidth ACHATES EMP simulator due to a unit amplitude, 100 MHz excitation.

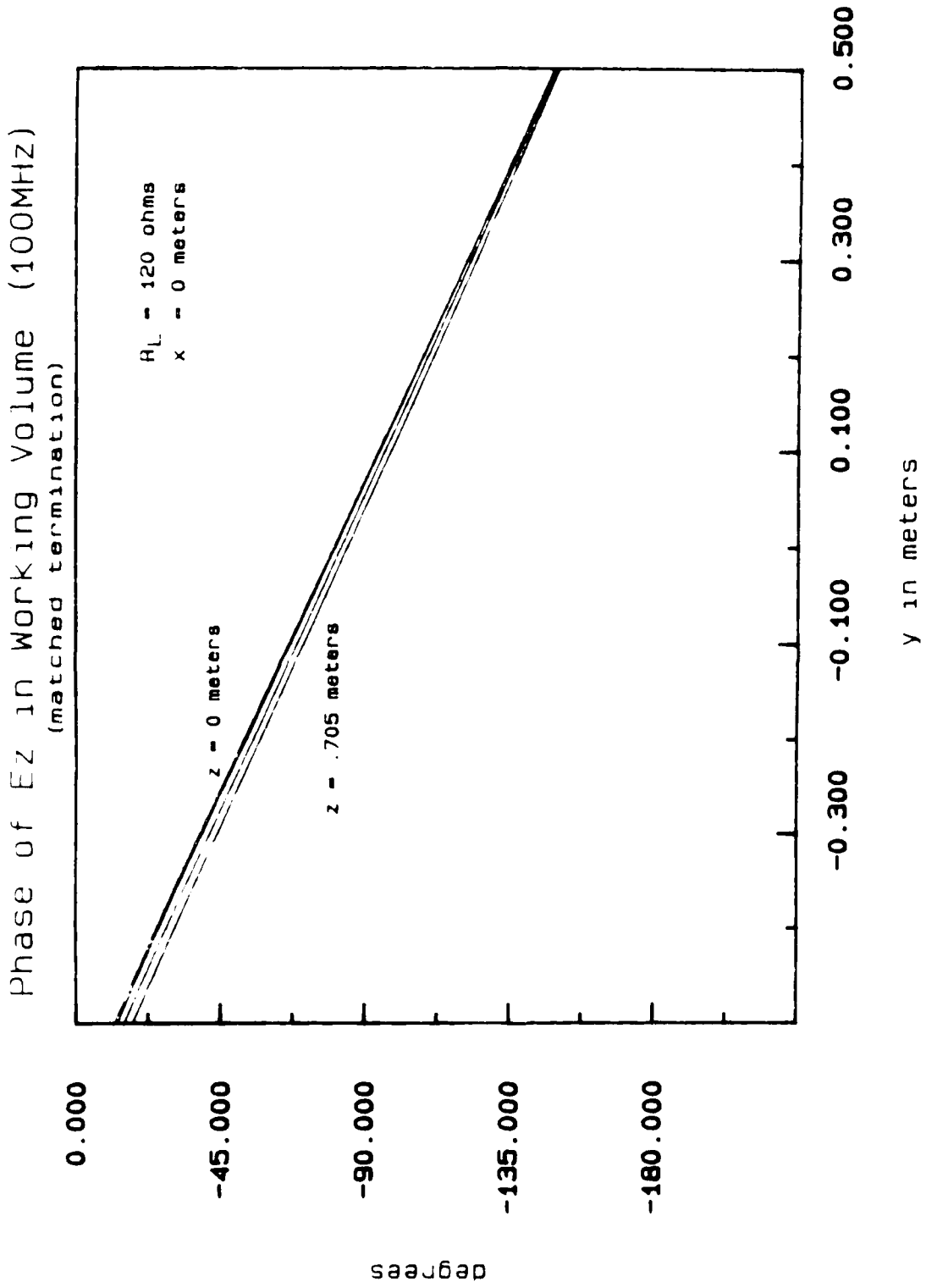
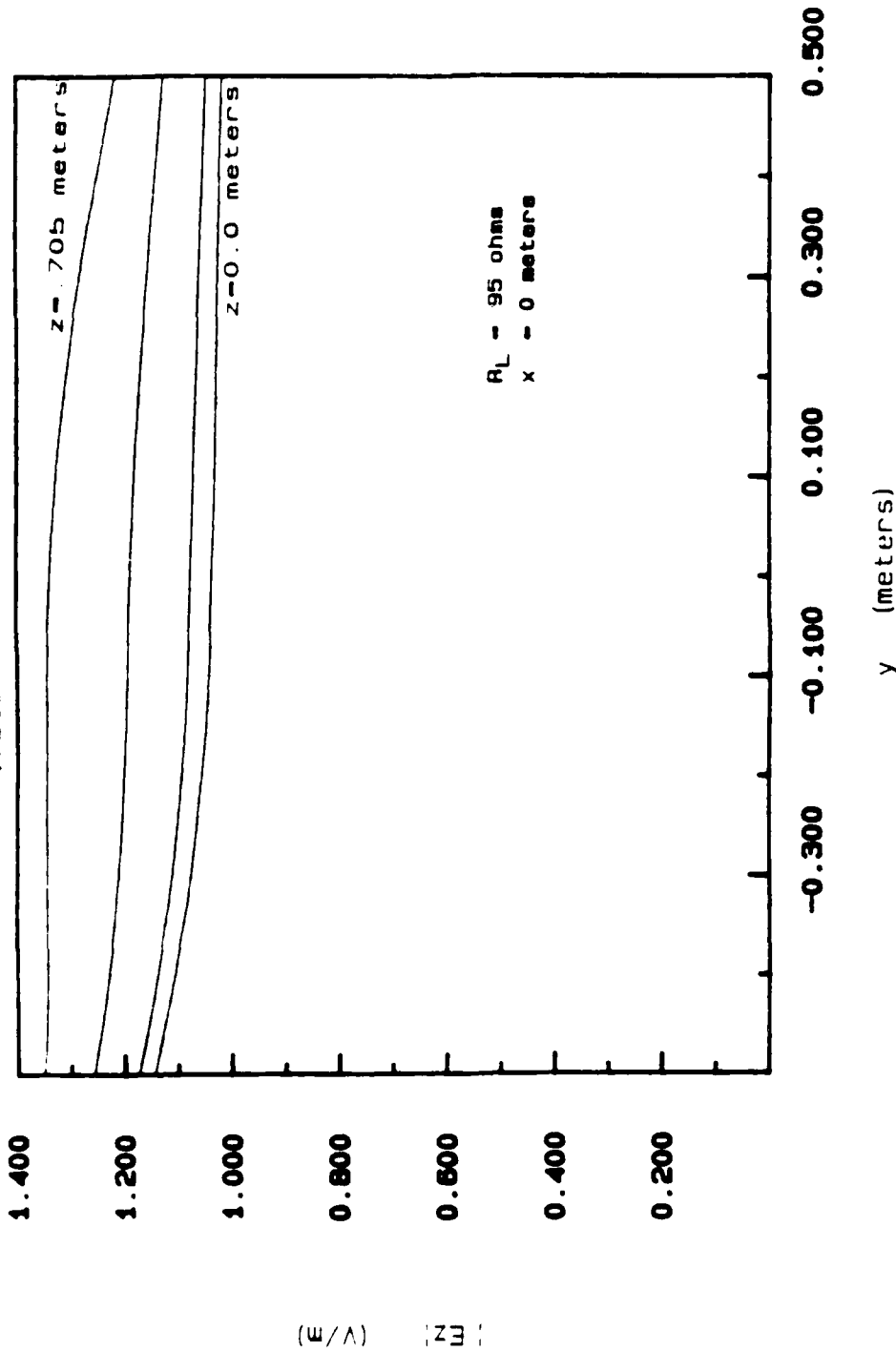


Figure 3.4. (b) Phase of E_z .

$|E_z|$ in Working Volume (125MHz)
(matched termination)



(a) Magnitude of E_z .
 Figure 3.5. Vertical E-field computed along the longitudinal direction in the parallel-plate region of the 450 MHz bandwidth ACHATES EMP simulator due to a unit amplitude, 125 MHz excitation.

Phase of E_z in Working Volume (125MHz)
(matched termination)

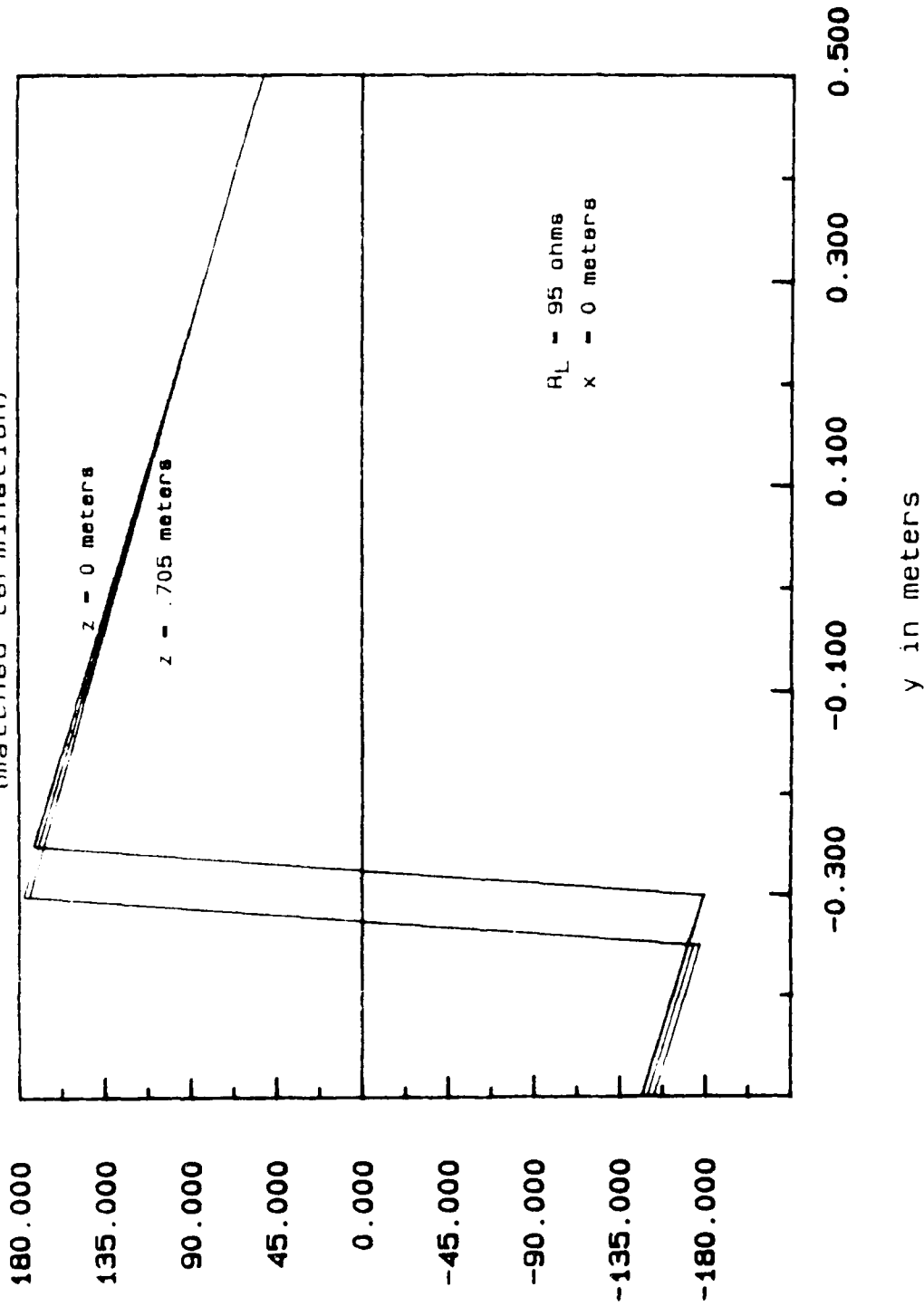


Figure 3.5. (b) Phase of E_z .

$|E_z|$ in Working Volume (75MHz)
(matched termination)

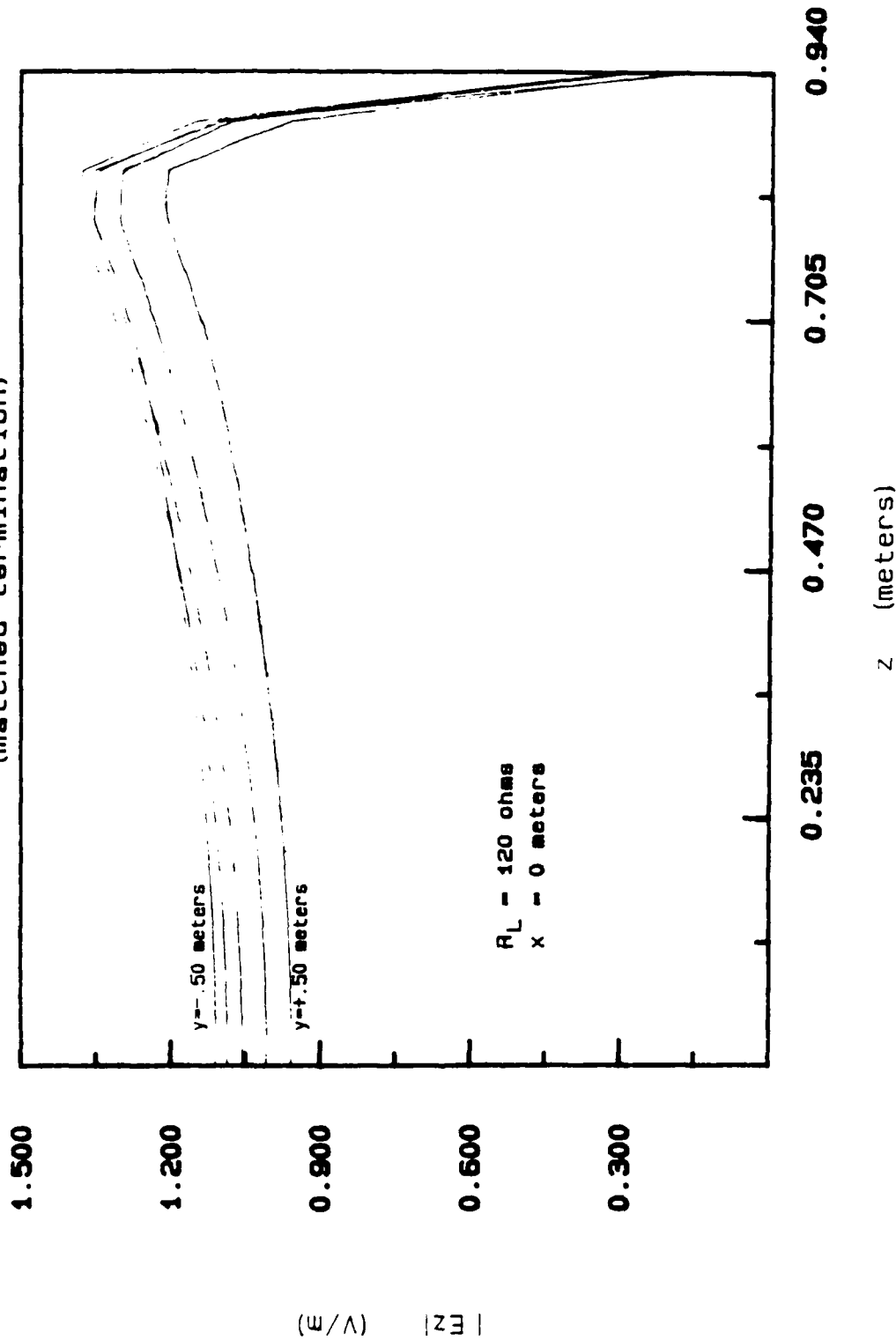


Figure 3.6. Magnitude of the vertical E-field computed along the vertical direction at various longitudinal positions ($y = -0.5, -0.25, 0.0, 0.25, 0.5 \text{ m}$) due to a unit amplitude, 75 MHz excitation.

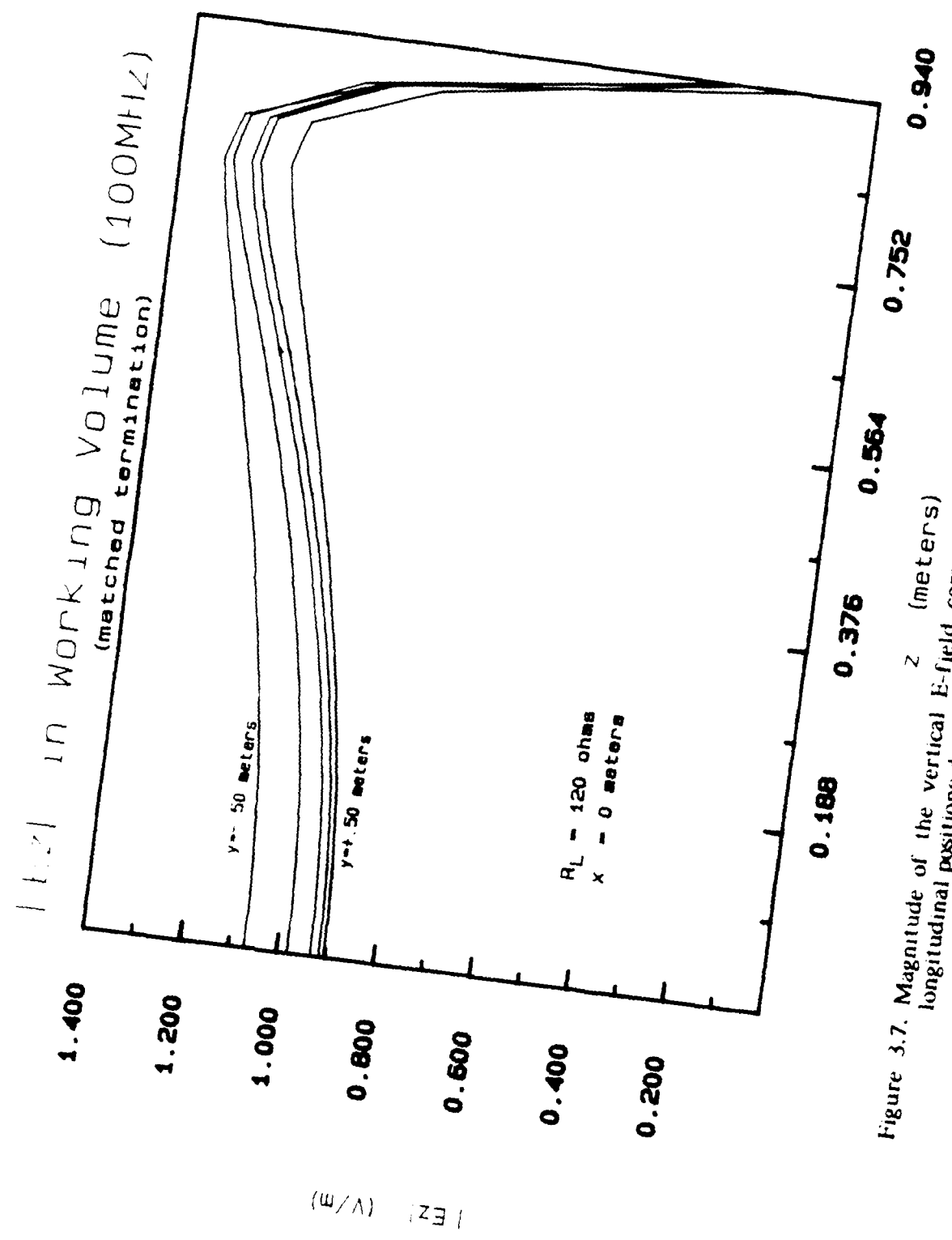


Figure 3.7. Magnitude of the vertical E-field computed along the vertical direction at various longitudinal positions due to a unit amplitude, 100 MHz excitation.

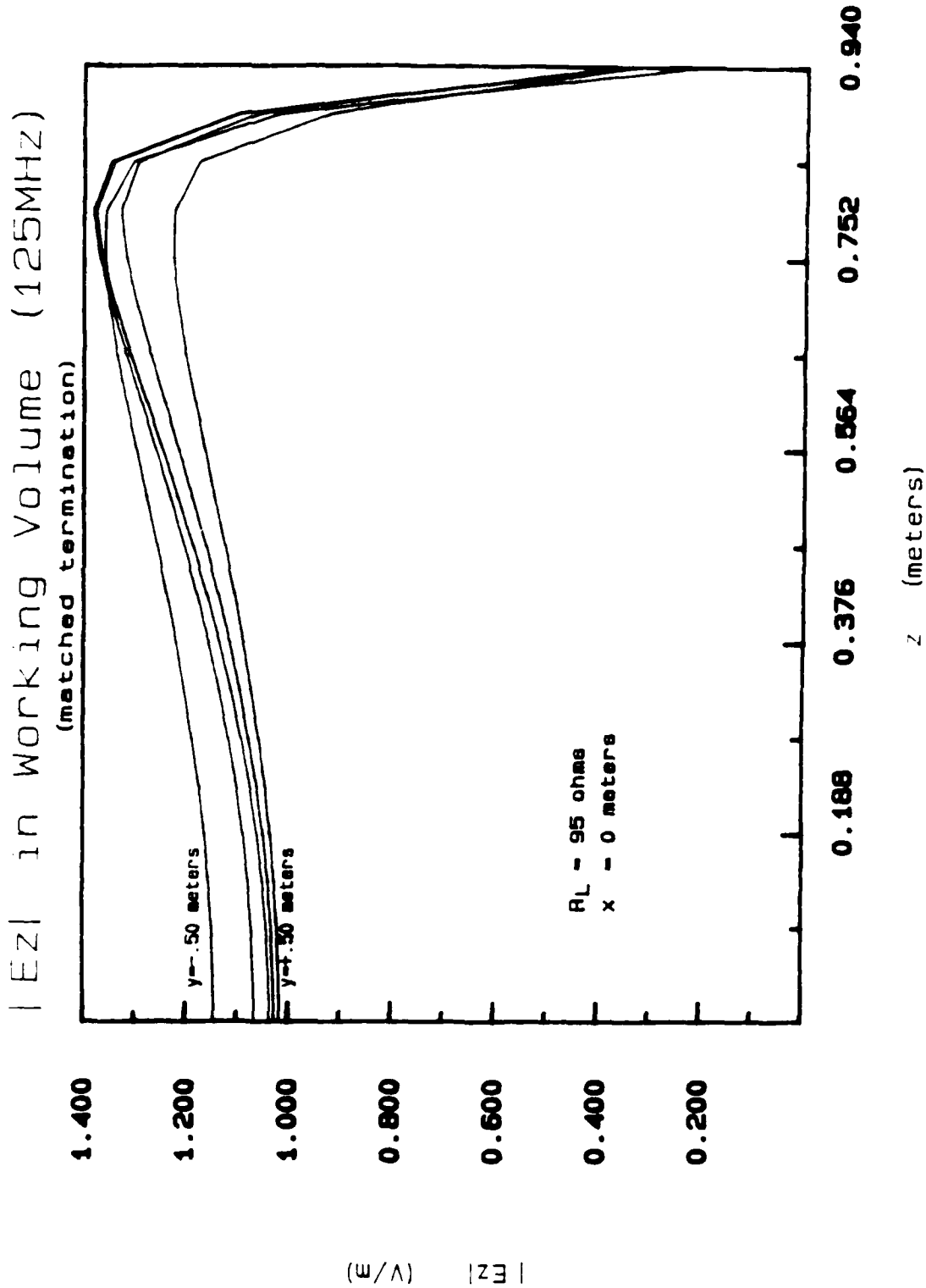


Figure 3.8. Magnitude of the vertical E-field computed along the vertical direction at various longitudinal positions due to a unit amplitude, 125 MHz excitation.

|E_z| in Working Volume (75MHz)
 (matched termination)

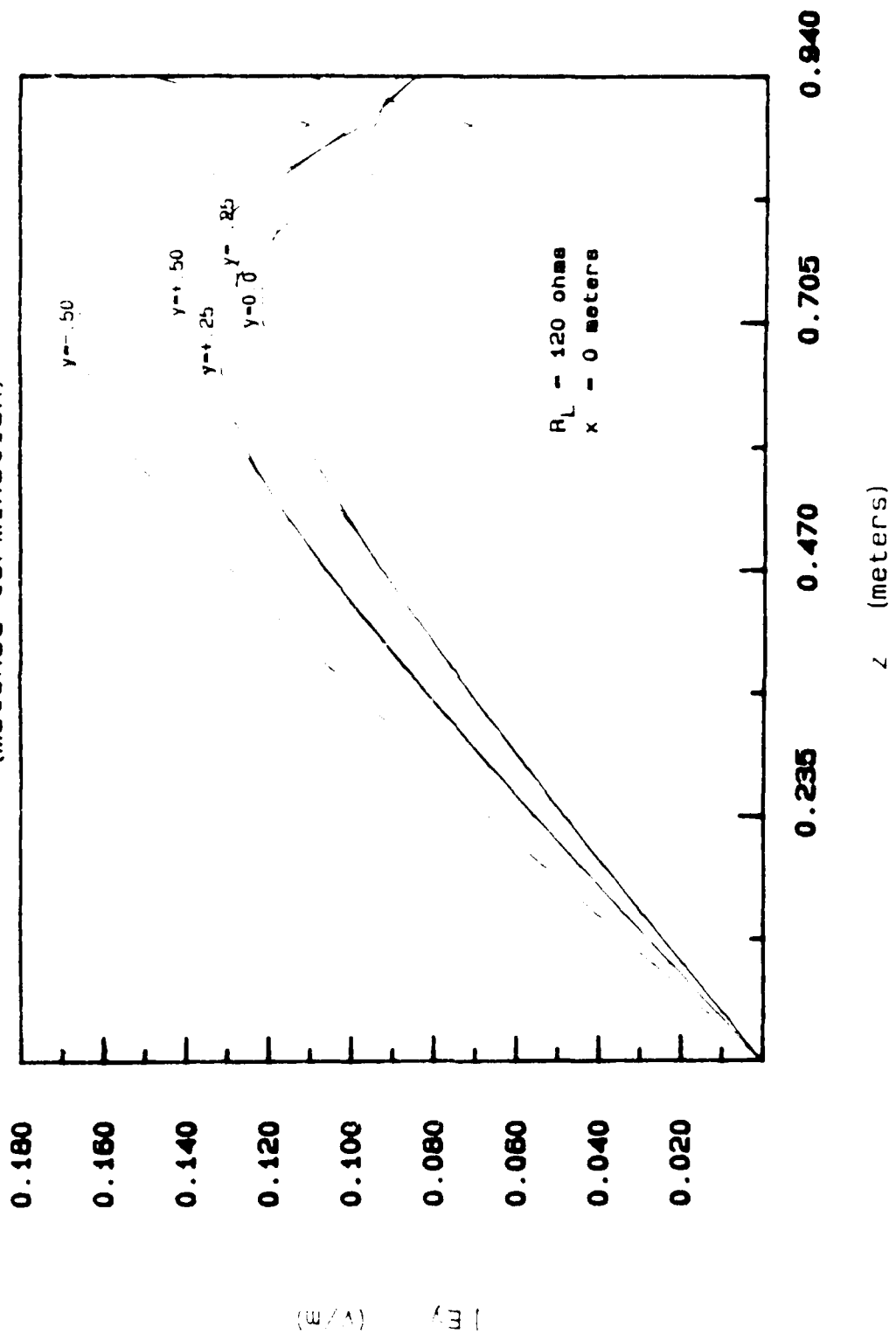


Figure 3.9. Magnitude of the longitudinal E-field computed along the vertical direction at various longitudinal positions due to a unit amplitude, 75 MHz excitation.

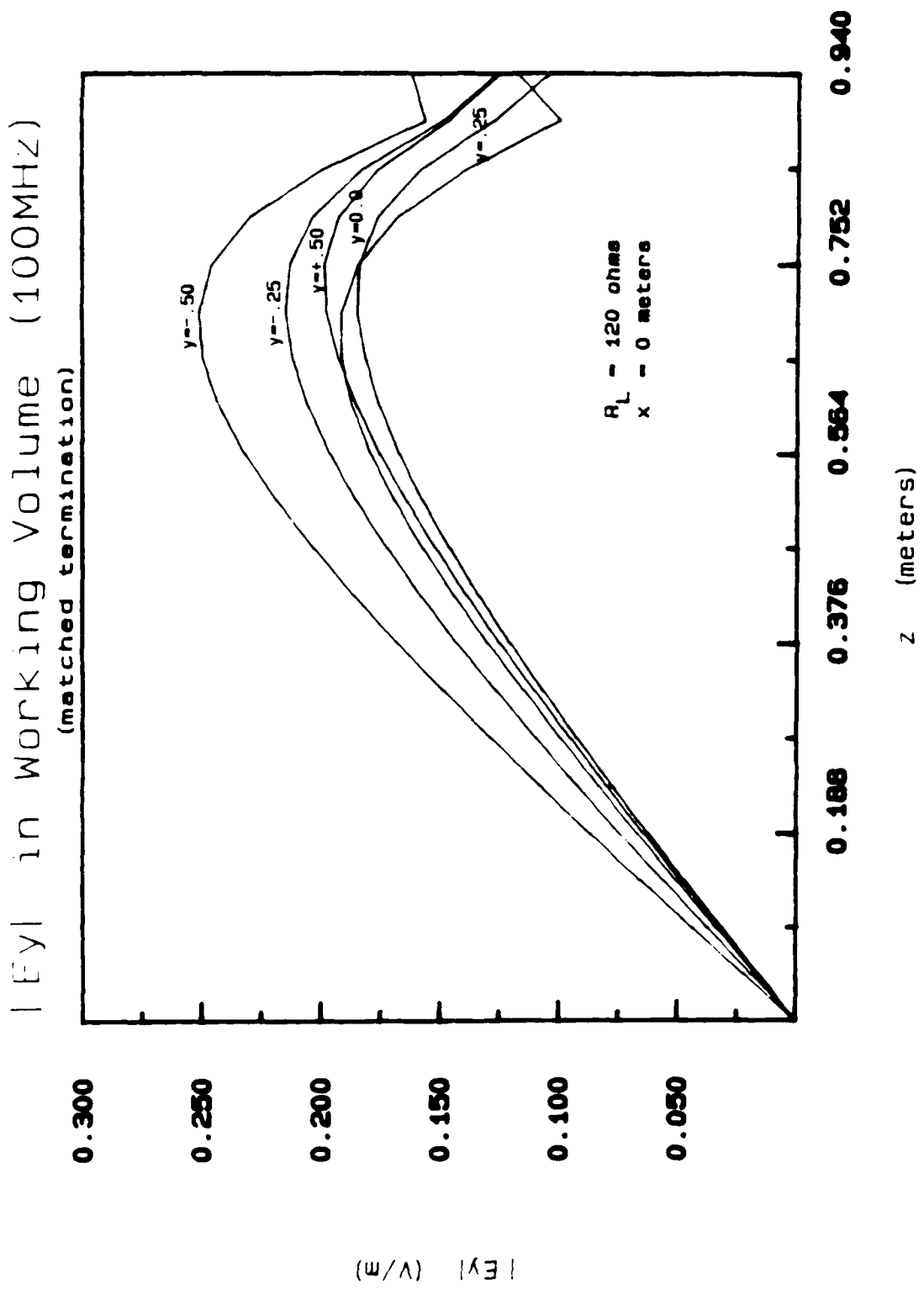


Figure 3.10. Magnitude of the longitudinal E-field computed along the vertical direction at various longitudinal positions due to a unit amplitude, 100 MHz excitation.

E_z in Working Volume (125MHz)
 (matched termination)

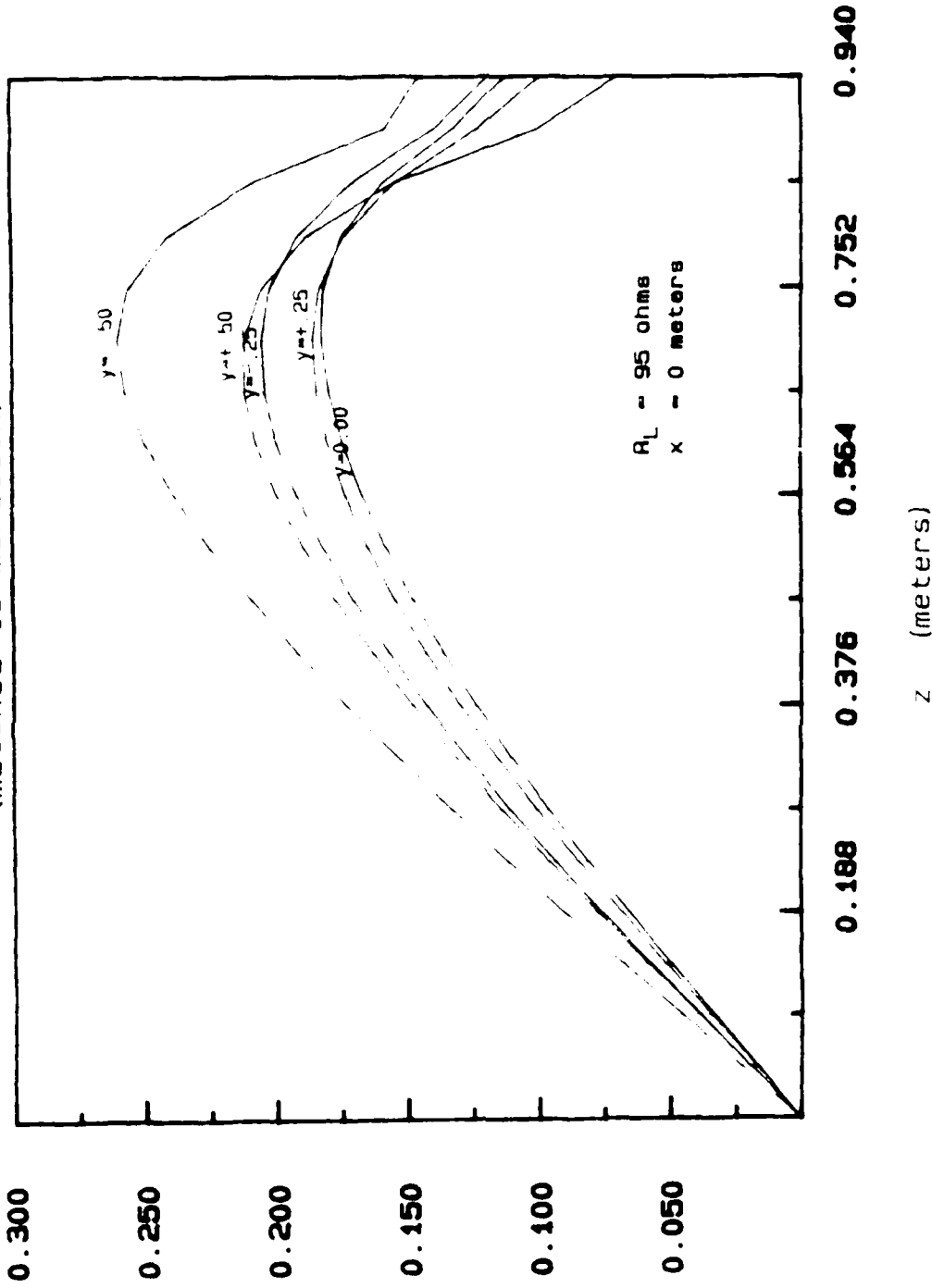
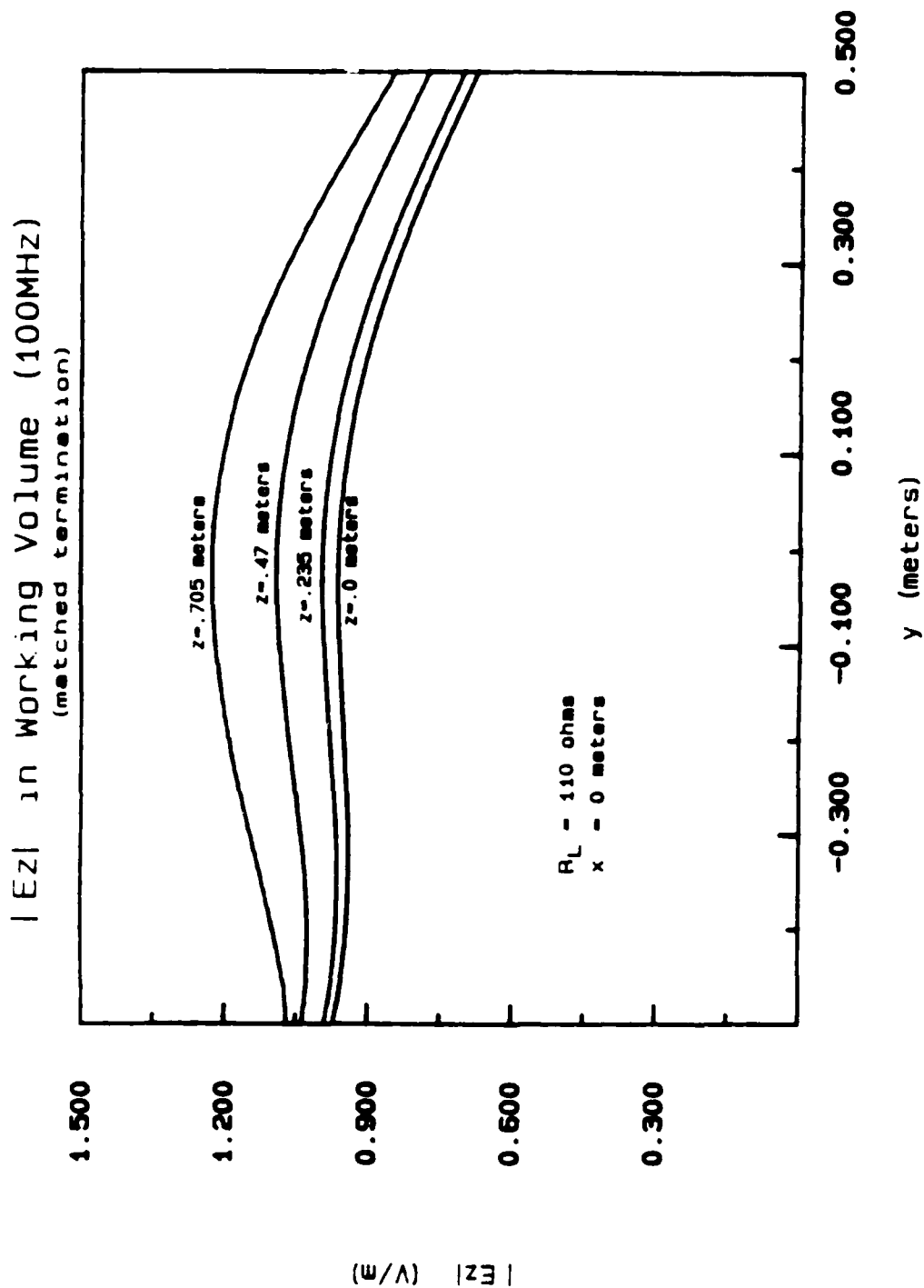


Figure 3.11. Magnitude of the longitudinal E_z field computed along the vertical direction at various longitudinal positions due to a unit amplitude, 125 MHz excitation.



(a) Magnitude of E_z .

Figure 3.12. Vertical E-field computed along the longitudinal direction at various heights in the parallel-plate region of the 200 MHz bandwidth ACHATES simulator due to a 100 MHz unit amplitude excitation.

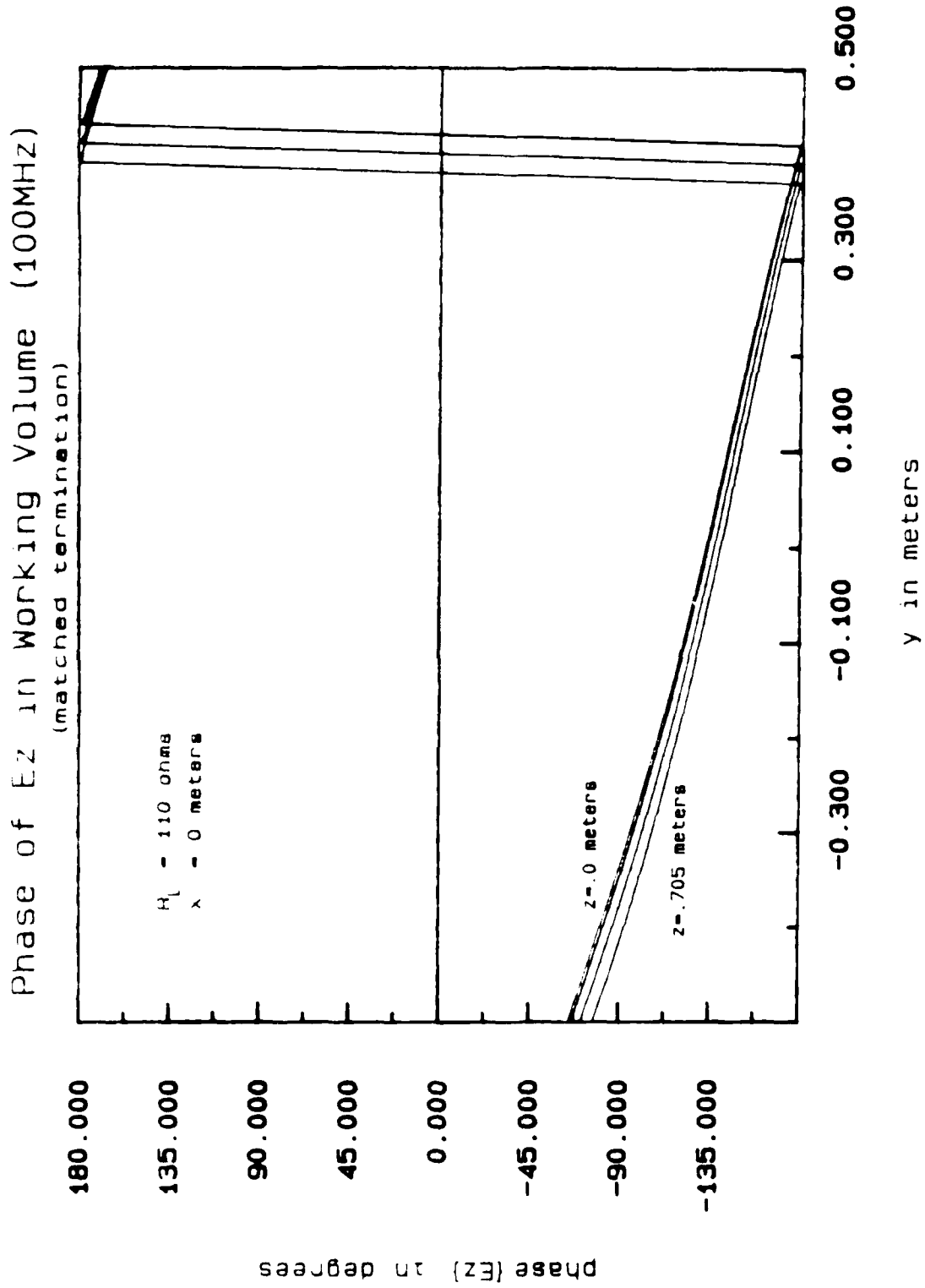
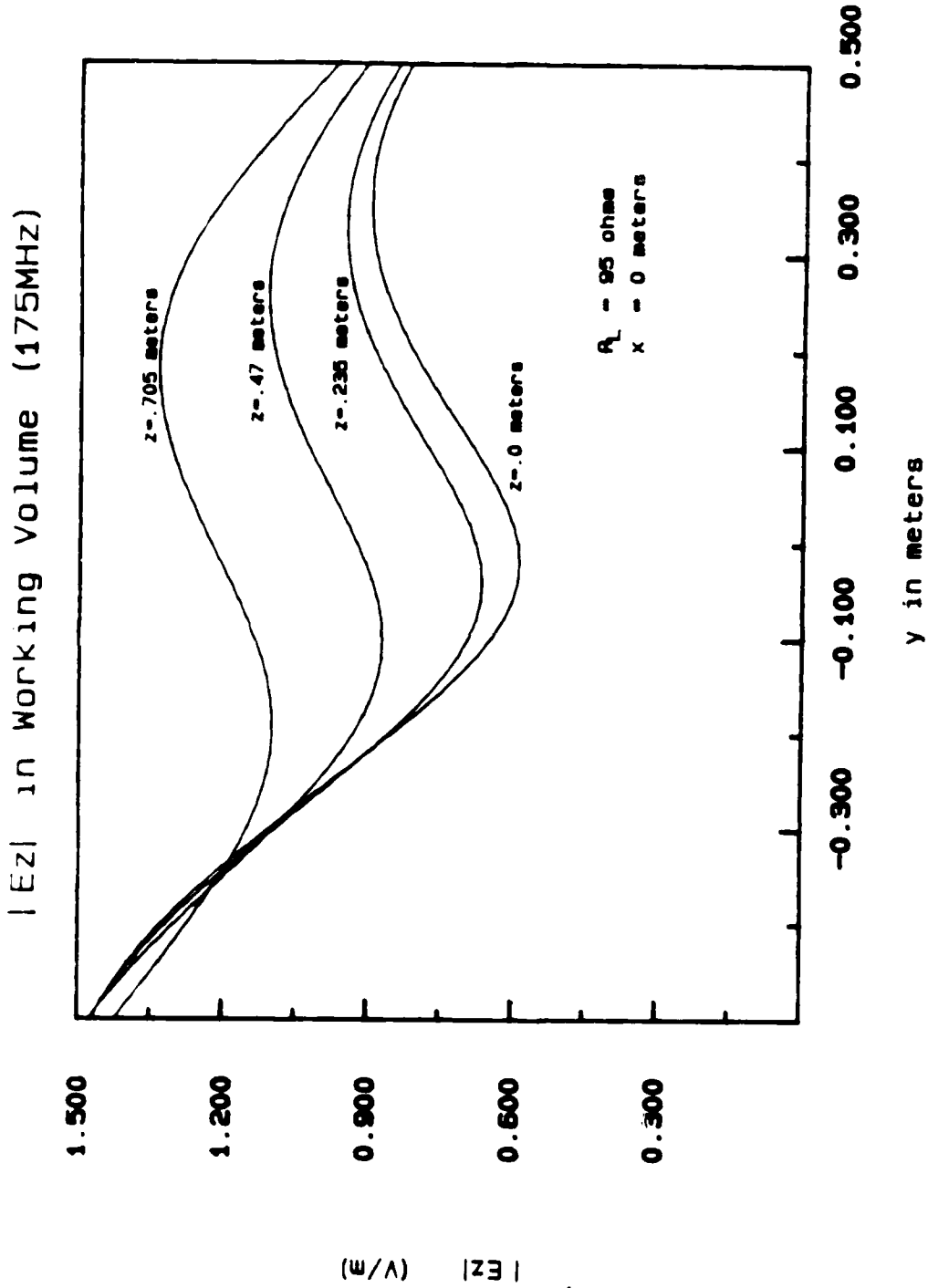


Figure 3.12. (b) Phase of E_z .



(a) Magnitude of E_z .

Figure 3.13. Vertical E-field computed along the longitudinal direction at various heights in the parallel-plate region of the 200 MHz bandwidth ACHATS simulator due to a 175 MHz unit-amplitude excitation.

Phase of E_z in Working Volume (175MHz)

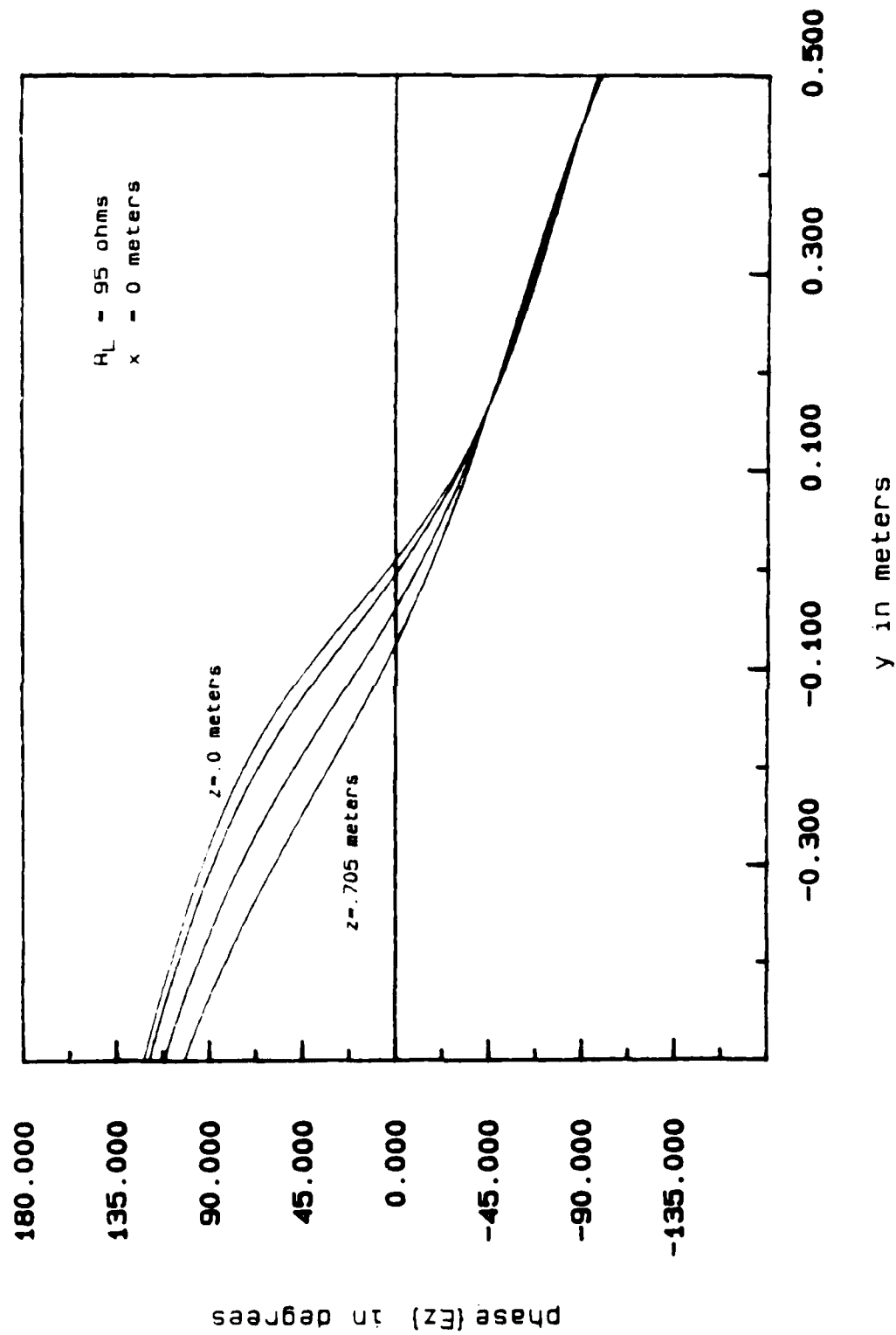


Figure 3.13. (b) Phase of E_z .

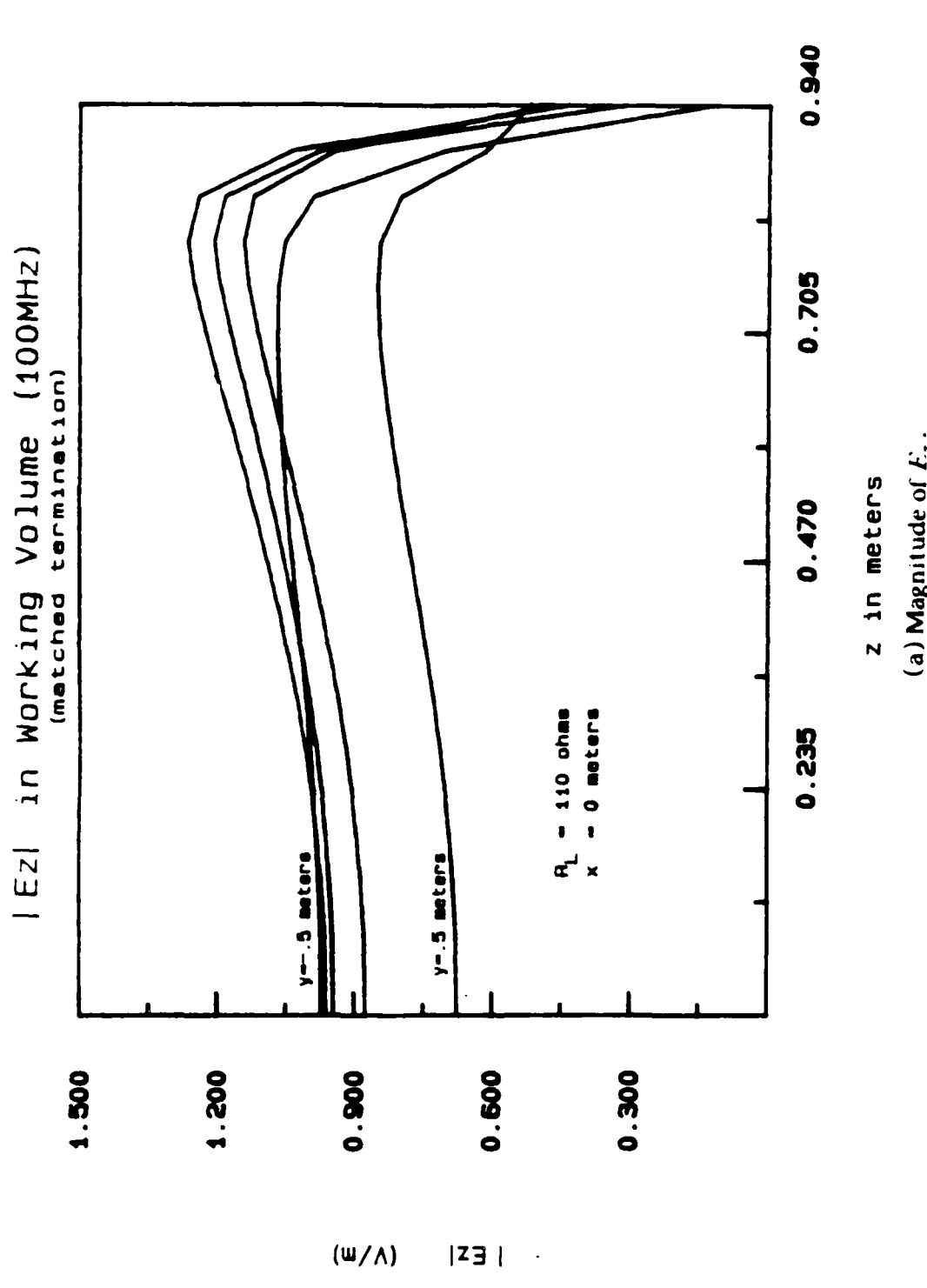


Figure 3.14. Vertical E-field computed along the vertical direction at various longitudinal positions in the parallel-plate region of the 200 MHz bandwidth ACHATES simulator due to a 100 MHz unit-amplitude excitation.

Phase of E_z in Working Volume (100MHz)

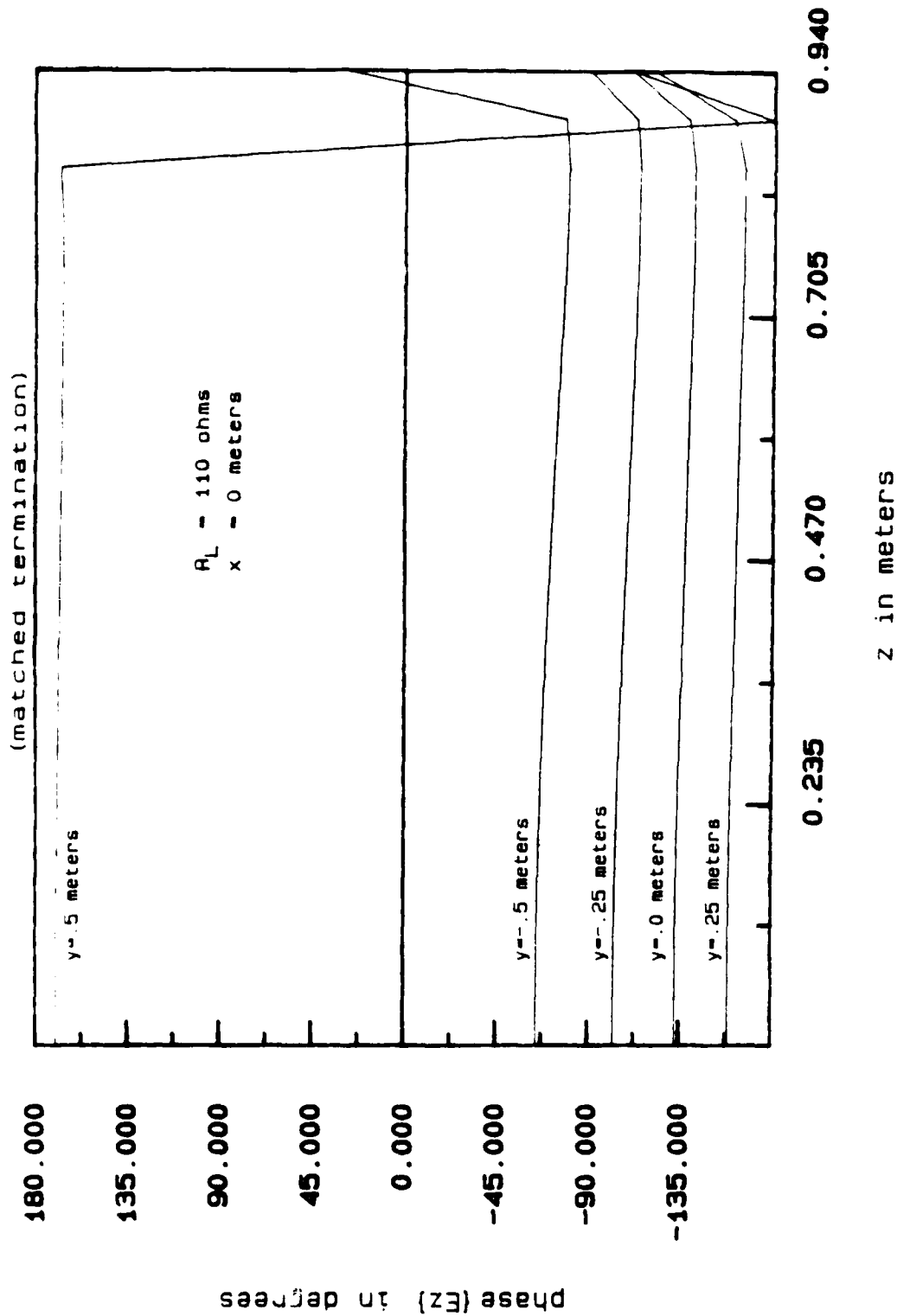
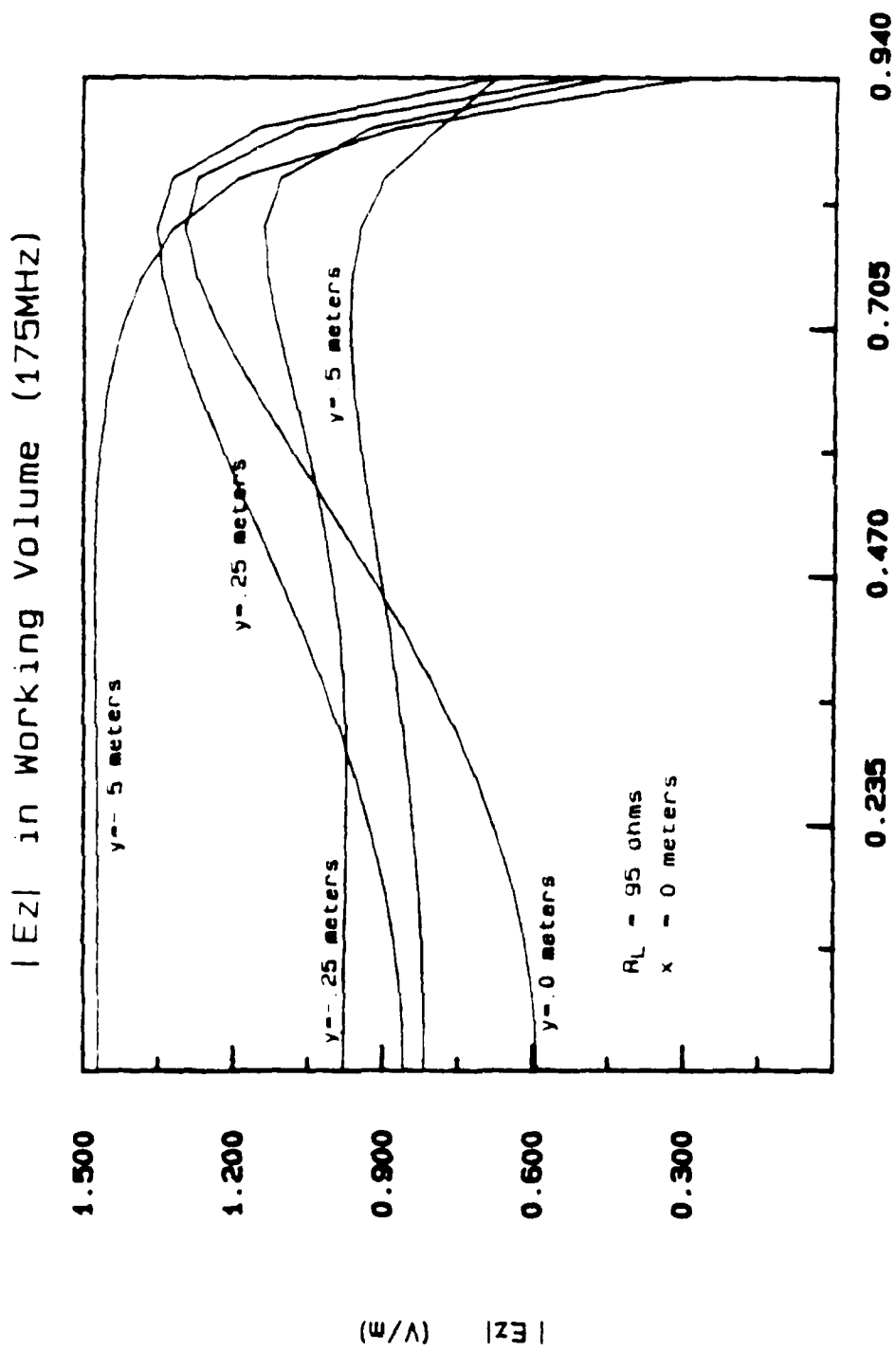


Figure 3.14. (b) Phase of E_z .



(a) Magnitude of E_z .

Vertical E-field computed along the vertical direction at various longitudinal positions in the parallel-plate region of the 200 MHz bandwidth ACHATES simulator due to a 175 MHz unit-amplitude excitation.

Phase of E_z in Working Volume (175MHz)

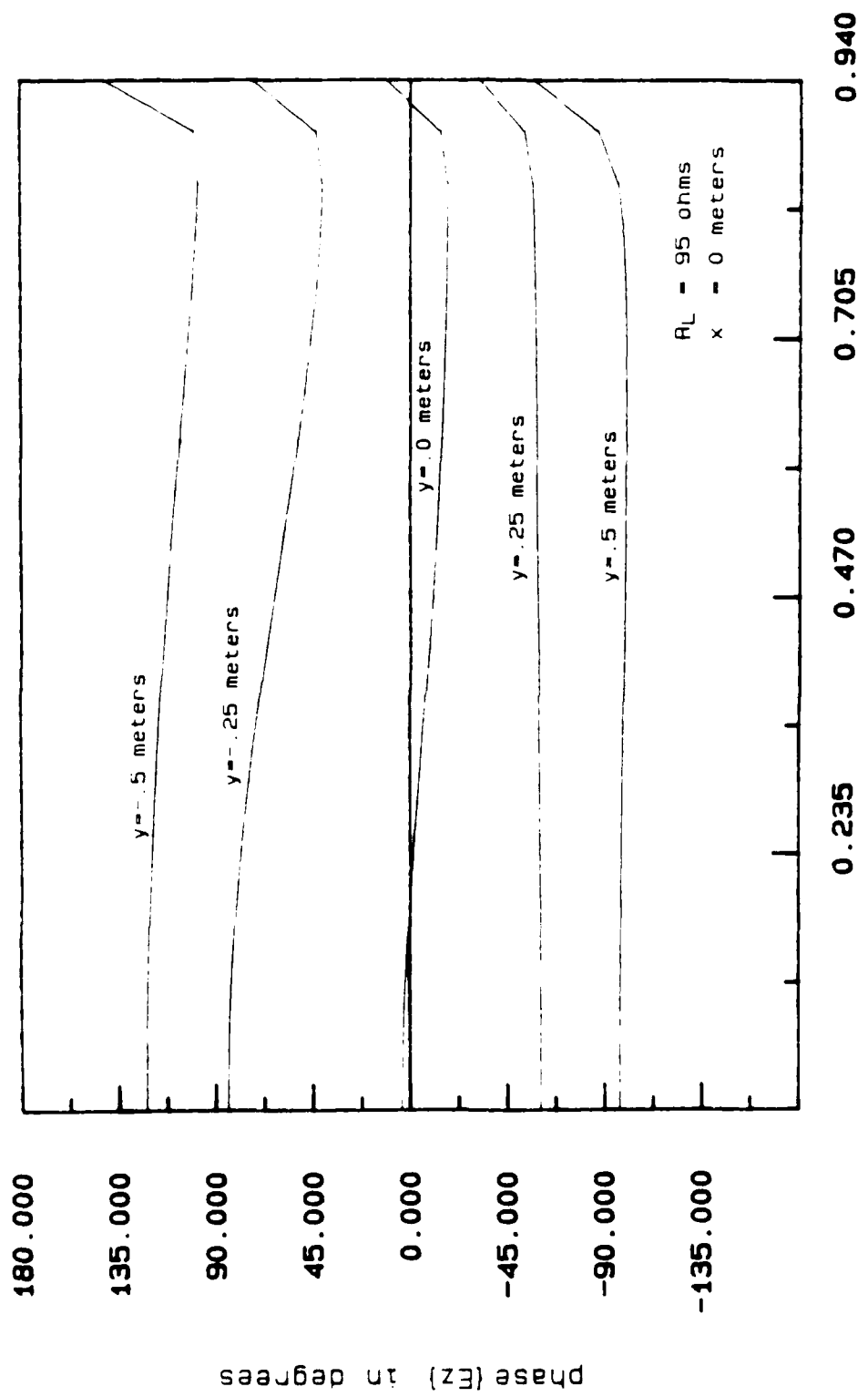
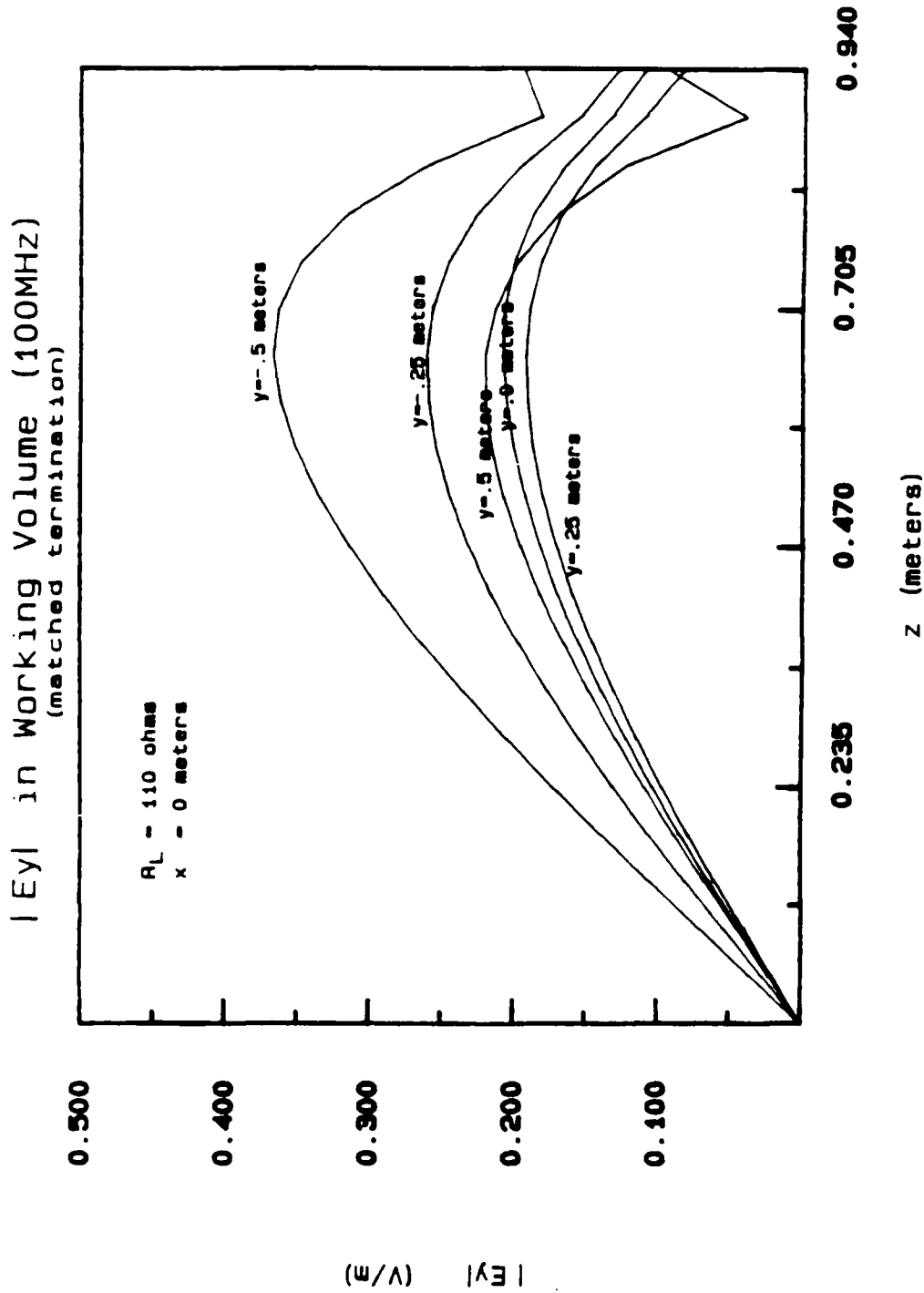


Figure 3.15. (b) Phase of E_z .



(a) Magnitude of E_y .

Figure 3.16. Longitudinal E-field computed along the vertical direction at various longitudinal positions in the parallel-plate region of the 200 MHz bandwidth ACHATES simulator due to a 100 MHz unit-amplitude excitation.

Phase of E_y in Working Volume (100MHz)

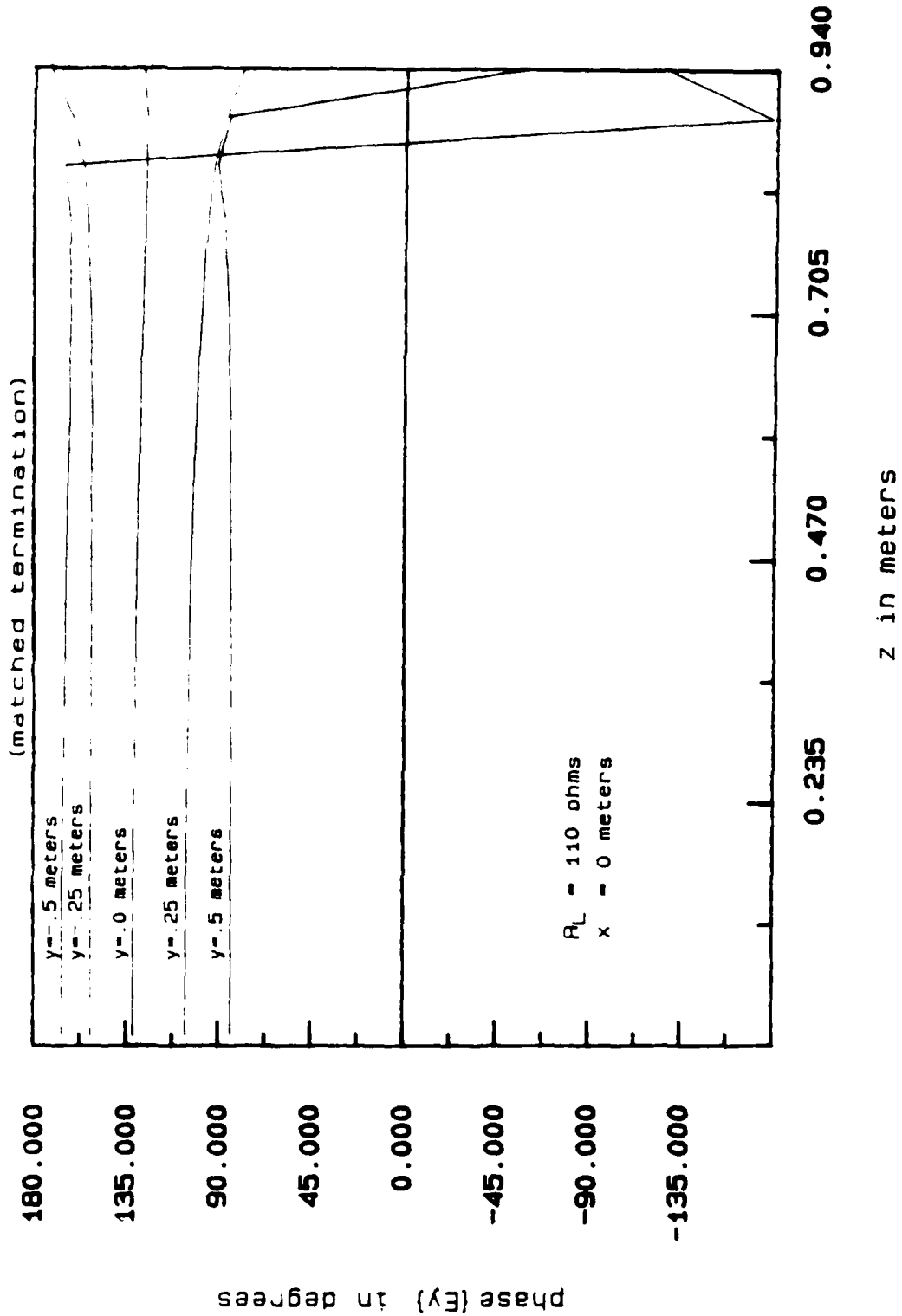
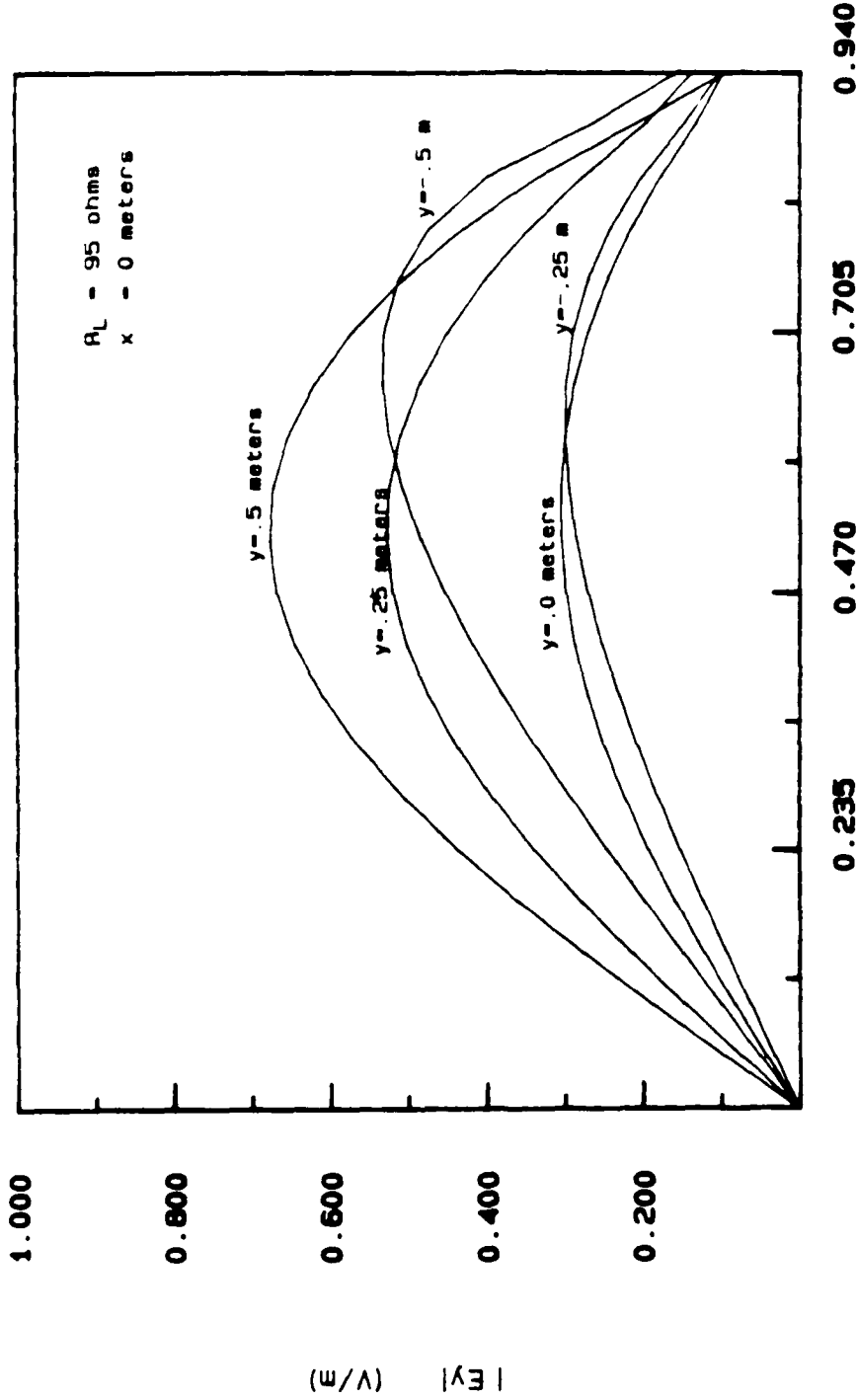


Figure 3.16. (b) Phase of E_y .

$|E_y|$ in Working Volume (175MHz)



z in meters

(a) Magnitude of E_y

Figure 3.17. Longitudinal E-field computed along the vertical direction at various longitudinal positions in the parallel-plate region of the 200 MHz bandwidth ACHATES simulator due to a 175 MHz unit-amplitude excitation.

Phase of Γ_y in Working Volume (175MHz)

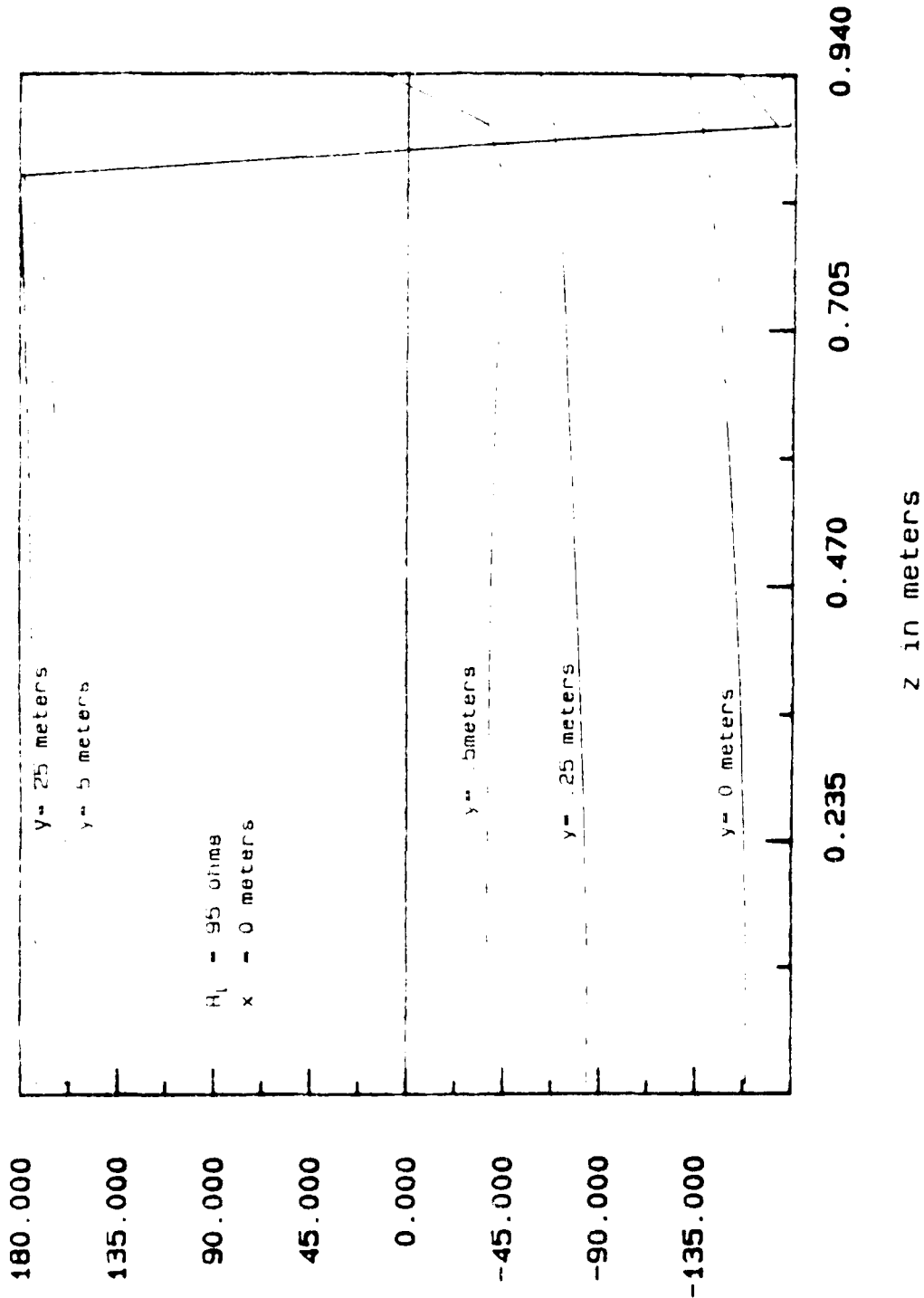


Figure 3.17. (b) Phase of Γ_y .

Longitudinal Current along Center Wire

(matched termination, 100MHz)

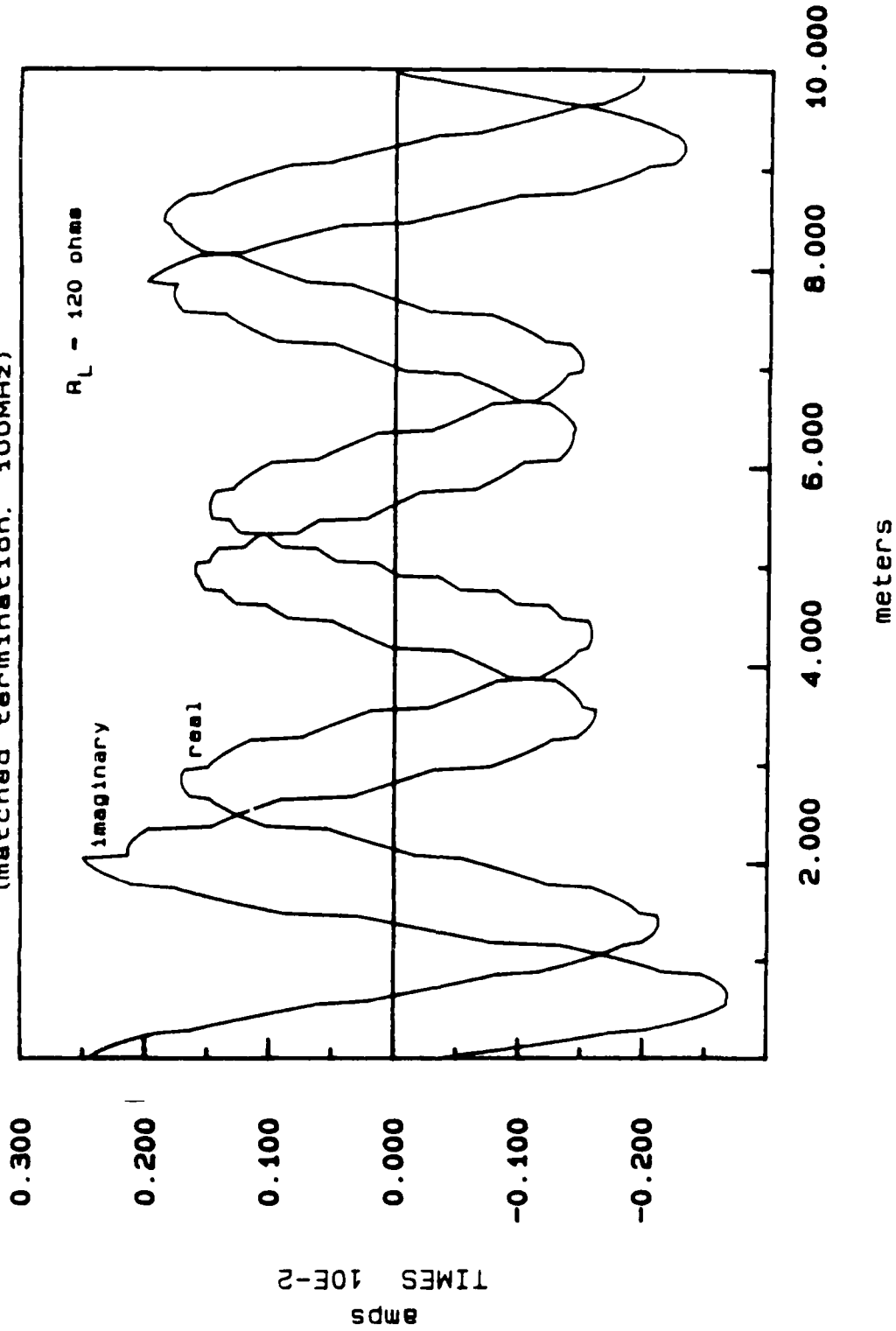


Figure 3.18. Longitudinal current computed near the center axis of the top conducting plate of the 450 MHz bandwidth ACHATES simulator due to a 100 MHz unit-amplitude excitation.

Tangential E-field On Conducting Surface

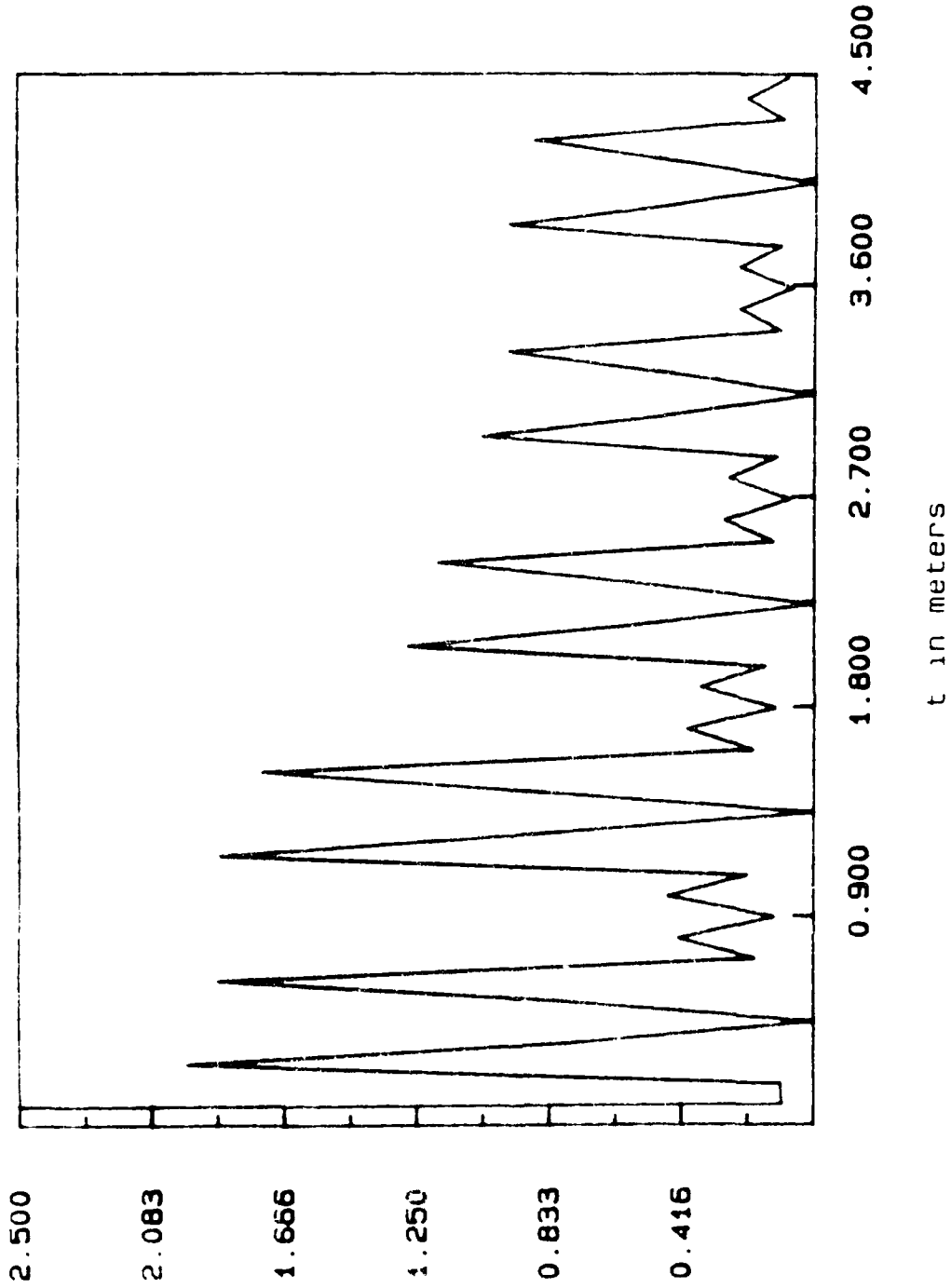


Figure 3.19. Boundary condition of the scattered E-field tangential to the conducting surface in the longitudinal direction. Computed along the source conical tapered end section due to a 100 MHz, unit amplitude excitation.

Interpolated vs. Discontinuous Currents

(matched termination, 100MHz)

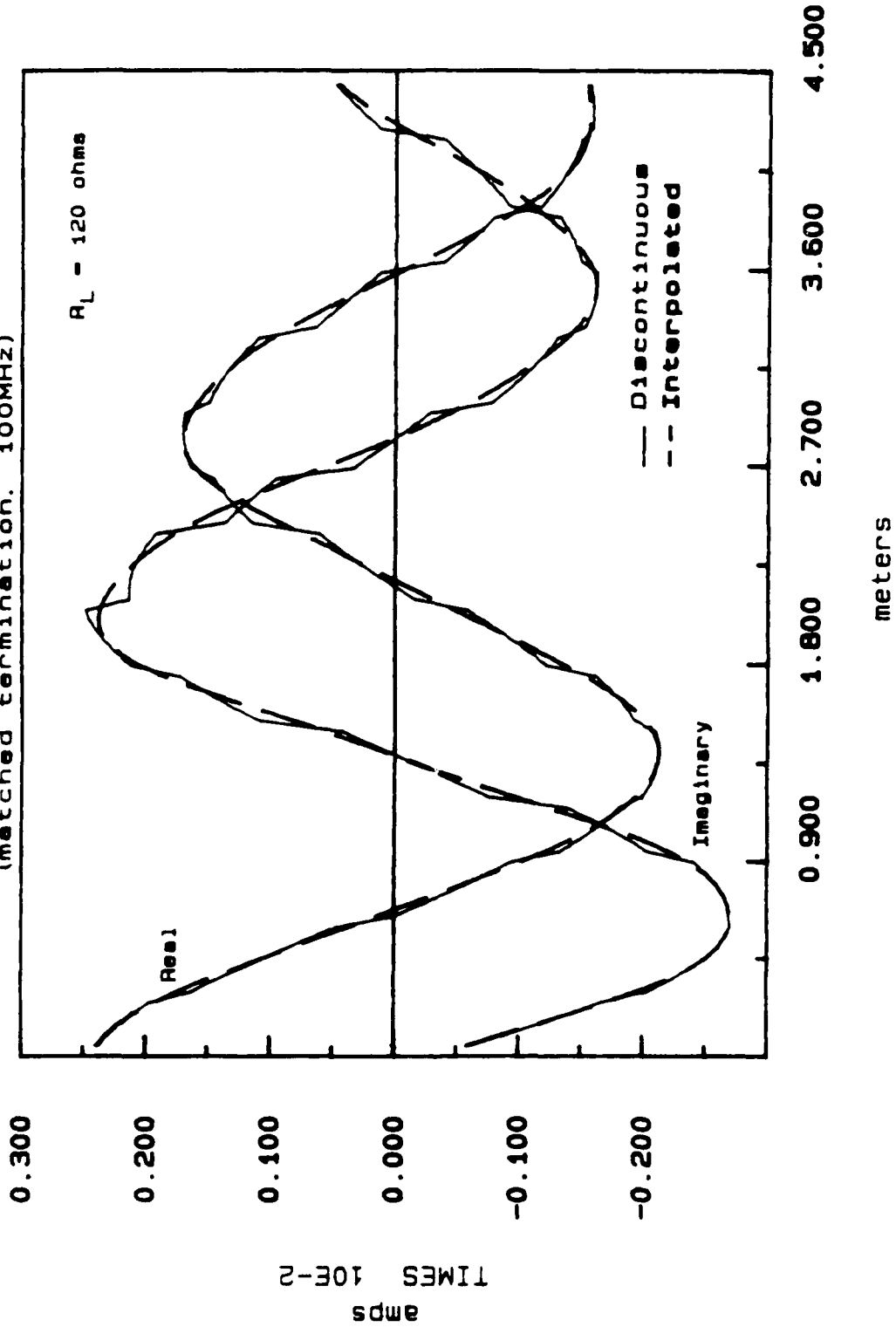
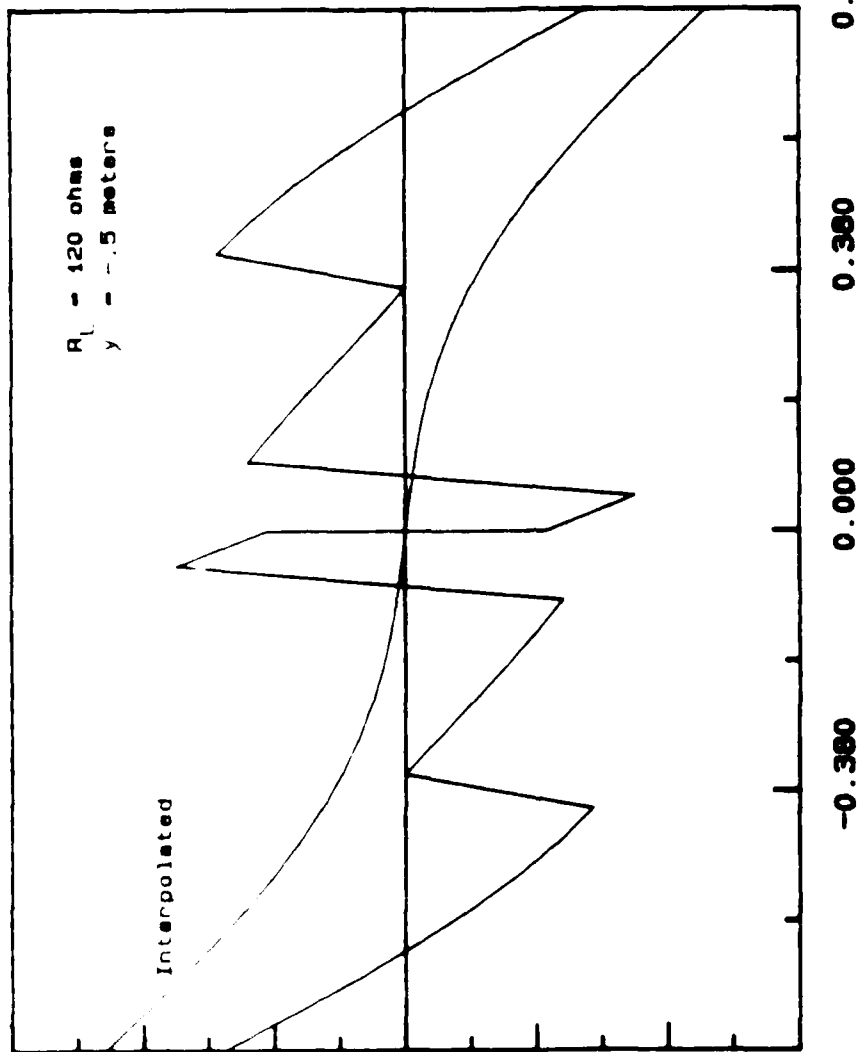


Figure 3.20. Comparison of the currents that are smoothed by Fourier sine series interpolation. The currents are produced by a 100 MHz, unit-amplitude excitation.

Interpolated vs. NEC Transverse Current

(matched termination, 100MHz)

$R_L = 120 \text{ ohms}$
 $y = -0.5 \text{ meters}$



(a) Real part, at $y = -0.5 \text{ m}$, with the edge condition imposed by the edge wire. Comparison of the currents on the transverse wires that are smoothed by a Fourier sine series interpolation. (Currents are normalized by a wavelength)

Interpolated vs. NEC Transverse Current
 (matched termination, 100MHz)

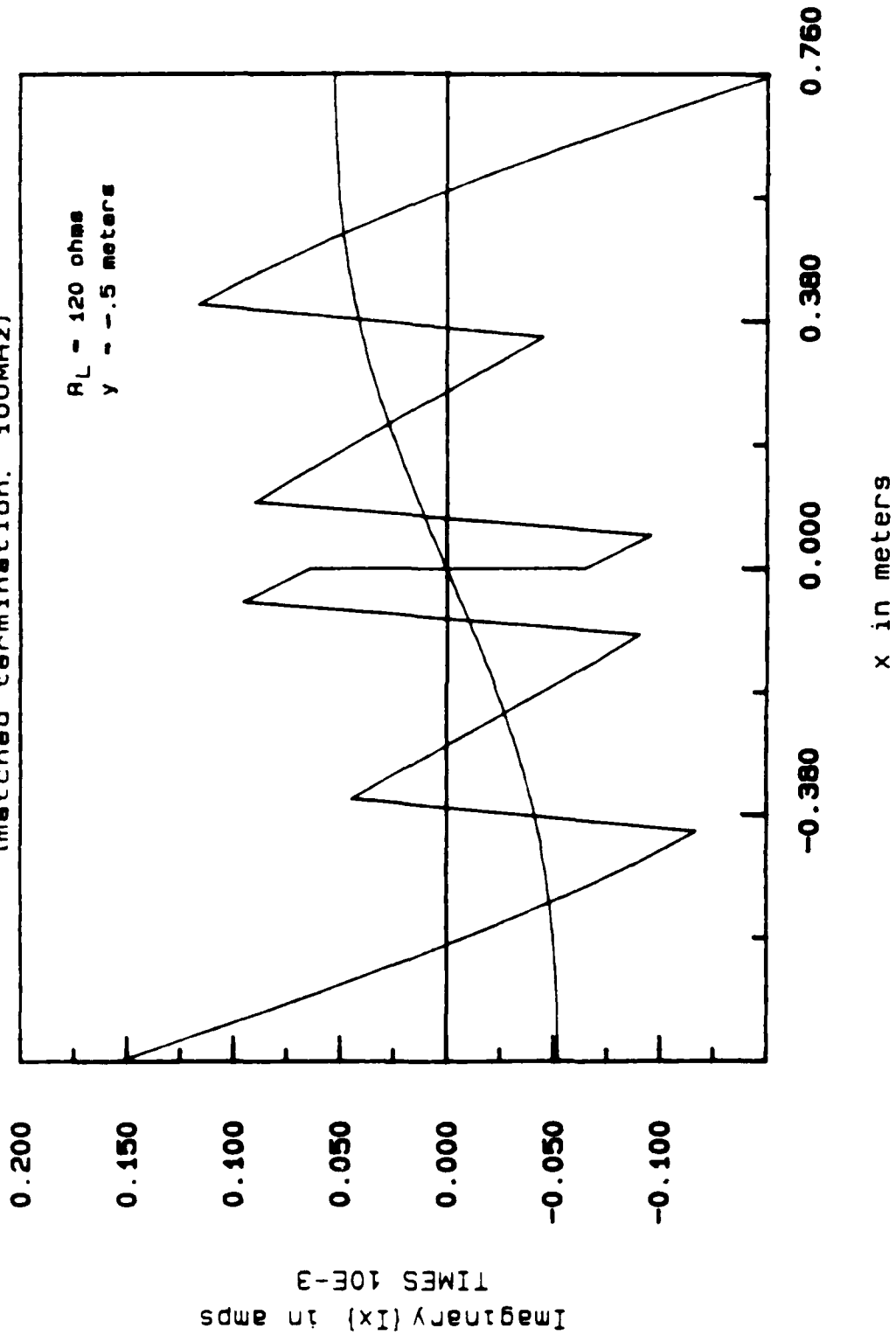


Figure 3.21. (b) Imaginary part, at $y = -0.5 \text{ m}$, with the edge condition imposed by the edge wire.

Interpolated vs. NEC Transverse Current
 (matched termination, 100MHz)

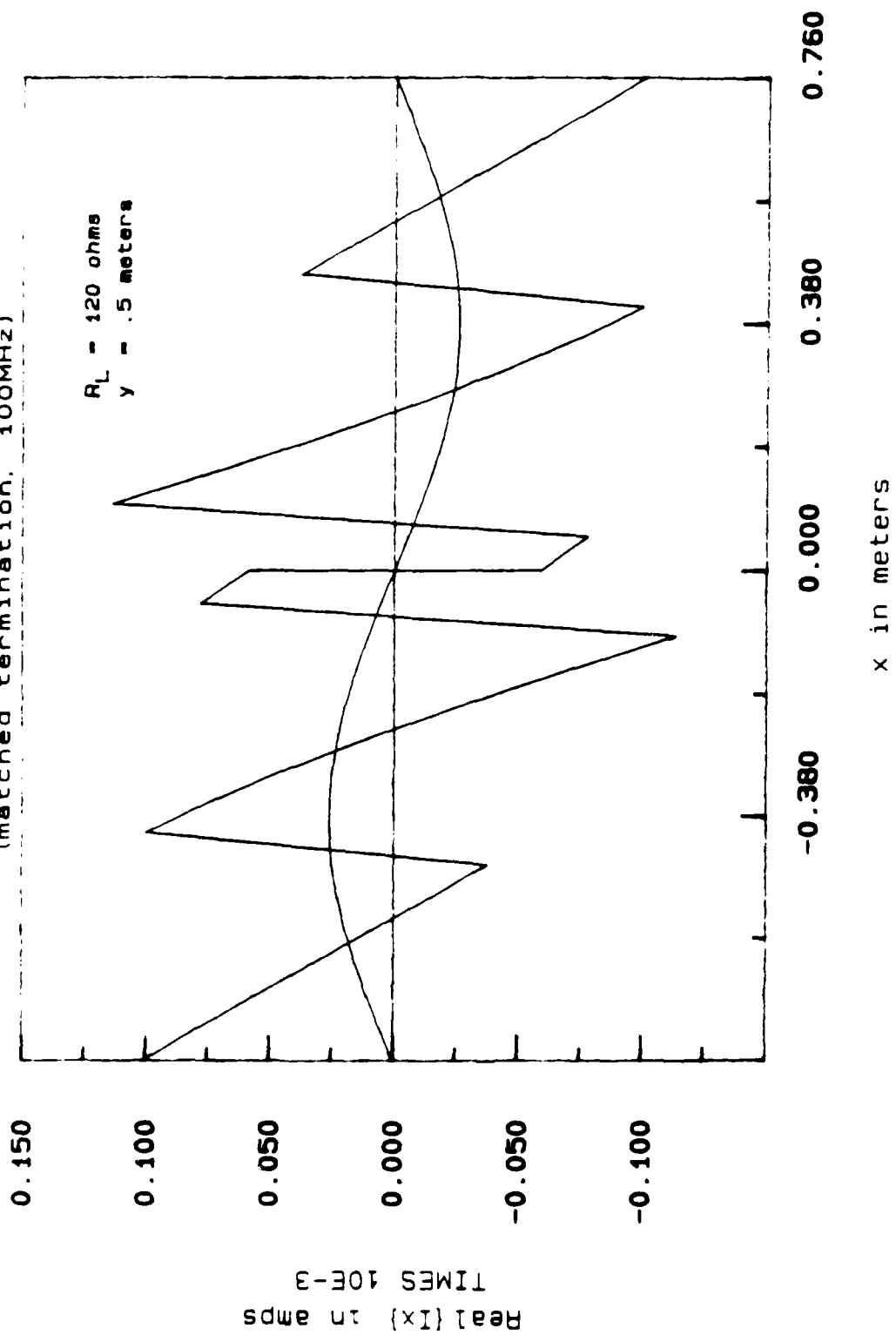


Figure 3.21. (c) Real part, at $y=+0.5 \text{ m}$, with a zero edge condition in the parallel plate region.

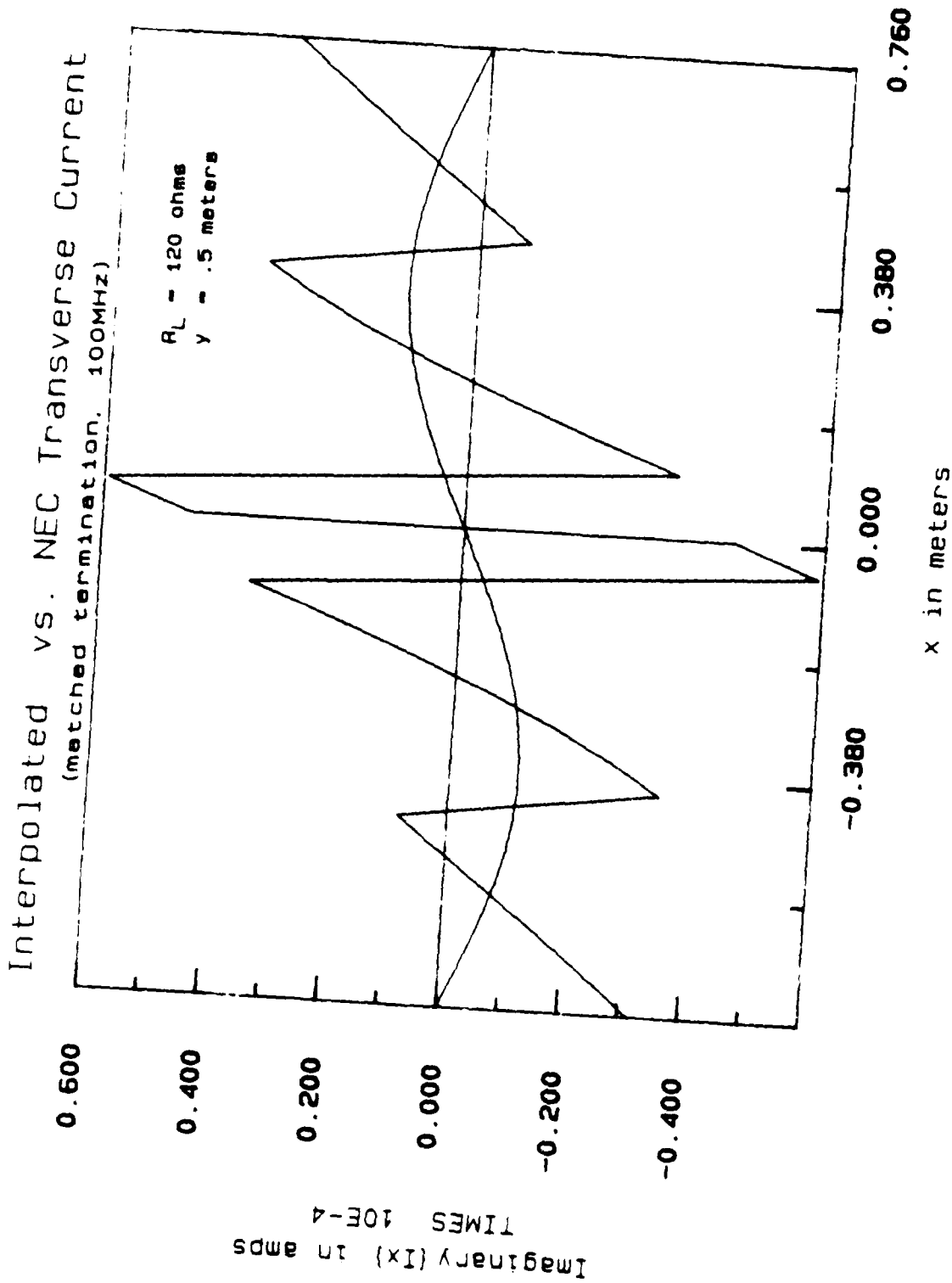


Figure 3.21. (d) Imaginary part, at $y=+0.5$ m, with a zero edge condition in the parallel-plate region.

|Ez| Computed From Interpolated Currents
 (matched termination, 100MHz)

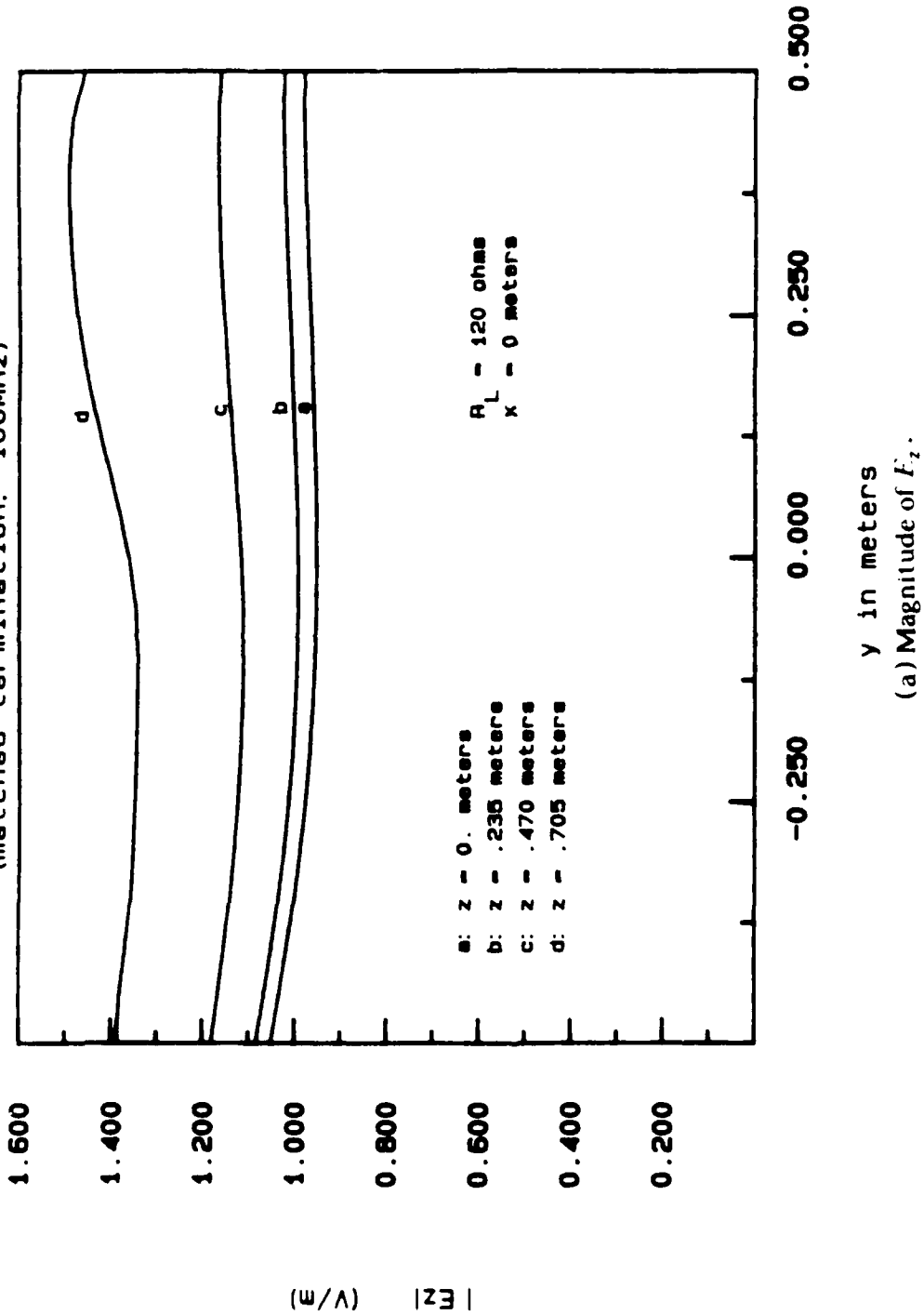


Figure 3.22. Vertical E-field computed from the interpolated currents due to a 100 MHz unit-amplitude excitation.

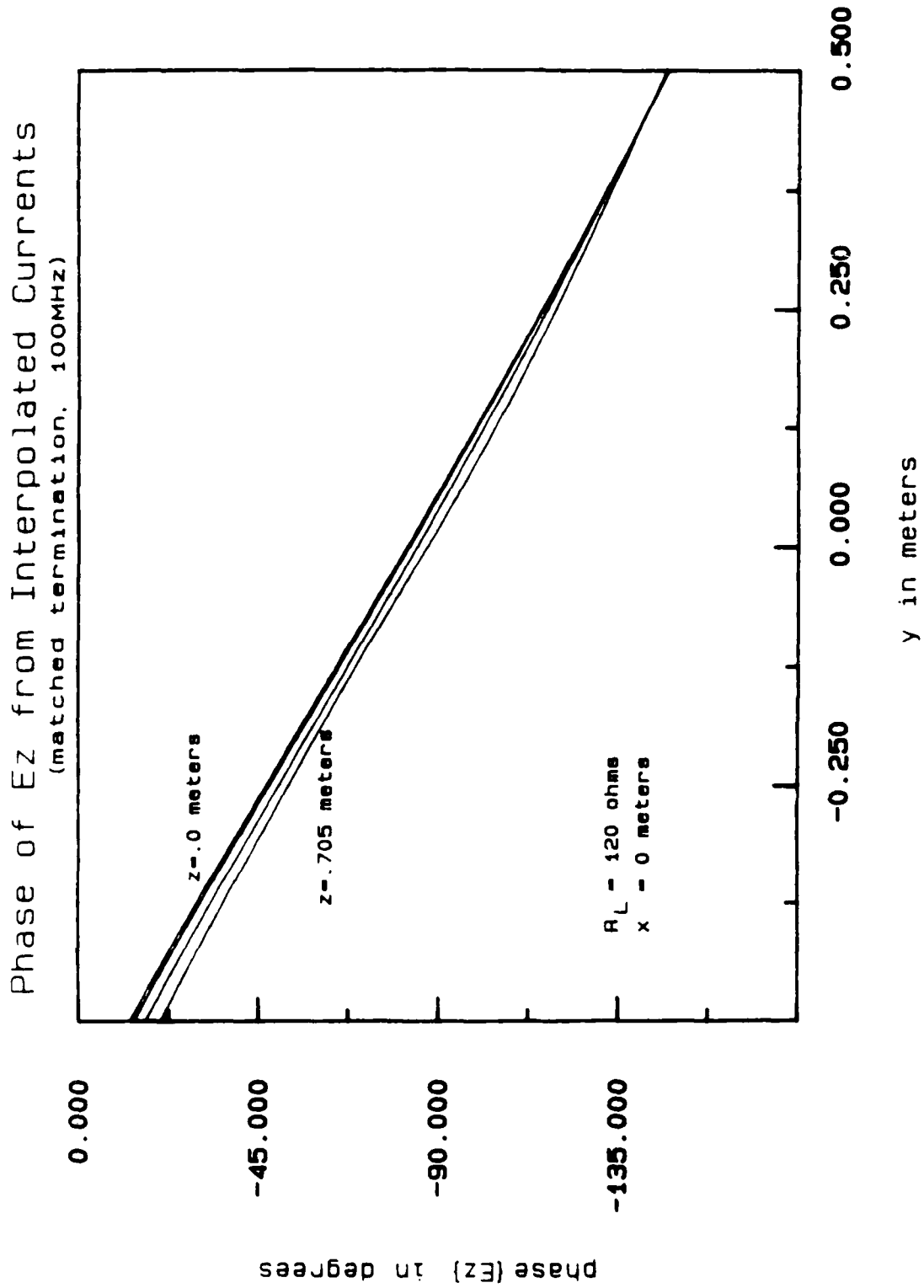


Figure 3.22. (b) Phase of E_z .

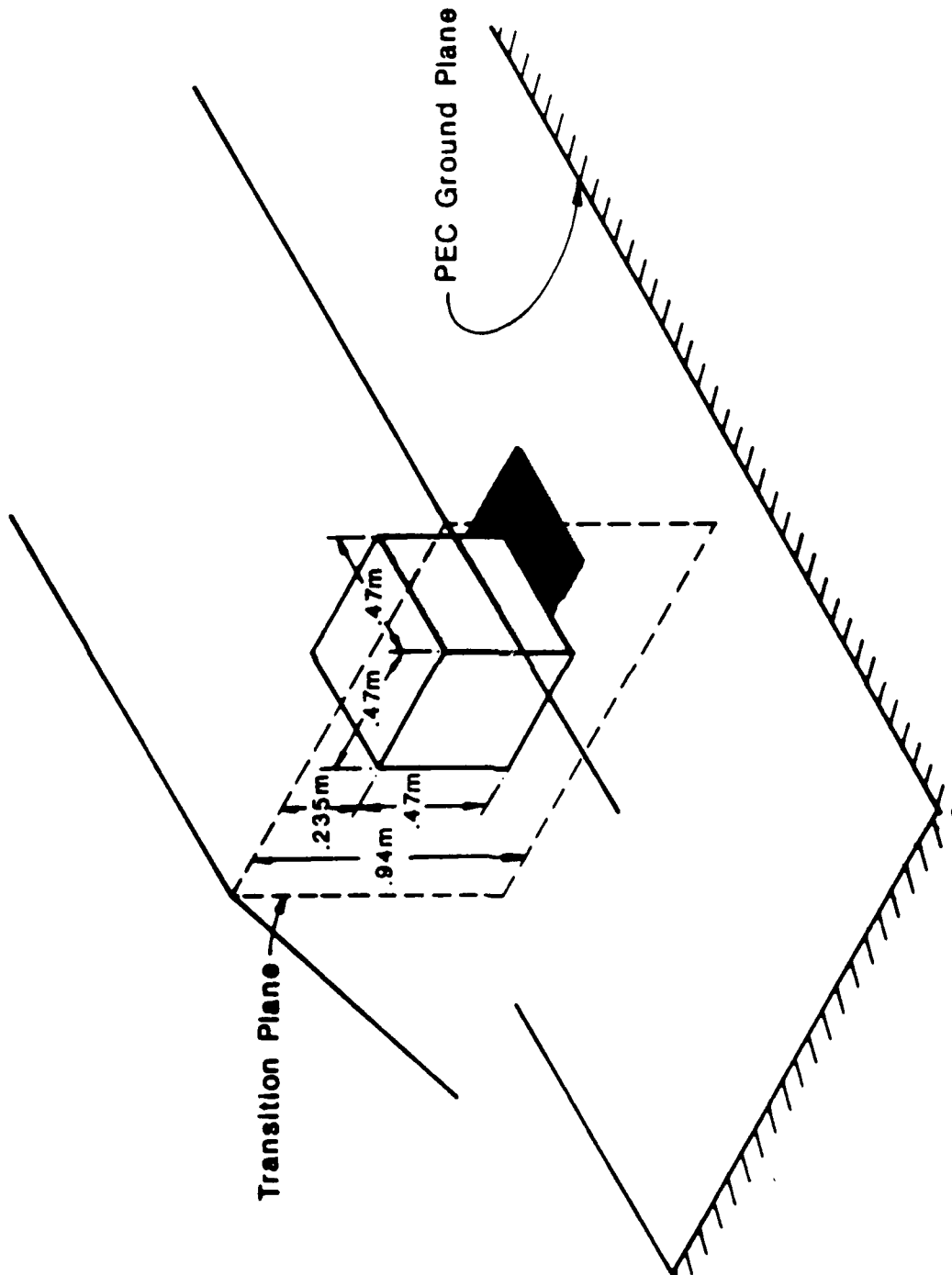
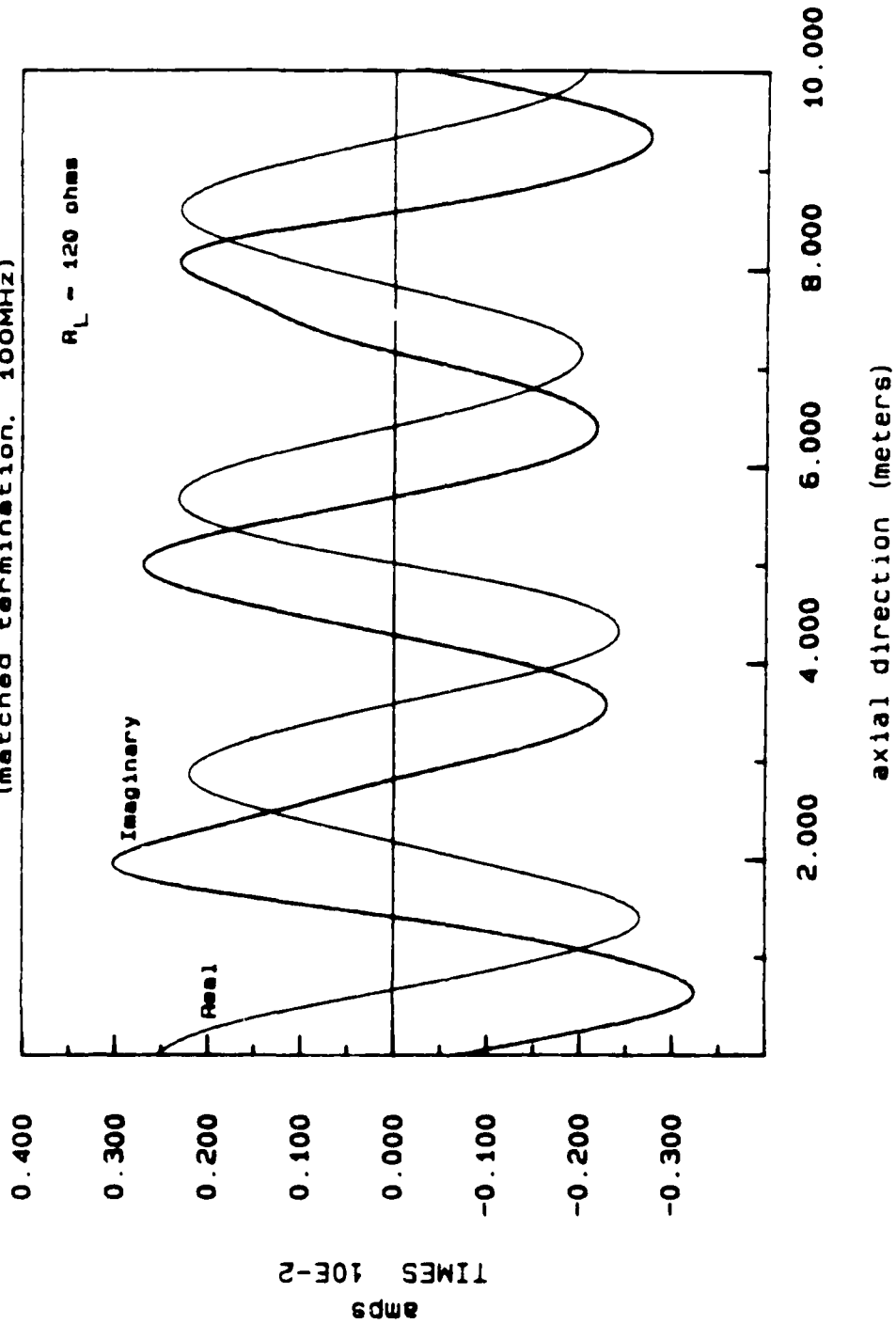


Figure 3.2.3. Cubic obstacle placed in the working volume, with the front face lying in the transition plane and placed symmetrically in the vertical and horizontal directions with respect to the parallel plate.

Edge Wire Current with Empty W.V.
(matched termination, 100MHz)



(a) Empty working volume.

Figure 3.24. Edge wire currents produced by a 100 MHz excitation.

Edge Wire Current with Obstacle in W.V.
(matched termination, 100MHz)

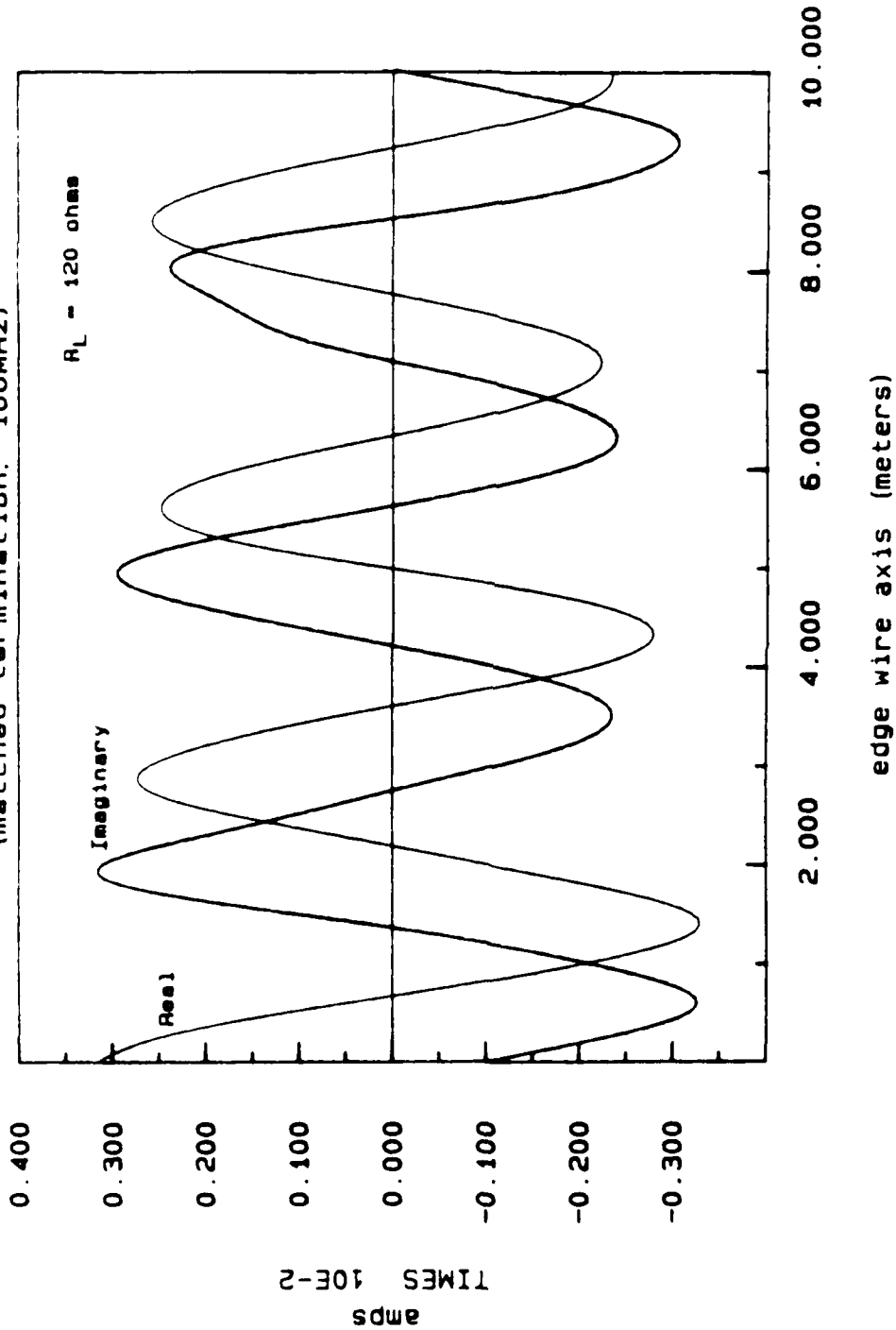


Figure 3.24. (b) Cubic obstacle in the working volume.

Obstacle-Simulator Interaction (matched termination, 100MHz)

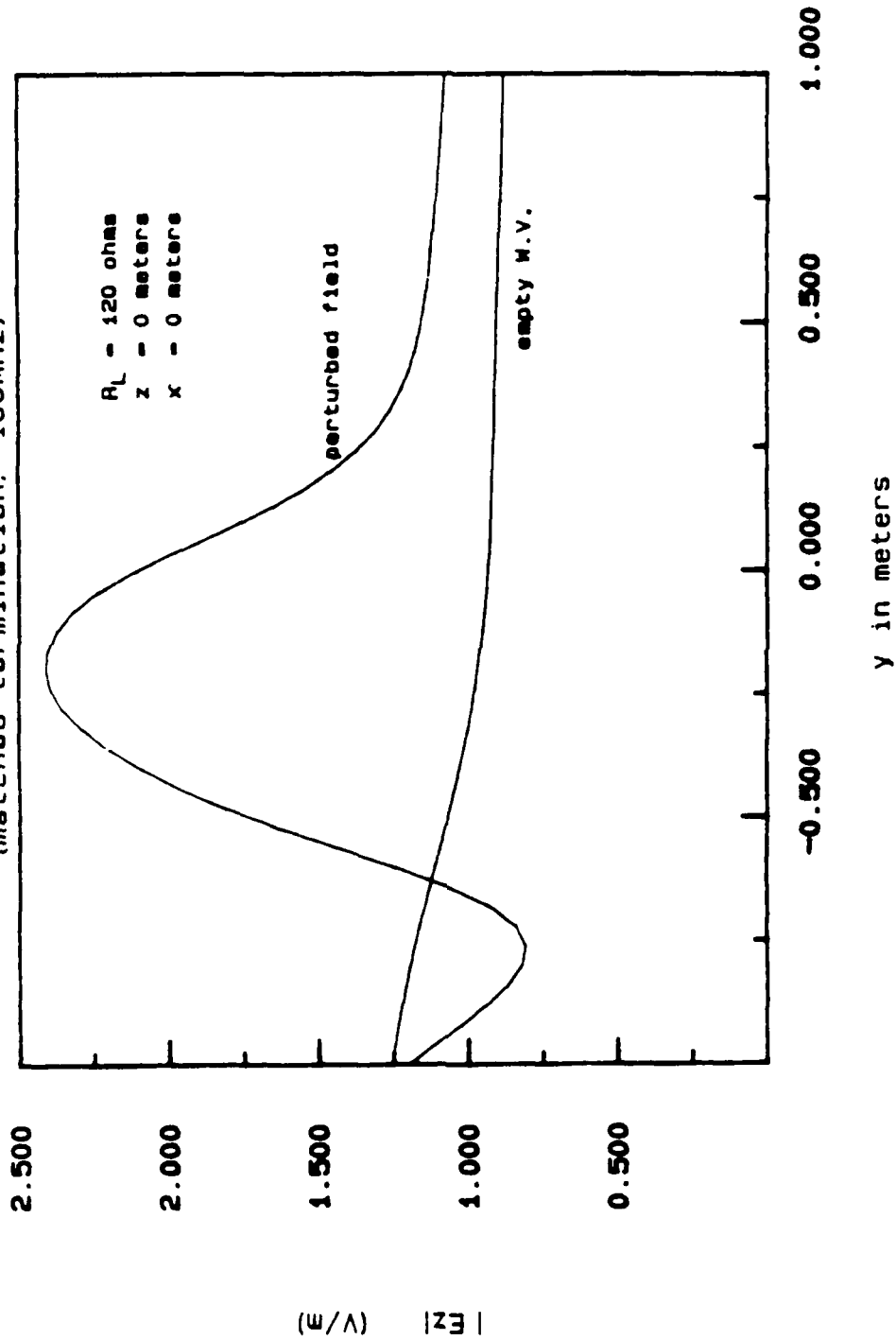


Figure 3.25. Vertical E-field computed along the ground plane of the 450 MHz bandwidth ACHATES EMP simulator. Comparison of fields in the empty working volume, with the perturbed fields in the presence of the obstacle.

Obstacle-Simulator Interaction (matched termination, 100MHz)

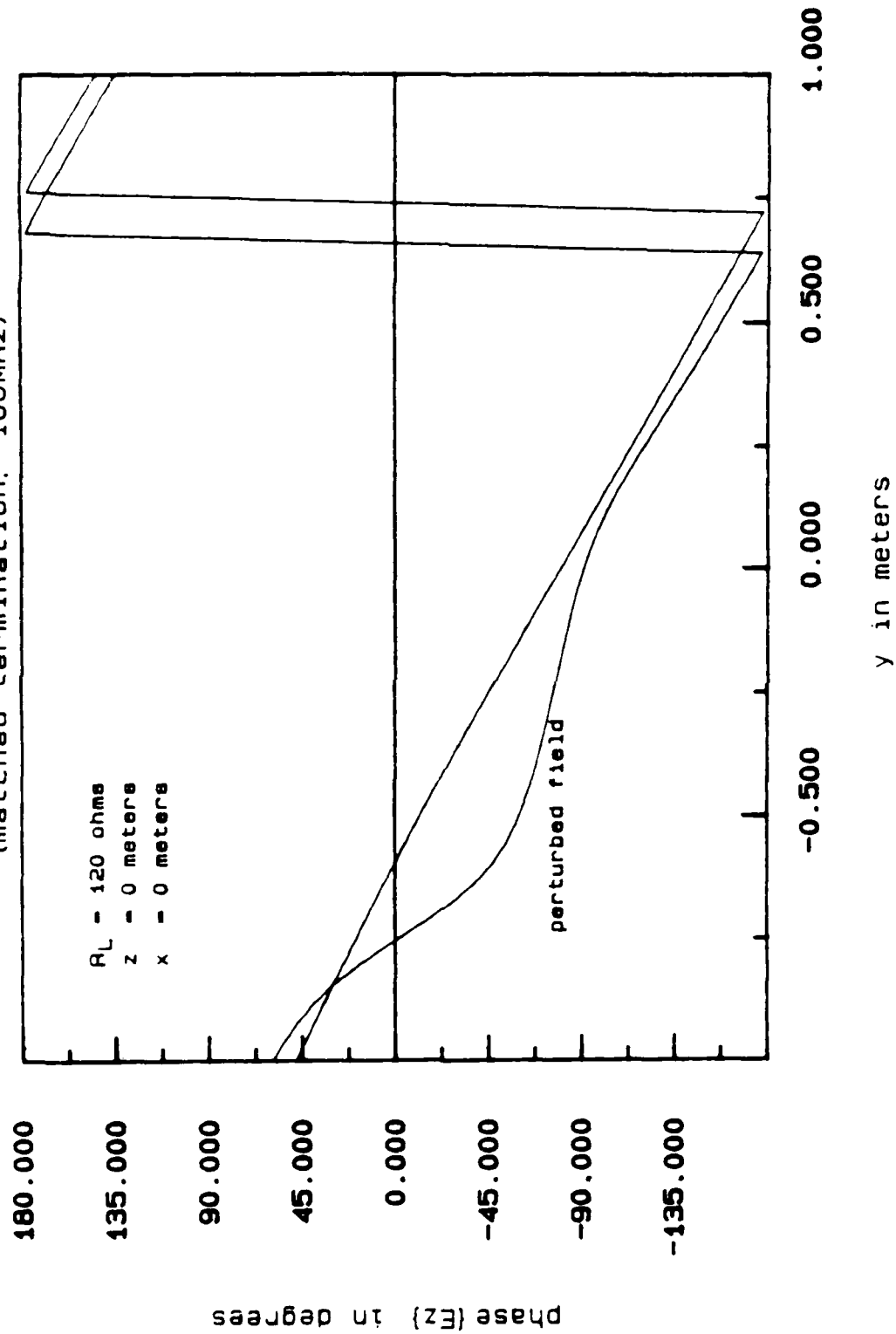


Figure 3.25. (b) Phase of E_z .

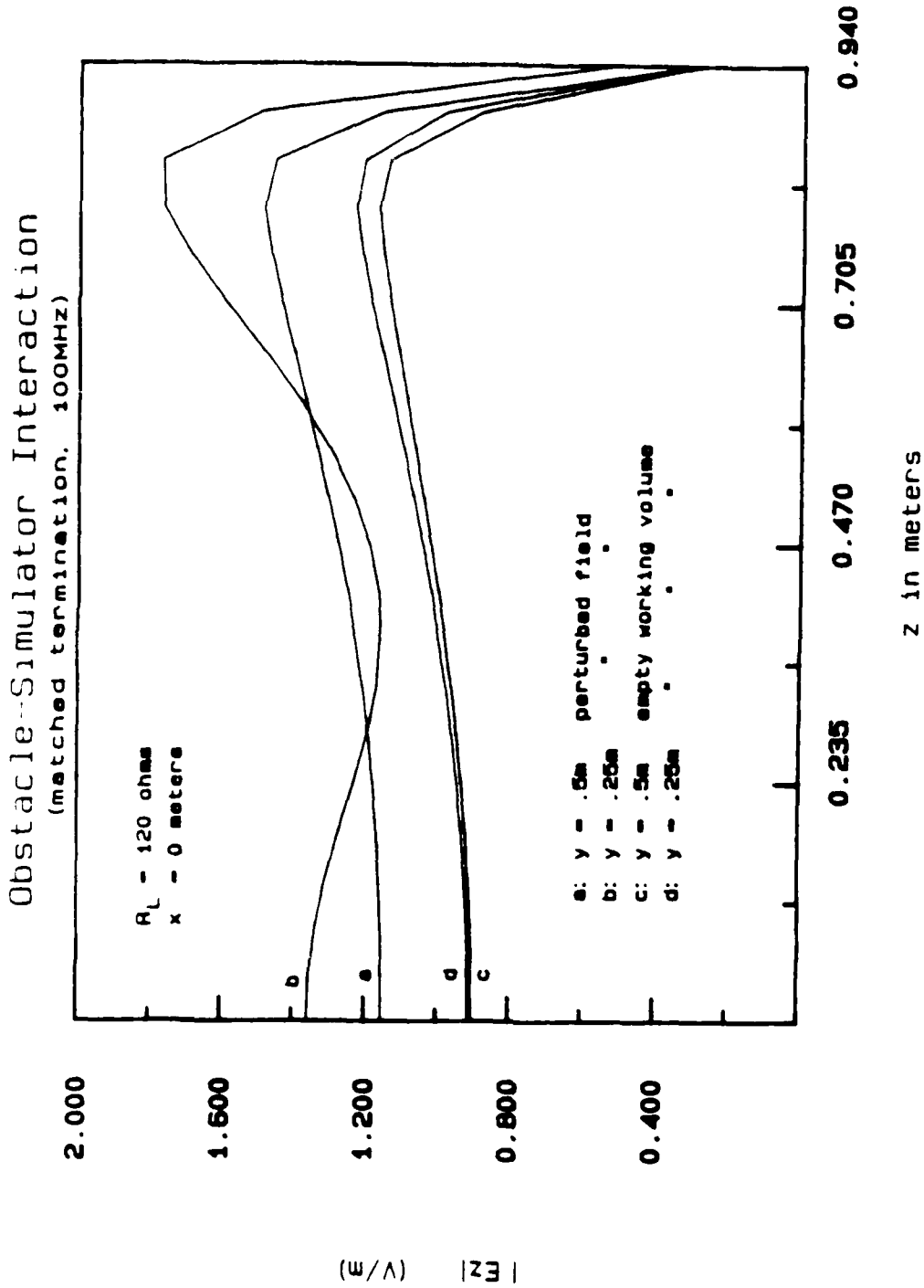


Figure 3.26. Vertical E-field computed in the vertical direction, behind the location of the cubic obstacle. Comparison of fields in the empty working volume with the perturbed fields in the presence of the obstacle.

Obstacle-Simulator Interaction

(matched termination, 100MHz)

$R_L = 120 \text{ ohms}$
 $x = 0 \text{ meters}$

- a: $y = .5m$ perturbed field
- b: $y = .25m$
- c: $y = .5m$ empty working volume
- d: $y = .25m$

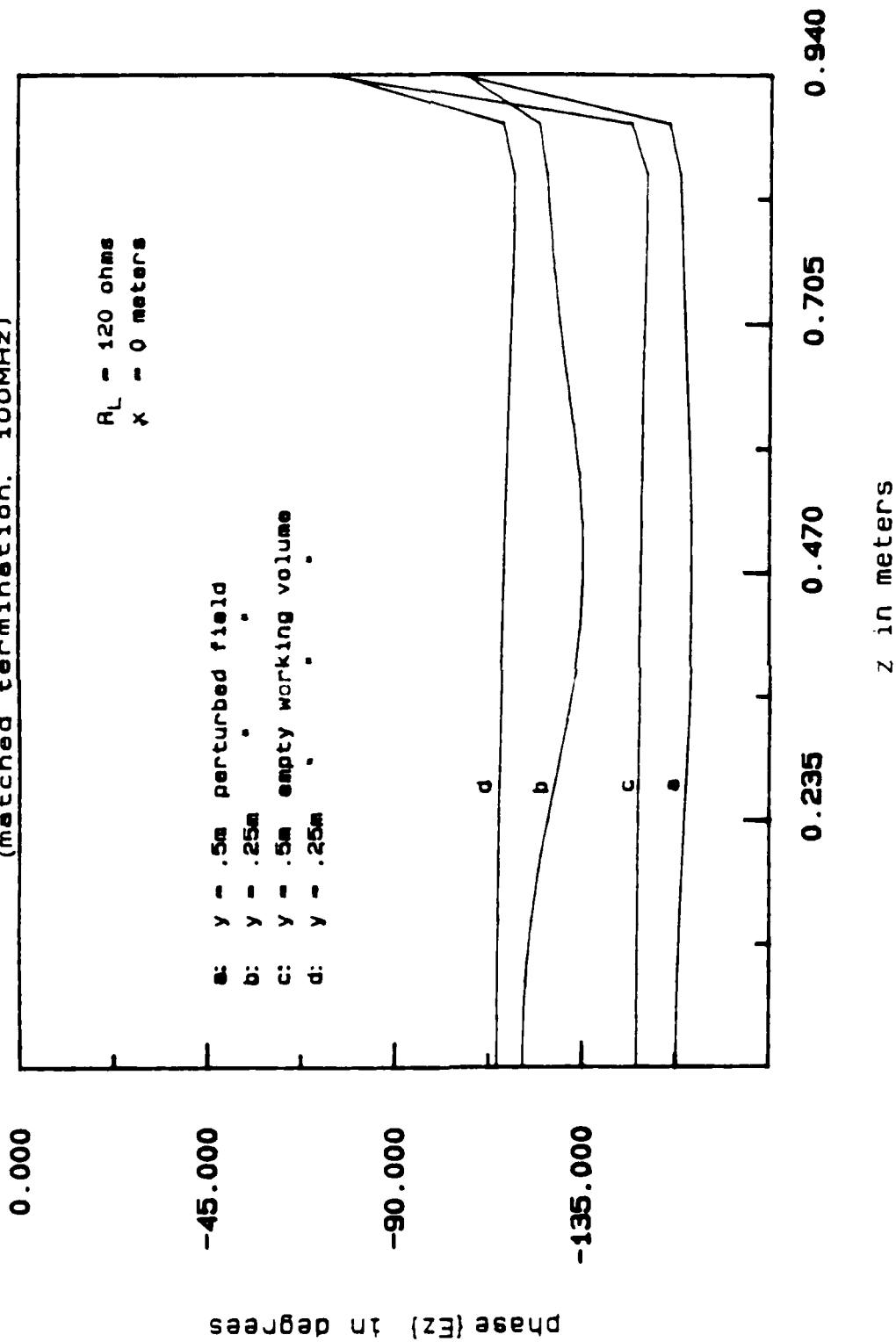
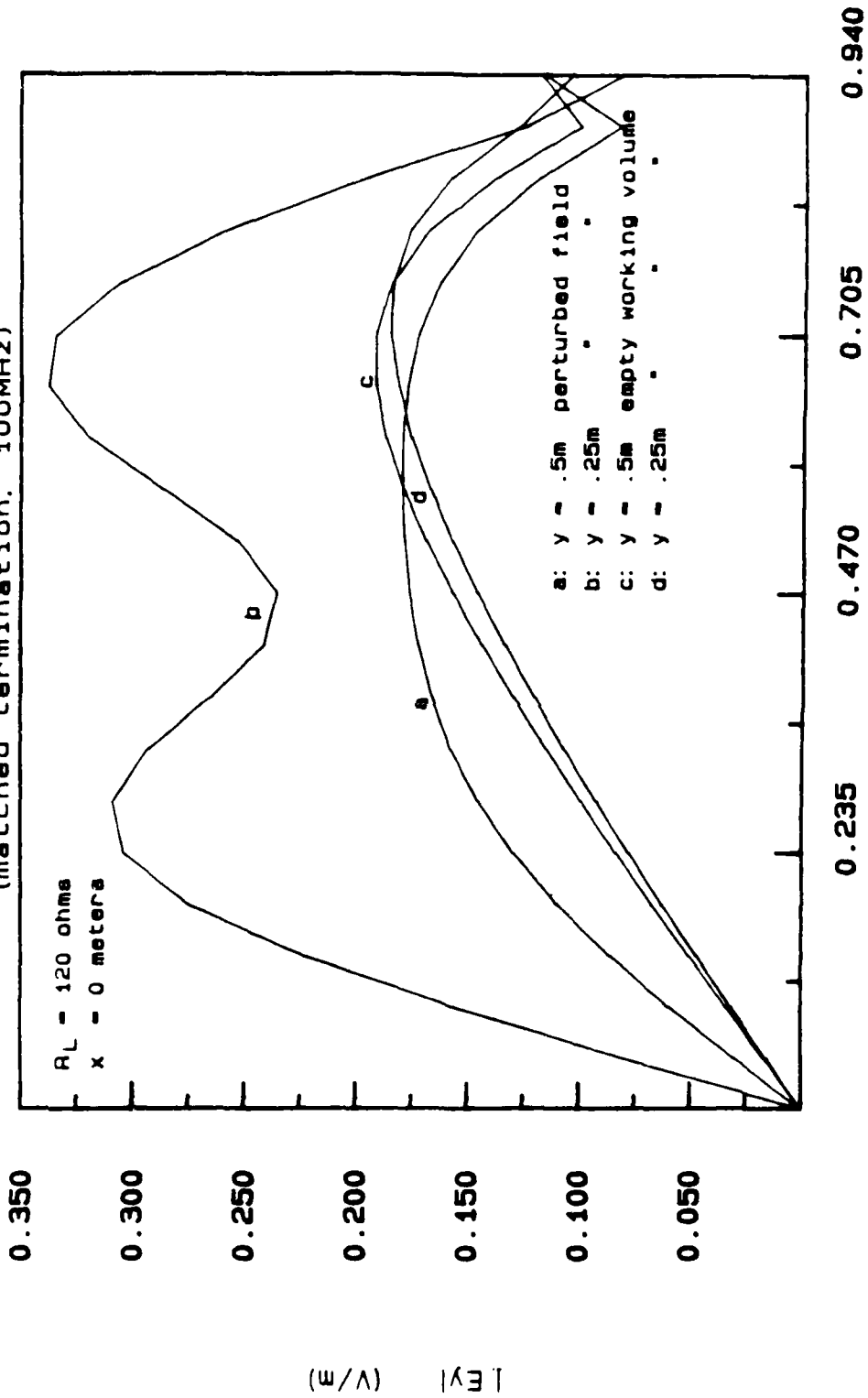


Figure 3.26. (b) Phase of E_z .

Obstacle-Simulator Interaction

(matched termination, 100MHZ)



z in meters

(a) Magnitude of E_z .

Figure 3.27. Longitudinal E-field computed in the vertical direction, behind the location of the cubic obstacle. Comparison of fields in the empty working volume with the perturbed fields in the presence of the obstacle.

CHAPTER 4

CONCLUDING REMARKS

The primary objective of this thesis was to develop the characteristics of a parallel-plate bounded transmission line simulator by scattering theory, using a thin-wire mesh approximation of the conducting surfaces and the Numerical Electromagnetics Code (NEC) [22]. It was found that NEC, which is a user-oriented computer code that offers a moment method solution of thin-wire scattering problems, can be an extremely useful tool for analyzing this problem. In order to develop the wire mesh model and an understanding of the limitations associated with it, Chapter 2 focused on developing complicated thin-wire scattering problems that in turn could be related to the parallel-plate simulator. The emphasis was placed on determining the limitations of the wire mesh approximation and developing a proper source and load model for the parallel-plate simulator.

In Chapter 2, the rhombic EMP simulator was analyzed. The rhombic simulator, like the parallel-plate simulator, is a transmission-line type of simulator. The source and load models were developed using a thin-wire approximation, and the resultant characteristics of the simulator were compared to theoretical and experimental data published by Shen and King of Harvard University [28,29]. The general characteristics, as well as the thin-wire conducting current and electric field distributions within the center region, compared extremely well with Shen and King's. It was found that at very high frequencies, when the source and load gaps are greater than 0.1λ , significant error in the value of the matched terminations occurs due to the wire segment approximation of the source and load. It is interesting that even though the value of the matched termination was in error, the currents and fields still compared extremely well with the results of Shen and King under matched conditions.

In Chapter 2 the thin-wire mesh approximation of a square PEC plate scatterer was employed in order to evaluate the limitations encountered in approximating a finite width flat conducting surface. The plate was illuminated by a normally incident TE plane wave and the currents induced on the plate were computed by NEC using the wire mesh approximation. These results were compared to those derived by a spectral Galerkin technique, solved by conjugate gradients. The wire mesh approximation provided an excellent approximation of the surface currents. However, it did not reproduce the edge singularity even when a reasonable number of unknowns were used to represent the current.

The incident E-field was chosen to be polarized in a direction parallel to an edge of the plate, which is referred to as the longitudinal direction. This was done such that the currents would be highly oriented in one direction, and extremely small in the transverse direction. The transverse currents, which are at least an order of magnitude smaller than the longitudinal currents, suffered a large amount of error. The reason for the error is due to the limited number of unknowns as well as large discontinuities encountered at the multiple wire junctions in the wire mesh. Furthermore, the discontinuities are a result of the enforcement of Kirchoff's current law on the axial currents entering each multiple wire junction. These current discontinuities, which exist in both the transverse and longitudinal directions, will lead to nonphysical singularities in the near electric field. Therefore, one must be careful as to how close the E-field can be computed to the wire mesh surface before suffering from singular distortion.

In Chapter 3, the conducting surface of the parallel-plate bounded wave simulator was approximated by a wire mesh which was developed using the results obtained from the examples studied in Chapter 2. The well-defined geometry of the ACHATES EMP simulator [34] was modeled. The NEC was used to solve for the

currents induced on the wire mesh due to a continuous wave excitation across the source gap. Using these results, the characteristics of the simulator were established over a broad-frequency region. The field distributions in the parallel-plate region, under matched conditions, were computed and shown to be predominately TEM for low frequencies with a linear progressive phase shift. However, at higher frequencies, when the operating wavelength was near that of the cutoff frequency of the simulator, higher-order modes became significant due to the mismatch of the conical tapered end section and the parallel-plate waveguide. As a result, the field distribution greatly deviates from the desired uniform characteristics. Finally, the wire mesh model was used to analyze the changes in the characteristics of the simulator when a large test object was placed in the working volume. It was found that a cube of side length equal to one-half of the height of the parallel plate above ground, placed symmetrically in the working volume, has a small effect on the characteristic impedance and the surface currents of the simulator. This small change introduces a small distortion to the field incident upon the test object. The simulator-obstacle interaction is important to understand when using the EMP simulator as a testing device, and is worthy of further investigation using similar techniques described in this thesis.

Overall, the Numerical Electromagnetics Code provides an extremely useful, and relatively simplistic, analysis of the parallel-plate bounded-wave simulator. However, it is an approximation that is not without its limitations. Initially the source and load gaps are limited to a one-dimensional thin-wire model of the two-dimensional gap. For the rhombic simulator, this had an effect on the characteristic impedance at higher frequencies. Furthermore, the wire mesh approximation introduces discontinuities in the currents which lead to nonphysical singularities in the near electric fields, whereas it was determined that fields computed at distances beyond $\frac{\lambda}{12}$ from the surface suffer little singular distortion. Finally, the number of

unknowns needed to approximate the conducting currents can become very large, since the simulator is generally much larger than a wavelength in the mid-frequency region. This limits the analysis of the high-frequency region for large simulators. Consequently, despite the limitations mentioned above, the technique of analysis mentioned herein provides a useful tool in the analysis of the parallel-plate bounded-wave EMP simulator in the low- and mid-frequency regions.

REFERENCES

- [1] Carl E. Baum, "Impedance and field distributions for parallel plate transmission line simulators." Sensor and Simulation Note 21, Air Force Weapons Laboratory, Kirtland AFB, NM, 6 June 1966.
- [2] T. L. Brown, and K.D. Granzow, "A parameter study of two parallel-plate transmission line simulators of EMP Sensor and Simulation Note 21." Sensor and Simulation Note 52, Air Force Weapons Laboratory, Kirtland AFB, NM, 19 April 1968.
- [3] C. E. Baum, D. V. Giri, and R. D. Gonzalez, "Electromagnetic field distribution of the TEM mode in a symmetrical two-parallel-plate transmission line." Sensor and Simulation Note 219, Air Force Weapons Laboratory, Kirtland AFB, NM, 1 April 1976.
- [4] F. C. Yang and K. S. H. Lee, "Impedance of a two-conical-plate transmission line." Sensor and Simulation Note 221, Air Force Weapons Laboratory, Kirtland AFB, NM, November 1976.
- [5] F. C. Yang and L. Marin, "Field distributions on a two-conical-plate and curved cylindrical-plate transmission line." Sensor and Simulation Note 229, Air Force Weapons Laboratory, Kirtland AFB, NM 87117, September 1977.
- [6] N. Marcuvitz, *Waveguide Handbook*, N.Y.: McGraw-Hill, 1951.
- [7] L. Marin, "Modes on a finite-width, parallel-plate simulator, I. Narrow plates." Sensor and Simulation Note 201, Air Force Weapons Laboratory, Kirtland AFB, NM, September 1974.
- [8] T. Itoh and R. Mittra, "Analysis of modes in a finite width parallel-plate waveguide." Sensor and Simulation Note 208, Air Force Weapons Laboratory, Kirtland AFB, NM, January 1975.
- [9] L. Marin, "Modes on a finite-width, parallel-plate simulator, II. Wide plates." Sensor and Simulation Note 223, Air Force Weapons Laboratory, Kirtland AFB, NM, November 1977.
- [10] L. Marin and G. C. Lewis, Jr., "Modes on a finite-width parallel-plate simulator, III. Numerical results for modes on wide plates." Sensor and Simulation Note 227, Air Force Weapons Laboratory, Kirtland AFB, NM, September 1977.
- [11] A. M. Rushdi, R. C. Menendez, R. Mittra and S.W. Lee, "Leaky modes in parallel plate EMP simulators." *IEEE Transactions on Electromagnetic Compatibility*, vol. EMC-20, pp. 443-451, August 1978.
- [12] V. Krichevsky, "Source excitation of an open, parallel-plate waveguide, numerical results." Sensor and Simulation Note 254, Air Force Weapons Laboratory, Kirtland AFB, NM, August 1978.

- [13] C-H. Tsao, E. Yung and R. Mittra, "The source excitation of a finite-width parallel-plate waveguide," *Sensor and Simulation Note 255*, Air Force Weapons Laboratory, Kirtland AFB, NM, February 1979.
- [14] J. Lam, "Excitation of the parallel-plate section of a bounded-wave EMP simulator by a conical transmission line," *Sensor and Simulation Note 263*, Air Force Weapons Laboratory, NM, 31 May 1979.
- [15] C. E. Baum, "The conical transmission line as a wave launcher and terminator for a cylindrical transmission line," *Sensor and Simulation Note 31*, Air Force Weapons Laboratory, Kirtland AFB, NM, 16 January 1967.
- [16] R. W. P. King and D. J. Blejer, "The electromagnetic field in an EMP simulator at high frequency," *IEEE Transactions on Electromagnetic Compatibility*, vol. EMC-21, pp. 263-269, August 1979.
- [17] D. V. Giri, T. K. Liu, F. M. Tesche and R. W. P. King, "Parallel-plate transmission line type of EMP simulators: A systematic review and recommendations," *Sensor and Simulation Note 261*, Air Force Weapons Laboratory, Kirtland AFB, NM, 1 April 1980.
- [18] R. W. Latham, "Interaction between a cylindrical test body and a parallel-plate simulator," *Sensor and Simulation Note 55*, Air Force Weapons Laboratory, NM, May 1978.
- [19] C. D. Taylor and G. A. Steigerwald, "On the pulse excitation of a cylinder in a parallel-plate waveguide," *Sensor and Simulation Note 99*, Air Force Weapons Laboratory, Kirtland AFB, NM, March 1970.
- [20] L. Marin, "A cylindrical post above a perfectly conducting plate, II (dynamic case)," *Sensor and Simulation Note 136*, Air Force Weapons Laboratory, Kirtland AFB, NM, August 1971.
- [21] A. D. Varvatsis and M. I. Sancer, "Electromagnetic interaction between a perfectly conducting sphere and a two-parallel-plate simulator, I (top plate removed)," *Sensor and Simulation Note 140*, Air Force Weapons Laboratory, Kirtland AFB, NM, October 1971.
- [22] G. J. Burke and A. J. Poggio, "Numerical Electromagnetics Code (NEC) - method of moments," *Naval Ocean Systems Center Technical Document 116*, volumes I and II, Lawrence Livermore Laboratory, January 1981.
- [23] K. A. Al-Badwaihy and J. L. Yen, "Extended boundary condition integral for perfectly conducting and dielectric bodies: Formulation and uniqueness," *IEEE Transactions on Antennas and Propagation*, vol. AP-23, July 1975.
- [24] R. F. Harrington, *Field Computations by Moment Methods*, N.Y.: MacMillan, 1968.
- [25] B. Halpern and R. Mittra, "On the use of the Numerical Electromagnetics Code (NEC) to solve for the input impedance and radiative efficiency of loaded, thin-wire antennas," Presented at the 1985 Antenna Applications Symposium, Robert Allerton Park, Monticello, IL, Sponsored by RADC and the University of Illinois, Champaign-Urbana, September 18-20, 1985.

- [26] Edward C. Jordan and Keith G. Balmain, *Electromagnetic Waves and Radiating Systems*, 2nd Ed. N.J.: Prentice-Hall, 1968.
- [27] A. E. Harper, *Rhombic Antenna Design*, N.Y.: D. Van Nostrand Co., Inc., 1941.
- [28] H. M. Shen and R. W. P. King, "The rhombic EMP simulator," *IEEE Transactions on Electromagnetic Compatibility*, vol. EMC-24, pp. 255-265, May 1982.
- [29] H. M. Shen and R. W. P. King, "Experimental investigation of the rhombic EMP simulator: Comparison with theory and parallel-plate simulator," *IEEE Transactions on Electromagnetic Compatibility*, vol. EMC-24, pp. 349-355, August 1982.
- [30] H. M. Shen and R. W. P. King, "An experimental investigation of the rhombic EMP simulator under pulse excitation," *IEEE Transactions on Electromagnetic Compatibility*, vol. EMC-25, pp. 40-46, February 1983.
- [31] H. M. Shen and R. W. P. King, "Theoretical analysis of the rhombic simulator under pulse excitation," *IEEE Transactions on Electromagnetic Compatibility*, vol. EMC-25, pp. 47-55, February 1983.
- [32] Scott L. Ray and Raj Mittra, "Spectral iteration analysis of electromagnetic radiation and scattering problems," EM Report No. 84-11, University of Illinois, Urbana, IL, 1984.
- [33] A. W. Glisson, "On the development of numerical techniques for treating arbitrary surfaces," Ph.D. dissertation, University of Mississippi, University, MS, 1978.
- [34] K. Chen, Capt G. Michaelidis, Carl Baum and D. V. Giri, "ACHATES design," ACHATES Memo no. 1, Air Force Weapons Laboratory, Kirtland AFB, NM, 5 November 1976.
- [35] C.E. Baum, "A sloped admittance sheet plus coplaner conducting flanges as a matched termination of a two-dimensional parallel-plate transmission line," Sensor and Simulation Note 95, Air Force Weapons Laboratory, Kirtland AFB, NM, 31 December 1969.
- [36] David L. Wright, "Sloped parallel resistive rod terminations for two-dimensional parallel-plate transmission lines," Sensor and Simulation Note 103, Air Force Weapons Laboratory, Kirtland AFB, NM, 7 May 1970.
- [37] Carl E. Baum, "General principles for the design of Atlas I and II, part III: additional considerations for the design of the terminations," Sensor and Simulation Note 145, Air Force Weapons Laboratory, Kirtland AFB, NM, 3 January 1972.
- [38] Cornelius Lanczos, *Applied analysis*, 3rd Ed. N.J.: Prentice-Hall, 1964.

DISTRIBUTION

Chief of Engineers

ATTN: CEEC-E (2)
ATTN: CERD-L
ATTN: CEIM-SL (2)

FESA, ATTN: Library 22060
ATTN: DET III 79906

US Army Engineer Districts
ATTN: Library (41)

US Army Engineer Divisions
ATTN: Library (14)

US Army Engineer District
Omaha 68102
ATTN: Chief, Engr Div

US Army Engineer Division
Huntsville 35807
ATTN: Chief, HNDED-SR

USA NATICK
R&D Cntr 01760-5017

Naval Air Systems Command
ATTN: Library

Hanson AFB, MA 01731
ATTN: HQ AFSC
ATTN: ESD/OCR-3

Naval Civil Engr Lab
ATTN: Library 93041

Harry Diamond Labs 20783
ATTN: DELHD-NW-E
ATTN: DELHD-NW-EA
ATTN: DELHD-NW-EC
ATTN: DELHD-NW-ED
ATTN: DELHD-NW-EE

US Govt Print Office 22304
Receiving Sect/Depository Copies (2)

Defense Technical Info. Center 22314
ATTN: DDA (2)

September 1987
(79)

END

FEB.

1988

DTIC